STATE OF CALIFORNIA DEPARTMENT OF TRANSPORTATION

TECHNICAL REPORT DOCUMENTATION PAGE

TR0003 (REV. 10/98)

1. REPORT NUMBER	2. GOVERNMENT ASSOCIATION NUMBER	3. RECIPIENT'S CATALOG NUMBER
CA09-1974		

4. TITLE AND SUBTITLE	5. REPORT DATE
Experimental and Computational Evaluation of Current and Innovative In-Span Hinge Details in Reinforced Concrete Box-Girder Bridges Part 1: Experimental Findings and Pre-Test Analysis	January 2009
	6. PERFORMING ORGANIZATION CODE

7. AUTHOR(S)	8. PERFORMING ORGANIZATION REPORT NO.
Matias A. Hube & Khalid M. Mosalam	PEER 2008/103

9. PERFORMING ORGANIZATION NAME AND ADDRESS	10. WORK UNIT NUMBER
Department of Civil and Environmental Engineering Pacific Earthquake Engineering Research Center College of Engineering University of California, Berkeley	11. CONTRACT OR GRANT NUMBER 59A0508

12. SPONSORING AGENCY AND ADDRESS	13. TYPE OF REPORT AND PERIOD COVERED
California Department of Transportation Division of Research and Innovation, MS-83 1227 O Street Sacramento CA 95814	Final Report
	14. SPONSORING AGENCY CODE

15. SUPPLEMENTAL NOTES

16. ABSTRACT

During the last three decades, considerable research efforts have sought to improve the seismic design of California highway bridges. However, the in-span hinge regions of concrete box girders have not been studied adequately. In-span hinges are classified as disturbed regions due to the concentrated bearing loads and the possible existence of utility and maintenance openings, which induce a three-dimensional (3D) behavior. Nevertheless, in-span hinges are commonly designed as two-dimensional (2D) short cantilevers, following standard procedures in ACI318. These designs typically lead to congested reinforcement, causing constructability concerns from practical and economic aspects. In this study, the strength of in-span hinges is assessed using a combined computational and experimental approach. For the experimental approach, five 1/3-scale specimens were tested at the University of California, Berkeley. The computational approach adopts nonlinear 3D finite elements that consider embedded reinforcement and cracking behavior for the concrete. As a result of this study, the failure modes are identified and realistic idealizations of the behavior and strength of the in-span hinges are developed aiming toward an improved design for better constructability of these disturbed regions. The findings from the experimental results revealed that in-span hinges fail with a combination of three failure modes: (1) one-dimensional shear, (2) 2D strut-and-tie, and (3) punching shear.

17. KEY WORDS	18. DISTRIBUTION STATEMENT	
Bridge, Hinge, RC Box Girder	No restrictions. This document is available to the public through the National Technical Information Service, Springfield, VA 22161	
19. SECURITY CLASSIFICATION (of this report)	20. NUMBER OF PAGES	21. PRICE
Unclassified	200	

DISCLAIMER STATEMENT

This document is disseminated in the interest of information exchange. The contents of this report reflect the views of the authors who are responsible for the facts and accuracy of the data presented herein. The contents do not necessarily reflect the official views or policies of the State of California or the Federal Highway Administration. This publication does not constitute a standard, specification or regulation. This report does not constitute an endorsement by the Department of any product described herein.

For individuals with sensory disabilities, this document is available in Braille, large print, audiocassette, or compact disk. To obtain a copy of this document in one of these alternate formats, please contact: the Division of Research and Innovation, MS-83, California Department of Transportation, P.O. Box 942873, Sacramento, CA 94273-0001.

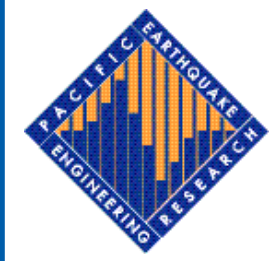

PACIFIC EARTHQUAKE ENGINEERING
RESEARCH CENTER

Experimental and Computational Evaluation of Current and Innovative In-Span Hinge Details in Reinforced Concrete Box-Girder Bridges

Part 1: Experimental Findings and Pre-Test Analysis

Matias A. Hube
Khalid M. Mosalam

University of California, Berkeley

PEER 2008/103
JANUARY 2009

Experimental and Computational Evaluation of Current and Innovative In-Span Hinge Details in Reinforced Concrete Box-Girder Bridges

Part 1: Experimental Findings and Pre-Test Analysis

Matias A. Hube
Department of Civil and Environmental Engineering
University of California, Berkeley

Khalid M. Mosalam
Department of Civil and Environmental Engineering
University of California, Berkeley

PEER Report 2008/103
Pacific Earthquake Engineering Research Center
College of Engineering
University of California, Berkeley

January 2009

ABSTRACT

During the last three decades, considerable research efforts have sought to improve the seismic design of California highway bridges. However, the in-span hinge regions of concrete box-girders have not been studied adequately. In-span hinges are classified as disturbed regions due to the concentrated bearing loads and the possible existence of utility and maintenance openings, which induce a three-dimensional (3D) behavior. Nevertheless, in-span hinges are commonly designed as two-dimensional (2D) short cantilevers, following standard procedures in ACI318. These designs typically lead to congested reinforcement, causing constructability concerns from practical and economic aspects. In this study, the strength of in-span hinges is assessed using a combined computational and experimental approach. For the experimental approach, five 1/3-scale specimens were tested at the University of California, Berkeley. The computational approach adopts nonlinear 3D finite elements that consider embedded reinforcement and cracking behavior for the concrete. As a result of this study, the failure modes are identified and realistic idealizations of the behavior and strength of the in-span hinges are developed aiming toward an improved design for better constructability of these disturbed regions. The findings from the experimental results revealed that in-span hinges fail with a combination of three failure modes: (1) one-dimensional shear, (2) 2D strut-and-tie, and (3) punching shear.

ACKNOWLEDGMENTS

This study was made possible by funding from the California Department of Transportation under contract number 59A0508. We would like to thank Craig Whitten, Fadel Alameddine, and Steve Sahs for the technical participation during the design and testing phases of this research program. Additionally, we would like to thank Jeffrey Kress for guiding the visits at the construction site in San Rafael.

The experiments presented in this report were conducted in the structural laboratory of Davis Hall, University of California, Berkeley. The assistance during testing from Bill MacCracken, Jeff Higginbotham, Richard Parson, and Chris Moy is greatly appreciated. We would also like to thank Dr. Shakhzod Takhirov of the Richmond Field Station for his assistance with the load cell construction and instrumentation setup. Thanks are also due students Daniel Wilcoxon, Mathew Gomez, Elyse Wong, and Kristopher Darnell for their assistance with the test setup.

The headed reinforcement used in the specimens was donated by Headed Reinforcement Corporation, HRC. The conventional reinforcing steel bars were donated by Concrete Reinforcing Steel Institute (CRSI). Both donations are gratefully acknowledged.

The support of the Pacific Earthquake Engineering Research Center (PEER) in publishing this report is gratefully acknowledged. The authors specifically thank Ms. Janine Hannel, Senior Publications Coordinator, for her editing of the report.

CONTENTS

LIST OF FIGURES

LIST OF TABLES

1 Introduction

Reinforced concrete (RC) box-girder bridges (with and without prestressing) are used extensively in California and throughout the world. The 1994 Northridge, California, earthquake caused the partial or complete collapse of 5 bridges, and damaged approximately 200 others (EERI 2005). The California Department of Transportation (Caltrans) has been developing design provisions for bridges based on significant research performed in the last three decades. The research has been focused mainly on the seismic design of columns, foundations, bent caps, and decks. Nevertheless, some issues of RC bridge design have still not been studied adequately. This is the case for the in-span hinges of RC box girders, which are located at the bridge deck and are used mainly to transmit vertical loads between two adjacent parts of the deck. Figure 1.1 shows photographs of in-span hinges in California bridges.

(a) Interstate 580 connector, San Rafael (b) Interstate 80 connector, Albany

Fig. 1.1 In-span hinges in RC box-girder bridges.

In-span hinges are necessary in RC box-girder bridges for two reasons (Caltrans 2006). The first reason is to accommodate the longitudinal expansion and contraction resulting from prestressed shortening, creep, shrinkage, and temperature variations. The second reason is to

allow independent vibrations of two adjacent bridge frames during an earthquake. If the vibrations of the frames are out-of-phase, large relative displacements may develop. To prevent unseating from such displacements, sufficient seat width and/or unseating prevention devices must be provided. In the transverse direction, hinges are provided with shear keys to transmit lateral shear forces generated by small earthquakes and service loads. For severe earthquakes, the shear keys are designed as sacrificial elements to limit the amount of shear that is transferred between the two adjacent bridge frames (Megally et al. 2002).

1.1 MOTIVATION AND OBJECTIVES

In-span hinges are used mainly to transmit vertical loads from one side of the hinge to the other. From the stress gradient point of view, in-span hinges are classified as disturbed regions characterized by a three-dimensional (3D) behavior induced by the concentrated bearing loads; they may contain utility and maintenance openings. Nevertheless, they are commonly designed as two-dimensional (2D) short cantilevers following standard procedure in ACI318 (ACI 2008; Caltrans 2004). Accordingly, in-span hinges are designed using the sliding shear friction concept, bending moment resistance, and a 2D strut-and-tie (SAT) model. These designs typically lead to congested reinforcement causing constructability concerns from practical and economical aspects.

The overall study program of in-span hinges is shown in Figure 1.2. This report focuses on the tasks shown in boxes 1 to 6. Other tasks in boxes 7 to 13 will be addressed in a future report. The study presented in this report aims at understanding the load path, the failure modes, and the strength of typical in-span hinges designed and constructed in California. This objective is achieved using a combined approach of computational and experimental research. The typical in-span hinge characteristics of California RC box-girder bridges are determined based on a survey of eight projects (box 1, Fig. 1.2). Findings from the experimental results revealed that in-span hinges fail with a combination of three failure modes: (1) one-dimensional (1D) shear, (2) 2D SAT, and (3) punching shear. Based on the experimental and computational results of two typical in-span hinges (phase I), three other specimens are designed and tested in phase II. The design of these specimens in phase II is aimed to reduce the steel congestion and improve the performance of in-span hinges. Another objective of the presented study is to determine the

influence of openings on the behavior and strength of in-span hinges. These openings are mainly introduced for maintenance purposes to allow routine inspection of the bearings.

The experimental results presented in this report will be used in the future to calibrate post-test finite element analysis (FEA) and to develop a nonlinear 3D SAT model, (boxes 8 and 9, Fig. 1.2). Subsequently, these models will be used to perform a parametric study and a reliability analysis of the in-span hinges. The final goal of the overall project is to develop design guidelines for the in-span hinges, which facilitate the hinge construction, inspection, repair, and replacement of the elastomeric or polytetrafluoroethylene (PTFE) bearings. The characteristics of the in-span hinge diaphragms used in this study correspond to configurations of bridges typically constructed in California. However, the final product of the entire study will be general enough to be applicable for box-girder bridges in other places in the U.S. and worldwide.

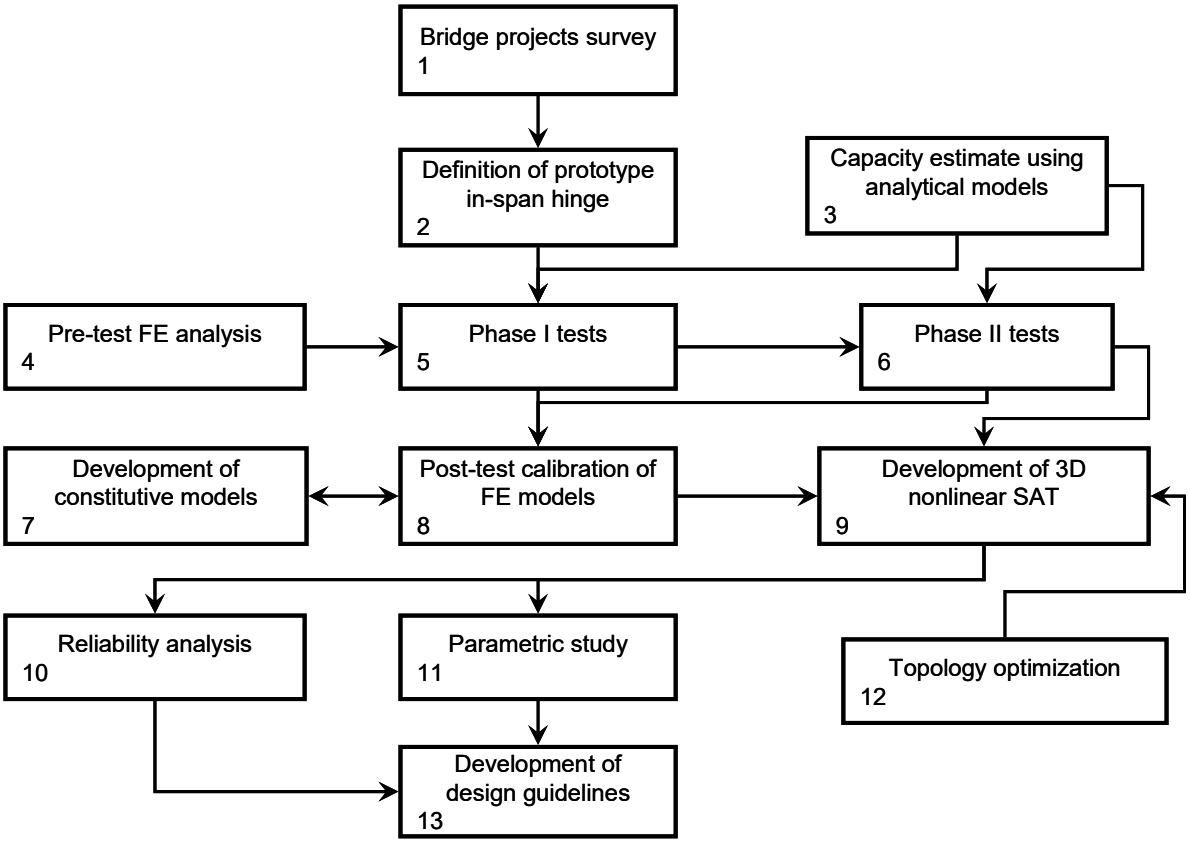

Fig. 1.2 Overview of study program.

1.2 COMPUTATIONAL APPROACH

In-span hinges are subjected to complex 3D loading conditions due to the discrete bearing locations, the small aspect ratio of the seat, and the geometric discontinuities when utility openings exist. Therefore, a 3D nonlinear FEA is conducted to the as-built in-span hinges of phase I. The FEA is intended to provide detailed results of the stress state, damage initiation and propagation, and deformation experienced in the in-span hinges. This task is conducted prior to finalizing the test plans to predict the response of the test specimens for the purpose of confirming the capacity of the test setup and for proper selection of the locations of the instruments.

The 3D FEA is conducted using models developed with concrete brick element having a trilinear displacement field and with embedded reinforcement. The nonlinear behavior of the concrete is modeled using the total strain concept with a rotating-crack model and considering linear tension softening. On the other hand, steel is modeled as an elastic-perfectly-plastic material.

1.3 EXPERIMENTAL APPROACH

For the experimental program, five 1/3-scale specimens are tested in two phases, I and II, in the structural engineering laboratory at the University of California, Berkeley. In the specimen configuration, the bottom half of the in-span hinge is constructed and tested in a 90° rotated position to simplify the loading application to be horizontal instead of vertical. The specimens are subjected to cyclic compression forces at the bearing locations at a quasi-static rate. For phase I, two specimens are tested. These specimens represent the as-built condition of typical in-span hinges of California RC box-girder bridges. Specimen 2 is detailed identical to specimen 1, but it contains utility openings to study the effect of such openings on the structural behavior of in-span hinges.

For phase II, three specimens are designed and tested. The designs of these specimens are based on the experimental results from phase I. Specimen 3 is designed identical to specimen 2 but has a larger loading plate to increase the punching shear capacity. Specimens 4 (without openings analogous to specimen 1) and 5 (with openings analogous to specimen 2) are designed with low reinforcement ratios aiming toward improving the performance and the constructability of in-span hinges.

1.4 ORGANIZATION OF REPORT

The present chapter, as discussed above, motivates the research project and introduces the fundamental aspects of in-span hinges for RC box-girder bridges in California. Chapter 2 presents the background of in-span hinges. In this chapter, a review of eight Caltrans projects is conducted to determine the main characteristics of in-span hinges built in California. Additionally, the in-span hinge design procedures are described. Moreover, Chapter 2 describes details about headed bars, which are extensively used in current designs of the in-span hinges in California.

The development of the experimental program is described in Chapter 3. Based on the review of the eight Caltrans projects in Chapter 2, a prototype in-span hinge is defined as the basis for the experimental program. Subsequently, the test matrix and test subassembly development are discussed. Finally, the test setup, instrumentation, and load protocol are presented at the conclusion of Chapter 3.

Chapter 4 describes the FEA conducted prior to the execution of the experimental program. Modeling aspects of RC in 3D with the use of embedded reinforcement are presented. This FE model is used to predict the behavior and strength of the first two specimens tested in phase I.

The experimental program of phase I is presented in Chapter 5. The design and the experimental results of the first two specimens with as-built in-span hinge characteristics are described in this chapter. The failure mechanism of as-built in-span hinges is identified and the comparison with the pre-test FEA is described. The experimental program of phase II is presented in Chapter 6. Three additional specimens are designed based on the behavior of the as-built in-span hinges of phase I. The test results of these new designs are presented and compared with the results of the as-built in-span hinges. At the end of Chapter 6, the analytical equations to assess the capacity of in-span hinges are discussed in light of the findings from tested specimens in phases I and II.

Finally, Chapter 7 presents the conclusion of this research project. An outline of the proposed future research activities to refine the FE model and perform a parametric study is also presented in this chapter.

Appendix A presents detailed design drawings of the tested five specimens; Appendix B presents the concrete and steel material properties obtained from quality control test specimens; and Appendix C describes the load cells fabrication and calibration.

2 Background

This chapter contains background information related to existing box-girder bridges in California to identify typical in-span hinge characteristics. Additionally, information about in-span hinge design loads and a brief background on headed reinforcement, used in modern details of in-span hinges, are given at the end of this chapter.

2.1 SEAT-WIDTH CALCULATION

To avoid unseating from the relative displacements induced by earthquakes of two adjacent bridge frames, sufficient seat width must be provided at the in-span hinges. To prevent high relative displacement at the in-span hinge, Caltrans (2006) recommends that the fundamental periods of vibration in the longitudinal and transversal directions of two adjacent frames satisfy the following condition:

$$\frac{T_i}{T_j} \geq 0.7 \tag{2.1}$$

where T_i and T_j are the natural periods of the less and more flexible frames, respectively. When the previous equation is not satisfied, the out-of-phase response between the two adjacent frames increases and the probability of unseating and collision also increases. The collision between adjacent frames will transfer seismic demands between each other, which can be critical for the capacity of each individual frame.

The seat width of an in-span hinge has to accommodate thermal movement, prestressed shortening, creep, shrinkage, and the relative earthquake displacement demand between the two frames (Caltrans 2006). The seat width N is calculated using the following Caltrans equation, but should not be taken less than 24" (600 mm):

$$\begin{aligned} N &\geq \Delta_{p/s} + \Delta_{cr+sh} + \Delta_{temp} + \Delta_{eq} + 2 \quad \text{[in.]} \\ N &\geq \Delta_{p/s} + \Delta_{cr+sh} + \Delta_{temp} + \Delta_{eq} + 10 \quad \text{[mm]} \end{aligned} \tag{2.2}$$

where $\Delta_{p/s}$, Δ_{cr+sh}, Δ_{temp} are the displacement due to the prestressed shortening, creep and shrinkage, thermal expansion or contraction, respectively, and Δ_{eq} is the relative displacement from the earthquake demand between the two frames, obtained from the displacement demand of each individual frame.

The seat width recommended by AASHTO (2002) is given by a simpler equation that depends on the bridge geometry and the seismic hazard level. The seat width for bridges located in high seismic areas (seismic categories C and D), which is common in California, is given by

$$\begin{aligned} N &\geq 12 + 0.03L + 0.12H \quad \text{[in.]} \\ N &\geq 305 + 2.5L + 10H \quad \text{[mm]} \end{aligned} \tag{2.3}$$

where L is the total span in feet (meter) and H is the average height in feet (meter) of the adjacent two columns of the in-span hinge.

2.2 TYPICAL IN-SPAN HINGE CHARACTERISTICS OF CALIFORNIA BOX-GIRDER BRIDGES

The representative dimension of a typical box-girder bridge in California was obtained from a study realized by Mosalam et al. (2002). In this study, the authors conducted a geometry survey for 16 box-girder bridges located in California. Based on this survey, they identified the following representative dimensions: bridge span of 150 ft (45.72 m), web spacing of 130" (3300 mm), cap beam height of 62" (1570 mm), box web width of 12" (305 mm), deck slab thickness of 8.3" (211 mm), and soffit slab thickness of 6.9" (175 mm).

To identify the typical in-span hinge characteristics of box-girder bridges, a survey initiated by Dwight (2006) was continued in this study. The survey was restricted to bridges built in California and to the bridge standard details sheets of Caltrans (2007). The survey considered a total of eight projects, listed in Table 2.1.

Table 2.1 List of Caltrans projects.

Project	Name
1	Standard Caltrans drawing XS1-010, box-girder hinge detail elastomeric, 1994
2	Standard Caltrans drawing XS1-020, box girder 610 mm hinge elastomeric, 1992
3	Standard Caltrans drawing XS1-160, prestressed box girder 610 mm hinge elastomeric, 1986
4	SFOBB San Francisco approach (replace) mainline, bridge number 34-0126RL, 2001
5	80/580 Interchange replacement, project plan, bridge number 33-51R, 2000
6	Truckee bridge river & overhead, bridge number 17-98, 1998
7	E91-S241 Connector overcrossing, bridge number 55-793G, 1999
8	405-55 Hov connector OC, bridge number 55-952E, 1999

2.2.1 General Characteristics

Based on the projects listed in Table 2.1, two types of in-span hinges are identified in box-girder bridges. The first type has a continuous diaphragm throughout the deck width and has small utility openings. The second type does not have a continuous diaphragm throughout the deck width and has large openings. The two types of in-span hinges are shown in Figure 2.1. The utility openings are introduced for maintenance purposes to allow routine inspection of the bearings. Additionally, smaller circular openings are provided in the diaphragm to install restrainers, as shown in Figure 2.1a. The first type of in-span hinges is used in short-span bridges where the depth of the girder is relatively small. This small depth requires a continuous diaphragm through the whole deck width to adequately transfer the vertical loads between the two sides of the in-span hinge, as shown in Figure 2.1a. The second type of in-span hinges is used in long-span bridges where the depth of the girder is deeper and a continuous diaphragm may not be required to transfer the vertical loads.

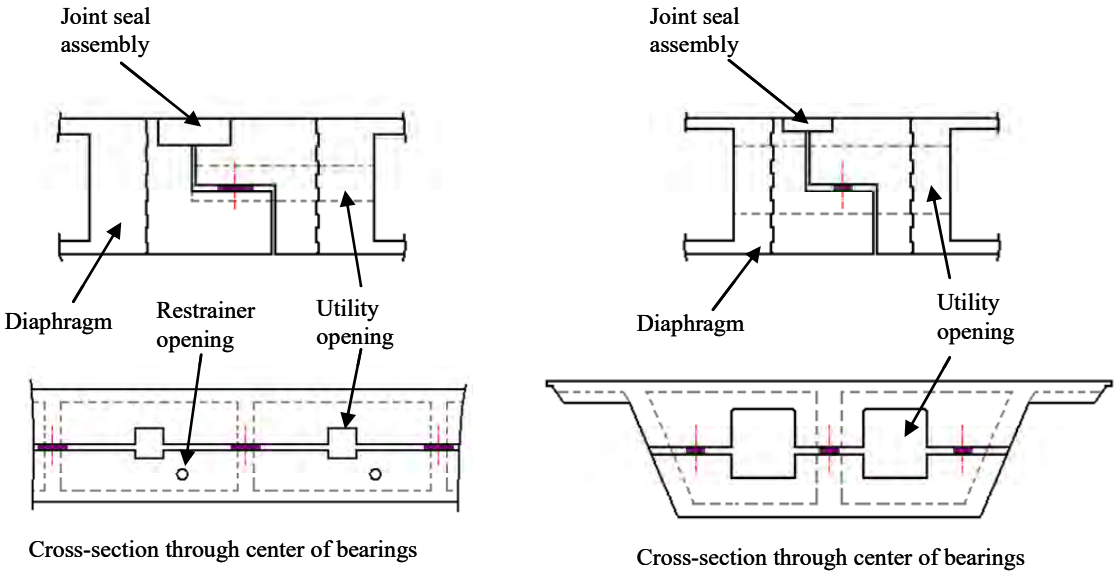

(a) Continuous diaphragm (b) Discontinuous diaphragm

Fig. 2.1 Types of in-span hinges in box-girder bridges (not in same scale).

The geometry of the in-span hinge is also affected by the presence of prestressing reinforcement in the box girders. For prestressed box girders, the diaphragm of the in-span hinge is divided into two parts with a construction joint, as shown in Figure 2.2a. The end diaphragm with prestressed blockout, shaded part in Figure 2.2a, is constructed monolithically with the webs, soffit, and deck slabs of the box girder, as shown in Figure 2.3a. This region is used to post-tension the steel tendons from the webs and slabs of the box girder. Before casting the concrete, embedded connection steel are installed, as shown in Figures 2.2a and 2.3b. Subsequently, the non-shaded part (see Fig. 2.2a) of the diaphragm and the seat are cast together anchoring the connection steel. For a non-prestressed box girder, the diaphragm does not have a construction joint. In this case, the diaphragm and the seat are cast monolithically with the webs and slabs of the box girder, as shown in Figure 2.2b. The prestressed box girders are characterized by having smaller depths. Therefore, in-span hinges in this case are more critical than for the non-prestressed box girders.

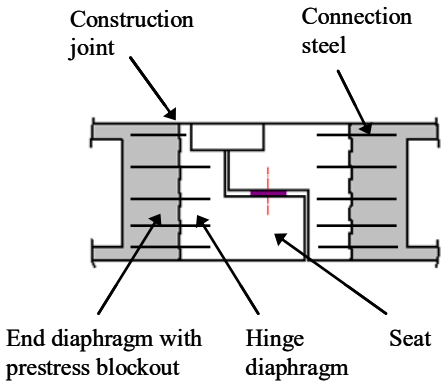

(a) Prestressed box girder

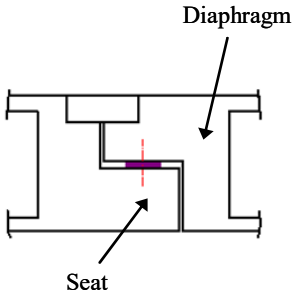

(b) Non-prestressed box girder

Fig. 2.2 In-span hinge cross sections for box girders with and without prestressed steel.

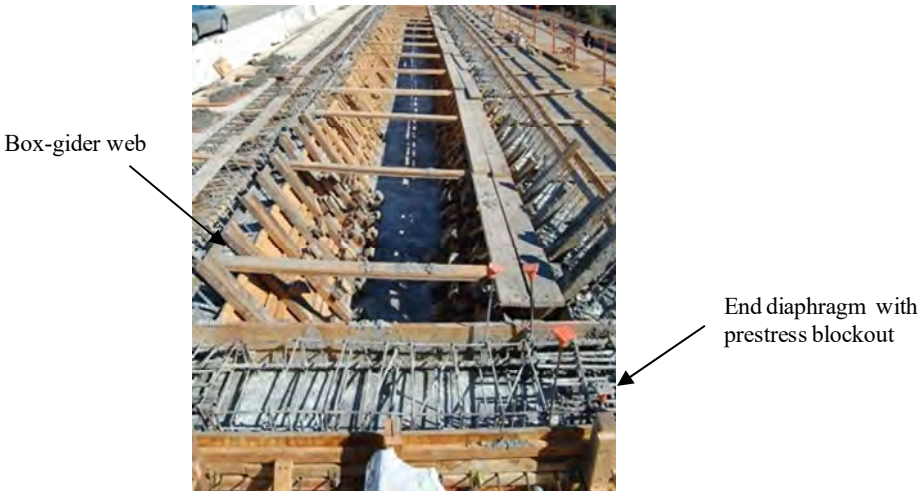

(a) Construction process

(b) Post-tensioned anchorage and connection steel

Fig. 2.3 End diaphragm with prestressed blockout.

Most in-span hinges contain shear keys to transfer the transverse service deck load between the two sides of the hinge (California 2006). For severe earthquakes, the shear keys are designed as sacrificial elements to limit the amount of shear that is transferred between the two adjacent bridge frames (Megally et al. 2002). Each shear key must have an adequate gap around it to eliminate binding of the two sides of the in-span hinge under service operation and to ensure lateral rotation, minimizing moment transfer across the in-span hinge. Based on the survey above, two types of shear keys are identified. The first type is constructed vertically on top of the seat. The second type is constructed horizontally extending a portion of the seat width.

The bearing pads transfer the vertical load between the two sides of the in-span hinge. Two types of bearing pads are identified in the survey. The first type is the PTFE (polytetrafluoroethylene) bearing pad. It is made of steel and has two sliding surfaces covered with a PTFE layer. The second type of bearing pad is the elastomeric bearing. It is made of rubber with embedded steel layers and has one planar horizontal sliding surface. This sliding surface is also covered with a PTFE layer. Both types of bearings are located on the seat, as shown in Figure 2.2. In most bridges, the bearings are centered with respect to the seat, but sometimes they are installed with an eccentricity. The distance between the bearings along the diaphragm length is equal to the web spacing of the box girder, and these bearings are generally located at the axis of each web, as shown in the cross sections of Figure 2.1.

After the collapse of several bridges in the 1971 San Fernando earthquake, the California Department of Transportation initiated a retrofit program to install cable restrainers at in-span bridge hinges of short seat width to reduce the risk of unseating (DesRoches and Fenves 2001). The restrainers are horizontal steel cables or rods that are installed to connect the diaphragms on each side of the in-span hinge to prevent unseating during earthquake motion. The Seismic Design Criteria (Caltrans 2006) specifies that a restrainer unit shall be placed at least in every other box-girder cell and that each hinge should be provided with a minimum of two restrainers. The installation of restrainers requires special openings or embedded tubes as shown in Figures 2.1a and 2.3. Additionally, equalizing bolts are usually installed at the in-span hinges. They are designed for service loads and are considered sacrificial during an earthquake.

Finally, all in-span hinges are provided with a joint seal assembly to provide continuity to the deck slab, as shown in Figure 2.1. This assembly makes the geometry of the two sides of the in-span hinge asymmetrical. The summary of the in-span hinge characteristics of the considered projects in this study is listed in Table 2.2.

Table 2.2 In-span hinge characteristics of considered Caltrans projects.

Project	Diaphragm type	Prestressed box girder	Shear key	Restrainers	Bearing pad
1	Continuous	No	Vertical	Yes	Elastomeric
2	Continuous	No	Vertical	Yes	Elastomeric
3	Continuous	Yes	Vertical	Yes	Elastomeric
4	Continuous	Yes	None	Yes	PTFE
5	Discontinuous	Yes	Horizontal	Yes	PTFE
6	Discontinuous	Yes	Horizontal	Yes	PTFE
7	Continuous	Yes	Vertical	Yes	Elastomeric
8	Continuous	Yes	Vertical	Yes	Elastomeric

Table 2.3 summarizes the dimensions of the in-span hinges of the selected eight projects. For clarity, these geometric parameters are illustrated in Figure 2.4. In Table 2.3, d_h is the diaphragm height, d_{b_total} is the total diaphragm width, d_b is the hinge diaphragm width, h is the seat height, b is the seat width and bp is the bearing plate size. Also in Table 2.3, $\alpha = b/h$ is the seat aspect ratio and $\gamma = e/b$ is the bearing eccentricity ratio with eccentricity e as defined in Figure 2.4.

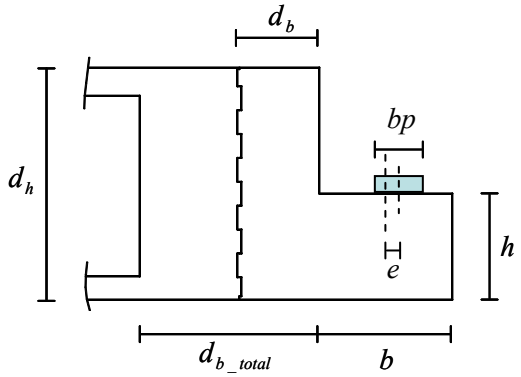

Fig. 2.4 Dimensions of in-span hinge.

Table 2.3 In-span hinge dimensions of considered Caltrans projects [in. (mm)].

Project	d_h	d_{b_total}	d_b	h	b	bp	α	γ
1	63 (1600)	17 (432)	17 (432)	33 (838)	14 (356)	9.8 (250)	0.42	0
2	77 (1950)	20.6 (525)	20.6 (525)	37.8 (960)	23.6 (600)	9.8 (250)	0.62	0
3	77 (1950)	41.3 (1050)	23.6 (600)	37.8 (960)	23.6 (600)	9.8 (250)	0.62	0
4	72 (1830)	54 (1370)	24 (610)	33 (838)	42 (1070)	13 (330)	1.27	0.17
5	68 (1730)	78 (1980)	42 (1070)	30 (762)	35 (889)	13 (330)	1.17	0
6	94 (2390)	98 (2500)	59 (1500)	33 (838)	52 (1320)	20.3 (515)	1.58	0
7	130 (3300)	48 (1220)	24 (610)	50 (1270)	36 (914)	18 (457)	0.72	0.08
8	112 (2850)	57.4 (1460)	33.5 (850)	45 (1140)	43.3 (1100)	16 (410)	0.96	0.07

2.2.2 Reinforcing Steel Characteristics

Reinforcing steel bars within the in-span hinge regions suffer from congestion, which makes these regions difficult and expensive to construct (see Fig. 2.5). For prestressed box girders, the in-span hinges are more critical than for RC box girders. For the former case, the ratio between the vertical load transmitted by the in-span hinge and the depth of the box girder is larger than in the latter case. In other words, to transfer the same vertical load, the available space for the seat height is smaller for prestressed box-girder bridges than for RC ones.

Because in-span hinges of prestressed box girders are more critical, this study is focused on those types of hinges. Two examples of reinforcing steel details of in-span hinges are shown in Figure 2.6. The figure shows the details of projects 3 and 4 from Table 2.1, both having prestressed box girders, which are characterized by a construction joint in the diaphragm. The left side of the hinge of project 3 does not have prestressed box girders in this case because the hinge is located at the vicinity of the bridge bent.

Fig. 2.5 Reinforcement congestion of in-span hinge of prestressed box-girder bridge.

To obtain representative reinforcing steel details of in-span hinges, projects 3–8 in Table 2.1 are considered. These six projects are characterized by having prestressed box girders. Based on these projects, several characteristics of the reinforcing steel details are identified. It is to be noted that some hinges have headed bars to reduce steel congestion, as shown in Figure 2.6b. Welding of bars is also identified as a way to reduce steel congestion.

To connect the diaphragm of the in-span hinge through the construction joint, connection bars are embedded in the diaphragm, as show previously in Figures 2.2a and 2.3. These bars are mostly horizontal, but some projects also have diagonal connection bars, as shown in Figure 2.6b. These bars start at the end diaphragm with prestressed blockout and end in the hinge diaphragm crossing the construction joint. In some cases, the connection bars end at the edge of the seat, as shown by the bar labeled 19 compared with that labeled 36 in Figure 2.6b.

The seat is detailed with horizontal bars distributed throughout the seat height. In some cases, these horizontal bars are concentrated in the bearing region to increase the bending capacity of the seat. Every project has diagonal bars at the seat, as shown by the bar labeled 10 in Figure 2.6b and at least one vertical bar at the edge of the seat, as shown by the bar labeled 11. Moreover, some projects have distributed vertical bars throughout the seat width.

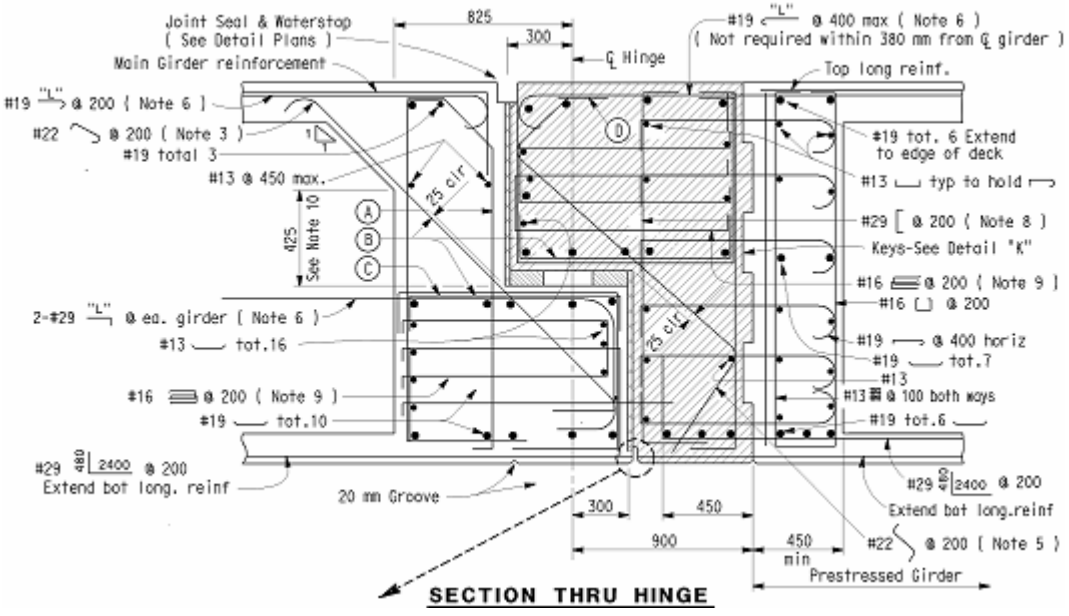

(a) Project 3

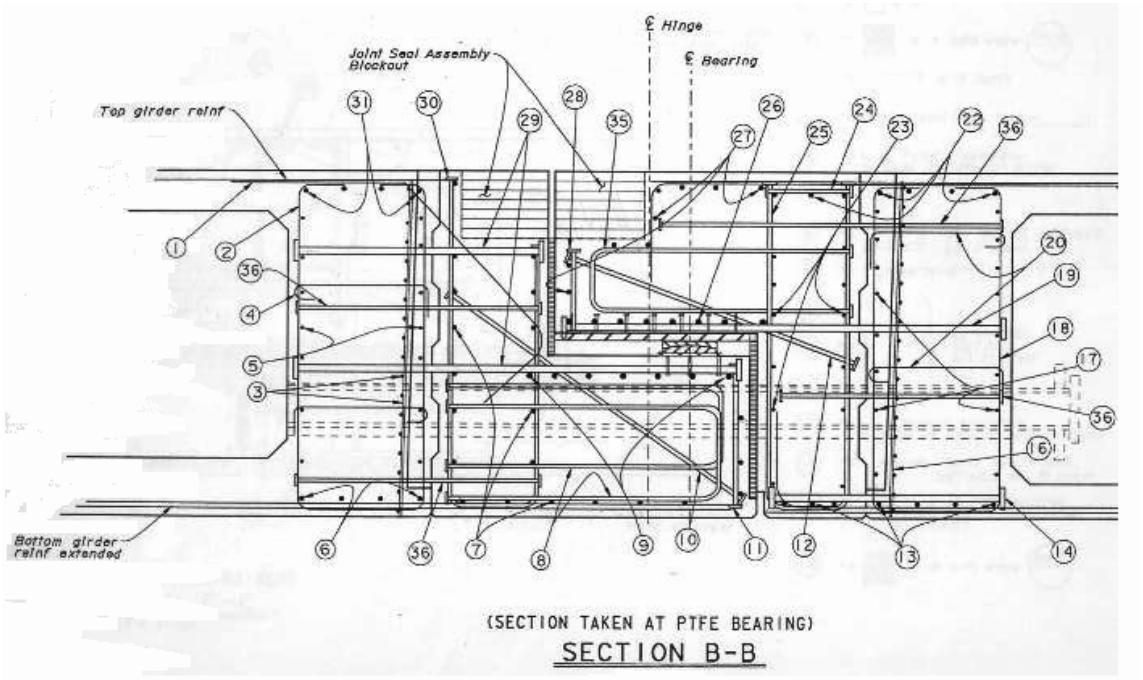

(b) Project 4

Fig. 2.6 In-span hinge reinforcing steel details.

The in-span hinges are detailed with longitudinal bars in the direction of the diaphragm. Most of these bars are concentrated at the seat, to confine the concrete adjacent to the bearing plates and to provide resistance to bending moments acting in the longitudinal direction of the diaphragm.

Finally, some projects are characterized by a concentrated (smaller) spacing of the steel in the vicinity of the bearings. The reinforcing steel characteristics of the six projects with prestressed box girders are summarized in Table 2.4. The reinforcing steel ratios of these projects are defined in Equation (2.4) and are listed in Table 2.5. In this table, ρ_{dh} is the ratio of the horizontal steel in the diaphragm with prestressed blockout, ρ_{dv} is the ratio of the vertical steel in the hinge diaphragm (the part of the diaphragm that is located beyond the construction joint), and ρ_{dd} is the ratio of the diagonal connection steel in the diaphragm. Also in Table 2.5, ρ_{sh} is the ratio of horizontal steel in the seat, ρ_{sv} is the ratio of vertical steel in the seat, ρ_{sd} is the ratio of diagonal steel in the seat, and ρ_{lon} is the ratio of longitudinal steel in the whole in-span hinge region beyond the construction joint. Note that s used in Equation (2.4) represents the associated spacing to each bar type. All of these reinforcing steel ratios are designated in Figure 2.7.

Table 2.4 Reinforcing steel characteristics of considered prestressed box-girder Caltrans projects.

	Project					
Property	3	4	5	6	7	8
Headed bars	No	Yes	Yes	No	No	Yes
Welded bars	No	No	No	Yes	No	No
Diagonal connection bars	No	Yes	No	No	Yes	Yes
Connection bars extended to the end of the seat	No	Yes	No	No	No	No
Diagonal bars at the seat	Yes	Yes	Yes	Yes	Yes	Yes
Distributed vertical bars throughout the seat width	No	No	Yes	Yes	No	No
Concentrated steel at vicinity of bearings	No	Yes	Yes	Yes	No	No

$$\rho_{dh} = \frac{A_{dh}}{d_h \cdot s} \qquad \rho_{dv} = \frac{A_{dv}}{d_b \cdot s} \qquad \rho_{dd} = \frac{A_{dd}}{d_h \cdot s}$$
$$\rho_{sh} = \frac{A_{sh}}{h \cdot s} \qquad \rho_{sv} = \frac{A_{sv}}{b \cdot s} \qquad \rho_{sd} = \frac{A_{sd}}{h \cdot s}$$
$$\rho_{lon} = \frac{A_{lon}}{d_h \cdot d_b + b \cdot h} \tag{2.4}$$

Table 2.5 In-span hinge reinforcing steel ratios (%) of considered prestressed box-girder Caltrans projects.

Project	ρ_{dh}	ρ_{dv}	ρ_{dd}	ρ_{sh}	ρ_{sv}	ρ_{sd}	ρ_{lon}
3	0.34	0.54	0.00	0.77	0.24	0.20	0.33
4	0.87	0.61	0.07	1.53	0.24	0.30	0.47
5	0.86	1.05	0.00	1.95	0.88	0.28	0.89
6	0.64	0.42	0.00	1.24	0.92	0.25	0.17
7	0.33	1.10	0.10	0.94	0.37	0.26	0.62
8	0.33	0.74	0.11	0.59	0.28	0.28	0.53

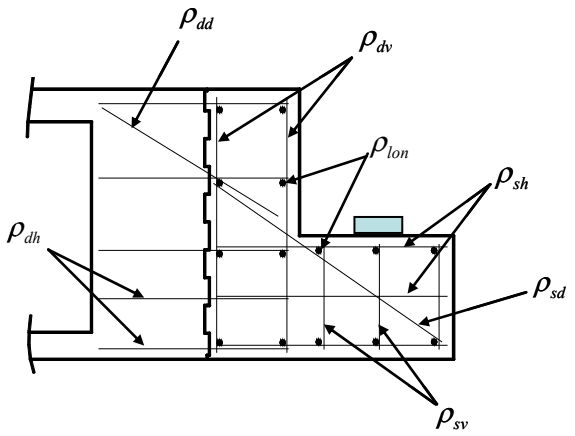

Fig. 2.7 Reinforcing steel ratios of in-span hinge.

2.3 IN-SPAN HINGE DESIGN LOAD

In-span hinges are designed to transfer vertical and horizontal loads. The design loads are calculated for each particular project using the geometry of the bridge, the location of the hinge, and the required traffic load. Nevertheless, Caltrans (2007) recommends vertical and horizontal design loads on the standard drawings. These recommended design loads depend on the girder depth and the prestressing condition of the box girder. The factored vertical hinge loads for prestressed and non-prestressed box-girder bridges are given in Table 2.6.

To check the design load proposed by Caltrans, an elastic analysis of a bridge frame is conducted. The representative box-girder bridge frame is obtained from Vlassis et al. (2004) and is shown in Figure 2.8. Considering a one-lane bridge model and the Caltrans load combinations (Caltrans 2004), the maximum factored vertical load at the in-span hinges occurs at the left hinge, labeled (A) in Figure 2.8. From the elastic analysis, the factored load at this hinge is 212 kip (943 kN), which is equivalent to 21.2 kip/ft (309 kN/m) for a typical lane width. Using Table

2.6 and a girder depth of 5' 2" (1.6 m), the suggested factored design load using the Caltrans recommendation is 50.4 kip/ft (735 kN/m). Therefore, for this representative bridge frame, the Caltrans factored design load is conservatively 2.4 times larger than the load obtained using an elastic bridge analysis. This preliminary observation explains the possible overdesign and reinforcement congestion of the in-span hinge region.

Table 2.6 Factored vertical design loads per unit length along bridge width, for in-span hinge seats.

Non-prestressed box girder		Prestressed box girder	
Girder depth [in (mm)]	Seat load [kip/ft (kN/m)]	Girder depth [in (mm)]	Seat load [kip/ft (kN/m)]
35.4 (900)	25.0 (365)	35.4 (900)	25.0 (365)
47.2 (1200)	32.0 (467)	47.2 (1200)	38.1 (555)
59.1 (1500)	37.1 (540)	59.1 (1500)	47.1 (686)
70.9 (1800)	43.0 (627)	70.9 (1800)	57.1 (832)
82.7 (2100)	50.1 (730)	82.7 (2100)	69.1 (1007)
>94.5 (>2400)	58.1 (846)	>94.5 (>2400)	83.1 (1211)

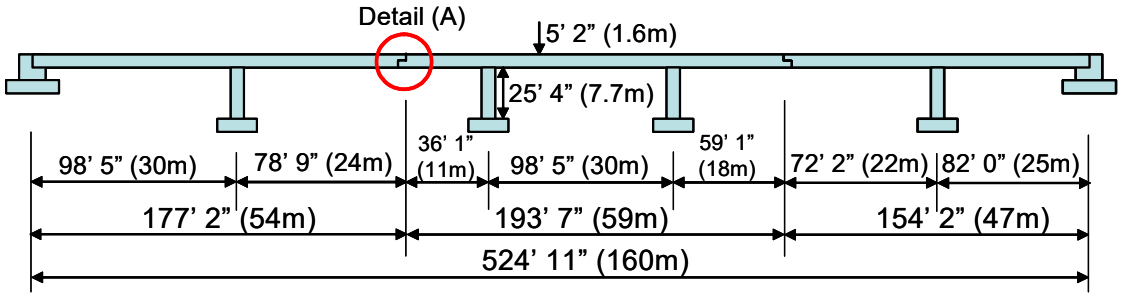

Fig. 2.8 Representative box-girder bridge frame.

2.4 IN-SPAN HINGE DESIGN METHOD

The current Caltrans design method for in-span hinges (Caltrans 2004) in based on ACI requirements for short cantilevers (ACI 2008). Accordingly, three analytical models are used to evaluate the capacity of in-span hinges: sliding shear friction, moment resistance, and strut-and-tie (SAT). This capacity is evaluated using two critical sections, at the seat and at the construction joint of the diaphragm. In this study, two additional analytical models are used to evaluate the capacity of in-span hinges, namely 1D shear (referred to in the following as "shear" for simplicity) and punching shear. The punching shear model is included because the discrete

load of the bearings induces a 3D stress state of the hinge region that may produce this type of failure.

2.4.1 Sliding Shear Friction Model

The sliding shear friction model assumes that a full crack develops through the sliding interface. Reinforcing steel must be provided across this crack to resist relative displacements. The assumed shear plane for the seat and diaphragm of an in-span hinge are shown in Figure 2.9.

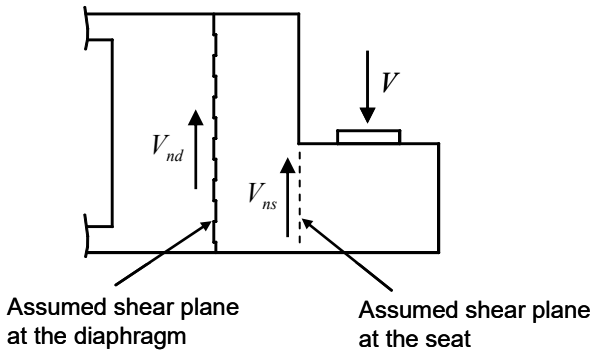

Fig. 2.9 Assumed shear planes in sliding shear friction model.

Using the ACI provisions (ACI 2008), the shear friction capacity of the in-span hinge is given by

$$V_n = A_{vf} f_y \mu \tag{2.5}$$

where A_{vf} is the area of reinforcing steel crossing the sliding interface, f_y is the yielding strength of the reinforcing steel and μ is the coefficient of friction. This coefficient is taken as 1.4λ for concrete cast monolithically and 1.0λ for concrete placed against hardened concrete with surface intentionally roughened. The former case is applicable to the seat, i.e., V_{ns} and the latter case is applicable to the diaphragm at the construction joint, i.e., V_{nd}. The coefficient λ is 1.0 for normal-weight concrete. When shear friction steel is inclined to the shear plane, as in the case of the in-span hinges, the capacity is given by

$$V_n = A_{vf} f_y (\mu \sin\psi + \cos\psi) \tag{2.6}$$

where ψ is the angle between the shear friction reinforcement and the sliding plane. The ACI provisions (ACI 2008) specify upper limits for shear strength because Equations (2.5) and (2.6) are not conservative for high values of V_n. The upper limit for the shear strength is given by

$$V_n \le \begin{cases} 0.2 f_c' A_c \\ 800 A_c \end{cases} \quad \text{[psi, in units]} \tag{2.7}$$

where A_c is the area of a concrete section resisting the shear transfer and f_c' is the 28-day concrete compressive strength of a standard cylinder. For in-span hinges with utility openings, A_c is computed by subtracting the areas of the openings.

2.4.2 Moment-Resisting Model

The moment-resisting capacity of an in-span hinge is evaluated at the seat and at the diaphragm as shown in Figure 2.10. This moment capacity is usually computed using the whole bridge width. The moment strength M_n at both sections is calculated using the ACI approach (ACI 2008). In this approach, an equivalent rectangular compression stress block is assumed in the concrete, and the neutral axis is computed using equilibrium adopting the Bernoulli's assumption that a plane section remains plane after bending (linear strain distribution along the depth). When evaluating the forces at each reinforcing bar, the corresponding location (and associated strain which is assumed the same for the concrete and the adjacent reinforcing steel, i.e., full bond without slip between the steel and the concrete) of the reinforcement is considered.

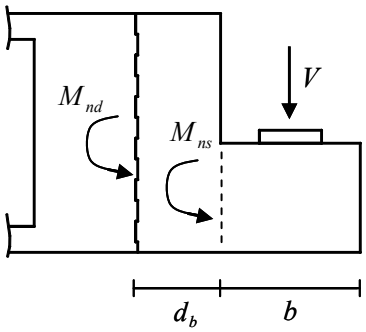

Fig. 2.10 Moment-resisting model.

After computing the moment strength at the two sections, the capacity of the in-span hinge using the seat strength and the diaphragm strength is given by

$$V_{ns} = \frac{M_{ns}}{b/2} \qquad V_{nd} = \frac{M_{nd}}{b/2 + d_b} \tag{2.8}$$

2.4.3 SAT Model

The SAT model is commonly used to design discontinuity regions, known as D-regions, where the classical beam theory does not apply (Macgregor 2005; Schlaich et al. 1987). The SAT model consists of concrete compressive struts, reinforcement tension ties, and nodal zones. Using the lower-bound theorem of plasticity, any SAT model that satisfies equilibrium and does not violate the yield criteria provides a lower-bound estimate of the capacity of an elastic-perfectly-plastic material. According to ACI provisions (ACI 2008), the stress limit for a compression strut is given by

$$f_{cu} = 0.85\beta_s f_c^{'} \tag{2.9}$$

where the parameter β_s depends on the shape of the strut, and on the presence of crack control reinforcement. For the case of a tie, the nominal strength is given by

$$F_{nt} = A_{st} f_y \tag{2.10}$$

where A_{st} is the reinforcing steel area of the tie. The points at which the forces in a SAT model meet are referred to as nodes. The concrete surrounding a node is referred to as a nodal zone. The nominal compressive strength of a nodal zone is given by

$$F_{nn} = f_{ce} A_{nz} \tag{2.11}$$

where f_{ce} is the effective strength of the concrete in the nodal zone and A_{nz} is the area of the face of the nodal zone perpendicular to the axis of the force. The effective strength of the concrete is computed from

$$f_{ce} = 0.85\beta_n f_c^{'} \tag{2.12}$$

where the parameter β_n depends on the type of forces acting on a nodal zone with $\beta_n = 1.0$ for Compression-Compression-Compression (C-C-C) node, $\beta_n = 0.8$ for compression-compression-tension (C-C-T) node and $\beta_n = 0.6$ for compression-tension-tension (C-T-T) node.

2.4.4 Shear Model

The 1D shear model is also included in this study to determine the capacity of in-span hinges. The shear failure surface in this case is shown in Figure 2.11, where it is assumed that the shear surface is continuous throughout the whole diaphragm length.

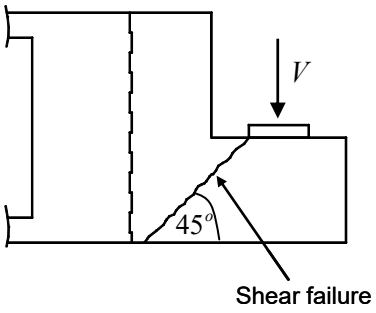

Fig. 2.11 Shear failure model.

The shear capacity of the in-span hinge is obtained using the ACI provisions (ACI 2008), where the total shear resistance is the sum of the contributions from the concrete (V_c) and the transverse reinforcing steel (V_s), i.e.,

$$V_n = V_c + V_s \tag{2.13}$$

The concrete contribution is simply give by

$$V_c = 2\sqrt{f_c'}\, b_w\, d \quad \text{[psi, in units]} \tag{2.14}$$

where b_w is the width, which is equivalent to the total length of the diaphragm; and d is the effective seat depth. For the case of in-span hinges, the contribution to the shear resistance is given by vertical and diagonal reinforcing bars (A_v) that cross the shear plane defined in Figure 2.11. Accordingly, the reinforcement contributions are computed for such bars as follows:

$$V_s = A_v f_{yt} \sin\theta \tag{2.15}$$

where f_{yt} is the yield strength of the transverse steel and θ is the acute angle between the diagonal reinforcement and the longitudinal axis of the member. Note that for vertical bars, $\theta = \pi/2$ and $V_s = A_v f_{yt}$.

2.4.5 Punching Shear Failure Model

In this study, a punching shear failure model is also considered to determine the capacity of the in-span hinge. This failure mode is included because the discrete load at the bearings induces a 3D stress state that can cause punching shear failure of the seat. The failure surface at the seat is a 3D truncated cone, and the cross section at the bearing is shown in Figure 2.12a.

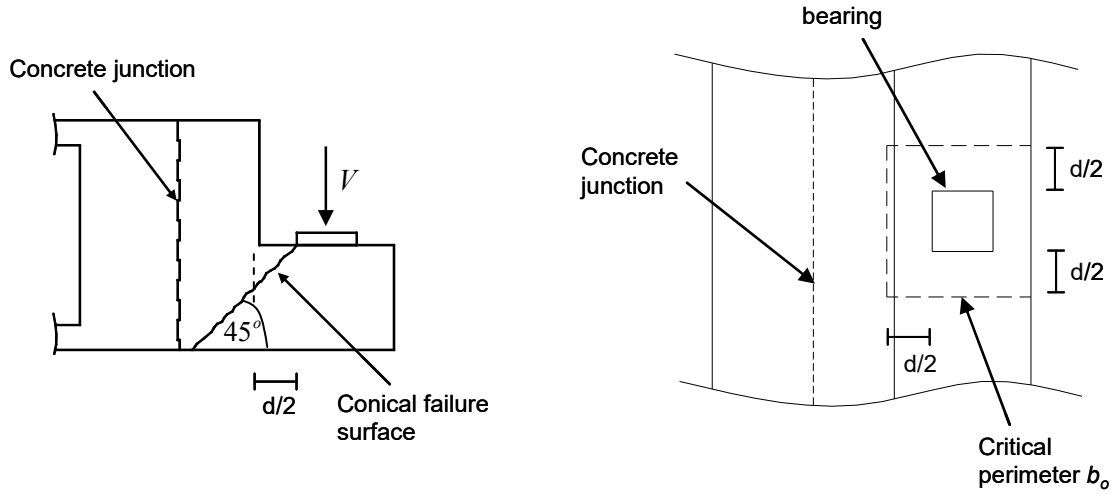

(a) Cross section (b) Plan view of critical perimeter b_0

Fig. 2.12 Punching shear failure.

The punching shear capacity of the in-span hinge is obtained using the ACI approach for slabs (ACI 2008). The total shear resistance is again given by Equation (2.13). For slabs having shear reinforcement, as the case of the in-span hinges, the concrete strength for normal-weight concrete is

$$V_c = 2\sqrt{f_c'}\, b_o d \quad \text{[psi, in units]} \tag{2.16}$$

where d is the effective seat depth and b_o is the critical perimeter defined in Figure 2.12b. The shear resistance attributed to the transverse reinforcement is computed using Equation (2.15) considering the bars that cross the conical failure surface illustrated in Figure 2.12. The diagonal bars of the seat act as inclined transverse reinforcement in the case of the in-span hinges. Finally, the total punching shear strength is limited in the ACI provisions (ACI 2008) by

$$V_n \le 6\sqrt{f_c'}\, b_o d \quad \text{[psi, in units]} \tag{2.17}$$

2.5 HEADED REINFORCEMENT

Headed reinforcement has been shown to be effective in reducing steel congestion, improving bond, increasing confinement and assisting in the development of local SAT models. Application of headed reinforcement to in-span hinges is clearly appropriate to reduce steel congestion and to provide adequate reinforcement development in the relatively small hinge region. The bond stress between the reinforcing steel bars and the surrounding concrete must be sufficient to resist

the tensile loading of the bar which often requires an impractical development length for the design scenario. There may be situations in which requirements for lap slices and straight bar anchorage cannot be satisfied within the available in-span hinge dimensions. Furthermore, using hooked bars to shorten the overall anchorage length can create steel congestion, especially for bars with large diameters requiring large hooks, leading to overly complicated construction region.

The historical use of headed bars started with the application of headed stud anchors in the 1960s (McMackin et al. 1973). Stud anchors are commonly used in composite construction to provide shear transfer between the steel girder and the RC slab. In the 1970s, shear studs were used in RC slabs to provide punching shear resistance (McMackin et al. 1973). In 1974, research funded by Caltrans studied headed reinforcement to determine a method to anchor large diameter bars in bridge structures (Stoker et al. 1974) where three methods of attaching heads to the end of bars were investigated. The commercial use of headed bars began in 1986, by a Norwegian contractor for the design and construction of offshore oil structures (Mitchel and Rooney 1994). This Norwegian contractor in association with the British company Metalock started mass production of headed bars. Subsequently, headed bars have been extensively used, e.g., in bridge beam-column joints (Naito et al. 2001; Mosalam et al. 2002), in bridge columns (Lehman et al. 2001) to repair pier walls (Haroun et al. 2000) and for ties in walls and columns (Dilger and Ghali 1997).

2.5.1 Types of Headed Reinforcement

Headed bars in the U.S. are fabricated by many companies. Caltrans (2005) provides a pre-qualified list of products from five different companies: Headed Reinforcement Corporation (HRC), ERICO, Dayton/Richmond, Bar Splice Products, and Dextra America. The headed bars from the first two companies are detailed below because of their relevance to the present experimental and computational study on in-span hinges.

HRC's headed bars are manufactured by pressing the end of a deformed reinforcing bar onto a spinning plate. The heat produced by the friction between the deformed bar and the plate causes the material from the bar to melt and form a weld below the head. The friction technique results in a mushroom-shaped weld at the plate connection, as shown in Figure 2.13a. The welded connection has a net section larger than the bar diameter, which ensures the full

development capacity of the bar (Naito et al. 2001). HRC produces bars with square, circular, rectangular, and oval terminator shapes. The shape of the plate is often chosen in such a way to accommodate for construction where access may be limited or in heavily reinforced regions (Berner et. al 1991). For this in-span hinge project, HRC fabricated #3 headed bars with welded terminator, as shown in Figure 2.13b. A classical welded connection instead of a friction-welded connection was used for these bars because HRC does not typically produce #3 headed bars. To perform the classical weld connection, a hole is made in the circular terminator and the end of the bar is introduced into this hole. Subsequently, the bar is welded as shown in Figure 2.13b.

The other major headed bar manufacturer is Electric Railway Improvement Company (ERICO), which produces their reinforcement by using a tapered thread connection between the bar and a nut that is screwed onto the bar to provide a head. This splicing device is known as a LENTON® terminator and is shown in Figure 2.14 (Thompson et al. 2002). The advantage of this terminator is that it can easily be installed in the field. However, this terminator cannot be used to completely eliminate the need for a development length. The tensile strength is limited to the thread capacity, which may not allow for full development of the bar anchorage (Naito et al. 2001).

(a) Friction welded (#4 and larger bars) (b) Welded (#3 bars)

Fig. 2.13 HRC terminators.

Fig. 2.14 ERICO threaded terminator.

The fabrication of headed reinforcement in the U.S. is standardized by the ASTM specifications for headed bars (ASTM 1997). The specifications require that the steel of the headed bars to have a minimum yield strength of 60 ksi (or be Grade 60 bars) and specify the welding procedure for classically welded, friction welded and threaded terminator. Finally, low-alloy steel bars which conform to Specification ASTM A706 should be used to manufacture welded headed bars. This specification limits the chemical composition and carbon equivalence which allows a greater ability for the material to be welded (ASTM 2004b).

2.5.2 Capacity of Headed Reinforcement

The development length of headed bars in tension was incorporated in the ACI provisions in 2008 (ACI 2008). These provisions establish that to reduce the development length of a headed bar in tension, the following conditions must be satisfied: (1) the neat bearing area of the head should not be less than 4 times the area of the bar, (2) the clear cover should be at least 2 times the bar diameter, d_b, and (3) the clear spacing should not be less than 4 times d_b. The development length l_{dt} for headed bars in tension is given by

$$l_{dt} = \frac{0.016\psi_e f_y}{\sqrt{f_c'}} d_b \geq \begin{cases} 8d_b \\ 6" \end{cases} \quad \text{[psi, in units]} \tag{2.18}$$

where ψ_e is 1.0 for uncoated reinforcement. Equation (2.18) was obtained from a simplification of a recent work performed by Thompson et al. (2006b). In this study, they suggested more sophisticated design equations for the anchorage of headed reinforcement for two common conditions: anchorage for CCT nodes, and anchorage for lap splices. These design equations are based on the experimental results of 40 beams reported by Thompson et al. (2005, 2006a) and are described below.

The design model for anchorage of headed bars includes two components: (1) the head bearing stress and (2) the bond stress. These components are calculated separately, and together contribute to the total bar anchorage capacity. The head bearing capacity is based on existing ACI equation for bearing strength. The anchorage stress provided by the head is computed as

$$f_{s,head} = 1.4\psi f_c' \left(\frac{c}{d_b} \right) \sqrt{\frac{A_{nh}}{A_b}} \tag{2.19}$$

where ψ is the radial disturbance factor that depends on the cover and the size of the head, c is the concrete cover, A_{nh} is the net head area (gross area of the head minus the area of the bar), and

A_b is the reinforcing bar area. It is proposed that a radial disturbance factor of 1.0 can be used conservatively in the calculations. The stress provided by Equation (2.19) is a characteristic strength in such a way that 5% of the tests showed a capacity lower than this equation.

The bond capacity of a headed bar is determined using the ACI equation for development length with a modification factor χ. This modification factor takes into account the reduction in bond stress that occurs from adding the head to the bar which is given by

$$\chi = 1 - 0.7\left(\frac{A_{nh}/A_b}{5}\right) \geq 0.3 \tag{2.20}$$

Using this reduction factor, the bond contribution to the total bar anchorage capacity is given by

$$f_{s,bond} = \chi\left(\frac{L_a}{L_d}\right) f_y \tag{2.21}$$

where L_a is the available anchorage length and L_d is the required development length calculated according to the ACI provisions (ACI 2008). With clear spacing not less than $2d_b$ and clear cover not less than d_b, the development length is given by

$$L_d = \left(\frac{f_y \psi_t \psi_e}{S\lambda\sqrt{f_c'}}\right) d_b \quad \text{[psi, in units]} \tag{2.22}$$

where the parameter ψ_t accounts for the position of the reinforcement and reflects the adverse effects of the top reinforcement. For normal cases ψ_t is taken as 1.0. The parameter S accounts for the bar size, which is taken as 20 for bars #7 and larger, and is taken as 25 for bars #6 and smaller.

The required anchorage length of headed bars for cover ratios c/d_b and typical head ratios A_{nh}/A_b is listed in Table 2.7. The table is computed considering $f_c^{'} = 5$ ksi (34.5 MPa) and $f_y = 60$ ksi (414 MPa). For different cover and head ratios, the anchorage stress $f_{s,head}$ is computed using Equation (2.19). The remaining stress to reach yielding of the reinforcement has to be resisted by bond, i.e., $f_{s,bond}$. Finally, the required anchorage length L_a/L_d is computed using Equation (2.21). The last column of Table 2.7 represents the required anchorage length L_a/L_d using Equation (2.18) of the ACI (2008). The table shows that for typical head ratios, a minimum $c/d_b = 2$ is required to reduce the development length L_d.

Table 2.7 Anchorage length L_a/L_d of headed bars.

c/d_b	A_{nh}/A_b	$f_{s,head}$ [ksi (MPa)]	$f_{s,bond}$ Required [ksi (MPa)]	L_a/L_d Thompson et al. (2006b)	L_a/L_d ACI (2008)
1	9	21.0 (145)	39.0 (269)	2.17	-
1	10	22.1 (153)	37.9 (261)	2.10	-
1	11	23.2 (160)	36.8 (254)	2.04	-
2	9	42.0 (290)	18.0 (124)	1.00	0.40
2	10	44.3 (305)	15.7 (108)	0.87	0.40
2	11	46.4 (320)	13.6 (94)	0.75	0.40
3	9	63.0 (434)	0.0 (0.0)	0.00	0.40
3	10	66.4 (458)	0.0 (0.0)	0.00	0.40
3	11	69.6 (480)	0.0 (0.0)	0.00	0.40

3 Development of Experimental Program

This chapter describes the experimental program that is used to study the structural behavior and strength of in-span hinges. The experimental program considers a total of five specimens at 1/3-scale that are tested in two phases. The first two specimens (phase I) represent the as-built condition of typical in-span hinges of RC box-girder bridges in California. Based on the test results of phase I, the remaining three specimens (phase II) are designed to improve the performance and to observe the behavior of different in-span hinge configurations. The two phases of the experimental program were conducted in the structural engineering laboratory at the University of California, Berkeley.

3.1 LITERATURE REVIEW OF SIMILAR TESTS

From a literature review, it was found that in-span hinges of RC box-girder bridges have not been tested. Megally et al. (2002) studied the seismic response of sacrificial shear keys in bridge abutments. In this research, they tested sacrificial internal and external shear keys using 2/5-scale specimens subjected to cyclic loading. The shear keys are short elements that are characterized by having a small aspect (height-to-width) ratio, as the case of in-span hinges. They tested six interior shear keys with aspect ratio varying from 0.3 to 0.5, and six exterior shear keys with different characteristics. The shear keys were built monolithically with a concrete base. The base was attached to the strong floor using a total of 10 rods stressed to a force of 150 kip (667 kN) each. The load was applied using two actuators connected to a loading frame. Due to the high stiffness of the shear keys, they were initially loaded in force control at increasing cycles. Then, the testing procedure was switched to displacement control with increasing cyclic amplitude until the failures of the specimens were achieved. The maximum load and displacement applied to the specimens were 285 kip (1268 kN) and about 8" (203 mm).

3.2 DEFINITION OF PROTOTYPE IN-SPAN HINGE

The representative box-girder bridge dimensions used in this study were obtained from the survey of 16 bridges conducted by Mosalam et al. (2002) that was described in Chapter 2. Since this survey does not account for in-span hinge dimensions, the dimensions related to the in-span hinge are determined from the eight projects discussed in Chapter 2. Based on the survey of 16 California bridges reported by Mosalam et al. (2002) and based on the survey of the eight projects in Chapter 2, the prototype in-span hinge geometry for this study is summarized in Table 3.1.

Table 3.1 Prototype in-span hinge geometry.

Box web spacing	130" (3300 mm)	Seat width b	40" (1020 mm)
Box web width	12" (305 mm)	Seat height h	32" (810 mm)
Diaphragm height d_h	70" (1780 mm)	Bearing plate size bp	13" (330 mm)
Total diaphragm width d_{b_total}	54" (1370 mm)	Seat aspect ratio α *	1.25
Seat diaphragm width d_b	24" (610 mm)	Eccentricity ratio γ	0.0

*The aspect ratio is reduced by a factor 2 if the load application point is considered.

For the prototype in-span hinge, a prestressed box girder of a multiple-lanes bridge is considered. This hinge has utility openings for maintenance and inspection purposes. One square opening is located between the bearings at mid-height of the diaphragm, as shown in Figure 3.1. The size of the openings is one third of the diaphragm height d_h.

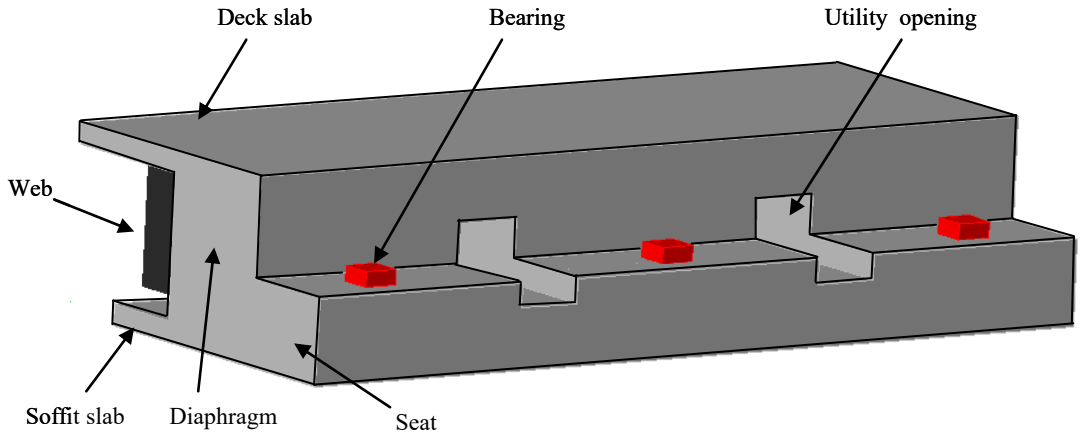

Fig. 3.1 3D view of utility openings and bearings of adopted prototype in-span hinge.

The reinforcing steel details, including headed steel reinforcement, are shown in Figure 3.2. For simplicity, it was assumed in the prototype in-span hinge that the horizontal steel of the diaphragm with prestressed blockout ρ_{dh} does not extend to the end of the seat. Additionally, a smaller spacing of the reinforcing steel is considered in the vicinity of the bearings. Based on the survey, the vicinity of the bearing is defined by an equivalent width of 1.5 times the seat height h, as show in section A-A of Figure 3.2. The adopted reinforcing steel ratios in the vicinity of the bearings are listed in Table 3.2. Beyond this region, the reinforcing steel ratios are reduced to 66% of the values listed in the table, except for the longitudinal steel ratio, which is kept constant throughout the diaphragm length.

Using the geometry of the prototype in-span hinge, the vertical factored design load can be computed using the Caltrans loads described in Chapter 2. Accordingly, a prestressed girder of 70" (1780 mm) is subjected to a factored design load using Table 2.6 of 56.4 kip/ft (823 kN/m). Considering the prototype web spacing, i.e., bearing spacing of 130" (3300 mm), the vertical factored load per bearing is estimated as 611 kip (2720 kN).

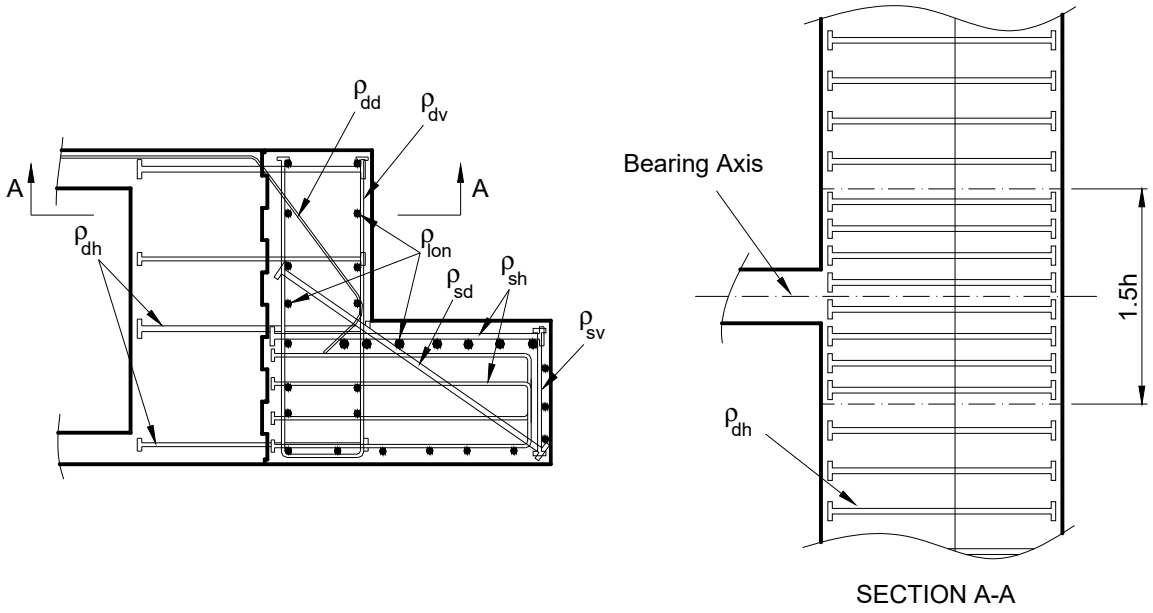

Fig. 3.2 Reinforcing steel details of adopted prototype in-span hinge.

Table 3.2 Reinforcing steel ratios of adopted prototype in-span hinge (%).

ρ_{dh}	ρ_{dv}	ρ_{dd}	ρ_{sh}	ρ_{sv}	ρ_{sd}	ρ_{lon}
0.87	0.61	0.07	1.53	0.24	0.30	0.47

3.3 TEST MATRIX

The experimental program of the in-span hinges consisted of a total of five specimens using a 1/3-scale. The experimental program was conducted in two phases and the test matrix is shown in Table 3.3. Phase I consisted of two specimens that represent the as-built conditions of typical California box-girder bridges with representative reinforcement ratios. The two specimens were identical, but specimen S2 had utility openings to study the effect of these openings on the behavior and strength of the as-built in-span hinge. The representative reinforcement ratios are based on the prototype in-span hinge defined previously.

Based on the results of phase I, the remaining three specimens constituting phase II were designed to improve the behavior of the in-span hinge. Specimen S3 was designed identical to specimen S2, but had larger bearing plates to eliminate the local punching shear failure mode observed in phase I specimens. Specimens S4 and S5 represented improved design with lower reinforcement ratios. These lower reinforcement ratios were aimed to improve constructability and to produce a comparable strength in all the possible failure modes of the in-span hinge.

Specimens S4 and S5 were identical, but specimen S5 had utility openings to study the effect of these openings on the behavior and strength of the new design of the in-span hinge.

Table 3.3 Test matrix.

Phase	Specimen	Utility opening	Description
I	S1	No	As-built condition of typical in-span hinges
I	S2	Yes	Identical to specimen S1 but with utility openings between bearings
II	S3	Yes	Identical to specimen S2 but with higher punching shear strength achieved using larger bearing plates
II	S4	No	New design with low reinforcement ratio to improve constructability and performance
II	S5	Yes	Identical to specimen S4 but with utility openings between bearings

3.4 SUBASSEMBLY DEVELOPMENT

The cross section of the prototype in-span hinge is shown in Figure 3.3a. The top and bottom halves of the hinge are almost identical. Some exceptions may exist due to the joint seal assembly and due to the possible existence of utility openings, as described in Chapter 2. The tested region consisted of the seat and the seat diaphragm, which are cast monolithically in the field. This tested region is shown shaded in Figure 3.3a. The end diaphragm with prestressed blockout, located beyond the concrete junction, was not considered in the experiments. This end diaphragm is cast at the field monolithically with the box girder and is prestressed. Thus, it is assumed that the end diaphragm with prestressed blockout is not a critical element of the in-span hinge and is therefore excluded from the test subassembly for simplicity of the test setup.

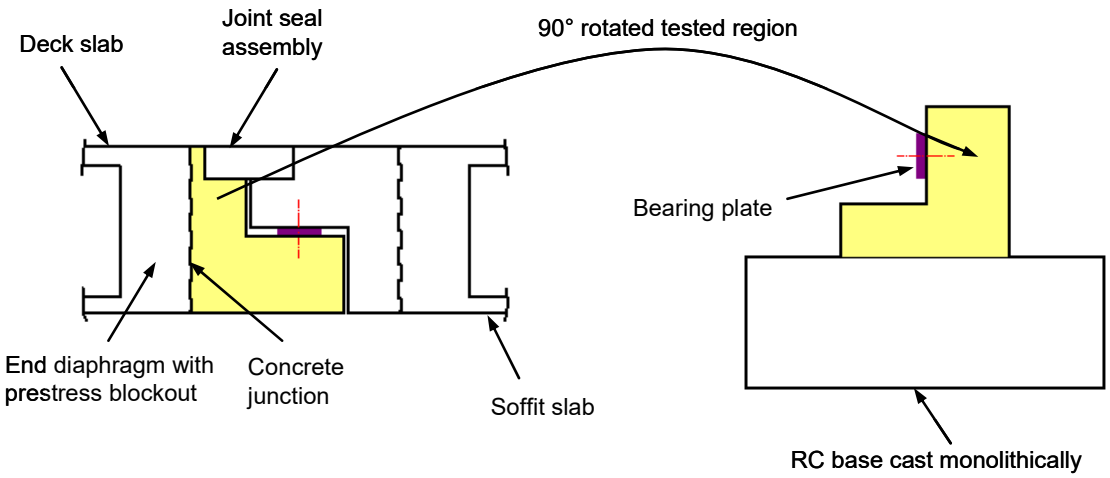

(a) Prototype cross section of in-span hinge (b) Test subassembly

Fig. 3.3 Development of test subassembly.

To facilitate the test program, the in-span hinge was tested in a 90° rotated position, as shown in Figure 3.3b. To connect the in-span hinge with the strong floor, a RC base was cast monolithically with the in-span hinge specimen. This base was designed to remain almost elastic with minimal damage to simulate the presence of the strong end diaphragm zone. Additionally, the joint seal assembly is neglected in the present experimental program to reduce the number of geometrical parameters and render the experimental results more general and less specific to particular project choices.

To simulate the structural behavior of the in-span hinge of a multiple-lanes bridge, a diaphragm of twice the web spacing is considered in the test subassembly. The top view of a multiple-lanes bridge deck, containing the bottom part of the in-span hinge is shown in Figure 3.4. The test region, containing two bearing plates, is shown shaded in this figure.

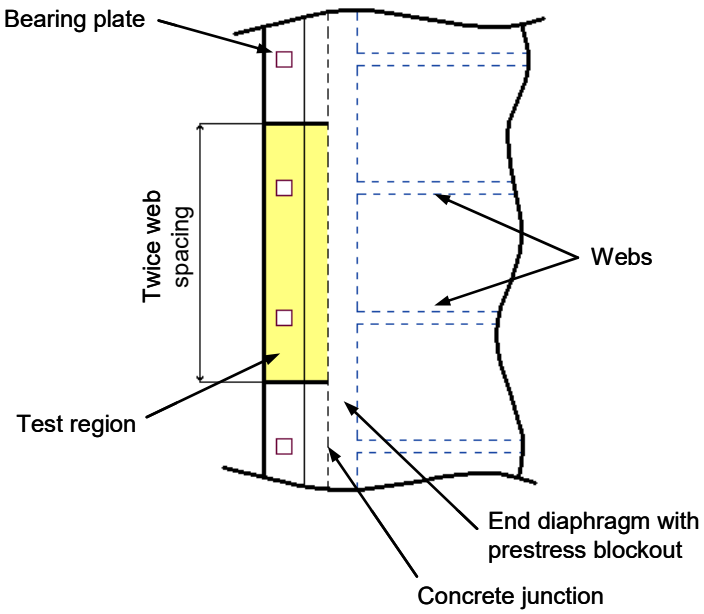

Fig. 3.4 Top view of test subassembly.

3.5 TEST SETUP

The specimens' geometry was obtained from the prototype in-span hinge using a 1/3-scale. The 1/3-scale was selected such that the reaction forces can be adequately transmitted from the specimen to the strong floor through the RC base. The setup of the test subassembly is shown in Figure 3.5. Details of the test setup are shown in elevation and plan views in Figure 3.6. The RC base that was cast with the test subassembly was used to transmit the horizontal load and the overturning moment from the test specimen to the laboratory strong floor. The depth of the RC base was 20" (508 mm). This depth was limited such that the actuator force was applied at the correct height of the in-span hinge seat. The actuator support was a massive steel structure and did not allow feasible modification of the actuator height. The length and width of the RC base were selected to be able to place the required post-tensioning rods. Finally, this base was anchored to the strong floor using 10 rods with a post-tension force of 120 kip (534 kN) each.

For constructability concerns, the in-span hinge seat was extended to the end of the RC base. Therefore, the length of the seat of 96" (2438 mm) was about 12% larger than two times the web spacing of 86" (2184 mm) specified in the original test subassembly (see Fig. 3.6).

To simulate the Polytetrafluoroethylene (PTFE) bearings, a 6"×6"×3/4" (152 mm×152 mm×19 mm) steel plate was placed at the location of each bearing, as shown in Figure 3.6. The dimensions of these plates were increased from the scaled size of the representative prototype

dimensions based on the conducted survey to prevent local bearing failure of the concrete during the experiments. Nevertheless, the thickness of the plates was selected to have an equivalent stiffness to the actual PTFE bearing.

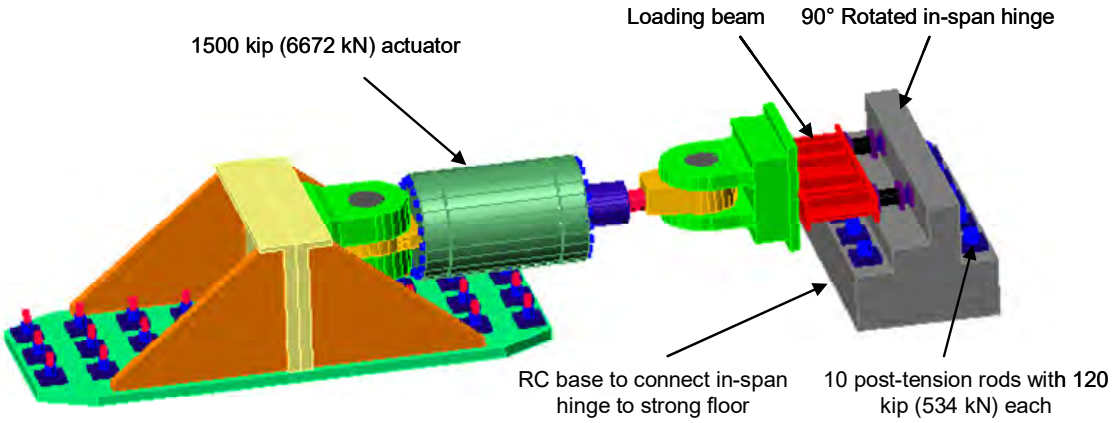

Fig. 3.5 Test setup.

The horizontal load was applied to the test specimens using an actuator with a compression capacity of 1500 kip (6672 kN). The actuator was supported vertically by a wooden block as shown in the elevation view of Figure 3.6. The actuator load was transferred to the bearings using a wide flange W23×104 steel beam (see Fig. 3.5) that was bolted to the actuator end plate. This loading beam was strengthened with stiffeners to prevent local buckling of the web. At each bearing location, a 300 kip (1334 kN) load cell was attached to the loading beam as shown in Figure 3.6. Finally, a tilt saddle was bolted at the end of each load cell. These title saddles allowed the application of the loads uniformly to the bearing plates, in spite of the rotation that took place at the seats during the experiments. The connections between the tilt saddles and the bearing plates were by direct contact.

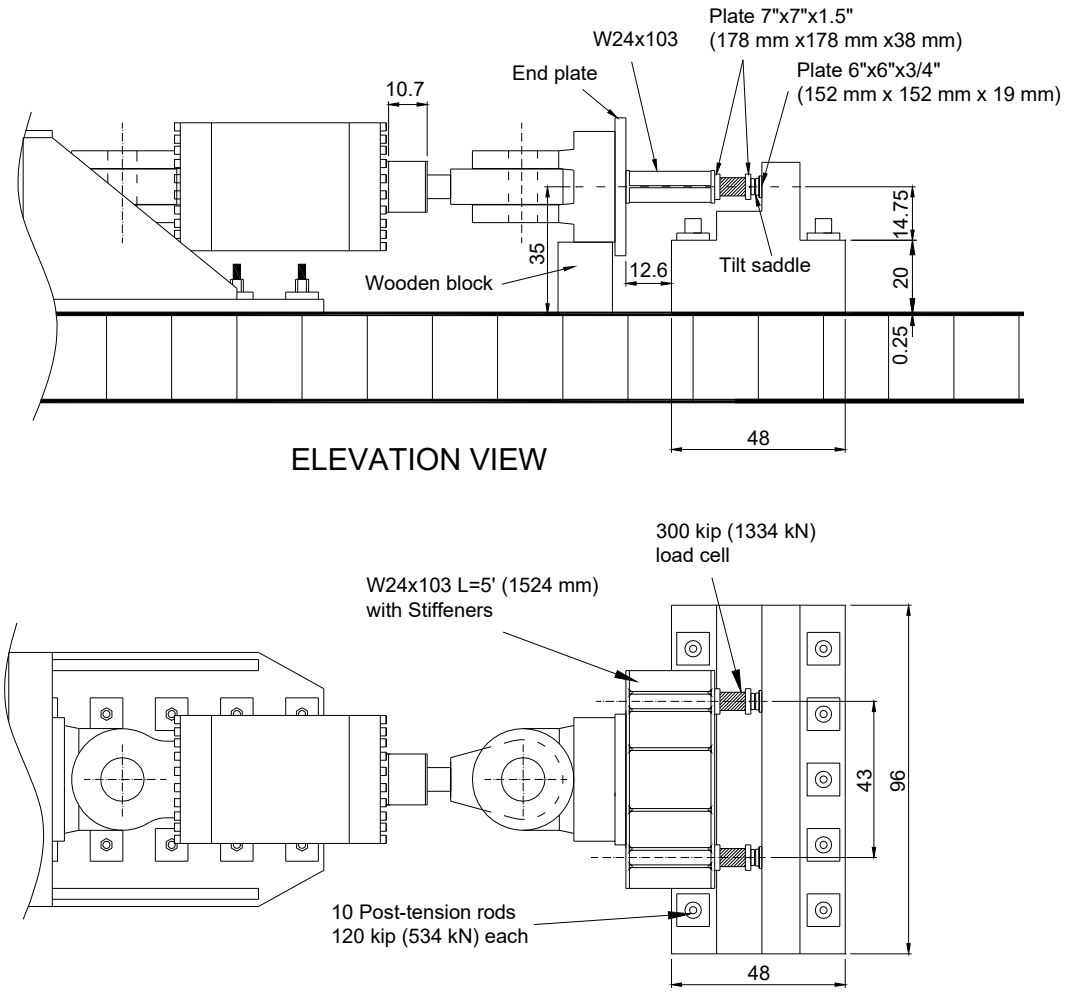

Fig. 3.6 Test setup views (Dimensions [in.]: 1"=25.4 mm).

The test setup described above provided the same force at the two bearings. Since the actuator was connected with two clevises, and the connection between the loading beam and the bearing plates were through contact, the resultant force passed through the longitudinal axis of the actuator. These characteristics of the setup resulted in equal forces at the two bearings. This loading condition of the test setup is representative of a bridge system that is subjected to uniform vertical load, resulting in equal vertical forces at the bearings of the in-span hinge.

Since the depth of the RC base was limited by the actuator height, the bases of the specimens were designed conservatively with a large amount of steel reinforcement to minimize damage. To resist the bending moment, the RC base was provided with #5 top and bottom reinforcement bars at 4" (102 mm) spacing. To increase the shear capacity of the RC base, #4

hooks were specified at 4" (102 mm) spacing. Additionally, three horizontal #4 bars at 4" (102 mm) spacing were specified through the base depth to provide confinement at the compression zone generated under the post-tensioning rods. In the longitudinal direction of the RC base, #5 bars were placed at the top and at bottom at 4" (102 mm) spacing. These reinforcement details are shown with the specimen drawings in Appendix A.

The dimensions of the specimens without utility openings, specimens S1 and S4, are shown in Figure 3.7. On the other hand, the dimensions of the specimens that consider utility openings, specimens S2, S3, and S5, are shown in Figure 3.8. For simplicity, the utility openings were introduced only at the test regions where these openings did not continue through the RC bases, as shown in section B-B of Figure 3.8.

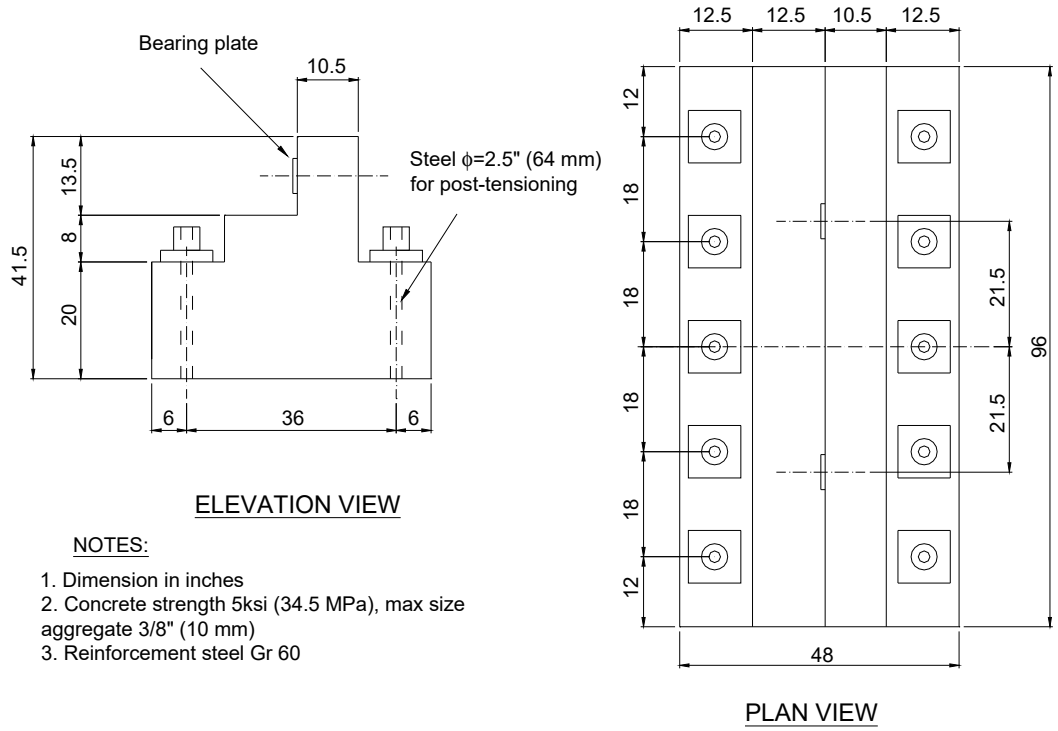

Fig. 3.7 Dimensions of specimens without utility openings, S1 and S4 (1"=25.4 mm).

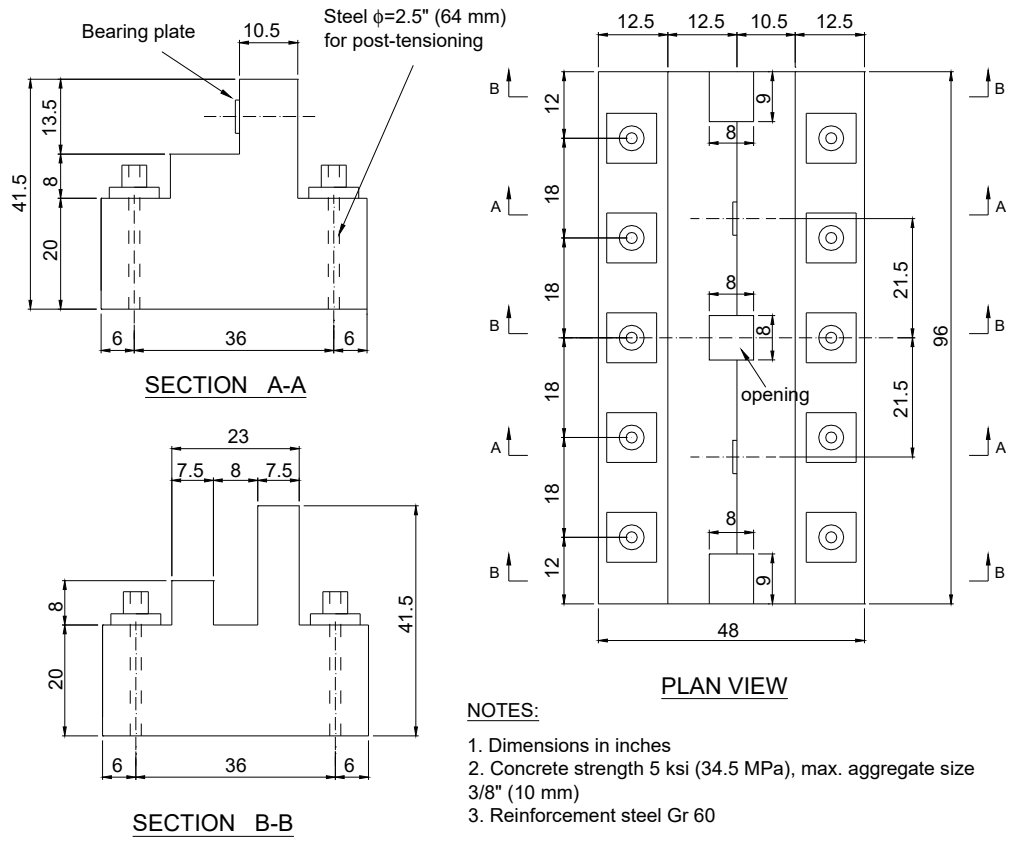

Fig. 3.8 Dimensions of specimens with utility openings, S2, S3 and S5 (1"=25.4 mm).

Normal-weight concrete was used with a specified design strength of 5 ksi (34.5 MPa) and 3/8" (10 mm) maximum aggregate size for the specimens of both test phases. The reinforcing steel used in the specimens was Grade 60, meeting the requirements of ASTM A706-04 [ASTM 2004b]. The five specimens considered headed and non-headed reinforcement. The headed bars were provided by HRC. These bars considered two types of heads that were fabricated by HRC. The #4 bars were fabricated using a friction weld procedure, and the #3 bars were fabricated using a conventional weld procedure. The photographs of the two types of heads are shown in Figure 2.13.

Finally, to place instrumentation to measure lateral deformation, a steel frame was built parallel to and independent from the test specimen. The photograph of the test setup of specimen S1 with the installed instrumentation is shown in Figure 3.9.

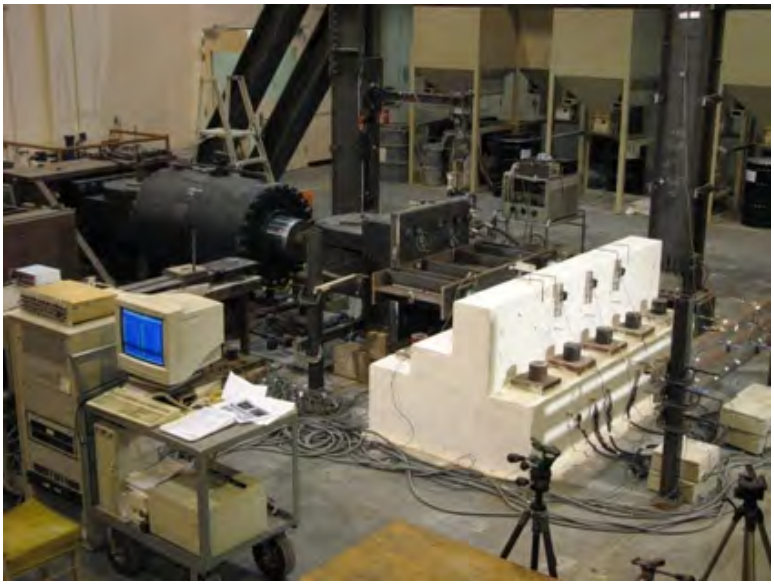

Fig. 3.9 Test setup of specimen S1.

3.6 INSTRUMENTATION

The five specimens of the two test phases were instrumented with three types of instruments: load cells, strain gages, and displacement transducers. Each specimen had a total of 3 load cells, 27 displacement transducers, and a variable number of strain gages. All the instruments were connected to a data acquisition system of a maximum of 128 channels.

3.6.1 Load Cells

Three load cells were used to measure the applied lateral load. The first one was the internal load cell of the actuator, which measured the total applied lateral load. This load cell was used to control the actuator in force control. The other two load cells were located between the loading beam and the test specimen. These load cells measured the applied force at each bearing as explained previously for the test setup.

Since the measured strength of the concrete was higher than the initially prescribed value of 5 ksi (34.5 MPa) (see Appendix B), the load cells attached to the beam were constructed specifically for this project. These load cells were built with a capacity of 300 kip (1334 kN) each. The construction process and calibration of these load cells are described in Appendix C.

3.6.2 Strain Gages

Strains were measured using strain gages attached to the reinforcing bars. The size of each gage was 5 mm by 2 mm with a post-yield deformation capacity of 10–15% strain. Each strain gage was glued to the surface of the reinforcing steel bar and was protected with three layers of coating: wax, butyl rubber (SB Tape®), and Araldite®. The preparation of the surface and the strain gage coating are shown in Figure 3.10.

(a) Preparation of bar surface

(b) Strain gages coated with wax (left) and SB tape (right)

Fig. 3.10 Placement of strain gages on reinforcing steel bars.

3.6.3 Displacement Transducers

A total of 27 displacement transducers were used to measure displacements during the experiment of each in-span hinge specimen. The locations of these instruments are shown in Figure 3.11. From these transducers, three were used to measure the actuator displacement, two for the loading beam displacement, ten for the seat horizontal deformation, six for the seat curvature, four for the base movement, one for the actuator bracket displacement and one for the slip of reinforcement.

The actuator displacement was measured with three instruments. The stroke of the actuator was measured with a built-in potentiometer. This potentiometer has a range of ±12 in. (610 mm) and was used to control the actuator under displacement control. The vertical and horizontal movements of the actuator were measured with two stick potentiometers (AVE and ATW in Fig. 3.11).

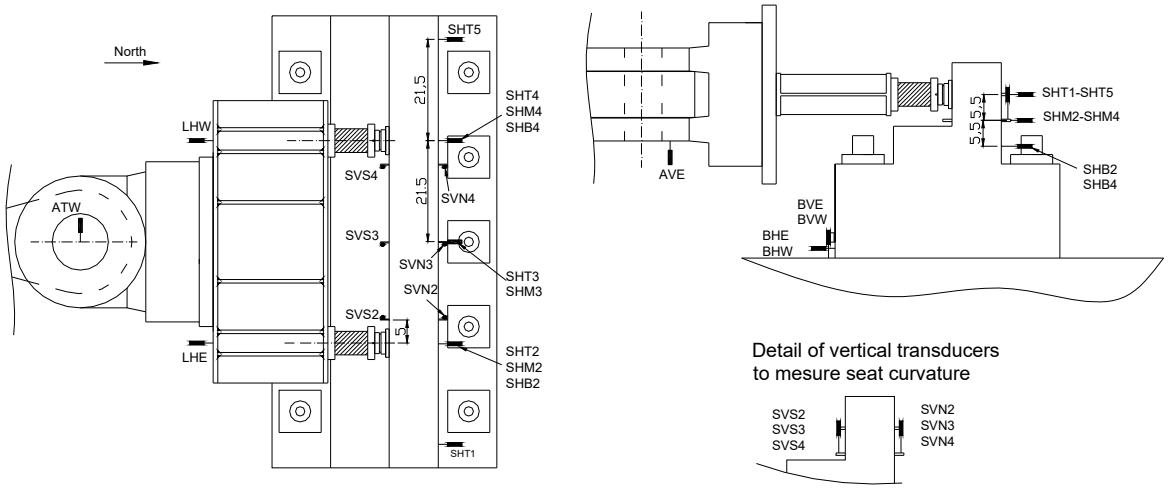

Fig. 3.11 Arrangement of displacement transducers.

The displacements of the loading beam at the loading points were measured with two stick potentiometers (LHE and LHW in Fig. 3.11). These two transducers allowed the measurements of any differential displacement between the two loading points.

The lateral displacement of the seat was measured with ten stick potentiometers. At the loading height, five stick potentiometers (SHT1–SHT5 in Fig. 3.11) were distributed throughout the diaphragm length to measure the displacement profile. At a medium height, three stick potentiometers were used to measure lateral displacement (SHM2–SHM4 in Fig. 3.11). Finally, at a lower height, two stick potentiometers were used (SHB2 and SHB4 in Fig. 3.11).

The curvature of the seat was measured in three locations, two at the vicinity of the bearings and one at the middle of the seat. The curvature measurements allowed identifying the bending action of the seat. At each location, two displacement transducers were connected to embedded threaded rods to measure relative vertical displacements (SVN2, SVS2, SVN3, SVS3, SVN4, and SVS4 in Fig. 3.11). The details of these instruments are shown in the small insert of Figure 3.11.

The relative movement of the RC base with respect to the strong floor was measure with four stick potentiometers. Two stick potentiometers were placed horizontally to measure any sliding of the RC base (BHW and BHE in Fig. 3.11), and the other two were placed vertically to measure any uplift or rotation of the RC base (BVW and BVE in Fig. 3.11). To measure the backward horizontal displacement of the actuator bracket, one stick potentiometer was connected at the actuator bracket (not shown in Fig. 3.11).

Finally, one stick potentiometer was used to measure the slip of a headed bar with respect to the surrounding concrete. The exact location of this instrument varied for the test specimens. To measure the slip with this instrument, a hole was prefabricated from the concrete surface to the head of the bar as shown in Figure 3.12a. Then, an external stick potentiometer was mounted on the top of the concrete surface and was connected in bearing to the bar head using a thin steel rod. Any relative deformation between the concrete surface and the head of the reinforcing steel bar was attributed to slip of the bar. Figure 3.12b shows a photograph of the instrument placed on specimen S1.

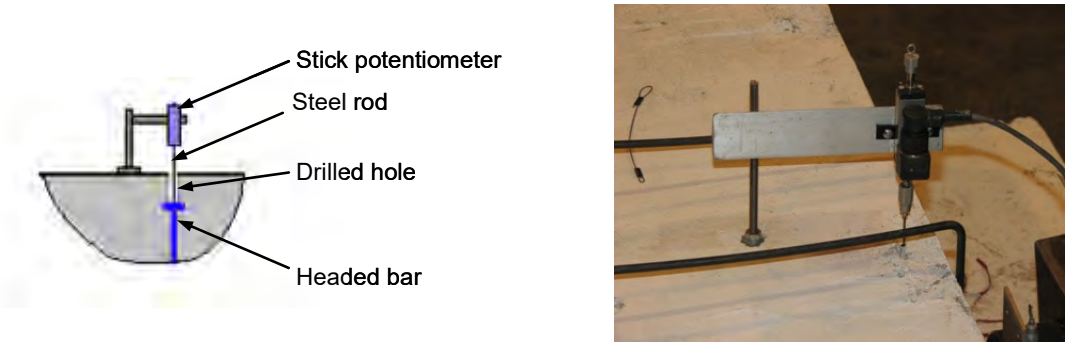

(a) Diagram (b) Photograph

Fig. 3.12 Instrumentation setup for headed bar slip measurement.

3.7 LOAD APPLICATION AND CONTROL

Due to the high stiffness prediction of the test specimens (obtained using FEA) and the low resolution of the actuator controller, two loading methods were specified for specimen S1: force control and displacement control. The force-control method was specified at the beginning of the experiment to determine the initial stiffness, initiation of cracking and onset of yielding of the reinforcing bars in the test specimen. Afterwards, the displacement-control method was specified to reach the peak strength and to capture the descending branch of the force-deformation relationship. Both loading methods were applied using compression cycles to evaluate the state of the in-span hinge after unloading from a peak load.

The force-control loading history applied to specimen S1 is shown in Figure 3.13. The loading rate was specified as 50 kip/min (222 kN/min) and the controller was configured for a theoretical resolution of 0.366 kip (1.63 kN) per step. The first cycle of 50 kip (222 kN) load corresponded to a low-level test that was used to check the behavior of the test setup and the instrumentation readings. The minimum load for the consecutive cycles was set to 10 kip (44.5

kN) to prevent movements of the loading beam. The test was paused at each peak load to inspect the specimen, to mark cracks, and to measure crack widths in the concrete.

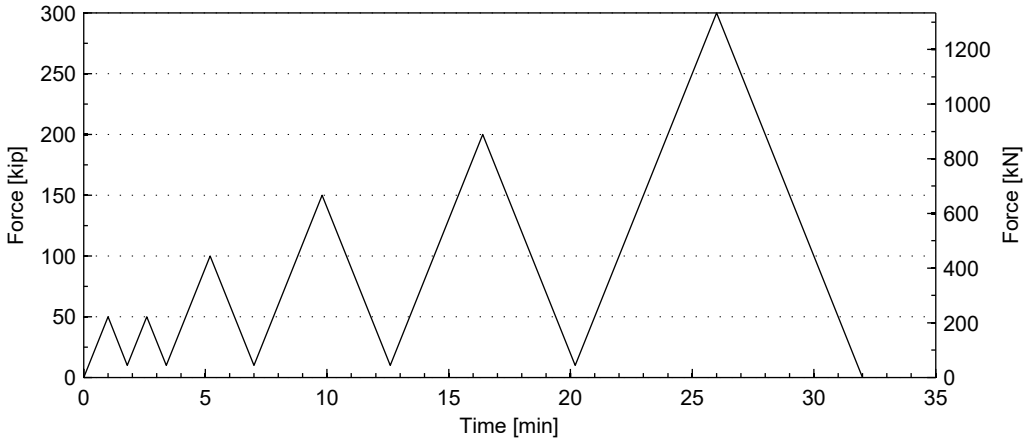

Fig. 3.13 Force-control loading history for specimen S1.

The displacement-control loading method was applied to reach the peak strength and to capture the descending branch of the force-deformation relationship. The displacement-control loading history is shown in Figure 3.14. The loading rate was specified as 0.04 in./min (1.02 mm/min) and the controller was configured for a theoretical resolution of 0.0014 in. (0.036 mm) per step. The zero displacement of the actuator for this loading method corresponded to the displacement at zero force in the load control method. The minimum displacement for the consecutive cycles was set to 0.1 in. (2.54 mm) to prevent movements of the loading beam. The final displacement was applied until a maximum displacement of 3 in. (76 mm) was achieved or until the specimen showed considerable strength reduction. The test was paused at each peak displacement to inspect the specimen, to mark cracks, and to measure the crack widths in the concrete.

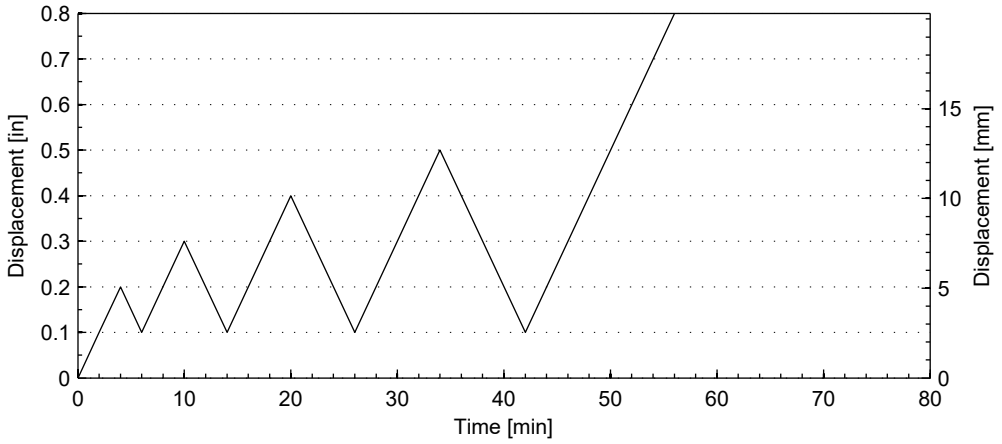

Fig. 3.14 Displacement-control loading history for specimen S1.

Since the measured stiffness of specimen S1 was small enough (compared to the initially predicted value from the FEA) for the actuator controller resolution, the remaining four specimens were tested using only displacement control. The target peak displacements of specimens S2–S5 were specified such that the loading history was equivalent to the history of specimen S1. The loading protocol used for these specimens is shown in Figure 3.15. For the last cycle, the minimum displacement was set to 0.2 in. (5.1 mm) to prevent movements of the loading beam with respect to the specimen. In this final cycle, the target displacement was set to 2.0 in. (50.8 mm).

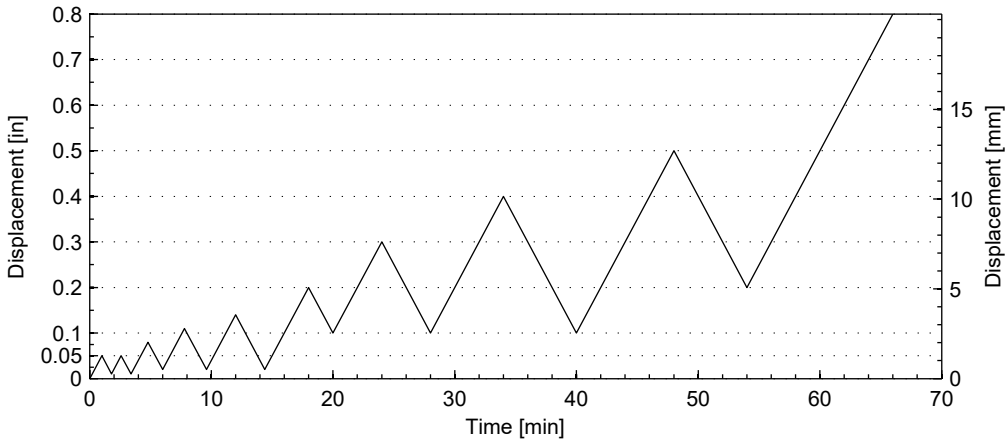

Fig. 3.15 Displacement-control loading history for specimens S2–S5.

4 Finite Element Pre-Test Analysis

In-span hinges are subjected to complex 3D loading conditions due to the discrete bearing locations, small aspect ratio of the seat, and the geometric discontinuities when utility openings exist. Therefore, evaluation of existing in-span hinges and development of design requirements can be improved with 3D models that take into account compatibility, equilibrium, and the constitutive properties of the different materials. Many computational methods exist for 3D modeling of structural systems; how well these models reflect the actual state of stresses is not clear (Vecchio and Collins 1986; Rots 1991; Selby and Vecchio 1993; Maekawa 2003). The 3D FEA in the presented research is intended to provide detailed results of the stress state, damage (cracking and plastification of concrete and yielding of steel reinforcement) initiation and propagation, and deformation experienced by the in-span hinges. This task was conducted prior to finalizing the test plans to check the capacity of the test setup and to select proper locations of the different instruments. After further calibration with the test results, the 3D FE models will be used to conduct parametric studies aiming toward providing guidelines for the future design of in-span hinges (see Fig. 1.2).

4.1 3D MODELING OF REINFORCED CONCRETE

The concrete is modeled using standard FE displacement formulation using 8-node isoparametric solid brick elements (Zienkiewicz and Taylor 2005; Hughes 2000). The brick element has 24 degrees of freedom and the displacement field is based on trilinear interpolation from the nodal displacements (Hughes 2000). To compute the stiffness matrix of each element, a Gauss integration scheme with 2×2×2 integration points is used. The nonlinear material behavior of the concrete is incorporated using nonlinear constitutive model.

4.1.1 Embedded Reinforcement

Modeling of reinforcement using FE is commonly performed by one of two different methods (Naito et al. 2001). The first method, which is less computationally demanding, involves the use of embedded reinforcement within the concrete. The embedded reinforcement action is introduced in the concrete element through which it passes (referred to as the "parent" element). Therefore, the stiffness of the concrete element is modified based on the path of the reinforcement through the element. The embedded reinforcement formulation implies perfect bond between the concrete and the reinforcement. The second method, which is more computationally demanding, involves separate discretization of the reinforcement from the surrounding concrete. In this case, the reinforcement is modeled as discrete 1D elements and is attached to the adjacent concrete nodes through interface elements. These interface elements between the concrete node and the reinforcement node allows for modeling bond slip effects. The drawbacks of the latter method are the additional nodes required and that the concrete mesh is restricted by the reinforcement locations. This restriction makes the concrete mesh difficult to generate, particularly in situations such as the in-span hinge which has high reinforcement ratios and several diagonal bars.

For the case of embedded reinforcement, two cases can be considered, smeared or discrete modeling. For the smeared case, the reinforcement is uniformly distributed in the concrete, and it is specified using a reinforcing ratio and an orientation (Vecchio and Collins 1986). For the discrete case, the location of each reinforcing bar is specified independently. The embedded reinforcement model available in the FE software DIANA (2007) considers the action of reinforcement only in the longitudinal direction. This assumption neglects the shear stiffness provided by the reinforcement and the dowel action of reinforcing bars across concrete cracks. The relationship between the longitudinal strain and stress of a bar is given by an assumed constitutive model. The strain of the bar $\varepsilon_{x'}$ in its longitudinal direction x' is given by (Freenstra 1995):

$$\varepsilon_{x'} = T\,\varepsilon \tag{4.1}$$

where for the 3D case, ε is the strain column vector in the xyz coordinate system and T is a coordinate transformation row vector, i.e.,

$$\varepsilon = \begin{bmatrix} \varepsilon_{xx} & \varepsilon_{yy} & \varepsilon_{zz} & \gamma_{xy} & \gamma_{xz} & \gamma_{yz} \end{bmatrix}^T \tag{4.2}$$

$$T = \begin{bmatrix} l_1^2 & l_2^2 & l_3^2 & l_1 l_2 & l_1 l_3 & l_2 l_3 \end{bmatrix} \tag{4.3}$$

where superscript T indicates the vector transposition. The terms l_1, l_2 and l_3 represent the direction cosines of the reinforcement direction x' with respect to the global xyz coordinate system (Ranjbaran 1991). The relationship between the strain of the embedded reinforcement and the nodal displacement of the parent concrete element is

$$\varepsilon_{x'} = T\,\varepsilon = T\,B\,d = B_s d \tag{4.4}$$

where B is the matrix that relates the strain field within the finite element to the nodal displacements of the parent concrete element (Hughes 2000). For the reinforcement, a non-dimensional coordinate r $(-1 \le r \le 1)$ is defined along the reinforcement path in the parent concrete element. Therefore,

$$l_1 = \frac{\partial x}{\partial x'} = \frac{\partial x}{\partial r}\frac{\partial r}{\partial x'} \qquad l_2 = \frac{\partial y}{\partial x'} = \frac{\partial y}{\partial r}\frac{\partial r}{\partial x'} \qquad l_3 = \frac{\partial z}{\partial x'} = \frac{\partial z}{\partial r}\frac{\partial r}{\partial x'} \tag{4.5}$$

Defining $C = \dfrac{\partial x'}{\partial r}$ and using the fact that $l_1^2 + l_2^2 + l_3^2 = 1$, one obtains

$$C = \sqrt{\left(\frac{\partial x}{\partial r}\right)^2 + \left(\frac{\partial y}{\partial r}\right)^2 + \left(\frac{\partial z}{\partial r}\right)^2} \tag{4.6}$$

With the initial (i.e., point at which reinforcing bar first intersects the concrete element), $(\xi_a, \eta_a, \varsigma_a)$, and final (i.e., point at which reinforcing bar last intersects the concrete element), $(\xi_b, \eta_b, \varsigma_b)$, isoparametric coordinates of the reinforcement in the parent concrete element, the position of the reinforcement along the non-dimensional path r is given by

$$\begin{aligned} \xi(r) &= 0.5r(\xi_b - \xi_a) + 0.5(\xi_b + \xi_a) \\ \eta(r) &= 0.5r(\eta_b - \eta_a) + 0.5(\eta_b + \eta_a) \\ \varsigma(r) &= 0.5r(\varsigma_b - \varsigma_a) + 0.5(\varsigma_b + \varsigma_a) \end{aligned} \tag{4.7}$$

Using the chain rule, the derivatives of x, y, and z with respect to the non-dimensional variable r are obtained from

$$\begin{bmatrix} \dfrac{\partial x}{\partial r} \\ \dfrac{\partial y}{\partial r} \\ \dfrac{\partial z}{\partial r} \end{bmatrix} = \begin{bmatrix} \dfrac{\partial x}{\partial \xi} & \dfrac{\partial x}{\partial \eta} & \dfrac{\partial x}{\partial \varsigma} \\ \dfrac{\partial y}{\partial \xi} & \dfrac{\partial y}{\partial \eta} & \dfrac{\partial y}{\partial \varsigma} \\ \dfrac{\partial z}{\partial \xi} & \dfrac{\partial z}{\partial \eta} & \dfrac{\partial z}{\partial \varsigma} \end{bmatrix} \cdot \begin{bmatrix} \dfrac{\partial \xi}{\partial r} \\ \dfrac{\partial \eta}{\partial r} \\ \dfrac{\partial \varsigma}{\partial r} \end{bmatrix} \tag{4.8}$$

where the 3×3 matrix of Equation (4.8) is the Jacobian of the isoparametric transformation for a 3D finite element (Hughes 2000). Finally, the stiffness contribution of the reinforcement to the parent concrete element is

$$k = \int_{x'} B_s^T A E_{sp} B_s \, dx' \tag{4.9}$$

where A is the area of the reinforcing bar and E_{sp} is its tangent modulus of elasticity. Changing variables, the previous integral can be written in terms of the non-dimensional variable r as

$$k = \int_{r=-1}^{1} B_s^T A E_{sp} B_s \, C \, dr \tag{4.10}$$

where C is the Jacobian of the transformation between the variables x' and r, given by Equation (4.6). The latter integral is evaluated numerically using two gauss integration points in this study.

4.2 CONSTITUTIVE MATERIAL MODELS

The constitutive material models used in the FEA are based on assumed idealized mechanical properties of the expected concrete and reinforcing steel materials. This is the case, as the simulations were executed before conducting any testing. The measured material parameters obtained from the material testing will be used for future post-test simulations and parametric studies.

4.2.1 Constitutive Model of Concrete

Concrete is a complex material with different tensile and compressive behavior, which depends on the confinement. When concrete reaches its tensile strength, it cracks with diminishing strength as the crack width increases. The cracks are geometrical discontinuities that separate the material. To model the cracking behavior of materials, there are two basic approaches, the discrete crack approach and the smeared-crack approach (Rots 1991; Bažant and Planas 1998). The discrete crack approach reflects the final damaged state most closely. It models the crack directly via a displacement-discontinuity in an interface element that separates two solid elements. Unfortunately, this discrete approach does not fit the nature of the finite element displacement method, and it is computationally more convenient to employ a smeared-crack approach. In this approach, a cracked solid is imagined to remain as a continuum and to continue permitting a description in terms of stress-strain relationships. This second approach is utilized in the presented FE model for the prediction of the behavior of the in-span hinges. However, the underlying assumption of displacement continuity in this approach contradicts with the nature of the geometrical discontinuities that occurs across a crack. This assumption in some cases is known to cause stress locking (Rots 1991).

The concrete behavior using the smeared-crack approach is utilized in the FE models presented herein using two different methods, namely the multi-directional fixed-crack method and the total strain-rotating-crack method. The multi-directional fixed-crack method considers that the orientation of the cracks remain constant, whereas the total strain rotating-crack method considers that the orientation of the cracks rotates with the directions of the principal strains. Both of these smeared-crack methods are described below for completeness.

The multi-directional fixed-crack method is based on the concept of decomposition of the total strain increments into concrete strain increments, $\Delta\varepsilon^{co}$, and crack strain increments, $\Delta\varepsilon^{cr}$ (Rots et al. 1985).

$$\Delta\varepsilon = \Delta\varepsilon^{co} + \Delta\varepsilon^{cr} \tag{4.11}$$

This decomposition allows the crack behavior to be treated separately from the constitutive behavior of the concrete between the cracks. Therefore, elastic, thermal, and creep strains can also be included in the concrete strain increments. In a 3D formulation, the crack opening displacement is replaced in the nst local coordinate system (Fig. 4.1) by a normal smeared-crack strain $\Delta\varepsilon^{cr}_{nn}$, and two perpendicular shear crack strains $\Delta\varepsilon^{cr}_{nt}$ and $\Delta\varepsilon^{cr}_{ns}$ located at the crack plane to represent sliding at the crack surface. The global crack strains increments $\Delta\varepsilon^{cr}$ are obtained by transforming the crack strains increments in local coordinates $\Delta e^{cr} = \left[\Delta\varepsilon^{cr}_{nn} \quad \Delta\varepsilon^{cr}_{nt} \quad \Delta\varepsilon^{cr}_{ns}\right]^T$ to the global coordinate system as follows:

$$\Delta\varepsilon^{cr} = \left[\Delta\varepsilon^{cr}_{xx} \quad \Delta\varepsilon^{cr}_{yy} \quad \Delta\varepsilon^{cr}_{zz} \quad \Delta\gamma^{cr}_{xy} \quad \Delta\gamma^{cr}_{xz} \quad \Delta\gamma^{cr}_{yz}\right]^T = N \cdot \Delta e^{cr} \tag{4.12}$$

where N is a geometry transformation matrix. Additionally, the stress increments at the crack interface ΔS^{cr} are related to the vector of the global stress increments $\Delta\sigma$ as

$$\Delta S^{cr} = \begin{bmatrix} \Delta\sigma^{cr}_{nn} \\ \Delta\sigma^{cr}_{nt} \\ \Delta\sigma^{cr}_{ns} \end{bmatrix} = N^T \cdot \left[\Delta\sigma_{xx} \quad \Delta\sigma_{yy} \quad \Delta\sigma_{zz} \quad \Delta\sigma_{xy} \quad \Delta\sigma_{xz} \quad \Delta\sigma_{yz}\right]^T = N^T \cdot \Delta\sigma \tag{4.13}$$

If multiple cracks occur at one integration point, the global vector of crack strain increments and that of crack stress increments for each crack ΔS^{cr}_j are computed using

$$\Delta\varepsilon^{cr} = \sum_j N_j \Delta e^{cr}_j \qquad \Delta S^{cr}_j = N^T_j \Delta\sigma \tag{4.14}$$

The initiation of cracks is governed by a tension cut-off criterion and a threshold angle between two consecutive cracks. Therefore, the successive initiation of cracks occurs if the principal stress violates the stress condition and the angle between the existing crack and the principal tensile stress exceeds the threshold angle (DIANA 2007). The stress-strain relationship for the cracked concrete is specified ignoring the coupling effect between the normal stress and

the shear stresses at the crack surface. This results in the following constitutive relationship for the crack j,

$$\Delta S_j^{cr} = D_j^{cr} \cdot \Delta e_j^{cr} \Rightarrow \begin{bmatrix} \Delta\sigma_{nn}^{cr} \\ \Delta\sigma_{nt}^{cr} \\ \Delta\sigma_{ns}^{cr} \end{bmatrix}_j = \begin{bmatrix} D^I & 0 & 0 \\ 0 & D^{II} & 0 \\ 0 & 0 & D^{III} \end{bmatrix}_j \cdot \begin{bmatrix} \Delta\varepsilon_{nn}^{cr} \\ \Delta\varepsilon_{nt}^{cr} \\ \Delta\varepsilon_{ns}^{cr} \end{bmatrix}_j \tag{4.15}$$

where D^I is the softening secant stiffness term for the normal stress, D^{II} and D^{III} are the softening secant stiffness terms for the shear stresses. These secants stiffness terms, for each crack j are determined using softening relationships.

The relationship between the vector of stress increments $\Delta\sigma$ and the vector of total strain increment $\Delta\varepsilon$ can be derived starting from the strain decomposition. Therefore,

$$\Delta\sigma = D^{co}\left(\Delta\varepsilon - \Delta\varepsilon^{cr}\right) \tag{4.16}$$

where D^{co} is the elastic constitutive matrix according to Hooke's law. Using the transformation matrix N and the crack secant stiffness matrix D^{cr} of Equation (4.15), the vector of stress increment when a single crack occurs can be computed as [Rots et al. 1985]:

$$\Delta\sigma = \left[D^{co} - D^{co}N\left[D^{cr} + N^T D^{co} N\right]^{-1} N^T D^{co}\right]\Delta\varepsilon \tag{4.17}$$

This equation shows that the cracking effect reduces the elastic stiffness D^{co} of the concrete. The multi-directional fixed-crack model was not used in the pre-test analysis of the in-span hinges presented in this report. However, this crack modeling method will be considered as an alternative in the post-test analysis and parametric studies.

The second smeared-crack method for concrete is the total strain method, which was developed along the lines of the 2D modified compression field theory (Vecchio and Collins 1986) and extended to 3D by Selby and Vecchio (1993). To model the stress-strain relationship two concepts are commonly used: the rotating crack and the fixed crack. The rotating-crack concept uses the coaxial stress-strain approach, in which the stress-strain relationships are evaluated in the principal directions of the strains, corresponding to the crack directions. For the fixed-crack concept, the stress-strain relationships are evaluated in a fixed coordinate system, which is set once cracking initiates. For the total strain method, the strain vector ε in the global coordinate system xyz at iteration $i+1$, for a nonlinear static loading, is updated with the strain increment $\Delta\varepsilon$ according to

$$\varepsilon^{i+1} = \varepsilon^i + \Delta\varepsilon^{i+1} \tag{4.18}$$

This strain vector is subsequently transformed to the crack directions nst (see Fig. 4.1) with a coordinate transformation matrix T. For the rotating-crack concept the transformation matrix

depends on the current strain vector $T^{i+1} = T\left(\varepsilon^{i+1}\right)$, while for the fixed-crack concept the transformation matrix is constant. Therefore, the strain vector in the crack direction *nst* is computed by

$$\varepsilon_{nst}^{i+1} = T^{i+1} \cdot \varepsilon^{i+1} \tag{4.19}$$

This transformation matrix is determined by calculating the eigenvectors of the strain tensor. Subsequently, the constitutive model is evaluated in the coordinate system of the crack, and then the stresses in the global coordinate system *xyz* are obtained with the transformation matrix,

$$\sigma_{nst}^{i+1} = \sigma\left(\varepsilon_{nst}^{i+1}\right) \qquad \sigma_{xyz}^{i+1} = \left[T^{i+1}\right]^T \sigma_{nst}^{i+1} \tag{4.20}$$

During loading, the concrete is subjected to both tensile and compressive stresses, which may result in cracking and crushing of the material. The deterioration of the material due to cracking and crushing in the 3D concrete material is monitored with six internal damage variables $\alpha_k, k = 1,\ldots,6$ (Fig. 4.1). The loading-unloading-reloading condition is monitored with unloading parameters $r_k, k = 1,\ldots,6$ (Fig. 4.1), which model the stiffness degradation in tension and compression separately. These parameters for tension and compression are respectively expressed as follows:

$$r_k = \begin{cases} 0 & \text{if } \varepsilon_k^{i+1} > \alpha_k \\ 1 & \text{if } \varepsilon_k^{i+1} \le \alpha_k \end{cases}, \quad k = 1,2,3 \tag{4.21}$$

$$r_k = \begin{cases} 0 & \text{if } \varepsilon_{k-3}^{i+1} < \alpha_k \\ 1 & \text{if } \varepsilon_{k-3}^{i+1} \ge \alpha_k \end{cases}, \quad k = 4,5,6 \tag{4.22}$$

With the assumption of no damage recovery (i.e., absolute values of the internal damage variables are increasing), the stress in direction j is given by

$$\sigma_j = f_j(\alpha, \varepsilon_{nst}) \cdot g_j(\alpha, \varepsilon_{nst}) \tag{4.23}$$

where f_j is the uniaxial stress-strain relationship and g_j is the loading-unloading function with $0 \le g_j \le 1$. If unloading and reloading is modeled with a secant approach, g_j is given by

$$g_j = \begin{cases} 1 - \dfrac{\alpha_j - \varepsilon_j}{\alpha_j} & \text{if } \varepsilon_j > 0 \\ 1 - \dfrac{\alpha_{j+3} - \varepsilon_j}{\alpha_{j+3}} & \text{if } \varepsilon_j \le 0 \end{cases} \tag{4.24}$$

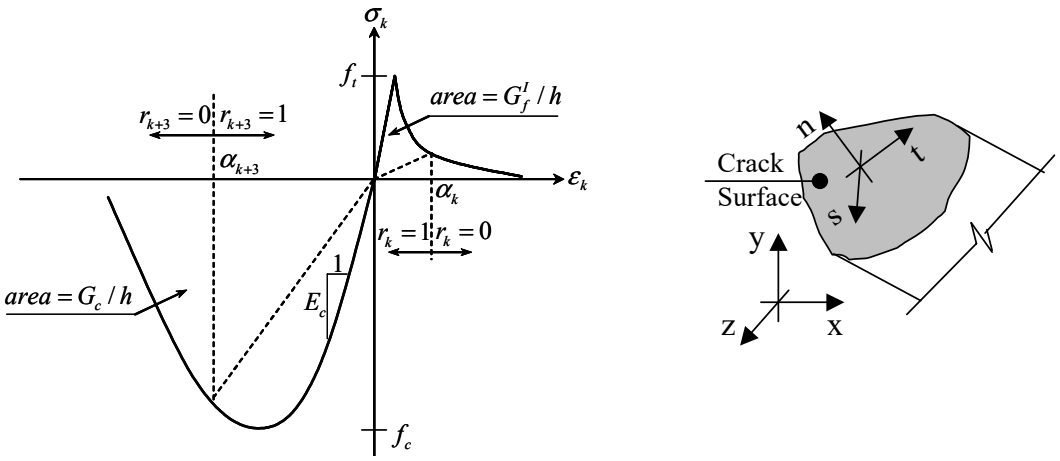

Fig. 4.1 Rotating-crack surface and unidirectional concrete material model in principal directions.

For the incremental-iterative solution scheme, the total strain method should define a stiffness matrix, which is utilized to achieve equilibrium. In this study, a secant stiffness matrix approach is adopted. This approach has proven to be robust and stable in RC structures with extensive cracking (DIANA 2007). For this purpose, the secant stiffness terms in the j-th cracking direction are presented below for the tension and compression regimes, respectively.

$$\overline{E}_j = f_j(\alpha, \varepsilon_{nst}) / \alpha_j \quad \text{for compression regime} \tag{4.25}$$

$$\overline{E}_j = f_j(\alpha, \varepsilon_{nst}) / \alpha_{j+3} \quad \text{for tension regime} \tag{4.26}$$

These secant stiffness terms can be geometrically interpreted as the slopes of the dashed inclined lines in Figure 4.1. The secant stiffness matrix in the nst coordinate system is given by

$$D_{secant} = \begin{bmatrix} \overline{E}_1 & 0 & 0 & 0 & 0 & 0 \\ 0 & \overline{E}_2 & 0 & 0 & 0 & 0 \\ 0 & 0 & \overline{E}_3 & 0 & 0 & 0 \\ 0 & 0 & 0 & \overline{G} & 0 & 0 \\ 0 & 0 & 0 & 0 & \overline{G} & 0 \\ 0 & 0 & 0 & 0 & 0 & \overline{G} \end{bmatrix} \tag{4.27}$$

Equation (4.27) corresponds to the stiffness matrix of an orthotropic material with zero Poisson's ratio in all directions. For the case of the fixed-crack concept, the shear modulus can be modeled as $\overline{G} = \beta_s G$ where the parameter β_s ($0 \le \beta_s \le 1$) is a non-dimensional shear retention factor that reduces the elastic shear modulus G of concrete after cracking to the constant value $\overline{G}$. Finally, the stiffness matrix in global coordinates xyz at each integration point is obtained using the coordinate transformation matrix T, Equation 4.19.

For the pre-test analysis of the in-span hinge regions, the total strain method with rotating cracks is used. The uniaxial stress-strain relationship for the concrete compressive behavior is based on elastic-perfectly-plastic behavior, shown in Figure 4.2a, and governed by the concrete compressive strength f_c. The tensile relationship is based on linear tension softening, shown in Figure 4.2b. Different stress-strain relationships in compression and tension will be explored in the post-test analysis and parametric studies. The tensile behavior depends on the concrete tensile strength f_t and the fracture energy G_f^I. When the tensile strain is larger than the ultimate strain $\varepsilon_u = 2G_f^I / hf_t$, the concrete loses its entire tensile capacity. This ultimate strain depends on the crack band-width h expressed as $h = \sqrt[3]{V_e}$ where V_e is the volume of the finite element. The initial linear parts of the compression and tension stress-strain relationships are governed by the initial material elastic modulus of concrete E_c (Fig. 4.1).

(a) Compression (b) Tension

Fig. 4.2 Concrete stress-strain relationships.

4.2.2 Constitutive Model of Reinforcing Steel

The embedded reinforcement is modeled using a uniaxial elastic-perfectly-plastic model with identical compression and tension behavior (Fig. 4.3). The yield stress f_y and the modulus of elasticity E_s represent the material parameters of the model. The stress hardening behavior commonly observed in tension test of reinforcing bars will be incorporated in the post-test analysis.

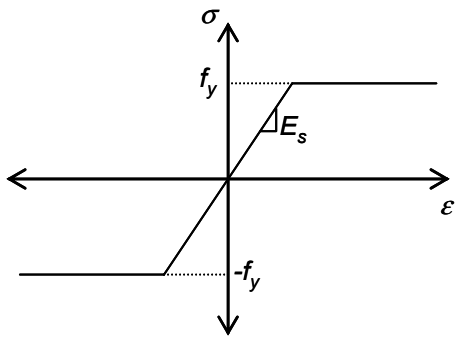

Fig. 4.3 Reinforcing steel stress-strain relationship.

4.3 NONLINEAR SOLUTION STRATEGY

In nonlinear FEA, the relationship between forces and displacements is no longer linear. Therefore, to achieve equilibrium, an incremental-iterative solution algorithm is necessary. The load (or imposed displacement) is applied with small increments and the equilibrium at each load step is achieved using iterations. The solution strategies typically used for FEA are: regular Newton-Raphson, modified Newton-Raphson and linear (Zienkiewicz and Taylor 2005). The regular and modified Newton-Raphson methods are shown in Figure 4.4. For the regular Newton-Raphson strategy, the tangent stiffness is calculated for every iteration at a given increment. This strategy yields a quadratic convergence, which means that the iteration process converges with a few iterations. The modified Newton-Raphson strategy computes the tangent stiffness at the start of the load increment and uses the same stiffness for all the iterations within this load increment. This method usually requires more iterations than the regular Newton-Raphson, but the computations are faster for each iterations, since tangent stiffness matrix is formulated, assembled, and decomposed only once at the beginning of each load increment. Finally, the linear strategy uses the initial linear stiffness matrix for all the iterations in all the load increments. The linear stiffness method is usually very robust, especially in nonlinear dynamic analysis (Mosalam and Mosallam 2001) but it is possible that the system follows an unstable equilibrium path after bifurcations (DIANA 2007).

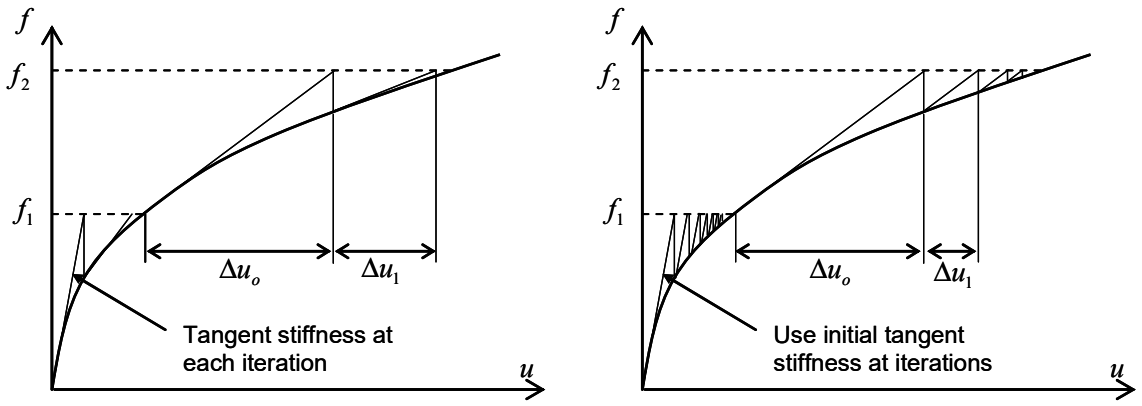

(a) Regular (b) Modified

Fig. 4.4 Newton-Raphson nonlinear solution strategies.

4.4 PRE-TEST FEA

To predict the behavior and the strength of the in-span hinge specimens, a pre-test FEA was conducted using the general-purpose finite element program DIANA (DIisplacement ANAlizer). This pre-test FEA was conducted for specimens S1 and S2 of the test matrix (see Chapter 3).

4.4.1 Mesh Development

Test specimens S1 and S2 were discretized to match the geometry and the boundary conditions. The finite element models include the in-span hinge region, the concrete base of the planned experiments and the steel loading plates. The concrete of specimen S1 is discretized using 4850 nodes and 3790 brick elements. This mesh is shown in Figure 4.5a. The mesh of specimen S2 is similar to that of specimen S1 but has fewer elements due to the presence of utility openings, as shown in Figure 4.5b. To model the steel, embedded reinforcement is used in the in-span hinge region and also in the concrete base. The embedded reinforcement of specimens S1 and S2 are shown in Figures 4.5c and d, respectively. Specimen S1 contains a total of 705 bars located throughout the specimen.

The boundary conditions of the concrete base are assumed pinned along the three global axes, and the post-tension forces of 120 kip (534 kN) are applied externally at the top of the concrete base at the locations of each anchoring rod. The steel bearing plates are modeled with a higher modulus of elasticity to simulate the stiffness provided by the loading swivels which are located adjacent to the loading plates (see the test setup in Chapter 3).

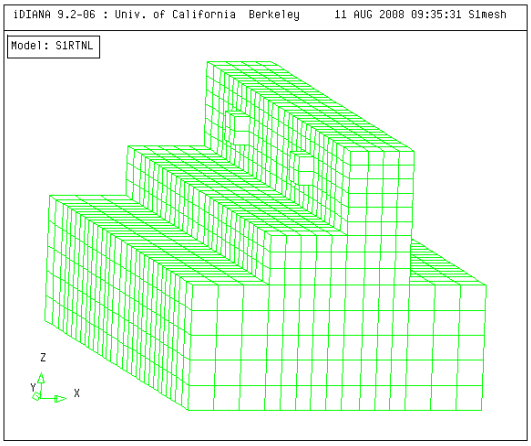

(a) Concrete mesh of specimen S1

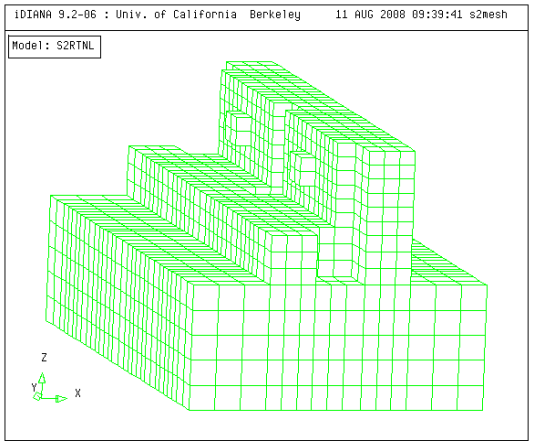

(b) Concrete mesh of specimen S2

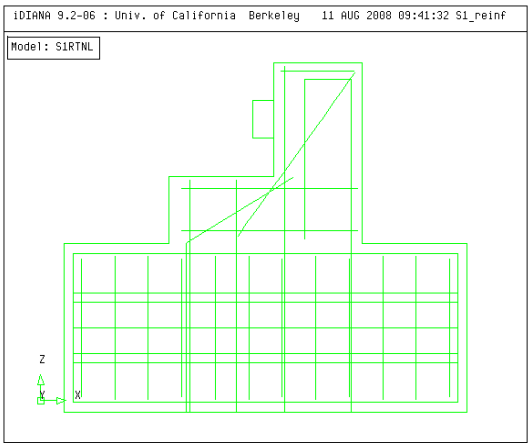

(c) Cross section showing embedded reinforcement of specimen S1

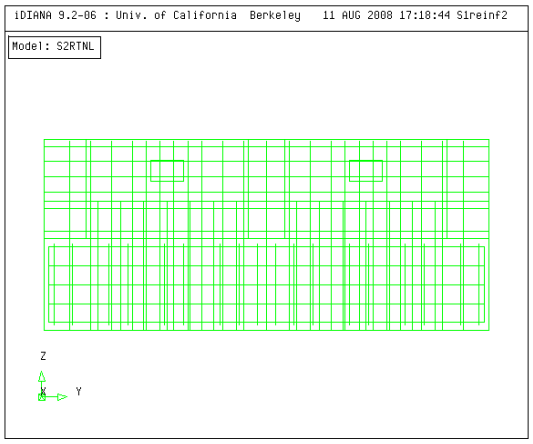

(d) Elevation view showing embedded reinforcement of specimen S2

Fig. 4.5 FEA models of specimens S1 and S2.

4.4.2 Capacity Estimation

The pre-test models of specimens S1 and S2 are analyzed to predict the behavior and strength of the in-span hinges. For these models, the concrete is represented using the total strain rotating-crack method. The uniaxial stress-strain relationship for the compressive behavior is based on elastic-perfectly-plastic idealization using a concrete strength of 6 ksi (41.4 MPa). The uniaxial tensile behavior is based on a linear tension softening with a tensile strength of $6\sqrt{f_c'} = 460$ psi (3.2 MPa) and an assumed fracture energy of 0.31 lbf/in. (54 N/m). The value of the fracture energy is obtained from the CEB recommendation (Comité 1990). The modulus of elasticity used in the concrete is 4400 ksi (30.4 GPa) based on the ACI provisions (ACI 2008). For the

reinforcing steel, an elastic-perfectly-plastic behavior is assumed with a yield stress of 70 ksi (483 MPa) and elastic modulus of 29000 ksi (200 GPa).

The solution strategy used in the pre-test analysis is regular Newton-Raphson. The load is applied symmetrically at the two bearing plates by simultaneously imposing displacement increments of 0.005" (0.127 mm) at the bearing plates. For both specimens, S1 and S2, the response was computed until no convergence was achievable in the iterative process.

The predicted load-displacement relationships at the bearings for specimens S1 and S2 are shown in Figure 4.6. Because the model is symmetric, only the relationship at one bearing is shown for each specimen. The shown displacements in Figure 4.6 correspond to the deformations of the concrete located behind the seats in the test configuration. These locations coincide with the position of instruments SHT2 and SHT4 of the test specimens (see Fig. 3.11). On the other hand, the loads shown in Figure 4.6 represent the applied forces on one bearing. Therefore, the total applied load to the specimen is twice the load shown in Figure 4.6. From the results shown in Figure 4.6, the predicted capacity per bearing is 209 kip (930 kN) and 203 kip (903 kip) for specimens S1 and S2, respectively. Therefore, the total capacity predicted for specimens S1 and S2 from the pre-test FEA are 418 kip (1859 kip) and 406 kip (1806 kip), respectively. These loads occur at a displacement of 0.33" (8.4 mm) and 0.48" (12.2 mm) for specimens S1 and S2, respectively.

Figure 4.6 shows that nonlinear behavior for both specimens S1 and S2 starts at about 50 kip (222 kN) of applied load at each bearing. In both specimens, this nonlinear behavior is initiated by cracking of the concrete in the corner between the seat and the diaphragm. Additionally, it is observed that the presence of the utility openings of specimen S2 does not affect the behavior for bearing loads lower than 170 kip (756 kN). Therefore, the FEA suggests that the considered size of the utility openings of the analyzed in-span hinges only affects the behavior at high load levels.

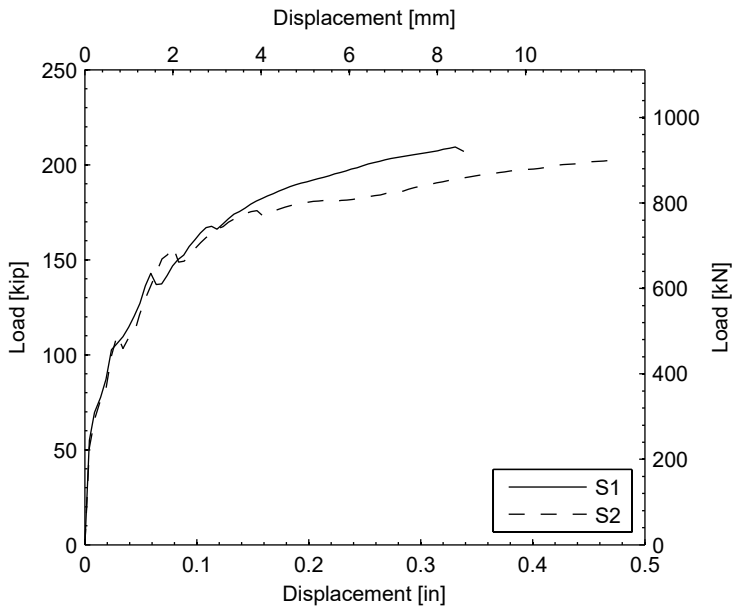

Fig. 4.6 FEA load-displacement relationships at bearings for specimens S1 and S2.

The response of specimen S1 is shown in Figure 4.7 for a load equivalent to 99% of the maximum estimated load capacity of the FEA. Figure 4.7a shows the deformed shape at the bearing cross section, which is characterized by clear shear deformation rather than bending deformation. The cracking behavior of the concrete at the bearing cross section is shown in Figure 4.7b, where the shown short lines are oriented perpendicular to the crack direction and their lengths are proportional to the crack normal strain (opening mode). It can be observed that at ultimate capacity, the larger cracks are predicted in an inclined plane. The reinforcement stresses (indicated by triangles of size proportional to the stress in the reinforcing bar) are shown in Figure 4.7c. It can be observed that yielding in tension is achieved in the diagonal bars of the seat, the horizontal (in the 90^o rotated test orientation) bars of the diaphragm, the vertical (in the 90^o rotated test orientation) bars of the seat, and in the longitudinal bars of the seat. Finally, the vertical (in the 90^o rotated test orientation) stresses in the concrete at the bearing cross section are shown in Figure 4.7d. The maximum tension of = 0.393 ksi (2.71 MPa) is located at the seat near the corner with the diaphragm, and maximum compression of 5.85 ksi (40.3 MPa) is located at the diaphragm near the corner with the base. This distribution of concrete stresses is highly affected by the concrete cracks and the presence of fully bonded embedded reinforcing steel bars.

The pre-test FEA described in this chapter confirmed that the test setup is adequate to conduct the experimental program. Moreover, it is confirmed that the experimental setup is able to apply the required maximum loads and deformations to the test specimens. The FEA described in this chapter will be improved to match the experimental results in a future phase of this research project. Different material models and solution strategies will be explored to obtain a realistic behavior of the FEA in comparison with the experimental findings discussed in Chapters 5 and 6.

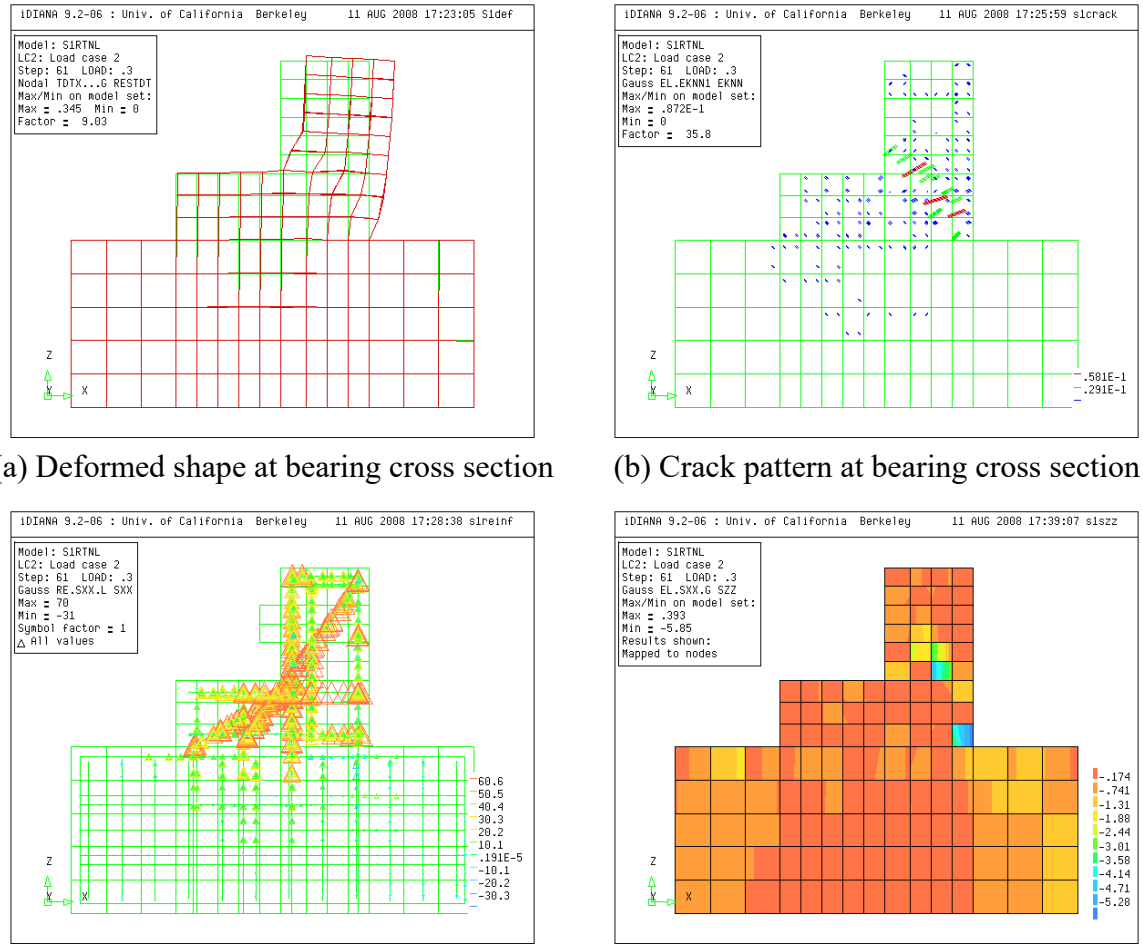

(a) Deformed shape at bearing cross section

(b) Crack pattern at bearing cross section

(c) Reinforcement stresses

(d) Vertical concrete stresses at bearing cross section

Fig. 4.7 FEA response of specimen S1 at 99% of maximum load.

5 Experimental Program Phase I: As-Built In-Span Hinges

This chapter describes the experimental program and the results of the first two specimens representing the as-built conditions of typical in-span hinges in California box-girder bridges. Specimen S2 was detailed identical to specimen S1, but it contained utility openings to study the effect of such openings on the structural behavior of in-span hinges. These tests were aimed to understand the behavior, load path and the failure mode of as-built in-span hinges. At the end of this chapter, concluding remarks are presented to motivate the design of the three specimens comprising phase II of this experimental research.

5.1 SPECIMEN DESIGN

Specimens S1 and S2 were designed considering the as-built conditions of typical in-span hinges of California box-girder bridges. The specimen characteristics were obtained from the prototype in-span hinge presented in Chapter 3 using 1/3-scale. The two specimens are identical, except for the presence of utility openings in specimen S2, which were added to study the effect of such openings on the behavior and strength of in-span hinges.

Both specimens considered conventional and headed reinforcing bars. The reinforcement details were obtained by scaling the prototype in-span hinge described in Chapter 3. These details were identical in both specimens, except for the modification of the reinforcement in the vicinity of the utility openings in specimen S2. The reinforcement details at the bearing cross section are shown in Figure 5.1, and the complete structural drawings are presented in Appendix A. Headed reinforcement (#3 and #4 bars) was used in both in-span hinge specimens. The reinforcement ratios in the two specimens are compared with the prototype ratios (defined previously in Chapter 3) in Table 5.1. The largest difference between these ratios is for the horizontal reinforcement of the seat ρ_{sh} (vertical reinforcement in the test orientation). This large

difference is due to the U-shape bar shown in Figure 5.1, where the available bar sizes can not be adjusted more precisely. Moreover, the largest percentage difference with respect to the prototype details is for the diagonal reinforcement in the diaphragm ρ_{dd}. This large percentage difference is attributed to the original small reinforcement ratio of this category in the prototype details, forcing the reduced-scale specimens S1 and S2 to have relatively higher ρ_{dd} due to the limited choices of practical bar sizes. The spacing of the reinforcement of the in-span hinge area, shown in Figure 5.1, is 3" (76 mm) in the vicinity of the bearings and 4.5" (114 mm) away from them (except for the reinforcement of the diaphragm ρ_{dd} which had a constant spacing of 5.0" (127 mm) and the longitudinal bars ρ_{lon}). The spacing layout is shown in the structural drawings of Appendix A.

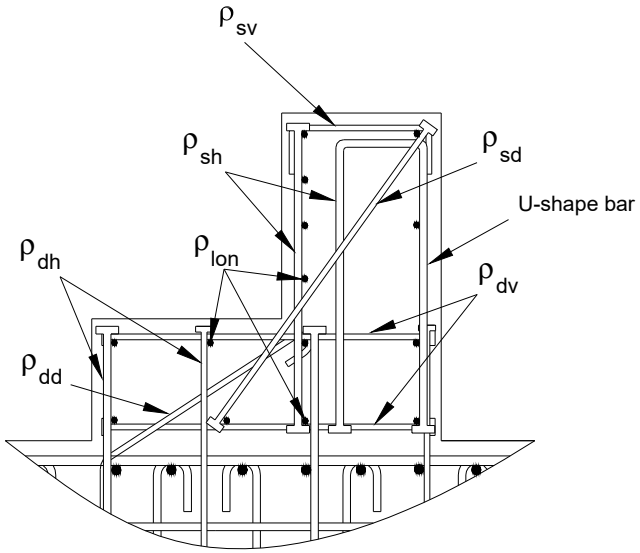

Fig. 5.1 Reinforcement details of specimens S1 and S2 (in test orientation).

Table 5.1 Comparison of reinforcing steel ratios between prototype and specimens S1 and S2 (%).

	ρ_{dh}	ρ_{dv}	ρ_{dd}	ρ_{sh}	ρ_{sv}	ρ_{sd}	ρ_{lon}
Prototype	0.87	0.61	0.07	1.53	0.24	0.30	0.47
S1 and S2	0.90	0.69	0.10	1.90	0.27	0.35	0.47
Difference	+0.03	+0.08	+0.03	+0.37	+0.03	+0.05	0.00
% difference	+3.5	+13.1	+42.9	+24.2	+12.5	+10.0	0.00

5.2 SPECIMEN CONSTRUCTION

Specimens S1 and S2 were constructed in the structural engineering laboratory of the University of California, Berkeley, by a professional contractor. The concrete was supplied by a local ready-mix plant and was cast using a pump. The concrete was cured with wet burlap for a period of 5 days inside the laboratory. At that age, the burlap was removed and the specimens were stripped from the formwork. Figure 5.2 shows photographs of the construction process of specimens S1 and S2.

5.3 MATERIAL PROPERTIES

Extensive material testing of the concrete and reinforcement was conducted as part of the research program. The material testing program was aimed to determine properties and constitutive relationships to be used in the FEA. The summary of the material properties is presented in this section. Further information about material testing is described in Appendix B.

(a) Starting construction

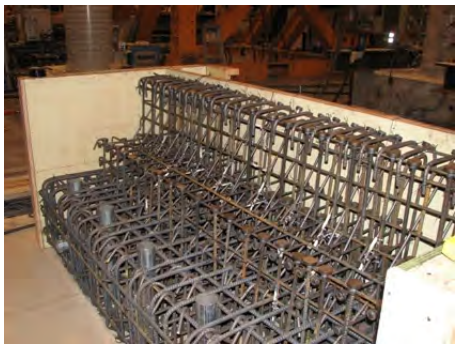

(b) Specimen S1 reinforcement

(c) Building forms

(d) Casting concrete

(e) Curing concrete

(f) Stripped specimens

Fig. 5.2 Construction process of specimens S1 and S2.

5.3.1 Concrete

Normal-weight concrete was used with specified design strength of 5 ksi (34.5 MPa) and 3/8" (10 mm) maximum aggregate size. The summary of the concrete properties for specimens S1 and S2 is shown in Table 5.2. This table shows that the measured concrete properties for specimen S2 were lower than those for specimen S1, due to the construction inherent variability. Since both specimens were built using the same concrete batch, the average values, reported in

Table 5.2, will be considered in the post-test FEA. The average splitting tensile strength and average modulus of rupture are equivalent to $6.3\sqrt{f_c'}$ [psi units] and $11.1\sqrt{f_c'}$ [psi units], respectively. The fracture energy obtained from the standard tests is about two times the value recommended by CEB-FIP code (Comité 1990), namely 0.33 lbf/in. (58.0 N/m).

Table 5.2 Properties of concrete in phase I.

Property	S1	S2	Average
Compressive strength f_c' [ksi (MPa)]	6.44 (44.4)	6.15 (42.4)	6.30 (43.4)
Strain at peak stress ε_o	0.0029	0.0029	0.0029
Modulus of elasticity E_c [ksi (GPa)]	3240 (22.4)	3100 (21.4)	3170 (21.9)
Splitting tensile strength f_{ct} [ksi (MPa)]	0.52 (3.59)	0.48 (3.31)	0.50 (3.45)
Modulus of rupture f_r [ksi (MPa)]	0.89 (6.14)	0.86 (5.93)	0.88 (6.03)
Fracture energy G_{ft} [lbf/in. (N/m)]	0.60 (105)	-	0.60 (105)
Age of testing [days]	77	110	-

The average stress-strain relationship of concrete in the compression of phase I in-span hinges is shown in Figure 5.3. The hardening response part of this curve (below the maximum strength) was obtained from the average of the force-control tests conducted for the two in-span hinge specimens of phase I. On the other hand, the softening response part of the curve was obtained from the average of the displacement-control tests also conducted for phase I. These tests are discussed in Appendix B.

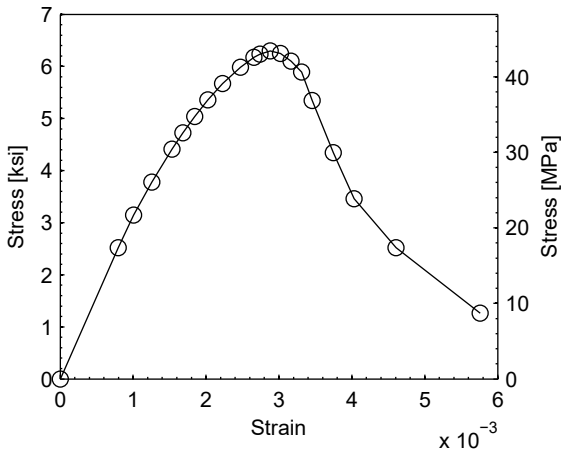

Fig. 5.3 Average stress-strain relationship of concrete in phase I.

5.3.2 Reinforcement

The reinforcing steel used in the specimens of phase I was Grade 60, meeting the requirements of ASTM A706-06 (ASTM 2004b). Specimens S1 and S2 considered headed and non-headed reinforcement, as explained in Chapter 3. The summary of the average reinforcing steel properties used in specimens S1 and S2 is show in Table 5.3.

Table 5.3 Average properties of reinforcing steel in phase I.

Property	#3 Non-headed	#3 Headed	#4 Headed
Yield stress f_y [ksi (MPa)]	69.9 (482)	69.5 (479)	68.7 (474)
Ultimate stress f_u [ksi (MPa)]	103.0 (710)	93.7 (646)	97.8 (674)
Yield strain ε_y	0.0025	0.0024	0.0024
Ultimate strain ε_u	0.137	0.114	0.123
Modulus of elasticity E_s [ksi (GPa)]	28020 (193)	29170 (201)	28390 (196)

The stress-strain relationships of the reinforcing steel are shown in Figure 5.4. These curves follow the Voce equation (Voce 1948), given below, which is implemented in the finite element software DIANA (DIANA 2007) used in this study.

$$f(\varepsilon) = \begin{cases} \varepsilon E_s \le f_y & \varepsilon \le \varepsilon_y + \varepsilon_{pl} \\ f_y + (f_u - f_y) \cdot \left(1 - exp\left[- \dfrac{\varepsilon - \varepsilon_y - \varepsilon_{pl}}{\varepsilon_{po}} \right] \right) & \varepsilon \ge \varepsilon_y + \varepsilon_{pl} \end{cases} \tag{5.1}$$

where $f(\varepsilon)$ is the stress corresponding to strain ε, ε_{pl} is the plateau strain, and ε_{po} is a parameter to adjust the strain-hardening region of the constitutive relation.

5.4 INSTRUMENTATION

Specimens S1 and S2 were instrumented with a total of 119 instruments each: 3 load cells, 89 strain gages, and 27 displacement transducers. All the instruments were connected to a data acquisition system of 128 channels. The description and location of load cells and displacement transducers were presented in Chapter 3. The locations of the strain gages on the reinforcing steel for specimens S1 and S2 are described below.

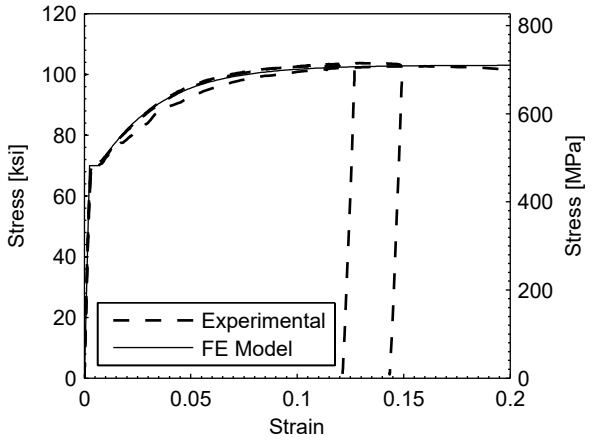

(a) #3 non-headed bar

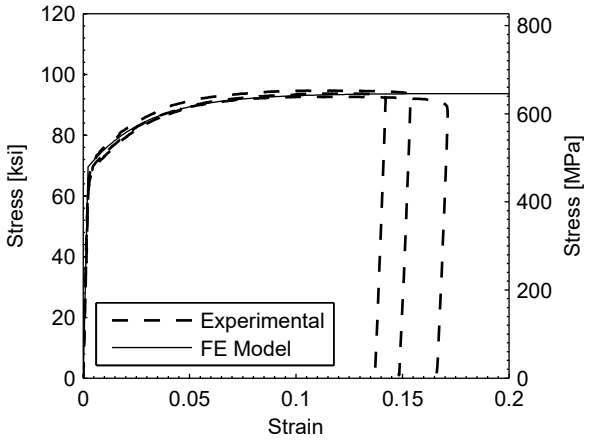

(b) #3 headed bar

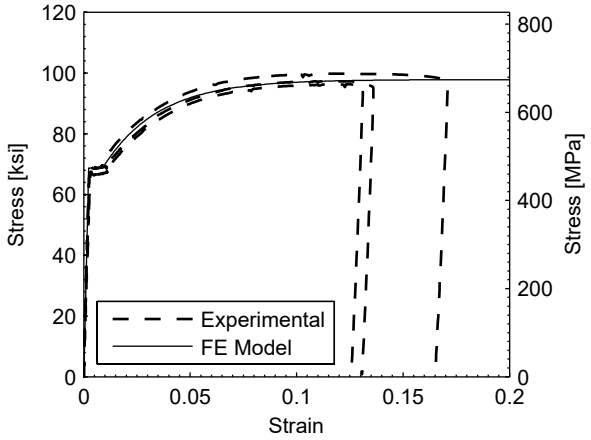

(c) #4 headed bar

Fig. 5.4 Stress-strain relationships for reinforcing steel in phase I.

The locations of the strain gages for specimens S1 and S2 are shown in Figure 5.5. A total of 20 strain gages were located in a cross section through each bearing (section b-b) to quantify the reinforcement stresses, and to identify the load transfer mechanism. At this cross section, 6 gages were located on horizontal bars (vertical in the test orientation) of the seat (H1-H6), 4 gages were located on vertical bars (horizontal in the test orientation) of the diaphragm (V1-V4), and 4 gages were located on diagonal bars (D1-D4). These 14 gages allowed identifying the possible failure modes of the seat: sliding shear friction, bending moment, 1D shear, SAT and punching shear. Finally, 6 gages of section b-b were located on horizontal bars (vertical in the test orientation) of the diaphragm (B1-B6) to measure the anchorage of the in-span hinge to the base.

A total of 36 gages were located in groups of 6 gages (H1, H2, V1, V2, D1 and D2) in cross sections c-c throughout the length of the specimen. These gages were used to measure the 3D effects of the load transfer from the bearing throughout the length of the diaphragm.

Finally, a total of 13 gages were located in longitudinal bars of the seat to measure the bending of the seat. From these gages, 8 (LP1-LP8) were used to measure the positive bending moment at the bearing locations, and 5 (LN1-LN5) were used to measure the negative bending moment between the two bearings.

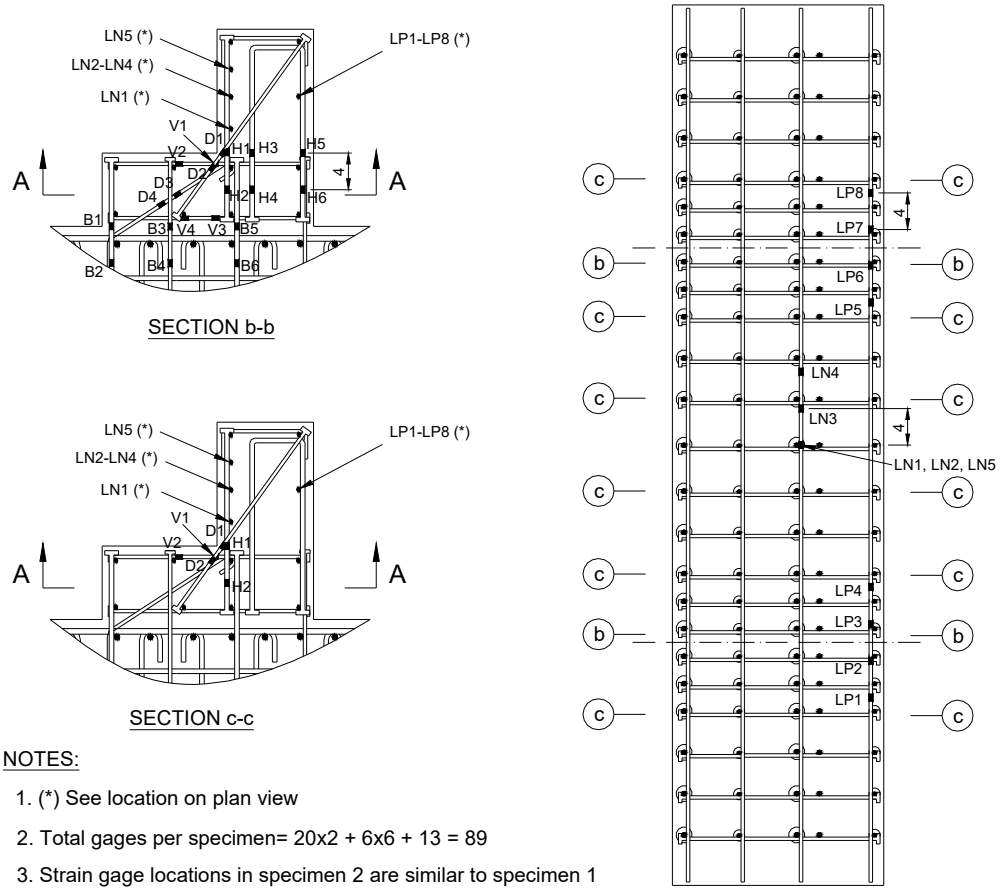

NOTES:

1. (*) See location on plan view
2. Total gages per specimen= 20x2 + 6x6 + 13 = 89
3. Strain gage locations in specimen 2 are similar to specimen 1

Fig. 5.5 Strain gage locations for specimens S1 and S2.

5.5 PRE-TEST STRENGTH ESTIMATION

The capacity of the in-span hinge specimens was estimated using the analytical models described in Chapter 2. These analytical models are sliding shear friction at the seat and at the diaphragm, moment strength at the seat and at the diaphragm, 1D shear strength at the seat, SAT, and punching shear. For the capacity estimates, the average strength of the materials at the time of the tests was used, as indicated in Tables 5.2 and 5.3 for concrete and steel, respectively.

The SAT capacity was computed using a 2D truss model. For specimens S1 and S2, the proposed truss topology is shown in Figure 5.6, where the continued lines represent tension ties and the dashed lines represent compression struts. The width of this truss considers the total width of the specimen, which is 96" (2438 mm). Therefore, the steel area of each tie is the sum of the bars along the specimen length. For specimen S2, the openings in the concrete were neglected in the truss model, but the areas of steel of the ties took into account the reduction of the number of bars at the openings. In this 2D SAT, the 3D behavior induced by the discrete loads at the bearings was neglected.

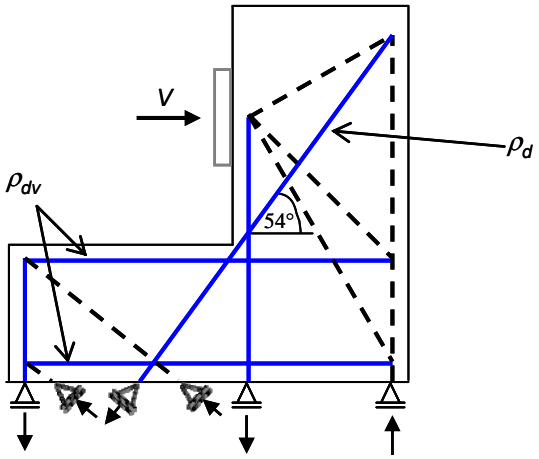

Fig. 5.6 Strut-and-tie model.

The larger SAT capacity of the statically indeterminate truss shown in Figure 5.6 was achieved when the diagonal tie of the seat ρ_d and the vertical ties of the diaphragm ρ_{dv} (horizontal ties in the test orientation) were yielding simultaneously. The SAT capacity was calculated and verified using the CAST software (Tjhin and Kuchma 2002; Tjhin 2004). The CAST solutions for specimens S1 and S2 are shown in Figure 5.7, with predicted SAT capacities of 370 kip (1646 kN) and 319 kip (1419 kN) for specimens S1 and S2, respectively.

Accordingly, the 2D SAT considering yielding of the steel throughout the whole in-span hinge length was expected to be an overestimation of the capacity because the 3D behavior induced by the discrete loads at the bearings was neglected. However, the experimental results were higher than this 2D SAT, possibly due to ignoring the concrete contribution in tension.

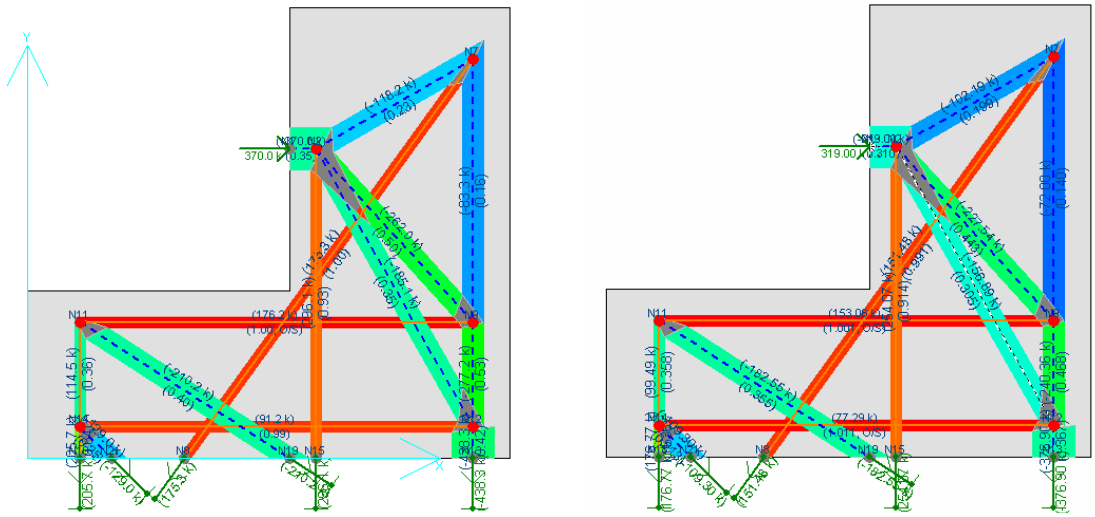

(a) Specimen S1 (b) Specimen S2

Fig. 5.7 SAT solutions using CAST (Tjhin 2004), forces in kip (1 kip = 4.45 kN).

The capacity estimates using the described analytical models are listed in Table 5.4. In the same table, the experimental results and the factored Caltrans design loads are tabulated for completeness. From this table, it can be observed that the strength of the seat is controlled by punching shear and SAT design methods. The sliding shear friction, bending moment, and shear design methods give much higher strength values, which means that these failure modes are not expected to control the response of the test specimens. From the test results, it is noted that the experimental capacity of both specimens S1 and S2 are larger than the SAT and punching shear strength estimates, but lower than the other modes of failure. Table 5.4 also shows that the predicted capacity for specimen S2 is 14% lower than that of specimen S1. This reduction of capacity is due to the presence of the utility openings, which reduces the number of effective reinforcing bars, i.e., areas of ties, throughout the seat length in the SAT model of specimen S2.

For the sliding shear friction mode, the strength was controlled by the ACI limit of $800A_c$ [lbf, in.], in spite of the large amount of longitudinal reinforcing steel. The factored Caltrans design loads for the test specimens were obtained by scaling the factored design load of the prototype in-span hinge defined in Chapter 3. Therefore, the factored design load for both

specimens was equal to $2\times611/(3)^2$ =136 kip (605 kN). The factored Caltrans design loads conservatively corresponded to only 29% and 32% of the real strength obtained from testing specimens S1 and S2, respectively.

Table 5.4 Strength estimates of specimens S1 and S2 [kip (kN)].

	S1	S2
Sliding shear friction at seat	806 (3585)	744 (3309)
Sliding shear friction at diaphragm	1170 (5204)	1127 (5013)
Moment strength at seat	695 (3092)	642 (2856)
Moment strength at diaphragm	766 (3407)	671 (2985)
1D Shear strength at seat	424 (1886)	375 (1668)
SAT	370 (1646)	319 (1419)
Punching shear	381 (1695)	381 (1695)
Experimental capacity	467 (2077)	425 (1890)
Factored Caltrans design load	136 (605)	136 (605)

5.6 SPECIMEN S1 TEST RESULTS

Due to the high predicted stiffness, specimen S1 was subjected to two consecutive loading protocols: force control and displacement control. The loading histories of both loading protocols were discussed in Chapter 3. It is to be noted that results shown as envelopes of the cyclic loading are consistent with the envelope of the global force-displacement relationship.

5.6.1 General Observations

The specimen was tested initially using load control protocol. The first crack appeared near the seat corner with the diaphragm at 100 kip (445 kN) peak cycle actuator load, as indicated by the arrow in Figure 5.8a. At 150 kip (667 kN) peak cycle actuator load, vertical (in the test orientation) bending cracks appeared behind the bearing plates as shown in Figure 5.8b. The last cycle of the force-control loading history, with a peak actuator load of 300 kip (1334 kN), was not executed, since the deformation achieved at the 200 kip (890 kN) peak cycle was sufficiently large to achieve acceptable resolution using the more stable displacement-control loading protocol. To change the loading protocol from load control to displacement control, the actuator was retracted completely, producing a gap between the loading beam and the specimen.

Subsequently, specimen S1 was tested using displacement control. When the specimen was contacted by the loading beam (precisely by the end plates of the load cells attached to the loading beam) connected to the actuator head, some adjustment of the loading system position was necessary. At the peak actuator cycle of 0.2" (5.1 mm), 45° inclined cracks appeared in the seat behind the bearing plates and next to them. These cracks are shown in Figures 5.8c–d. At this displacement level, a horizontal (in the test orientation) crack was observed in the diaphragm below the load cell, as shown in Figure 5.8d. The damage propagation for the 0.4" peak displacement cycle is shown in Figures 5.8e–f.

When reaching the maximum strength of the specimen, the deformation and damage start concentrating at the west side of the specimen. On this side, the width of diagonal cracks increased considerably measuring up to 0.06" (1.5 mm). When the peak load was reached, a major vertical (in the test orientation) crack appeared in the middle of the seat as shown in Figure 5.8g. After this crack was observed, the strength of the west bearing started to decrease considerably and a punching shear failure mode was observed, as shown in Figure 5.8h. The diagonal punching shear crack at the top of the seat (in the test orientation) appeared only toward the center of the specimen, as marked with an arrow in Figure 5.8h. Additionally, spalling of the concrete was observed near the corner between the diaphragm and the concrete base due to the relative deformation induced by the punching shear mechanism, as shown in Figure 5.8g.

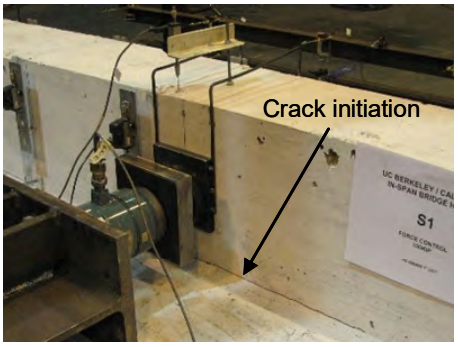

(a) Crack initiation at 100 kip (445kN), east side

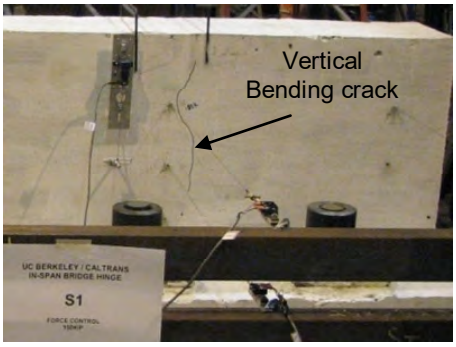

(b) Bending crack at 150 kip (665 kN), west side

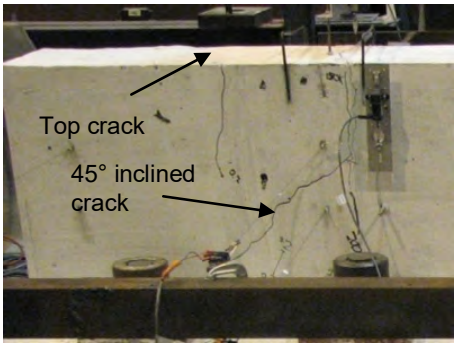

(c) 0.2" (5.1 mm) displacement, east side

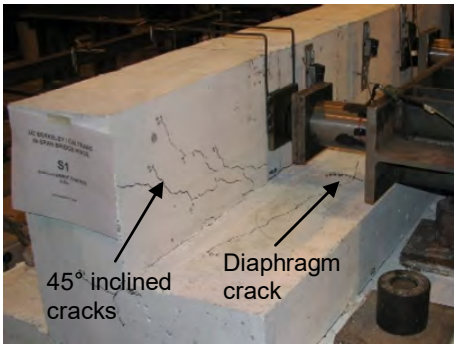

(d) 0.2" (5.1 mm) displacement, west side

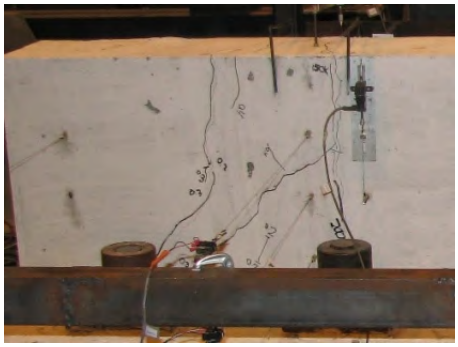

(e) 0.4" (10.2 mm) displacement, east side

(f) 0.4" (10.2 mm) displacement, west side

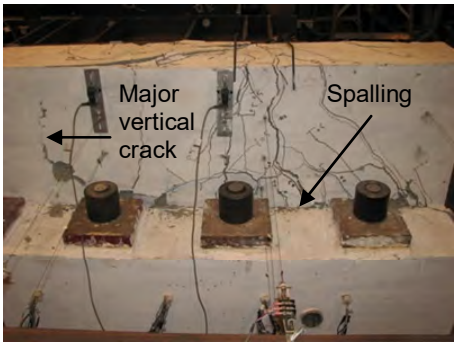

(g) At failure, west side

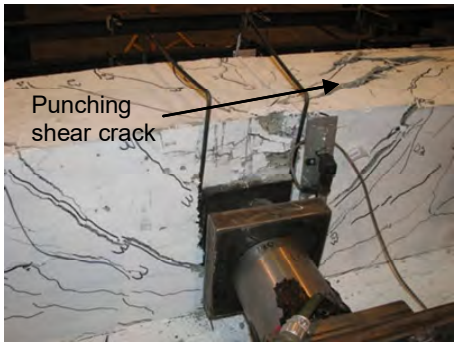

(h) At failure, west bearing detail

Fig. 5.8 Damage propagation during test of specimen S1.

The test was terminated at about 1" (25.4 mm) displacement, since the total strength of the specimen was reduced considerably. At that displacement level, rotation of the loading beam was observed toward the west side due to the differential displacements of the two bearings caused by the concentration of damage in the vicinity of the west bearing.

The test of specimen S1 was also used to evaluate the stability and accuracy of the test setup. It was concluded that the test setup is suitable for the intended test objectives, and it was confirmed that almost identical loading was applied at each of the two bearings. The load measured at each bearing, and the total actuator load, are shown in Figure 5.9. The difference between the actuator force and the sum of the two bearing forces is less than +4%. This difference may be attributed to a small part of the actuator load being utilized to overcome the friction of the actuator with its vertical wooden support placed between the actuator and the strong floor (Fig. 3.6). Therefore, the sum of the two bearing forces is considered as the total applied force to the specimen in the subsequent sections.

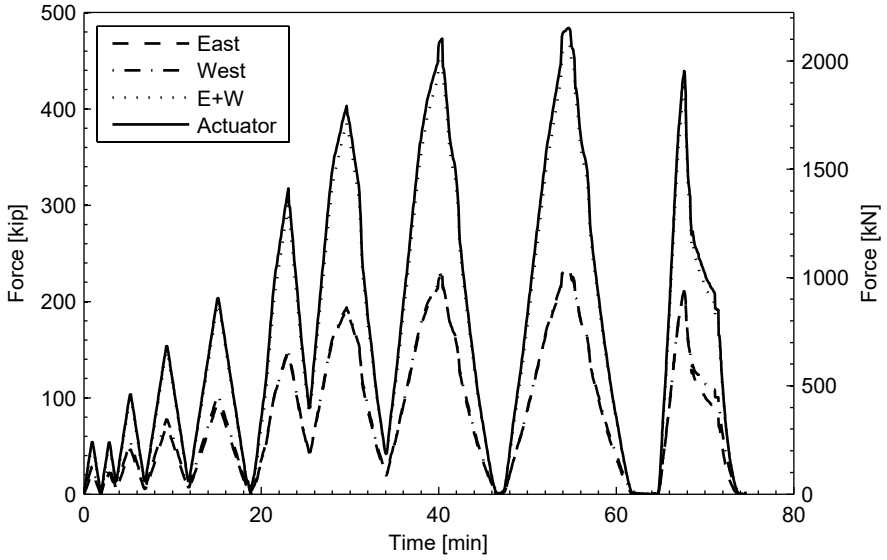

Fig. 5.9 Force equilibrium during test of specimen S1.

5.6.2 Load-Displacement Relationships

The applied load-displacement relationship of specimen S1 is shown in Figure 5.10. The displacement was measured with the built in actuator transducer. This displacement transducer was used to control the actuator under displacement control. The peak total load of 467 kip (2077

kN) was achieved at 0.49" (12.5 mm) displacement. After the peak load was achieved, the relationship shows a rapid decrease in the capacity and the strength was provided mainly by the tensile force of the diagonal bars, the friction in the punching shear mechanism, and the dowel action of the horizontal (vertical in the test orientation) bars.

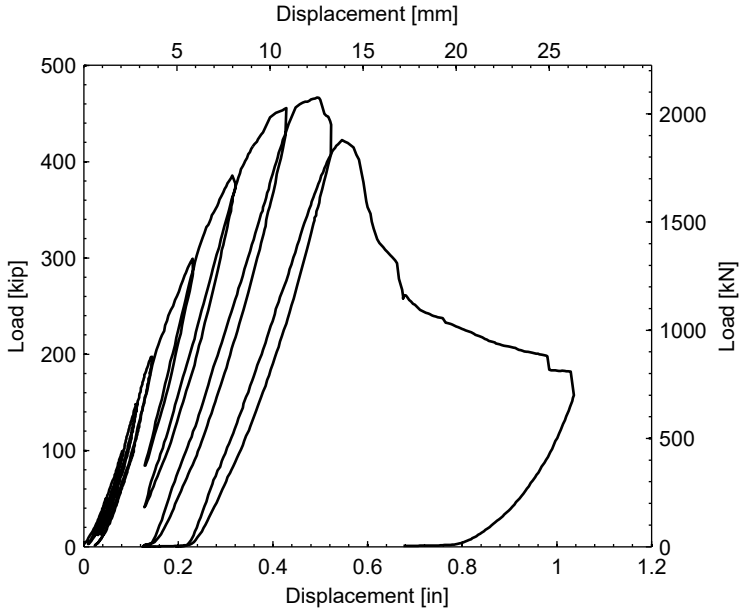

Fig. 5.10 Load-displacement, specimen S1.

The load-displacement relationships at both bearings are shown in Figure 5.11. The figure shows these relationships using two different displacements: the displacement of the loading steel beam (Figs. 5.11a–b) and the displacement of the concrete seat (Figs. 5.11c–d). During the test, the displacements of the loading beam and the concrete seat were measured with the instruments (LHE, LHW) and (SHT2, SHT4), respectively. From Figure 5.11, it can be observed that the initial stiffness is lower when the displacement is measured from the loading steel beam than from the concrete seat. This lower stiffness is attributed to the flexibility of the steel beam and the loading system. The relationships show that the east bearing did not fail during the test, since the east deformation decreased when the west bearing started to fail. The decrease of the east deformation is due to the lower load that was applied by the system caused by the punching shear failure observed on the west side.

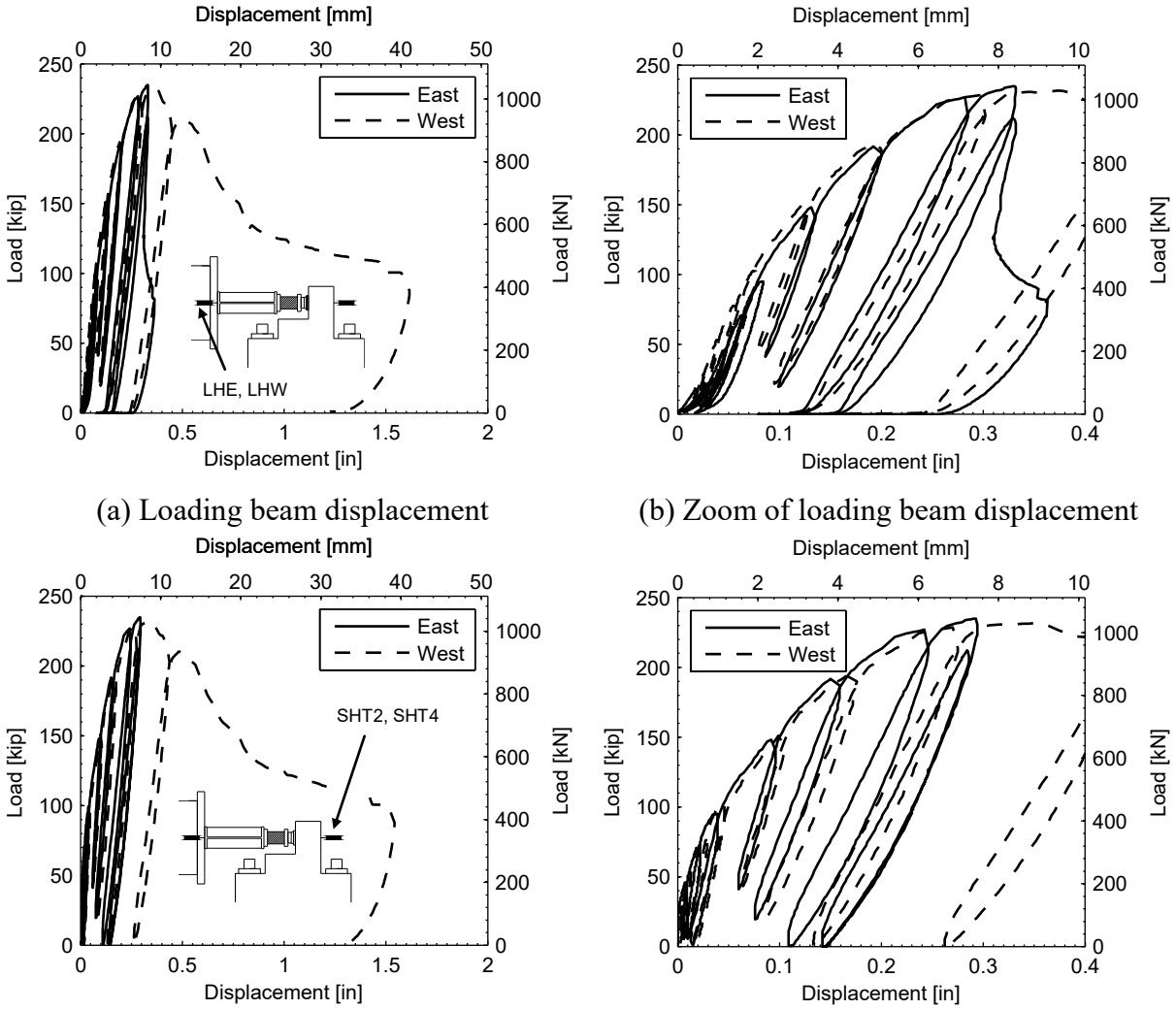

(a) Loading beam displacement

(b) Zoom of loading beam displacement

(c) Concrete displacement

(d) Zoom of concrete displacement

Fig. 5.11 Load-displacement at bearings for two displacement measurements of specimen S1.

The maximum strengths of the east and west bearings were 235 kip (1045 kN) and 232 kip (1032 kN), respectively. The corresponding displacements at the peak loads were 0.29" (7.4 mm) and 0.35" (8.9 mm) for the east and west bearings, respectively. The initial stiffnesses considering the concrete seat displacement were 5050 kip/in. (884 kN/mm) and 5060 kip/in. (886 kN/mm) for the east and west bearings, respectively. These values correspond to secant stiffness computed using a 50 kip (22 kN) load.

5.6.3 Seat Deformation Profiles

The seat deformation profile along the in-span hinge length (horizontal deformation of the seat in the test orientation) is shown in Figure 5.12a. The figure shows the displacement at 50%, 75%, and 100% of the maximum specimen load. The displacement profile was measured with 5 instruments, where the instruments SHT2 and SHT4 corresponded to the cross sections of the east and west bearings, respectively. The figure shows that the displacements at the two bearing cross sections were equivalent for 50% and 75% of the maximum load. For 75% of the maximum load, the displacements measured with the instruments at the edges and at the middle represent 39% and 67%, respectively, of the displacement measured at the two bearings. This deformation profile suggested that the load was resisted mainly by the regions of the seat located in the vicinity of the bearings. At 100% of the maximum load, the displacement of the west bearing increased considerably, which agreed with the failure observed at the west side during the test.

The displacement profile along the specimen height at the two bearing cross sections is shown in Figure 5.12b. The figure shows the displacement at 50%, 75%, and 100% of the maximum specimen load. This horizontal displacement (in the test orientation) was measured with top (T), middle (M) and bottom (B) displacement transducers. The exact location of these instruments is described in Chapter 3. Figure 5.12b shows a linear displacement variation along the height, which implies a shear deformation profile of the specimen. In contrast, a bending deformation profile is characterized by a cubic displacement variation along the height. This shear deformation profile was consistent with the lower shear capacity estimate of the seat compared to the bending capacity estimate computed earlier.

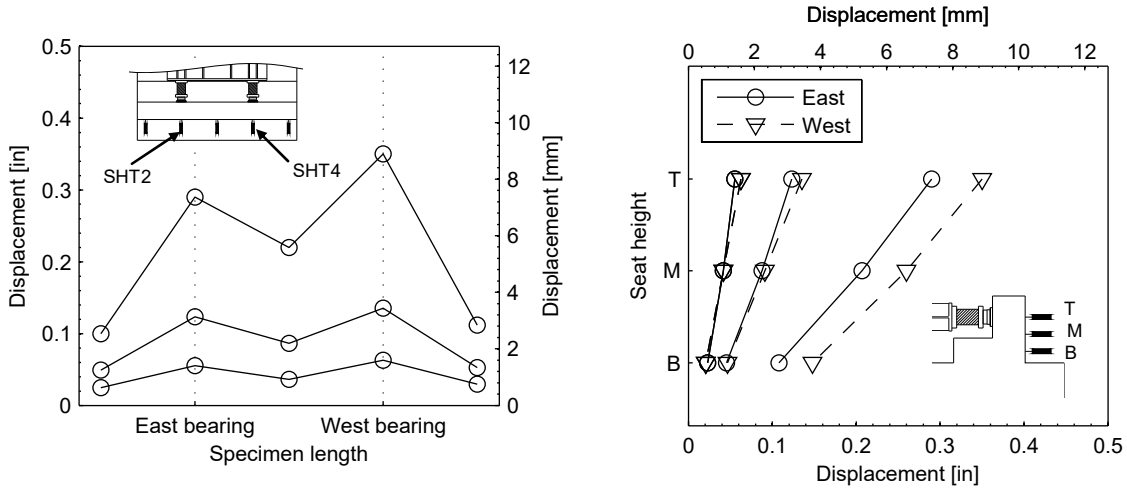

(a) Displacement profile along specimen length

(b) Displacement profile along specimen height, at the bearing cross sections

Fig. 5.12 Seat deformation profiles at 50%, 75%, and 100% of peak load of specimen S1.

5.6.4 Reinforcing Steel Behavior

The strains in the reinforcing steel bars of specimen S1 were measured with a total of 89 strain gages. The details of the reinforcement and the location of the most important strain gages are shown in Figure 5.13. From the strain measurements, reinforcing bar stresses were computed using the stress-strain relationships obtained from the reinforcing bar material tests (Fig. 5.4).

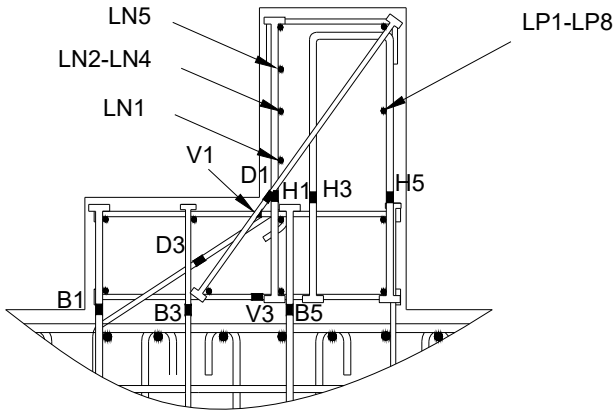

Fig. 5.13 Strain gage locations in specimens S1 and S2 (in test orientation).

The relationships of the envelopes of the reinforcement stresses versus the applied load, at both bearing cross sections (east and west), are shown in Figure 5.14. The figure shows that yielding initiated in diagonal bar D1 (Fig. 5.14a) located at the seat, which yielded at an applied

load of 224 kip (996 kN). This initial yielding was consistent with the crack initiation near the seat corner with the diaphragm.

The stresses of the horizontal (vertical in test orientation) bars of the seat are shown in Figure 5.14b. The figure shows that the horizontal bars at the locations H1 and H3 reached the yielding at applied forces of 368 kip (1637 kN) and 426 kip (1895 kN), respectively. At these larger loads, the diagonal, vertical (as discussed below), and horizontal bars have yielded, which corresponded to the development of the SAT mechanism. The horizontal bar H5 initially showed a compressive stress induced by the bending action of the seat, but a tensile stress at the end of the test. The unequal stresses at these horizontal (vertical in the test orientation) bars confirm that the sliding shear mechanism in the seat did not develop during the test. Moreover, major horizontal cracks at the seat-diaphragm sliding surface were not observed during the test.

Figure 5.14c shows that the second bar that reached yielding after diagonal bar D1 was the vertical (horizontal in the test orientation) bar at V1, which yielded at an applied load of 334 kip (1486 kN). The yielding of the diagonal bars and the vertical (horizontal in the test orientation) bars V1 suggests that a 1D shear or punching shear failure mode was the first that developed at the bearing cross sections.

The stresses in the horizontal (vertical in the test orientation) bars of the diaphragm are shown in Figure 5.14d. The figure shows that yielding occurred only in the bar with the strain gage labeled B5. Again, the unequal stresses of the base bars suggest that the sliding shear mechanism in the diaphragm did not develop during the test, which was confirmed by the absence of major horizontal cracks at the diaphragm-base sliding surface during the test.

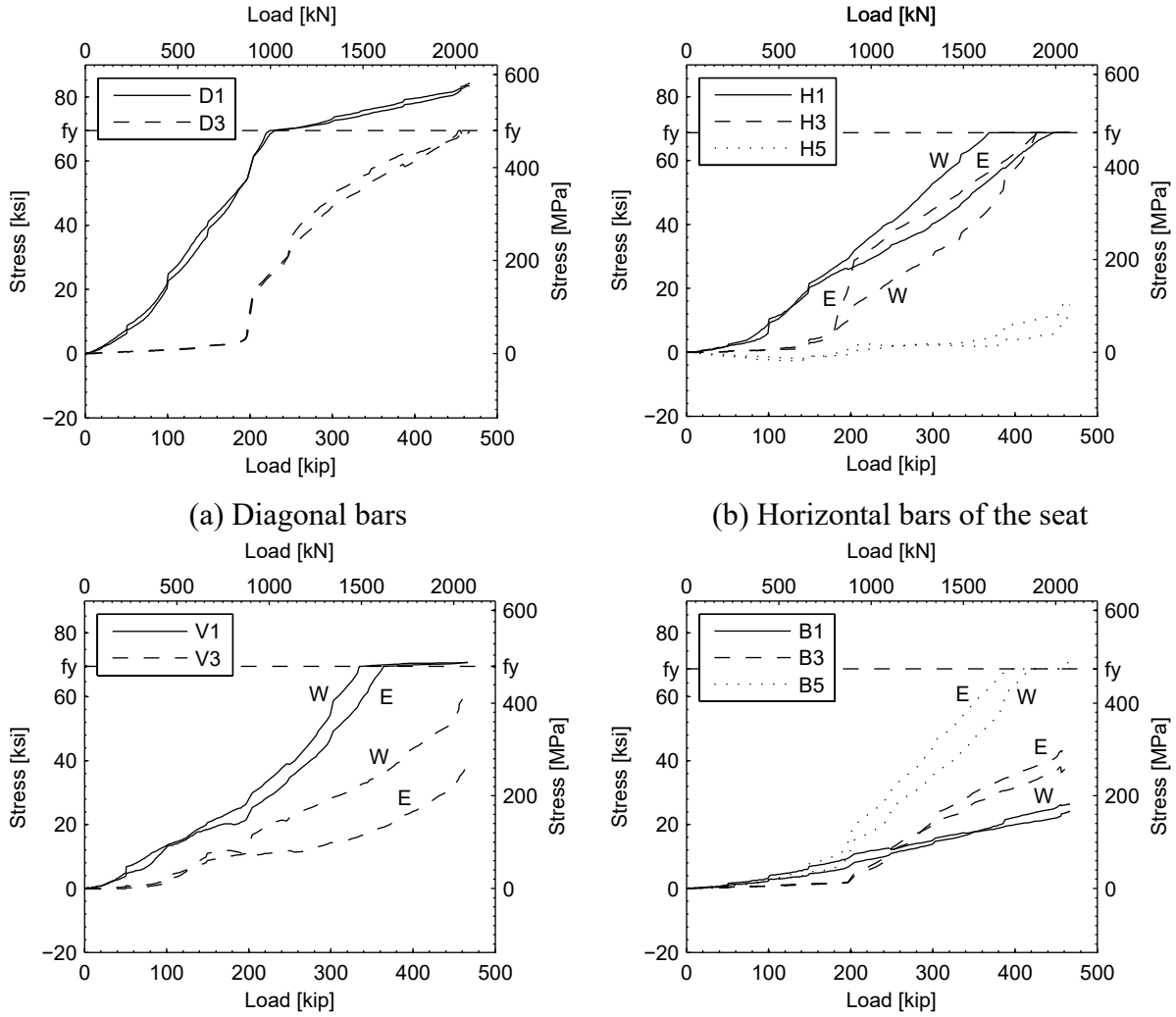

(a) Diagonal bars

(b) Horizontal bars of the seat

(c) Vertical bars

(d) Horizontal bars of the diaphragm

Fig. 5.14 Stresses in reinforcement at bearing cross sections versus applied load of specimen S1.

The strain distribution at the seat and at the diaphragm in the bearing cross sections are shown in Figure 5.15. These distributions are shown for 25%, 50%, 75%, and 100% of the maximum applied load at the east and west bearing cross sections. The strain distribution along the seat width (Fig. 5.15a) shows that it is not linear when the maximum strength was achieved. Therefore, Bernoulli's hypothesis of plane section remaining plane after bending becomes doubtful. The strain distribution along the diaphragm is shown in Figure 5.15b. This distribution shows that the Bernoulli's hypothesis is not applicable at the diaphragm either. The higher strain was recorded at the bar B5, rather than at the extreme bar B1. For both the seat and the

diaphragm, the high bending capacity provided and the strain distribution observed make bending failure mode unlikely to occur.

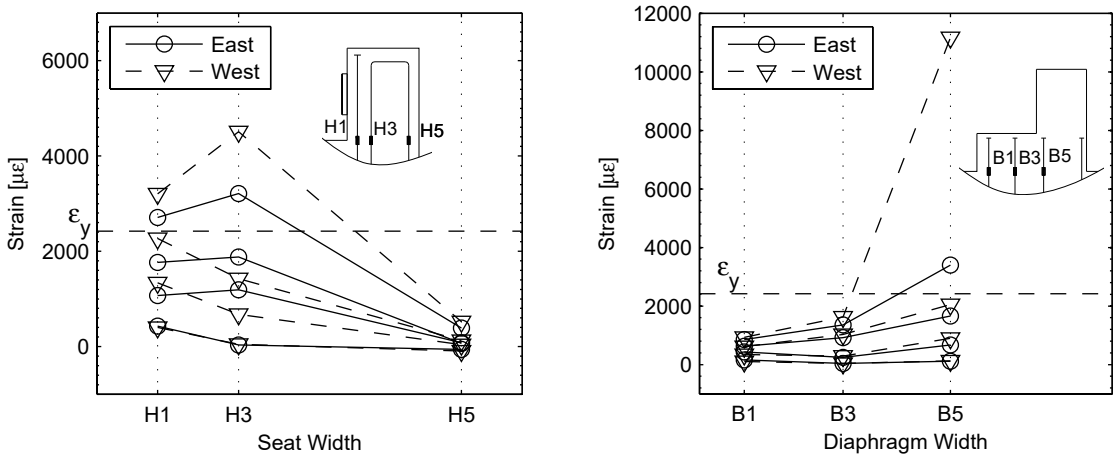

(a) Seat (d) Diaphragm

Fig. 5.15 Horizontal (vertical in test orientation) strain distribution along seat and diaphragm widths at 25%, 50%, 75%, and 100% of peak load of specimen S1.

The stress distribution in the longitudinal bars of the seat is shown in Figure 5.16 for 25%, 50%, 75%, and 100% of the maximum applied load. The stress of the longitudinal bar located at the bottom part of the seat (in the prototype orientation) was obtained from 8 strain gages (LP1-LP8) located in the vicinity of the bearings. The stress distributions of this bar, shown in Figure 5.16a, demonstrate bending action of the seat about the direction perpendicular to the diaphragm. This bending behavior agrees with the observed seat deformation profile and with the vertical (in the test orientation) bending cracks shown in Figure 5.8b. The stress of the longitudinal bar located at the top part of the seat (in the prototype orientation) was obtained from 3 strain gages (LN2-LN4) located between the two bearings. At this middle cross section of the specimen, the bending action induced about the direction perpendicular to the diaphragm is smaller, without any bar yielding, and the maximum stress was 47 ksi (324 MPa), as shown in Figure 5.16b.

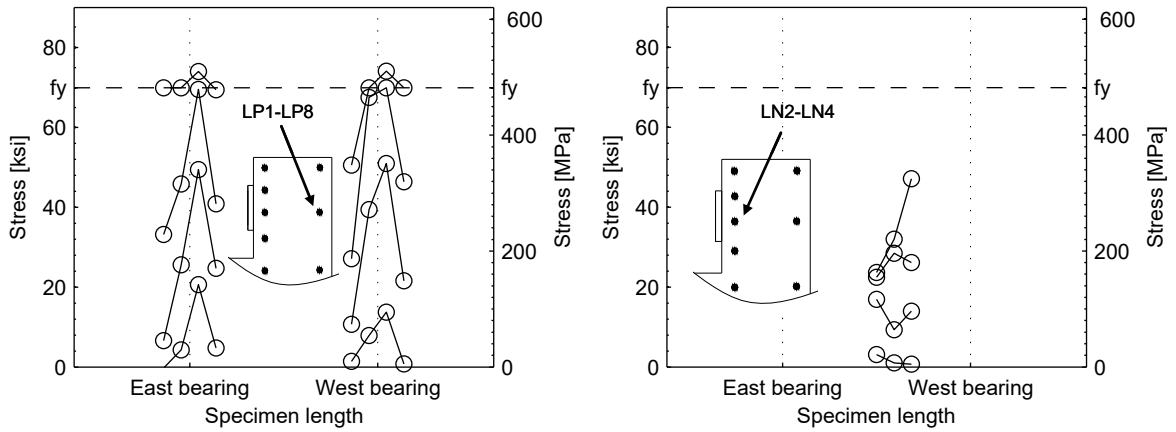

(a) Bottom longitudinal (b) Top longitudinal bar

Fig. 5.16 Stress distributions of longitudinal reinforcing bars at 25%, 50%, 75%, and 100% of peak load of specimen S1.

The distribution of strain and stresses on the reinforcing bars throughout the specimen length is shown in Figure 5.17 for 25%, 50%, 75%, and 100% of the maximum applied load. The locations of the bars with their strain gages are shown in Figure 5.13. From the test results, the larger strains were observed in diagonal bars D1 of the seat. The strain and stress distributions of these bars are shown in Figures 5.17a and b, respectively. It can be observed that a peak strain of 28600 $\mu\varepsilon$ (~2.9%) was measured in the vicinity of the west bearing at the maximum applied load. This large strain is about 12 times larger than the yield strain of the reinforcing bar. The stress distribution shows that the stresses of these diagonal bars were concentrated in the vicinity of the bearings for 25% and 50% of the maximum load. At these low load levels, an effective seat length parallel to the diaphragm axis can be considered to resist the applied load, whereas when the maximum strength of the in-span hinge was achieved, yielding was spread throughout the whole seat length and an effective seat length was not observed.

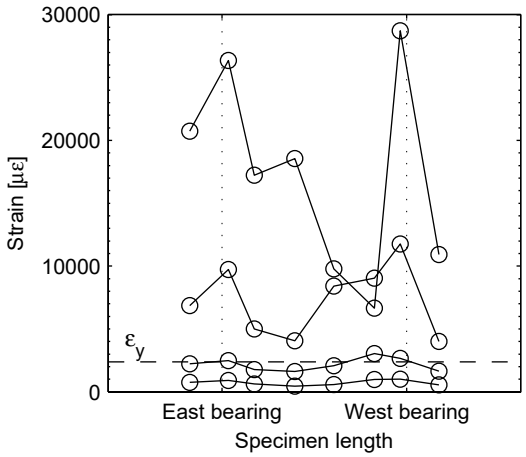

(a) Strains of diagonal bars D1

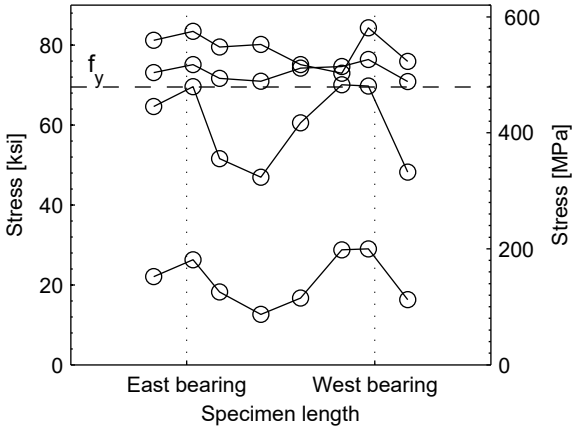

(b) Stresses of diagonal bars D1

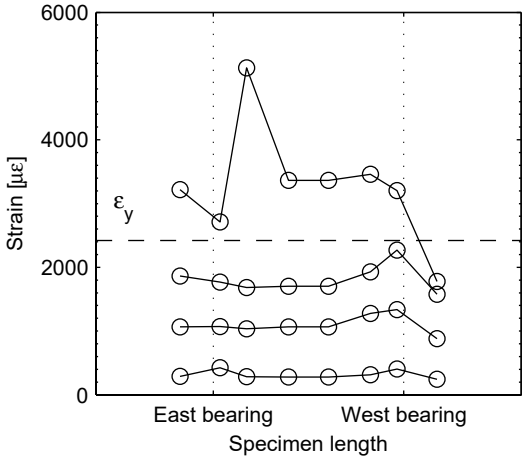

(c) Strains of horizontal bars H1

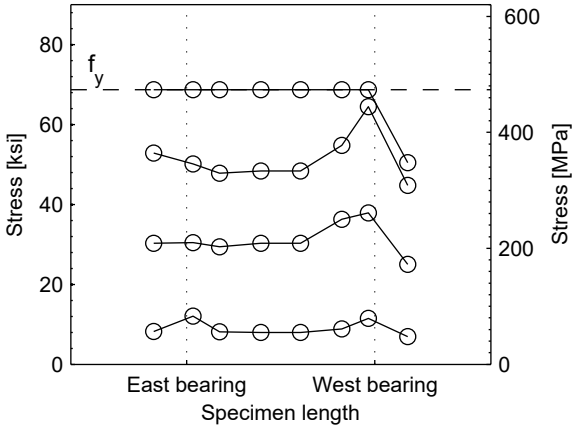

(d) Stresses of horizontal bars H1

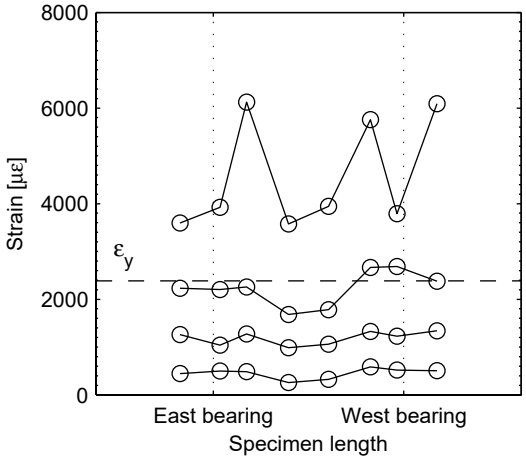

(e) Strains of vertical bars V1

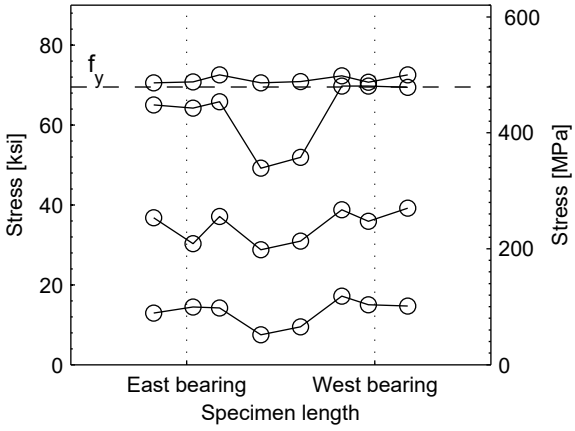

(f) Stresses of vertical bars V1

Fig. 5.17 Behavior of reinforcing bars throughout in-span hinge length at 25%, 50%, 75%, and 100% of peak load of specimen S1.

The strains and stresses of the horizontal (vertical in the test orientation) bars H1 and the vertical (horizontal in the test orientation) bars V1 are shown in Figures 5.17c–f. Note that the reinforcing bar with strain gage H1 has a yield plateau (Fig. 5.4), which makes the stress plot in Figure 5.17d have a constant yield stress for the majority of the specimen length at 100% of the peak load. The stresses of these horizontal and vertical bars were lower than those of the diagonal bars, with more uniform stress distributions throughout the diaphragm length. At the maximum strength of the seat, the yielding of both H1 and V1 bars was also observed throughout the whole length of the diaphragm.

5.7 SPECIMEN S2 TEST RESULTS

The experimental results of specimen S2 are presented in this section. Specimen S2 was identical to specimen S1 but had utility openings. Specimen S2 was subjected to the displacement-control loading history shown in Section 3.7. The force-control test was not applied, since the stiffness of specimen S1 was low enough for the actuator resolution to run the test using only displacement control. Therefore, in specimen S2, the more stable displacement-control approach was followed. It is to be noted that results shown as envelopes of the cyclic loading are consistent with the envelope of the global force-displacement relationship.

5.7.1 General Observations

Similar to specimen S1, the initial crack appeared near the seat corner with the diaphragm at 0.08" (2.0 mm) peak displacement cycle, as indicated by the arrow in Figure 5.18a. At this displacement, the specimen load was 82 kip (365 kN). At 0.11" (2.8 mm) peak displacement cycle, vertical (in the test orientation) bending cracks appeared behind the bearings as shown in Figure 5.18b. At this displacement, the specimen load was 125 kip (556 kN).

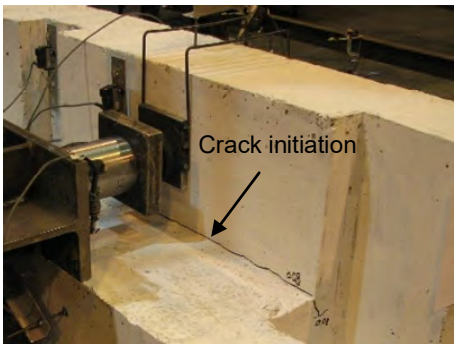

(a) Crack initiation at 82 kip (365kN), east side

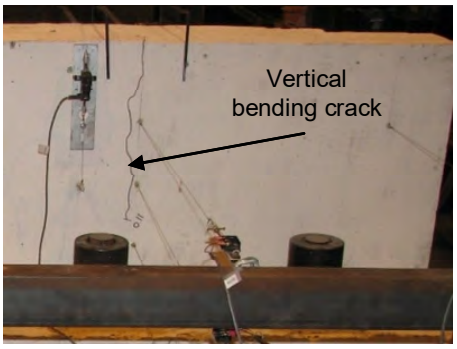

(b) Bending crack at 125 kip (556 kN), west side

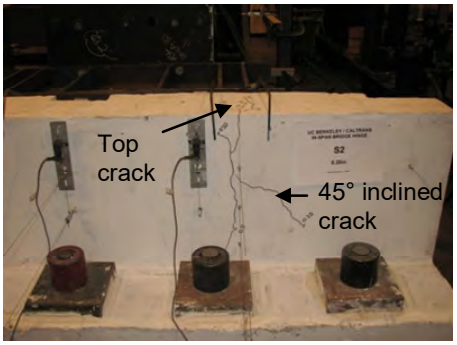

(c) 0.2" (5.1 mm) displacement, west side

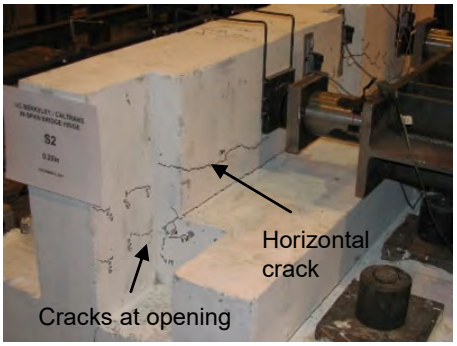

(d) 0.2" (5.1 mm) displacement, west side

(e) 0.4" (10.2 mm) displacement, west side

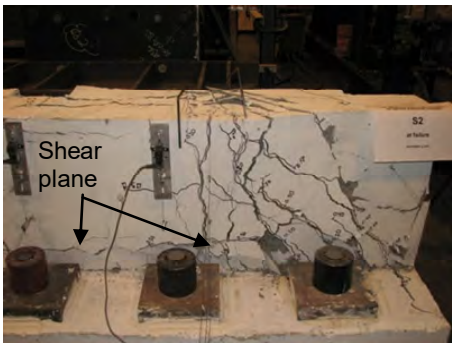

(f) At failure, west side

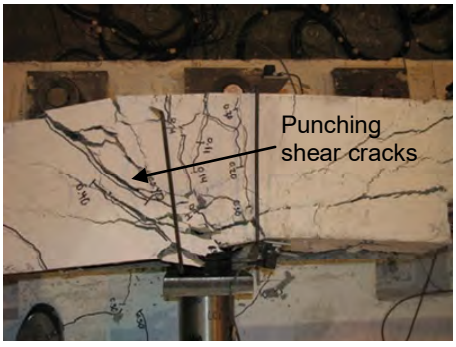

(g) At failure, west bearing

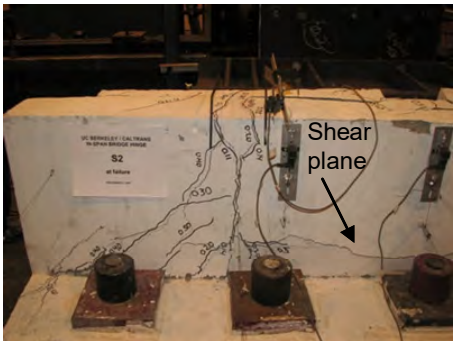

(h) At failure, east side

Fig. 5.18 Damage propagation during test of specimen S2.

The first diagonal crack appeared at the 0.2" (5.1 mm) peak displacement in the seat behind the bearing plates, as shown in Figure 5.18c. The angle of inclination of this crack was 45°. At this load level, a horizontal (in the test orientation) bending crack appeared at the seat in the bearing side as shown in Figure 5.18d. Additionally, small cracks appeared at the utility openings, indicating that the load was transferred from the bearing to the diaphragm throughout the whole seat length. The damage propagation at the west side for the 0.4" peak displacement cycle is shown in Figure 5.18e.

For specimen S2, both bearing sides reached their maximum strength and then, both bearing sides started to unload toward the descending branch. When the maximum strength was achieved, the vertical (in the test orientation) and diagonal cracks located in the seat behind the bearing plates had widths of 0.08" (2.0 mm) and 0.05" (1.3 mm), respectively. Subsequently, a punching shear failure mode was observed in the west side, and a 1D shear failure mode was observed in the east side. Figures 5.18f and g show the punching shear failure of the west side, where the diagonal punching shear crack at the top of the seat (in the test orientation) appeared only toward the free end of the specimen, as marked with an arrow in Figure 5.18g. Toward the middle of the specimen, the west side experienced a 1D shear failure, which was connected with the 1D shear failure mode of the east bearing. This shear plane is shown in Figures 5.18f and h and did not extend toward the free end of the east bearing.

The test of specimen S2 was terminated at about 2" (50.8 mm) displacement and the total force was reduced to about 30% of the maximum strength. At that displacement level, rotation of the loading beam was observed toward the west side due to the differential displacements of the two bearings caused by the more concentration of damage in the vicinity of the west bearing.

5.7.2 Load-Displacement Relationships

The applied load-displacement relationship of specimen S2 is shown in Figure 5.19. The displacement was measured with the built in actuator transducer, and the load corresponded to the sum of the two load cells attached to the loading beam. The peak total load of 425 kip (1890 kN) was achieved at 0.45" (11.4mm) displacement. This strength was 9% lower than that of specimen S1 and its reduction can be explained by the presence of the utility openings. After the peak load was achieved, the relationship shows a rapid decrease in the capacity, and the strength

was provided mainly by the tensile force of the diagonal bars, the friction in the punching shear mechanism, and the dowel action of the horizontal (vertical in the test orientation) bars.

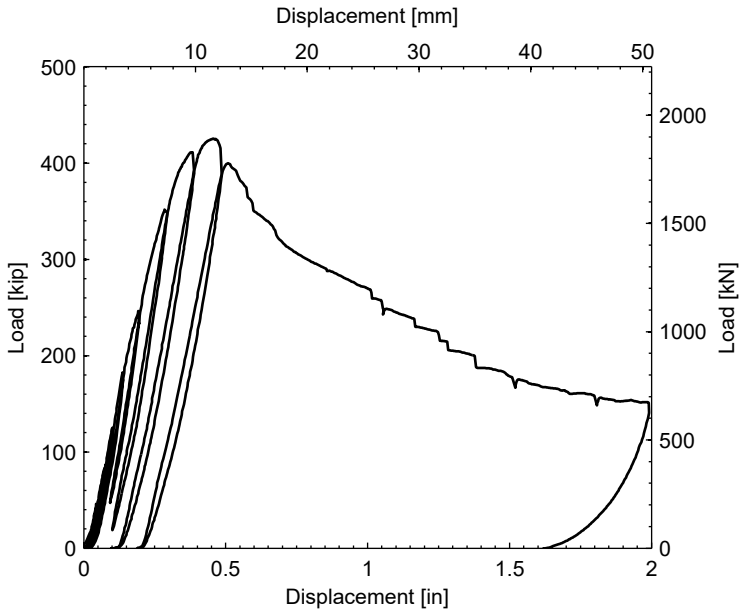

Fig. 5.19 Load-displacement of specimen S2.

The load-displacement relationships at both bearings are shown in Figure 5.20. The figure shows the responses using the displacement of the concrete seat, measured with the instruments SHT2 and SHT4 (Fig. 3.11) for the east and west sides, respectively. The relationships show that both sides of the in-span hinge failed during the test because descending branches were observed for both bearings. However, a less pronounced descent was observed for the east bearing compared to the west bearing, after the maximum strength was achieved, as shown in Figures 5.20a–b. The recording of the east bearing displacement was interrupted at about 0.5" (12.7 mm) because the instrument located at the concrete surface of the east bearing was pulled out due to the presence of a major concrete crack.

The maximum strengths of the east and west bearings were 209 kip (930 kN) and 218 kip (970 kN), respectively. The corresponding displacements at the peak loads were 0.32" (8.1 mm) and 0.30" (7.6 mm) for the east and west bearings, respectively. The initial stiffnesses considering the concrete seat displacement were 3590 kip/in. (629 kN/mm) and 4240 kip/in. (743 kN/mm) for the east and west bearings, respectively. These values correspond to secant stiffness computed using a 50 kip (22 kN) load.

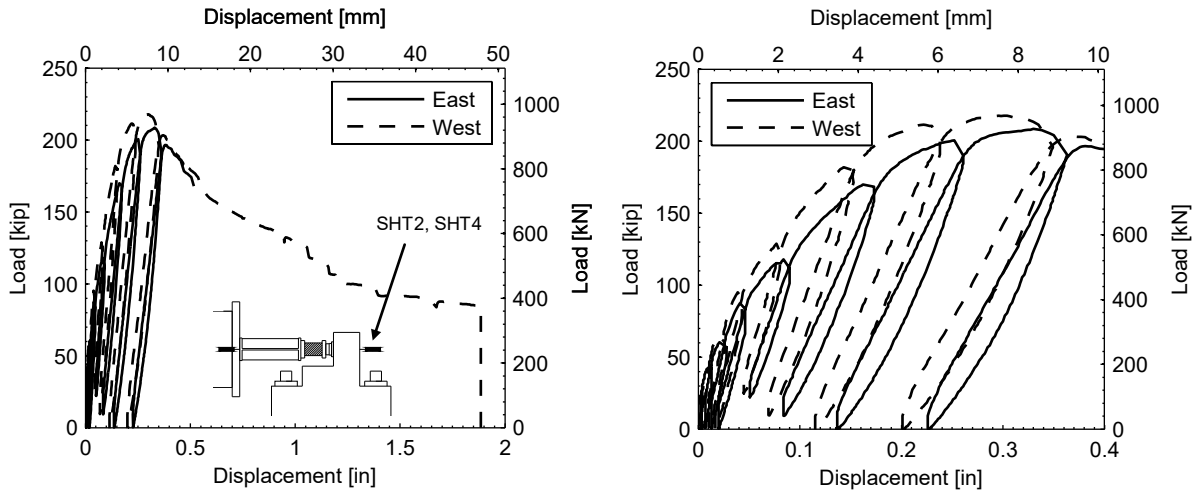

(a) Concrete displacement (b) Zoom of concrete displacement

Fig. 5.20 Load-displacement at bearings of specimen S2.

5.7.3 Seat Deformation Profiles

The seat deformation profile along the in-span hinge length (horizontal deformation of the seat in the test orientation) is shown in Figure 5.21a. The figure shows the displacement at 50%, 75%, and 100% of the maximum specimen load. The displacement profile was measured with 5 instruments, where the instruments SHT2 and SHT4 corresponded to the cross sections of the east and west bearings, respectively. The figure shows that the displacements at the two bearing cross sections were equivalent for 50% and 75% of the maximum load. For 75% of the maximum load, the displacements measured with the instruments at the edges and at the middle represented 46% and 69%, respectively, of the displacement measured at the two bearings. This deformation profile suggested that the load was resisted mainly by the regions of the seat located in the vicinity of the bearings. At 100% of the maximum load, the displacements of both bearings increased considerably, which agreed with the load displacement relationships of Figure 5.20 where both bearings reached the maximum strength during the test.

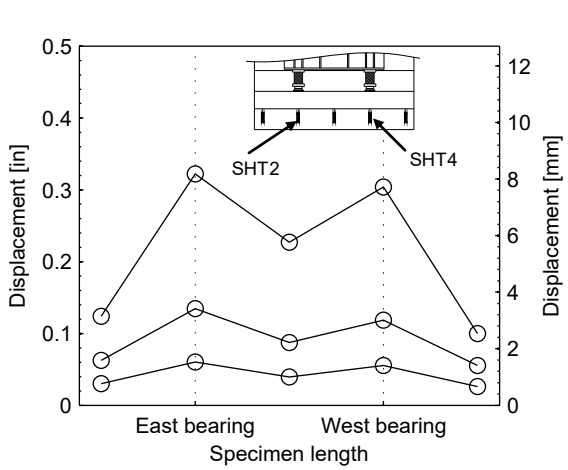

(a) Displacement profile along specimen length

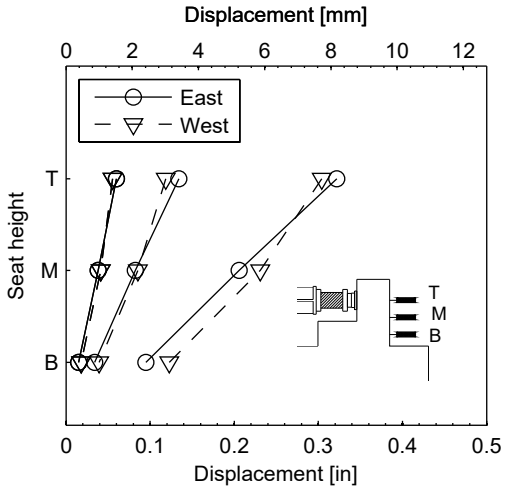

(b) Displacement profile along specimen height, at the bearing cross sections

Fig. 5.21 Seat deformation profiles at 50%, 75%, and 100% of peak load of specimen S2.

The displacement profile along the specimen height at the two bearing cross sections is shown in Figure 5.21b. The figure shows the displacement at 50%, 75%, and 100% of the maximum specimen load. This horizontal displacement (in the test orientation) was measured with top (T), middle (M) and bottom (B) displacement transducers. The exact locations of these instruments is described in Chapter 3. Figure 5.21b shows a linear displacement variation along the height, which implies a shear deformation profile of the specimen in contrast to a bending deformation profile, which is characterized by a cubic displacement variation along the height. This observation in specimen S2 is analogous to that of specimen S1.

5.7.4 Reinforcing Steel Behavior

Similar to specimen S1, the strains in the reinforcing steel bars of specimen S2 were measured with a total of 89 strain gages. The details of the reinforcement and the location of the most important strain gages are shown in Figure 5.13. From the strain measurements, reinforcing bar stresses were computed using the stress-strain relationships obtained from the reinforcing bar material tests (Fig. 5.4).

The relationships of the envelopes of the reinforcement stresses versus the applied load, at both bearing cross sections (east and west), are shown in Figure 5.22. The figure shows that yielding was initiated in diagonal bar D1 (Fig. 5.22a) located at the seat, which yielded at an

applied load of 188 kip (836 kN). This initial yielding was consistent with the crack initiation near the seat corner with the diaphragm.

The stresses of the horizontal (vertical in the test orientation) bars of the seat are shown in Figure 5.22b. The figure shows that the horizontal bars at the locations H1 and H3 reached the yielding at applied forces of 327 kip (1455 kN) and 412 kip (1833 kN), respectively. At these larger loads, the diagonal, vertical (as discussed below) and horizontal bars have yielded, which corresponded to the development of the SAT mechanism. The horizontal bar H5 showed initially a compressive stress induced by the bending action of the seat, but a tensile stress at the end of the test. Similar to specimen S1, the unequal stresses at these horizontal (vertical in the test orientation) bars confirm that the sliding shear mechanism in the seat did not develop during the test. Moreover, major horizontal cracks at the seat-diaphragm sliding surface were not observed during the test.

Figure 5.22c shows that the second bar that reaches yielding after diagonal bar D1 was the vertical (horizontal in the test orientation) bar at V1, which yielded at an applied load of 320 kip (1423 kN). The yielding of the diagonal bars and the vertical (horizontal in test orientation) bars V1 suggests that a 1D shear or punching shear failure mode was the first one that developed at the bearing cross section.

The stresses in the horizontal (vertical in the test orientation) bars of the diaphragm are shown in Figure 5.22d. The figure shows that yielding occurred only in the bar with the strain gage labeled B5. Again, the unequal stresses of the base bars suggest that the sliding shear mechanism in the diaphragm did not develop during the test, which was confirmed by the absence of major horizontal cracks at the diaphragm-base sliding surface during the test.

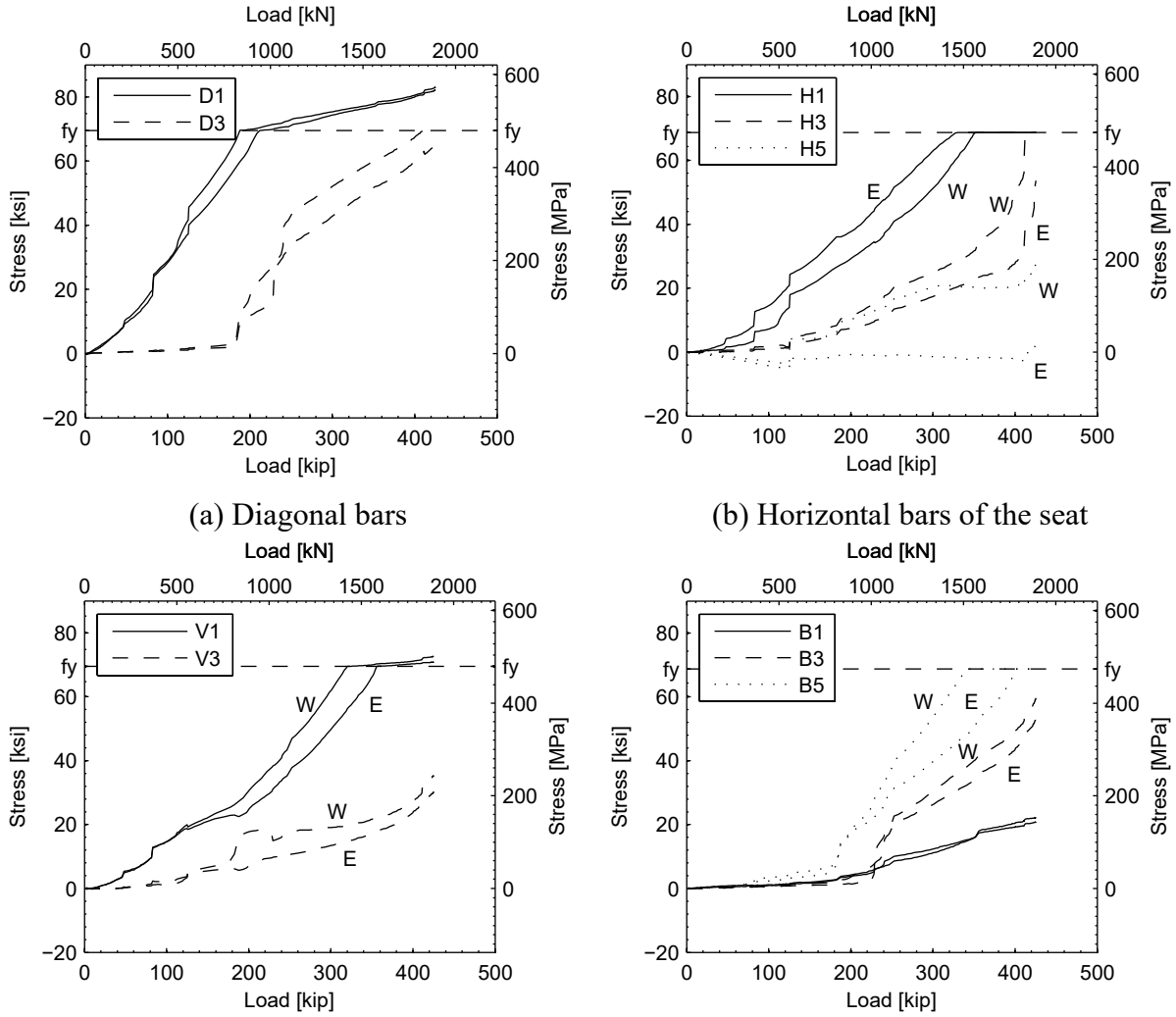

(a) Diagonal bars

(b) Horizontal bars of the seat

(c) Vertical bars

(d) Horizontal bars of the diaphragm

Fig. 5.22 Stresses in reinforcement at bearing cross sections versus applied load of specimen S2.

The strain distribution at the seat and at the diaphragm in the bearing cross sections are shown in Figure 5.23. These strain distributions are shown for 25%, 50%, 75%, and 100% of the maximum applied load at the east and west bearing cross sections. The strain distribution along the seat width (Fig. 5.23a) shows that it is not quite linear, although closer to being linear than is the case for specimen S1. Therefore, Bernoulli's hypothesis of plane section remaining plane after bending becomes inaccurate. The strain distribution along the diaphragm (Fig. 5.23b) confirms that the Bernoulli hypothesis is not applicable at the diaphragm either. The higher strain was recorded at the bar B5, rather than at the extreme bar B1. For both the seat and the

diaphragm, and similar to specimen S1, the high bending capacity provided and the strain distribution observed make bending failure mode unlikely to occur. Significant differences between specimens S1 and S2 are the following: (1) the maximum horizontal (vertical in the test orientation) seat strain took place in H3 for specimen S1 but in H1 for specimen S2, and (2) the west side (the only side that failed) had significantly higher strains for specimen S1 than the east side, especially for the horizontal (vertical in the test orientation) diaphragm strain, while for specimen S2, both sides (both sides failed) had comparable strain values.

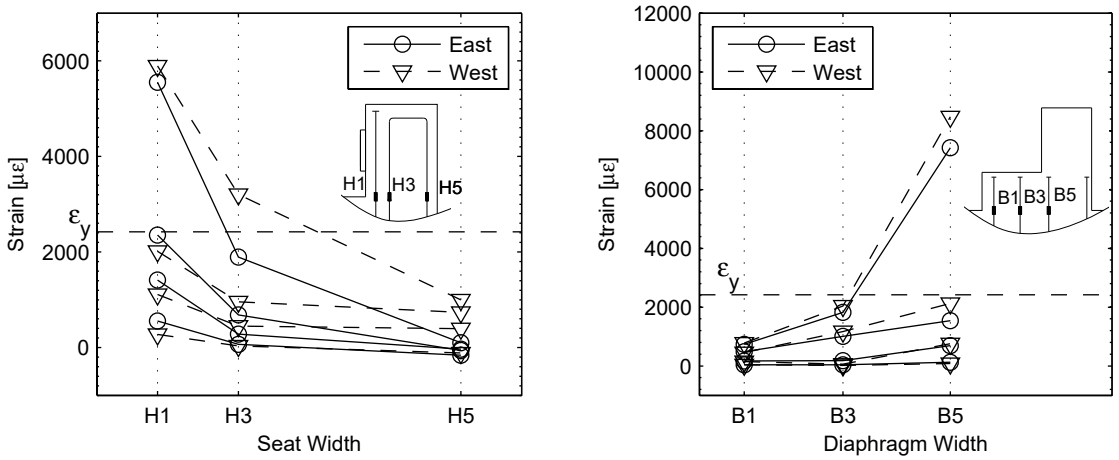

(a) Seat (b) Diaphragm

Fig. 5.23 Horizontal (vertical in test orientation) strain distribution along seat and diaphragm widths at 25%, 50%, 75%, and 100% of peak load of specimen S2.

The stress distribution in the longitudinal bars of the seat is shown in Figure 5.24 for 25%, 50%, 75%, and 100% of the maximum applied load. Analogous to specimen S1, the stress of the longitudinal bar located at the bottom part of the seat (in the prototype orientation) was obtained from eight strain gages (LP1-LP8) located in the vicinity of the bearings. The stress distributions of this bar, shown in Figure 5.24a, demonstrate the bending action of the seat about the direction perpendicular to the diaphragm. This bending behavior agrees with the observed seat deformation profile and with the vertical (in the test orientation) bending cracks shown in Figure 5.18b. Analogous to specimen S1, the stress of the longitudinal bar located at the top part of the seat (in the prototype orientation) was obtained from 3 strain gages (LN2-LN4) located between the two bearings. At this middle cross section of the specimen, the bending action induced about the direction perpendicular to the diaphragm is negligible, as shown in Figure 5.24b. This bending action is smaller than that of specimen S1 because the utility openings

reduced the area of the seat cross section at the middle of the specimen. Additionally, this bending action of specimen 2 was reduced because the longitudinal bar was bent to the inside of the seat to avoid the opening, and this brought it closer to the neutral axis of the seat (see Appendix A).

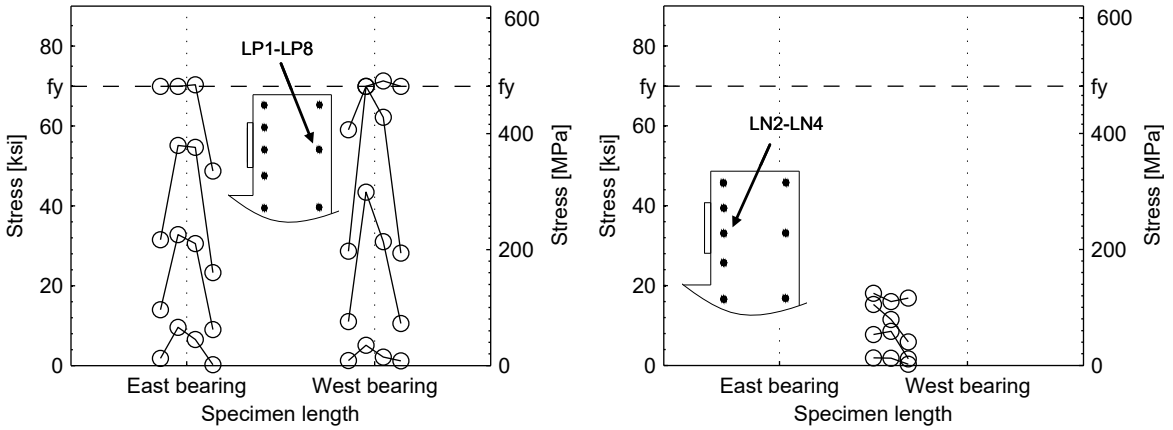

(a) Bottom longitudinal bar (b) Top longitudinal bar

Fig. 5.24 Stress distributions of longitudinal reinforcing bars at 25%, 50%, 75%, and 100% of peak load of specimen S2.

The strain and stress distributions on the reinforcing bars throughout the specimen length are shown in Figure 5.25 for 25%, 50%, 75%, and 100% of the maximum applied load. The locations of the bars with their strain gages are shown in Figure 5.13. From the test results, the larger strains were observed in diagonal bars D1 of the seat. The strain and stress distributions of this bar are shown in Figures 5.25a and b, respectively. It can be observed that a peak strain of 27500 $\mu\varepsilon$ (~2.8%) was measured in the vicinity of the west bearing at the maximum applied load. Similar to specimen S1, this large strain is about 11 times larger than the yield strain of the reinforcing bar. The stress distribution shows that the stresses of these diagonal bars were concentrated in the vicinity of the bearings for 25% and 50% of the maximum load. At these low load levels, an effective seat length parallel to the diaphragm axis can be considered to resist the applied load. In contrast, when the maximum strength of the in-span hinge was achieved, yielding was spread throughout the whole seat length, and an effective seat length was not observed.

The strains and stresses of the horizontal (vertical in the test orientation) bars H1 and vertical (horizontal in the test orientation) bars V1 are shown in Figures 5.25c–f. The stresses of

these horizontal and vertical bars were lower than those of the diagonal bars. From Figure 5.25d, it is observed that yielding was not achieved in the horizontal bars (H1) at the middle of the specimen. Therefore, unlike S1, the development of the 2D SAT model is questionable at the middle of specimen S2. In contrast, the vertical bars (V1) yielded throughout the whole specimen length, as shown in Figure 5.25f. The yielding of these vertical bars together with the diagonal bars demonstrates that a global 1D shear or a punching shear failure mode was achieved at the maximum strength of specimen S2.

5.8 SEAT REINFORCING BAR SLIP

The slip measurements discussed in Section 3.6.3 and shown in Figure 3.12 are briefly discussed in this paragraph. It was concluded from specimens S1 and S2 that slip was unlikely to occur, especially for headed bars located in the seat of the in-span hinge. This conclusion is based on the slip measurements from specimens S1 and S2. Figure 5.26a shows the slip measurement of a horizontal bar (vertical in the test orientation) of specimen S1 located in the vicinity of the east bearing plate. The recorded data show no clear evidence of slip during the execution of the test because the displacement is within the measurement accuracy. Figure 5.26b shows the slip measurement of a diagonal bar of the seat of specimen S2 located in the vicinity of the east bearing plate. At the final stage of the test, however, a maximum slip of 0.004" (0.10 mm) was measured; at this stage specimen S2 was responding along the descending branch of the load-displacement relationship (exactly at 63% of the maximum strength) (see Fig. 5.19). Therefore, these recordings justify the use of the embedded reinforcement assumption in the FEA discussed in Chapter 4.

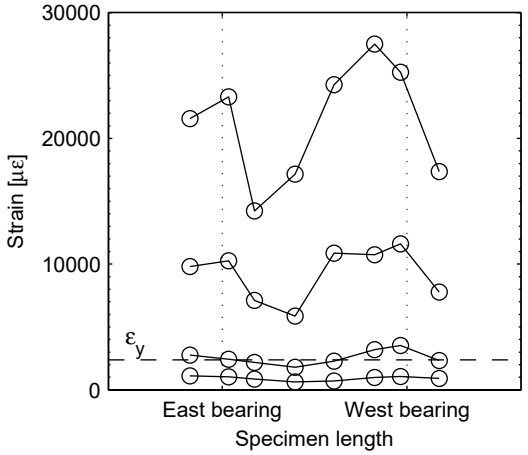

(a) Strains of diagonal bars D1

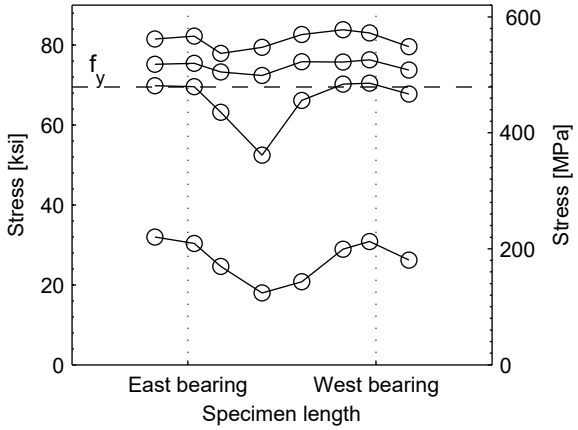

(b) Stresses of diagonal bars D1

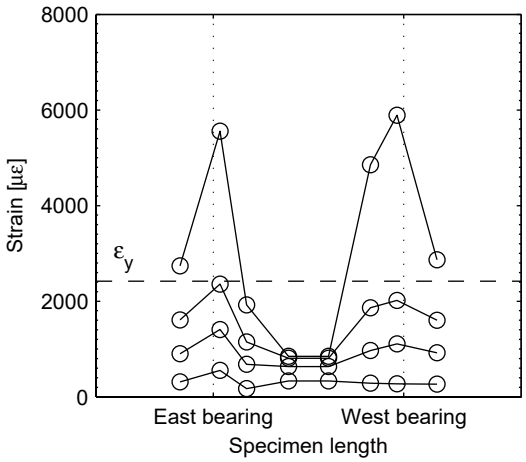

(c) Strains of horizontal bars H1

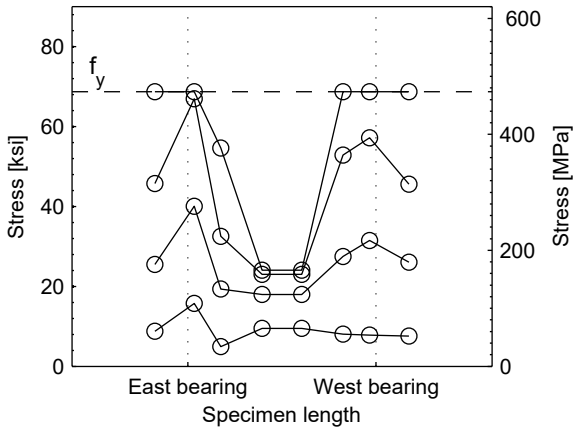

(d) Stresses of horizontal bars H1

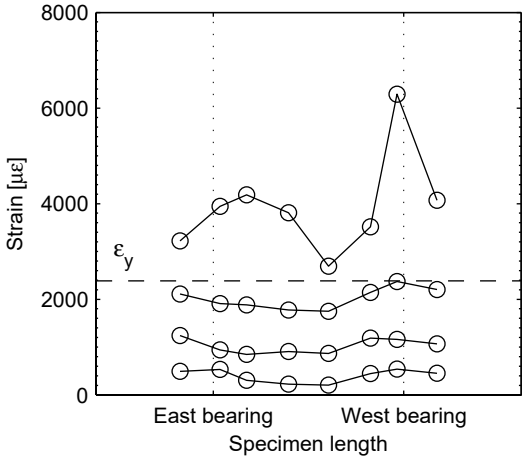

(e) Strains of vertical bars V1

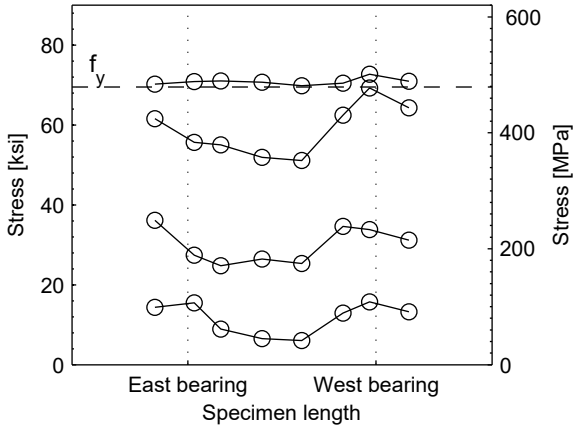

(f) Stresses of vertical bars V1

Fig. 5.25 Behavior of reinforcing bars throughout the in-span hinge length at 25%, 50%, 75%, and 100% of peak load of specimen S2.

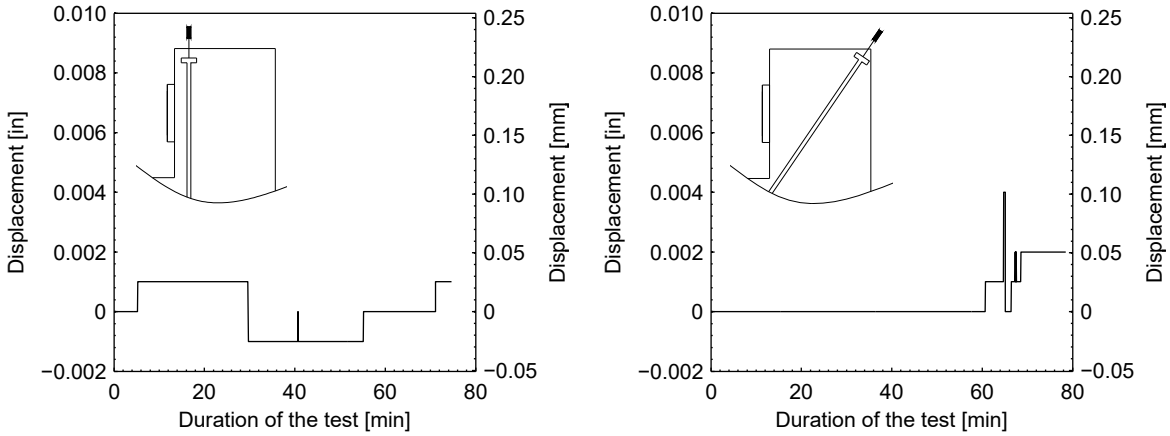

(a) Horizontal bar H1 of specimen S1 (b) Diagonal bar D1 of specimen S2

Fig. 5.26 Slip measurements of headed reinforcing bars of specimens S1 and S2.

5.9 CONCLUDING REMARKS OF AS-BUILT SPECIMENS

The test results of specimens S1 and S2 are summarized in Table 5.5. The table shows that only the west side failed in specimen S1 and that both sides failed in specimen S2. From the test results, it is concluded that the presence of utility openings in specimen S2 reduced the strength of the in-span hinge by 9%. In spite of the presence of utility openings, the displacement of the bearings at maximum load is equivalent for both specimens. The average secant stiffness at the bearings of specimen S2 is 22% lower than that of specimen S1. This difference is attributed to the presence of utility openings and also to measurement imprecision at low displacement levels. The yield initiation of the reinforcing steel for both specimens occurred in the diagonal headed bar of the seat. At this bar, yielding started at 48.0% and 44.2% of the maximum applied load for specimens S1 and S2, respectively.

The comparison between the load-displacement envelopes at each of the bearings is shown in Figure 5.27. It can be observed that the behavior of both specimens is similar, but the strength of specimen S2, which includes utility openings, is smaller. Additionally, the figure clearly shows that the east side of specimen S1 did not fail during the test.

Table 5.5 Comparison of test results for specimens S1 and S2.

	S1	S2
Specimen side that fails	west	both
Specimen strength [kip (kN)]	467 (2077)	425 (1890)
Average strength per bearing [kip (kN)]	233 (1036)	213 (947)
Average bearing displacement at maximum load [in (mm)]	0.32 (8.1)	0.31 (7.9)
Average secant stiffness at bearings [kip/in. (kN/mm)]	5055 (885)	3915 (686)
Initiation of yielding [% of maximum load]	48.0	44.2

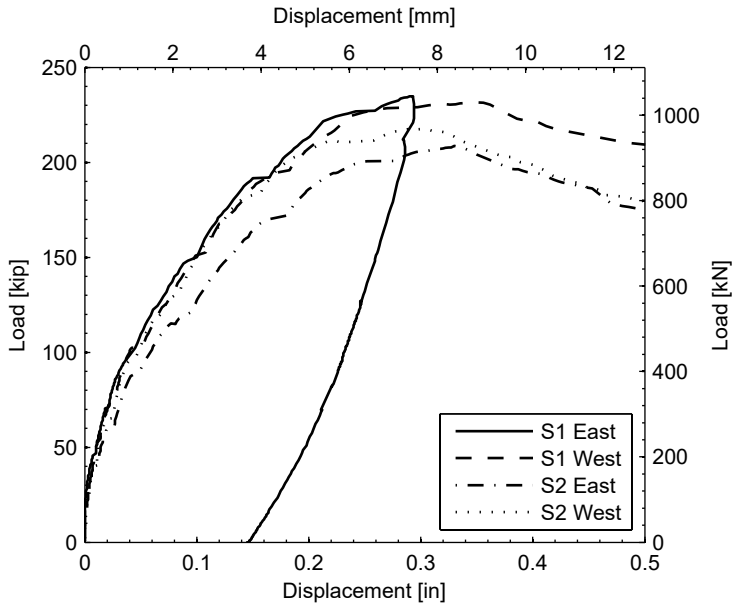

Fig. 5.27 Comparisons of load-displacement relationships at bearings for specimens S1 and S2.

The behavior of the in-span hinge of both specimens is initially characterized by a bidirectional bending deformation. Then, yielding of the diagonal bars of the seat and the vertical (horizontal in the test orientation) bars of the diaphragm suggest that a 1D shear or punching shear mechanism was the first mode of failure that developed at the bearing cross sections. Finally, yielding of the horizontal (vertical in the test orientation) bars of the seat was observed, which is associated with the SAT mechanism. At the maximum load of both specimens, yielding in the reinforcement was observed throughout the whole seat length. Therefore, an effective seat length of the in-span hinge can not be considered. Accordingly, it is concluded that a combination of these three failure modes occurred in both in-span hinges S1 and S2: 1D shear,

SAT, and punching shear. For example, the west bearing of specimen S2 showed a punching shear crack toward the free end of the west side and a 1D shear crack toward the middle of the specimen, as shown in Figure 5.28. On the other hand, the east bearing of specimen S2 showed a 1D shear crack that did not extend toward the east side of the specimen, as shown in the elevation view of Figure 5.28.

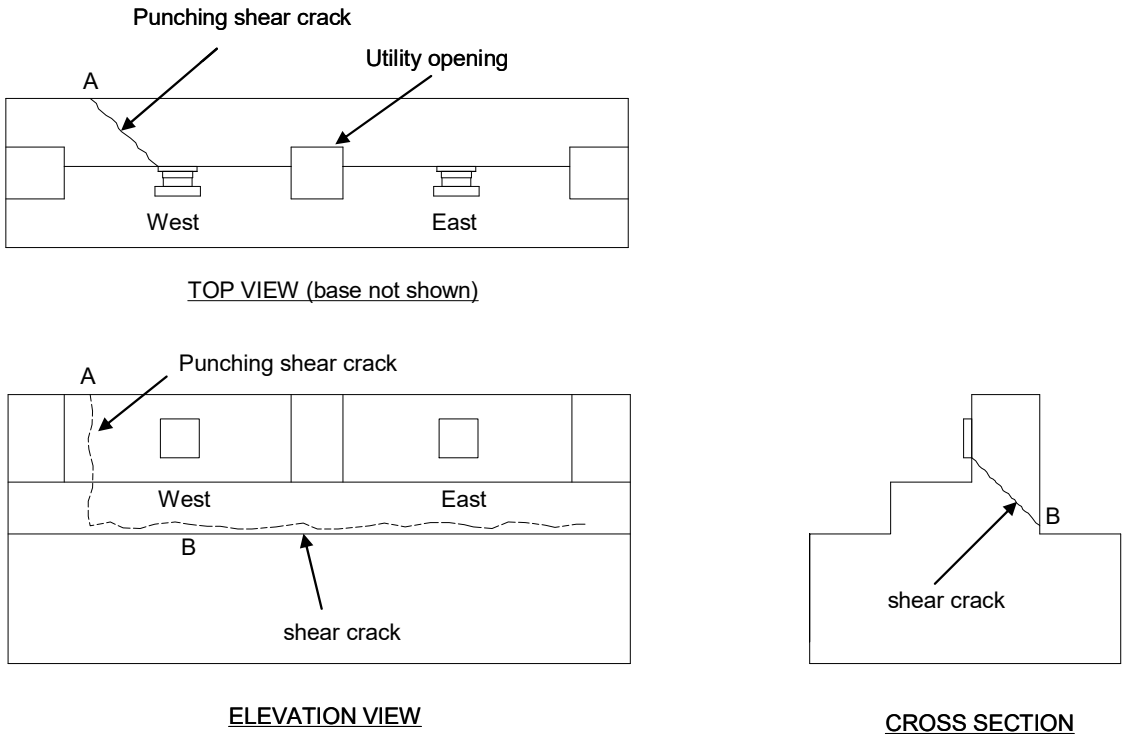

Fig. 5.28 Failure mode of specimen S2.

The sliding shear capacities provided at the seat are 73% and 76% larger than the experimental capacities of specimens S1 and S2, respectively. At the diaphragm, the sliding shear capacities are 151% and 165% larger than the experimental capacities of specimens S1 and S2, respectively. From the test of both specimens, it is concluded that the provided high sliding shear capacities make this failure mode unlikely to occur. Therefore, the diaphragm and seat are over-reinforced for preventing sliding shear friction.

The bending capacities provided at the seat are 49% and 51% larger than the experimental capacities of specimens S1 and S2, respectively. At the diaphragm, the bending capacities are 54% and 68% larger than the experimental capacities of specimens S1 and S2, respectively. It is concluded that the seat and diaphragm are also over-reinforced for preventing bending failure. Therefore, this mode of failure is unlikely to occur. Additionally, from the strain

distributions obtained from the tests, it is concluded that Bernoulli's hypothesis of plane section remaining plane after bending is inappropriate, especially in the diaphragm. This behavior is characteristic of the disturbed regions [MacGregor 2005].

The comparisons of the load-displacement relationships at the bearings between the pre-test FEA and the test results of specimens S1 and S2 are shown in Figure 5.29. The figure shows that the FEA predicts a higher initial stiffness but a lower maximum load. This lower strength of the FEA may be attributed to the used lower material strength properties in the FEA compared to the real properties measured for specimens S1 and S2. The calibration of the FEA to match more precisely the observed response will be conducted in a future phase (post-test FEA) of this research project.

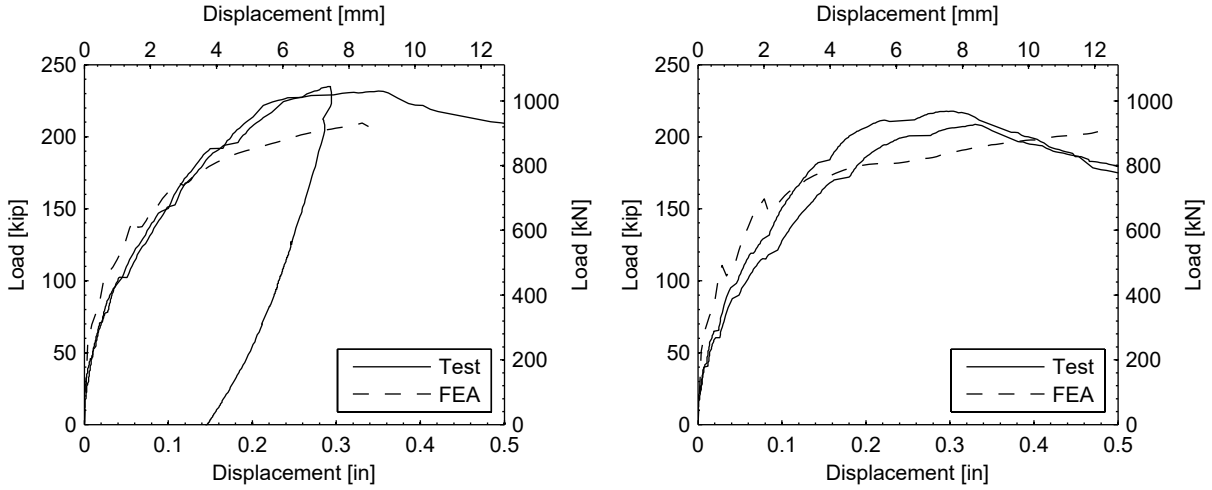

(a) Specimen S1 (a) Specimen S2

Fig. 5.29 Comparisons of load-displacement at the bearings.

On the local level, the comparisons of the reinforcement stresses between the pre-test FEA and the experimental results of specimen S1 are shown in Figure 5.30. The stress distributions of the diagonal bars of the seat (D1) are compared in Figure 5.30a for an applied load of 250 kip (1112 kN) and 400 kip (1779 kN). At the load of 400 kip, both the pre-test FEA and the test results show that the diagonal bars are yielding throughout the whole length of the specimen. The stress distributions of the vertical (horizontal in the test orientation) bars (V1) are shown in Figure 5.30b for the same two load levels as D1 bars. This figure shows good agreement between the pre-test FEA and the test results at both load levels.

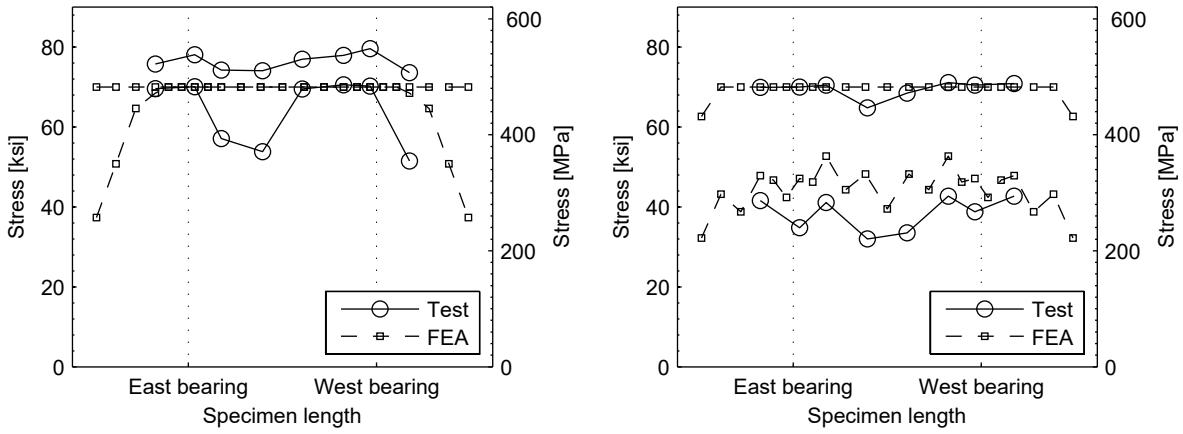

(a) Diagonal bar D1 (b) Vertical bar V1

Fig. 5.30 Comparisons of reinforcement stresses for specimen S1 at 250 kip (1112 kN) and 400 kip (1779 kN) of total load.

Based on the experimental results of the two specimens of phase I, namely S1 and S2, the pre-test FEA results, and the observed excess of capacity provided to some failure modes, the effectiveness of the reinforcing bars is assessed. Using the obtained stresses of reinforcing bars for both specimens (by converting strain readings into stresses using the material stress-strain relationships), the bars are classified as effective bars, less effective bars or ineffective bars. This classification is used for the design of the specimens of phase II (see Chapter 6). The labeling of the reinforcement is shown in Figure 5.31, and the obtained classification in Table 5.6. The stresses shown in the table represent the average for both specimens considering all the instrumented bars for each category of bars. For the reinforcement without instrumentation (bars labeled 4, 11 and 12), the classification is performed based on the experimental observations (e.g., crack patterns) and the pre-test FEA. The horizontal (in the prototype orientation) bar of the diaphragm labeled 4 is classified as ineffective because it has a maximum compressive stress in the pre-test FEA of 26.7% f_y. The vertical (in the prototype orientation) bar of the seat labeled 11 is classified as an effective bar because it provided strength to the punching shear mechanism observed in both specimens; it has a maximum tensile stress of 100% f_y in the pre-test FEA. Finally, the longitudinal bar of the diaphragm labeled 12 is classified as ineffective because it has an average tensile stress in the pre-test FEA of 27.0% f_y.

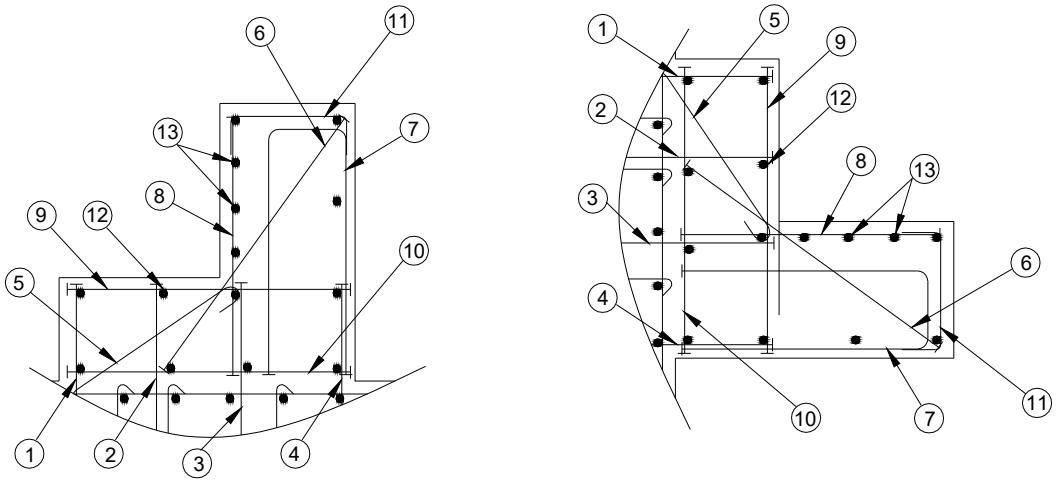

(a) Test orientation (b) Prototype (real) orientation

Fig. 5.31 Reinforcement labels.

Table 5.6 Classification of reinforcing bars.

Bar label	Stress f_y [%]	Classification
1	33.9	Ineffective
2	71.8	Less effective
3	101.1	Effective
4	-	Ineffective
5	98.1	Effective
6	115.3	Effective
7	57.7	Less effective
8	92.3	Effective
9	102.3	Effective
10	60.1	Less effective
11	-	Effective
12	-	Ineffective
13(t)	28.1	Ineffective
13(b)	96.2	Effective

(t) Top longitudinal bars in the prototype orientation
(b) Bottom longitudinal bars in the prototype orientation

6 Experimental Program Phase II: New Design of In-Span Hinges

This chapter describes the experimental program and the results of the last three specimens representing phase II, where new designs of in-span hinges were considered. The designs of these specimens were based on the experimental results of the first two in-span hinges tested in phase I. Specimen S3 was designed identical to specimen S2 but had larger loading plates to increase the punching shear capacity. Specimens S4 (analogous to specimen S1) and S5 (analogous to specimen S2) were designed with low reinforcement ratios aimed to improve the performance and the constructability of in-span hinges. At the end of this chapter, concluding remarks about phase II specimens are presented and the new designs are compared with the designs of the as-built in-span hinges of phase I.

6.1 SPECIMEN DESIGN

The failure mode observed in the two specimens of phase I was a combination of 1D shear, SAT and punching shear. The objective of specimen S3 was to test an in-span hinge with a possible global failure mechanism, preventing the localized punching shear failure. This was intended to observe a more ductile failure mode which effectively utilized the reinforcement in the in-span hinge. Therefore, further assessment of the effectiveness of the different reinforcing bars is achievable. Specimen S3 also provided fundamental data set to complement those of specimens S1 and S2 to study the behavior of a specimen with a global failure mechanism. This additional data is of great relevance for the intended future parametric study using the developed computational model and the planned post-test FEA. To prevent the local punching shear failure mode, specimen S3 was designed identical to specimen S2, but with oversized bearing plates to increase the punching shear strength. The size of each bearing plate was increased from 6"×6"×3/4" (152 mm×152 mm×19 mm) to 6"×14"×3" (152 mm×356 mm×76 mm). The length

of this larger plate was selected to be one third of the distance between the bearing plates. The test setup of specimen S3 with the larger bearing plates is shown in Figure 6.1.

Fig. 6.1 Bearing plate detail of specimen S3.

From the test results of specimens S1 and S2, it was identified that the current in-span hinges are over-reinforced for sliding shear and bending moment resistance. The design of specimen S4 was performed using the effectiveness of the reinforcing bars of the first two specimens, described at the conclusion of Chapter 5. The design philosophy of specimen S4 revolves around making the strengths corresponding to all of the failure mechanisms of the in-span hinge region to be uniform and consistent. This was achieved by making the design more integral and economical. Moreover, attention to practicality for better performance was exercised in the design. Specimen S5 was identical to specimen S4 but access openings were included in specimen S5. Therefore, the relationship between the new integral designs of specimens S4 and S5 was analogous to that between the as-built designs of specimens S1 and S2.

The reinforcement details at the bearing cross section of specimens S4 and S5 is shown in Figure 6.2 and the complete structural drawings are shown in Appendix A. The comparisons between the reinforcement ratios of the real in-span hinge projects with prestressed box girders presented in Chapter 2, the first three specimens, and specimens S4 and S5 are shown in Figure 6.3. The figure shows that specimens S4 and S5 had reinforcement ratios that were close to the minimum ratios observed in the real in-span hinge projects. The reinforcement ratios of all the specimens and the prototype (defined in Chapter 3) are listed in Table 6.1. Specimens S4 and S5 represented a reduction of the total steel of the in-span hinge region of 45%. The largest reduction of the reinforcement ratio was applied to the horizontal (vertical in the test orientation) reinforcement of the seat, ρ_{sh}, which was reduced from 1.90% to 0.63%.

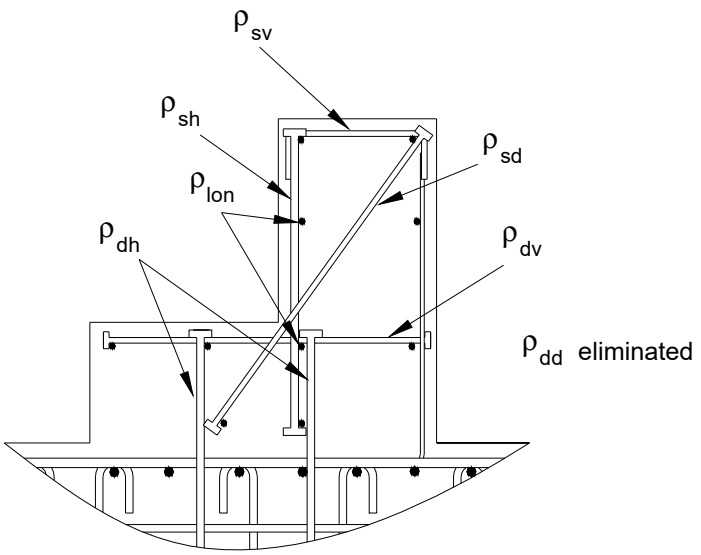

Fig. 6.2 Reinforcement details of specimens S4 and S5 (in test orientation).

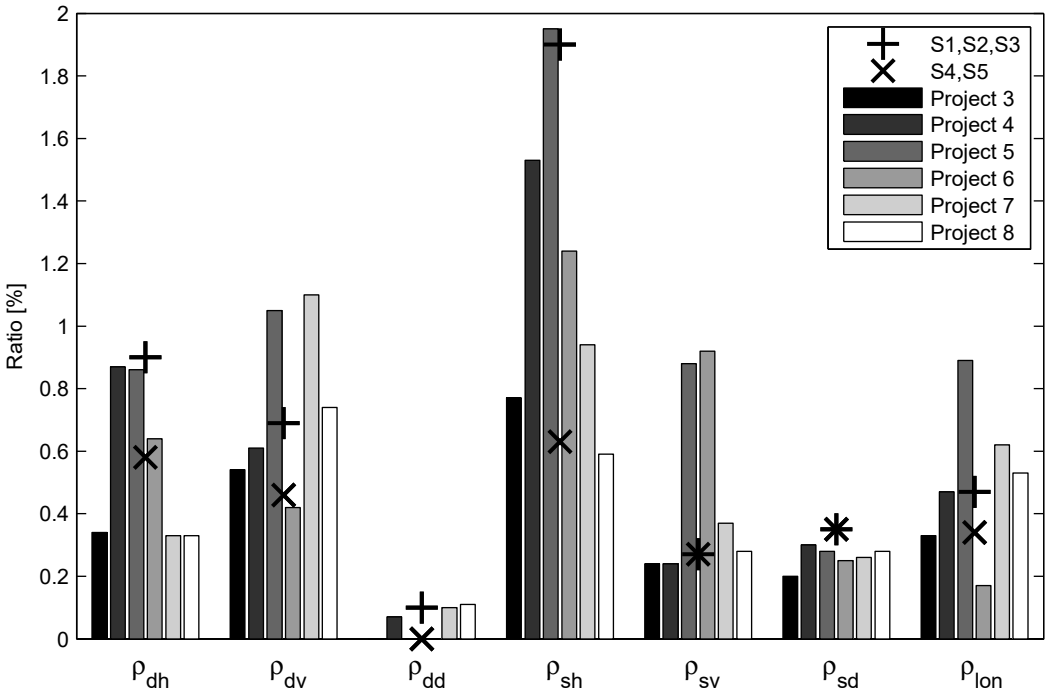

Fig. 6.3 Reinforcing steel ratios of test specimens and real projects.

Table 6.1 Reinforcing steel ratios (%) in in-span hinge region.

	ρ_{dh}	ρ_{dv}	ρ_{dd}	ρ_{sh}	ρ_{sv}	ρ_{sd}	ρ_{lon}
Prototype (Chapter 3)	0.87	0.61	0.07	1.53	0.24	0.30	0.47
S1, S2, and S3	0.90	0.69	0.10	1.90	0.27	0.35	0.47
S4 and S5	0.58	0.46	0.00	0.63	0.27	0.35	0.34

6.2 SPECIMENS CONSTRUCTION

Specimens S3, S4 and S5 were constructed in phase II at the structural engineering laboratory of the University of California, Berkeley, by a professional contractor. The concrete was supplied by a local ready-mix plant using two trucks and was cast using a pump. The concrete of the first truck was used to construct the bases of the three specimens and the concrete of the second truck was used to construct the in-span hinge regions of the three specimens. Concrete was cured with wet burlap for a period of 6 days inside the laboratory. At that age, the burlap was removed and the specimens were stripped from the formwork. Figure 6.4 shows photographs of the construction process of specimens S3, S4, and S5.

6.3 MATERIAL PROPERTIES

Analogous to phase I specimens, extensive material testing was conducted to concrete and reinforcement for phase II specimens as part of the research program. The material testing program was aimed to determine properties and constitutive relationships to be used in the future post-test FEA. The summary of the material properties is presented in this section. Further information about material testing is described in Appendix B.

(a) Specimen S3 base

(b) Specimen S3 reinforcement

(c) Specimen S4 reinforcement

(d) Casting concrete

(e) Curing concrete

(f) Stripped specimens

Fig. 6.4 Construction process of specimens S3, S4, and S5.

6.3.1 Concrete

Normal-weight concrete was used with a specified design strength of 5 ksi (34.5 MPa) and 3/8" (10 mm) maximum aggregate size. The summary of the concrete properties for specimens S3, S4, and S5 is shown in Table 6.2. In this table, the measured concrete properties did not significantly increase with concrete age beyond the standard 28 days. Accordingly, and since all test specimens of phase II were constructed using the same concrete batch, the average values of

the three specimens, reported in Table 6.2, will be considered in the post-test FEA. The average splitting tensile strength and average modulus of rupture are equivalent to $6.9\sqrt{f_c'}$ [psi units] and $11.2\sqrt{f_c'}$ [psi units], respectively. The fracture energy test was not conducted for these specimens, and the average value to be used will correspond to the fracture energy obtained from the specimens of phase I.

As in phase I, the average stress-strain relationship of concrete in compression of the phase II in-span hinges is shown in Figure 6.5. The hardening response part of this curve (below the maximum strength) was obtained from the average of the force-control tests conducted for the three in-span hinge specimens of phase II. On the other hand, the softening response part of the curve was obtained from the average of the displacement-control tests conducted for phase I. These tests are discussed in Appendix B.

Table 6.2 Properties of concrete in phase II.

Property	S3	S4	S5	Average
Compressive strength f_c' [ksi (MPa)]	6.89 (47.5)	6.82 (47.0)	6.91 (47.6)	6.87 (43.4)
Strain at peak stress ε_o	0.0035	0.0037	0.0034	0.0036
Modulus of elasticity E_c [ksi (GPa)]	2940 (20.3)	2860 (19.7)	2940 (20.3)	2910 (20.0)
Splitting tensile strength f_{ct} [ksi (MPa)]	0.62 (4.27)	0.54 (3.72)	0.56 (3.86)	0.57 (3.93)
Modulus of rupture f_r [ksi (MPa)]	1.00 (6.90)	-	0.86 (5.93)	0.93 (6.41)
Fracture energy G_{ft} [lbf/in. (N/m)]	-	-	-	-
Age of testing [days]	29	37	50	-

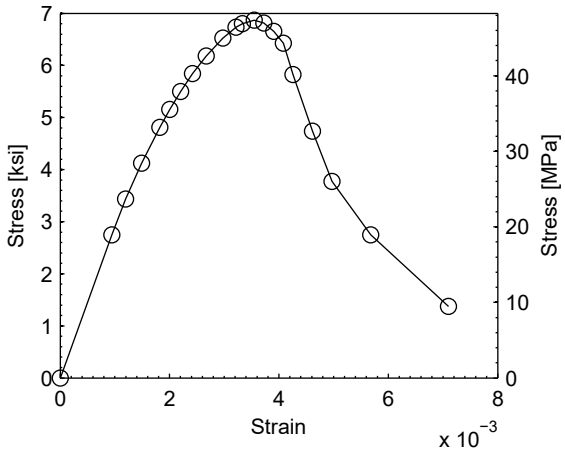

Fig. 6.5 Average stress-strain relationship of concrete in phase II.

6.3.2 Reinforcement

The reinforcing steel used in the specimens of phase II was Grade 60, meeting the requirements of ASTM A706-06 (ASTM 2004b). Specimens S3, S4, and S5 considered headed and non-headed reinforcement as explained in Chapter 3. The summary of the average reinforcing steel properties used in specimens of phase II is shown in Table 6.3.

The stress-strain relationships of the reinforcing steel to be used in the FEA are shown in Figure 6.6. These curves follow the Voce equation (Voce 1948), which is implemented in the finite element software DIANA (DIANA 2007).

Table 6.3 Average properties of reinforcing steel in phase II.

Property	#3 Non-headed	#3 Headed	#4 Headed
Yield stress f_y [ksi (MPa)]	74.9 (516)	73.4 (506)	66.8 (460)
Ultimate stress f_u [ksi (MPa)]	102.7 (708)	95.1 (656)	94.7 (653)
Yield strain ε_y	0.0028	0.0026	0.0023
Ultimate strain ε_u	0.109	0.081	0.121
Modulus of elasticity E_s [ksi (GPa)]	26640 (184)	28140 (194)	28070 (194)

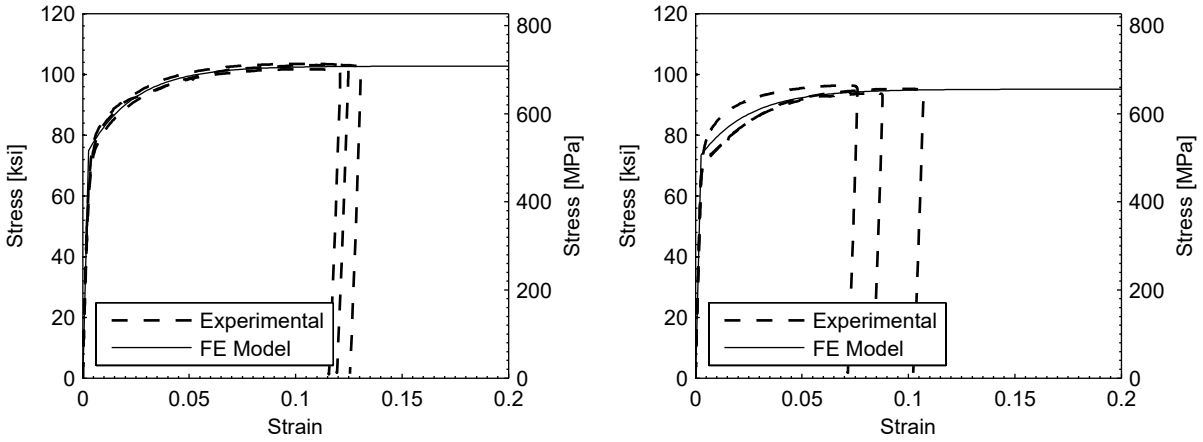

(a) #3 non-headed bar (b) #3 headed bar

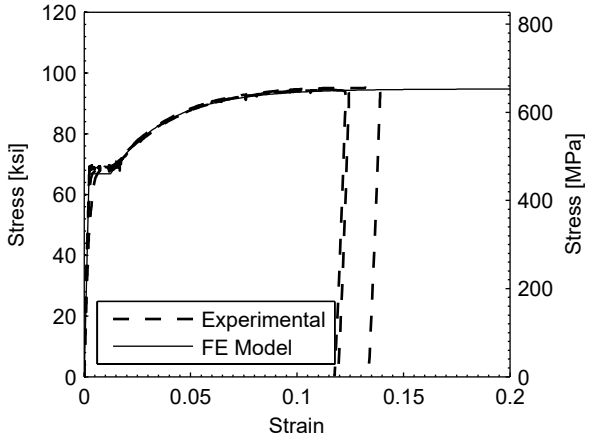

(c) #4 headed bar

Fig. 6.6 Stress-strain relationships for reinforcing steel in phase II.

6.4 INSTRUMENTATION

Specimens S3, S4, and S5 were instrumented with a total of 3 load cells and 27 displacements transducers as described in Chapter 3. Specimens S3 was additionally instrumented with 60 strain gages, and specimens S4 and S5 with 50 strain gages. All the instruments were connected to a data acquisition system of 128 channels. The locations of the strain gages on the reinforcing steel of phase II specimens are described below.

The locations of the strain gages of specimen S3 are similar to those of specimens S1 and S2. For specimen S3, most of the bars were instrumented with only one gage, and two additional bars, compared to specimens S1 and S2, were also instrumented. These strain gages are shown in Figure 6.7. A total of 11 strain gages were located in a cross section through each bearing

(section b-b) to quantify the reinforcement stresses, and to identify the load transfer mechanism. At this cross section, 3 gages were located on horizontal bars (vertical in the test orientation) of the seat (H1, H3, and H5), 2 gages were located on vertical bars (V1 and V5), and 2 gages were located on diagonal bars (D1 and D3). These 7 gages allowed identifying the possible failure modes of the seat: sliding shear friction, bending moment, 1D shear, SAT, and punching shear. The remaining 4 gages of cross section b-b are located on horizontal bars (vertical in the test orientation) of the diaphragm (B1, B3, B5, and B7) to measure the anchorage of the in-span hinge to the base.

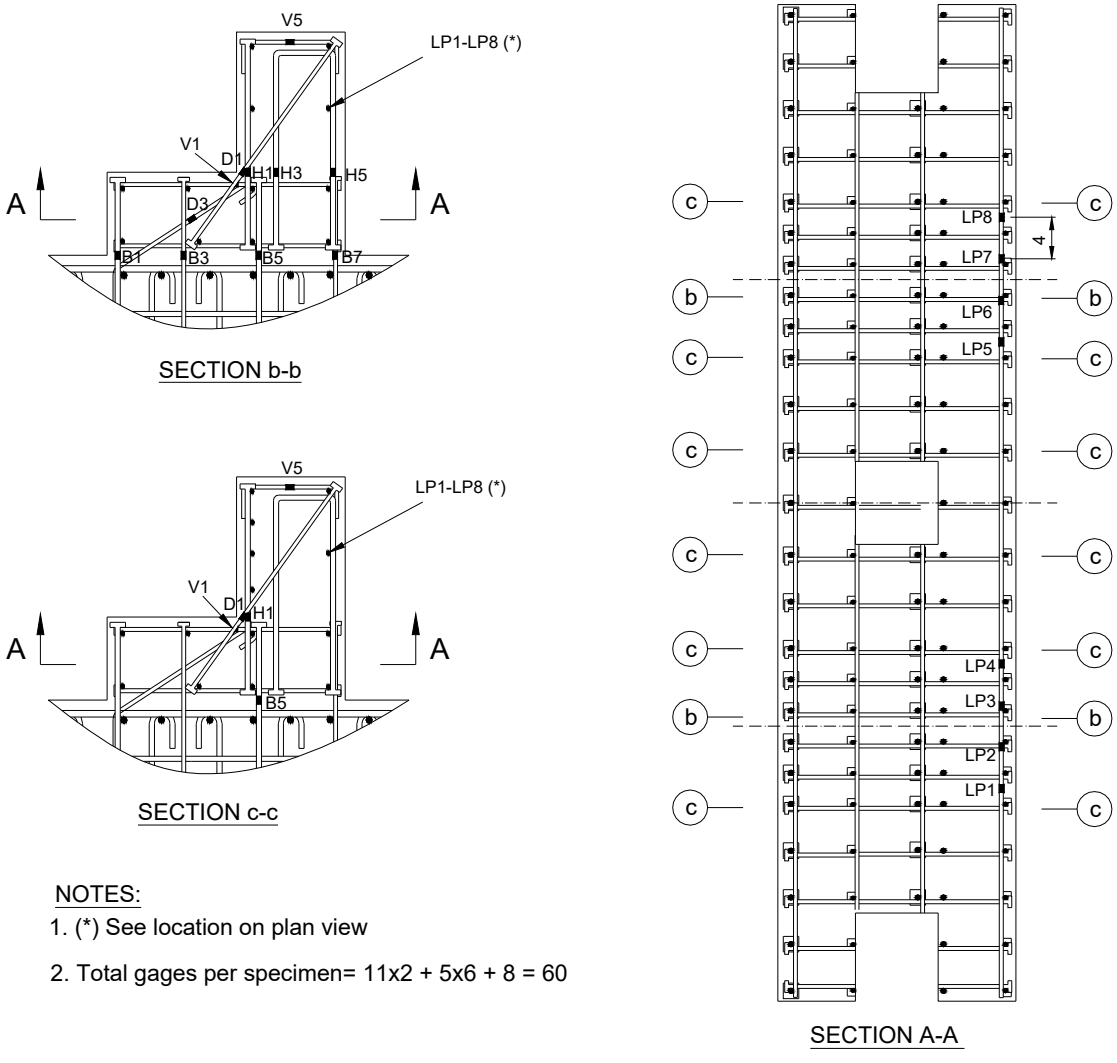

Fig. 6.7 Strain gage locations for specimen S3.

A total of 30 gages were located in groups of 5 gages (H1, V1, V5, D1, and B5) in cross sections c-c throughout the length of the specimen. These gages were used to measure the 3D effects of the load transfer from the bearing throughout the length of the diaphragm. Finally, a total of 8 gages (LP1-LP8) were located on longitudinal bars of the seat to measure the bending of the seat.

Specimens S4 and S5 were instrumented with 50 gages each as shown in Figure 6.8. A total of 6 strain gages were located in a cross section through each bearing (section b-b) to quantify the reinforcement stresses and to identify the load transfer mechanism. At this cross section, 1 gage was located on a horizontal bar (vertical in the test orientation) of the seat (H1), 2 gages were located on vertical bars (V1 and V5), and 1 gage was located on a diagonal bar (D1). These 4 gages allowed identifying the possible failure modes of the seat: sliding shear friction, bending moment, 1D shear, SAT, and punching shear. The remaining 2 gages of cross section b-b were located on horizontal bars (vertical in the test orientation) that connect the seat to the base (B3 and B5) to measure the anchorage of the in-span hinge to the base. The remaining 38 gages for other locations than cross sections b-b were located in the same positions as the ones described for specimen S3.

6.5 PRE-TEST STRENGTH ESTIMATION

The capacity of the in-span hinge specimens was estimated using the analytical models described in Chapter 2. These analytical models are sliding shear friction at the seat and at the diaphragm, moment strength at the seat and at the diaphragm, 1D shear strength at the seat, SAT, and punching shear. For the capacity estimates, the average strength of the materials at the time of the tests was used, as indicated in Tables 6.2 and 6.3 for concrete and steel, respectively.

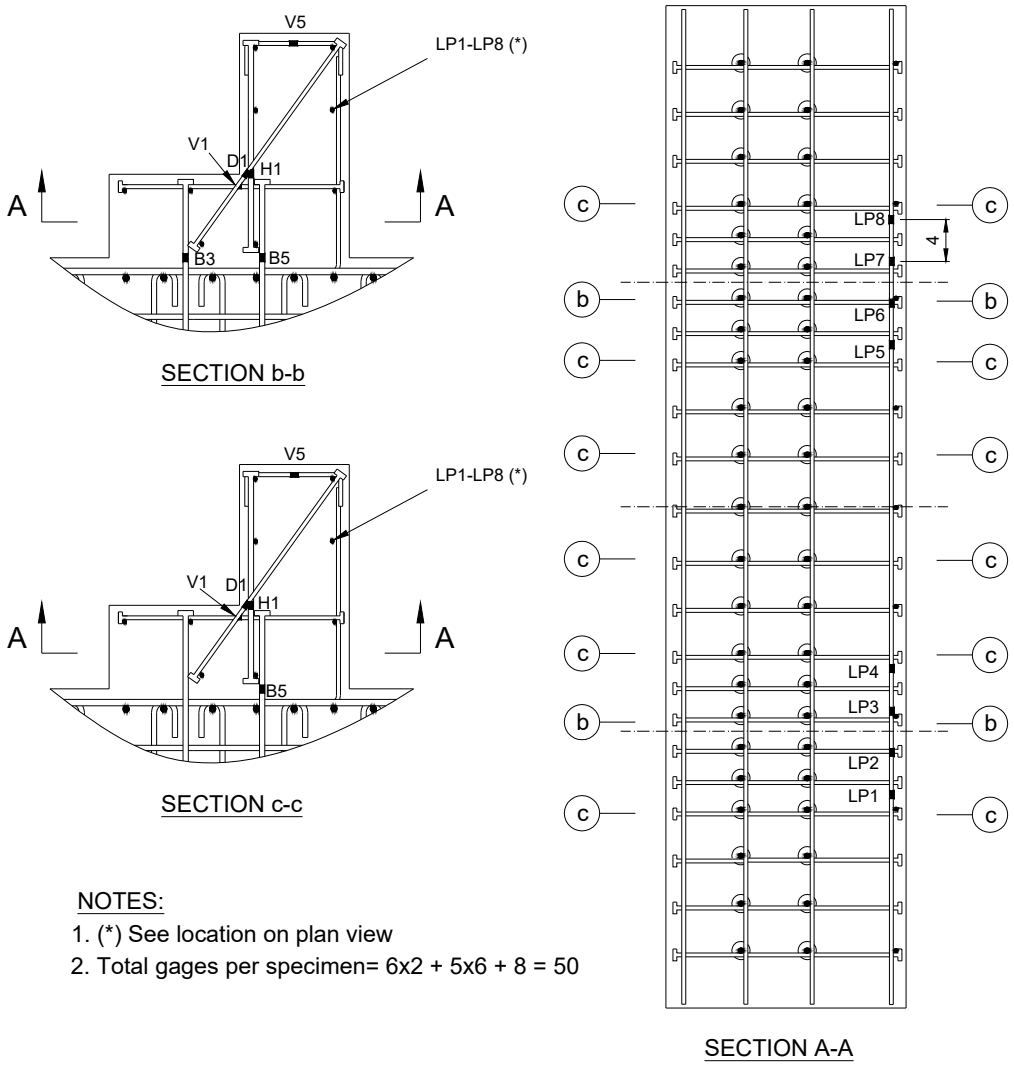

Fig. 6.8 Strain gage locations for specimens S4 and S5.

The SAT capacity was computed using a 2D truss model. The SAT model of specimen S3 was identical to that of specimens S1 and S2 described in Chapter 5. For specimens S4 and S5, the proposed truss topology is shown in Figure 6.9. The width of this truss considered the total width of the specimen, which is 96" (2438 mm). Therefore, the steel area of each tie was the sum of the bars along the specimen length. For specimen S5, the openings in the concrete were neglected in the truss model, but the areas of steel of the ties took into account the reduction of the number of bars at the openings. In this 2D SAT, the 3D behavior induced by the discrete loads at the bearings was neglected.

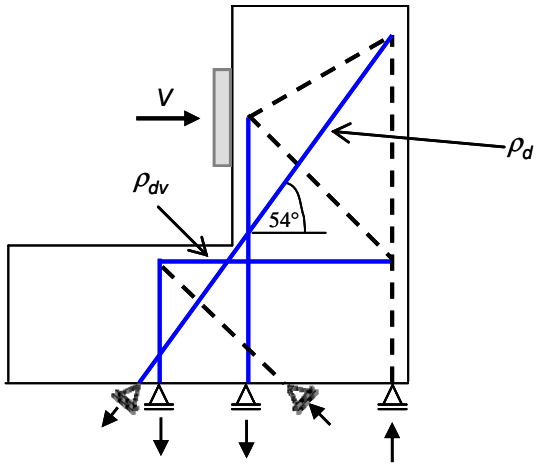

Fig. 6.9 Strut-and-tie model for specimens S4 and S5 (in test orientation).

The larger SAT capacity of the statically indeterminate truss shown in Figure 6.9 was achieved when the diagonal tie of the seat ρ_d and the vertical tie of the diaphragm ρ_{dv} (horizontal tie in the test orientation) were yielding simultaneously. The SAT capacities for specimens S4 and S5 were 295 kip (1312 kN) and 256 kip (1139 kN), respectively. These capacities are lower than those of specimens S1 and S2 because the new design had only one vertical tie (horizontal tie in the test position) in the diaphragm ρ_{dv} instead of two for the as-built design (Fig. 5.6).

The capacity estimates using the described analytical models are listed in Table 6.4. In the same table, the experimental results and the factored Caltrans design loads are tabulated for completeness. From this table, it can be observed that the punching shear capacity of specimen S3 is increased due to the effect of the larger bearing plates by increasing the amount of concrete that contributed in the punching shear mechanism. These larger bearing plates increased the punching shear capacity by 23% compared to specimens S1 and S2. For specimens S4 and S5, it can be observed that the strength prediction of the different failure modes was more uniform than that for specimens S1 and S2, as intended by the reduction of the different reinforcement ratios discussed in Section 6.1. It is to be noted that the low strength prediction given by the SAT model was found to be conservative in specimens S1 and S2 because it neglected the concrete contribution in tension. For specimens S4 and S5, the sliding shear friction at the diaphragm and the bending moment strength at both the seat and the diaphragm were reduced considerably by reducing the reinforcement ratios. The 1D shear strength at the seat and the punching shear strength were equivalent to those of specimens S1 and S2 because the same reinforcement ratios

contributed to these failure modes. The 5% increase of the predicted strength of specimens S4 and S5 compared to specimens S1 and S2 for these modes of failure was attributed to the different material properties.

Table 6.4 Strength estimates of specimens S3, S4, and S5 [kip (kN)].

	S3	S4	S5
Sliding shear friction at seat	744 (3309)	721 (3207)	627 (2789)
Sliding shear friction at diaphragm	1096 (4875)	615 (2736)	534 (2375)
Moment strength at seat	628 (2793)	406 (1806)	388 (1726)
Moment strength at diaphragm	651 (2896)	473 (2104)	414 (1842)
1D shear strength at seat	395 (1753)	446 (1984)	395 (1753)
SAT	337 (1499)	295 (1312)	256 (1139)
Punching shear	493 (2193)	400 (1779)	400 (1779)
Experimental capacity	535 (2380)	380 (1690)	384 (1708)
Factored Caltrans design load	136 (605)	136 (605)	136 (605)

For the sliding shear friction mode at the seat and at the diaphragm, the strength of specimen S3 was controlled by the ACI limit of $800A_c$ [lbf, in.],whereas for specimens S4 and S5, at the seat and diaphragm reductions of the sliding shear strength were observed. This is attributed to the lower reinforcement ratio of the reinforcing bars that crossed the sliding plane.

The factored Caltrans design loads for the test specimens were obtained by scaling the factored design load of the prototype in-span hinge defined in Chapter 3. Therefore, analogous to phase I specimens, the design load for specimens S3, S4, and S5 was equal to $2\times611/(3)^2$ =136 kip (605 kN). The factored Caltrans design loads conservatively corresponded to only 25%, 36% and 35% of the real strength obtained from testing specimens S3, S4, and S5, respectively.

6.6 SPECIMEN S3 TEST RESULTS

The experimental results of specimen S3 are presented in this section. Specimen S3 was identical to specimen S2 but had larger bearing plates to increase the punching shear strength and produce a global mode of failure. It is to be noted that results shown as envelopes of the cyclic loading are consistent with the envelope of the global force-displacement relationship.

6.6.1 General Observations

Equivalent to the specimens of phase I, the initial crack appeared near the seat corner with the diaphragm at 0.08" (2.0 mm) peak displacement cycle, as indicated by the arrow in Figure 6.10a. At this displacement, the specimen load was 85 kip (378 kN). At 0.11" (2.8 mm) peak displacement cycle, vertical (in the test orientation) bending cracks appeared behind the bearing plates as shown in Figure 6.10b. At this displacement, the specimen load was 102 kip (454 kN). At the 0.2" (5.1 mm) peak displacement cycle, only vertical (in the test orientation) bending cracks were observed behind the seat, as shown behind the instrument in Figure 6.10c. The diagonal cracks observed in specimens S1 and S2 did not appear in specimen S3 due to the effect of the larger bearing plates. However, at this load level, a diagonal crack appeared in the bearing side toward the free end of the specimen, as shown in Figure 6.10d. The damage propagation for the 0.4" peak displacement cycle is shown in Figures 6.10e–f.

When reaching the maximum strength of the specimen, the initial crack located near the seat corner with the diaphragm became wider and it was spread over the entire length of the specimen, as shown in Figure 6.10h. Consequently, a global shear failure mode was observed throughout the whole seat length. When the specimen was responding on the descending branch, the east bearing started to deform considerably and a punching shear mechanism was observed, as shown in Figures 6.10g–h. The shear plane induced by the shear failure mode is also shown in Figure 6.10g

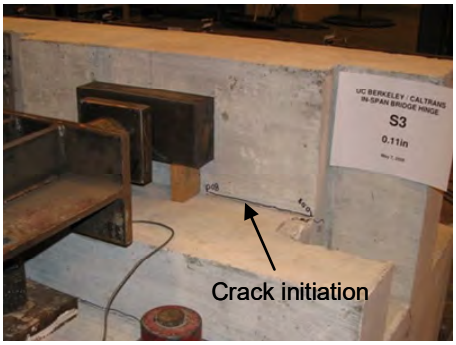

(a) Crack initiation at 0.08" (2.0 mm), east side

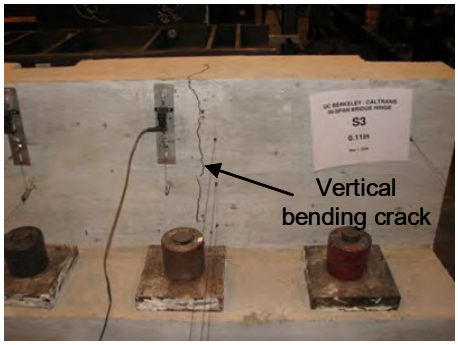

(b) Bending crack at 0.11" (2.8 mm), west side

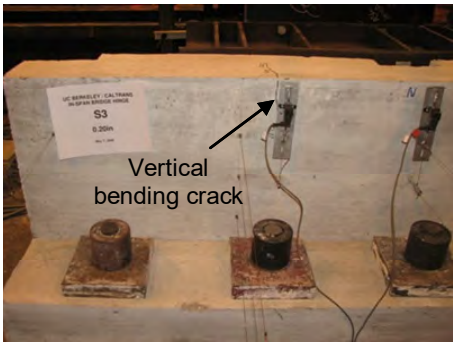

(c) 0.2" (5.1 mm) displacement, east side

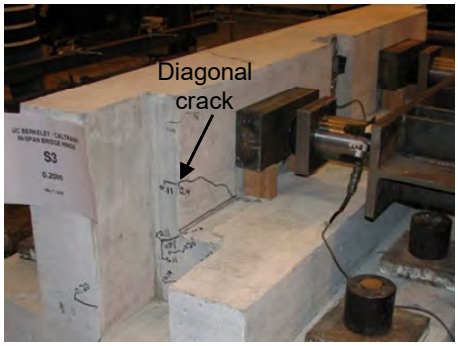

(d) 0.2" (5.1 mm) displacement, west side

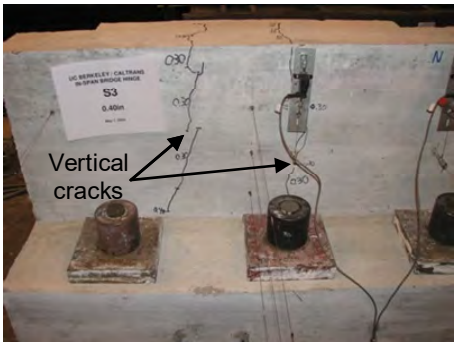

(e) 0.4" (10.2 mm) displacement, east side

(f) 0.4" (10.2 mm) displacement, west side

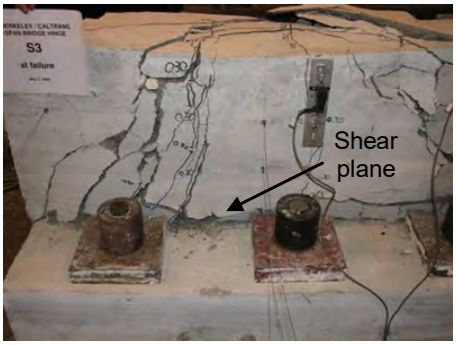

(g) At failure, east side

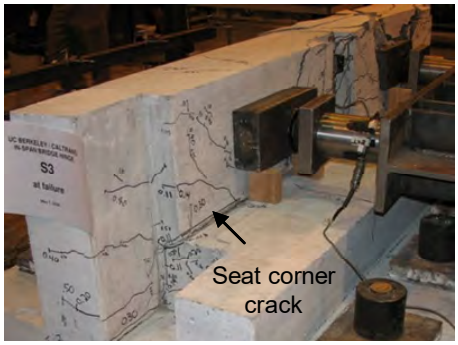

(h) At failure, west side

Fig. 6.10 Damage propagation during test of specimen S3.

The test of specimen S3 was terminated at about 2" (50.8 mm) displacement. At this displacement level, fracture of bars in tension was observed in some diagonal bars located in the vicinity of the bearings. At this displacement, the total force was reduced to about 30% of the maximum strength, and rotation of the loading beam was observed toward the east side. The rotation was due to the differential displacements of the two bearings caused by the concentration of damage in the vicinity of the east bearing.

6.6.2 Load-Displacement Relationships

The applied load-displacement relationship of specimen S3 is shown in Figure 6.11. The displacement was measured with the built in actuator transducer, and the load corresponded to the sum of the two load cells attached to the loading beam. The peak total load of 535 kip (2380 kN) was achieved at 0.62" (15.7mm) displacement. This strength was 26% larger than that of specimen S2 because a global shear failure was observed in specimen S3, where the whole in-span hinge length was fully effective in resisting the applied load. After the peak load was reached, the relationship shows a constant force level that was not observed in phase I specimens. Subsequently, the relationship shows a rapid decrease in the capacity. At the final load, the strength was provided mainly by the tensile force of the diagonal bars, the friction in the global shear mechanism, and the dowel action of the horizontal (vertical in the test orientation) bars through the shear failure plane.

The load-displacement relationships at both bearings are shown in Figure 6.12. The figure shows the response using the displacement of the concrete seat, measured with the instruments SHT2 and SHT4 (Fig. 3.11) for the east and west sides, respectively. The relationships show that both sides of the in-span hinge failed during the test because descending branches were observed (although less pronounced for the west side than the east side) after the maximum strength (Fig. 6.12a). However, the west side started to unload at about 0.8" (20.3 mm) and the displacement started to concentrate in the east side (opposite to the response of specimens S1 and S2 where the displacement started to concentrate in the west side). The relationships of both bearings show a yielding plateau of about 0.5" (12.7 mm) that was not observed in phase I specimens.

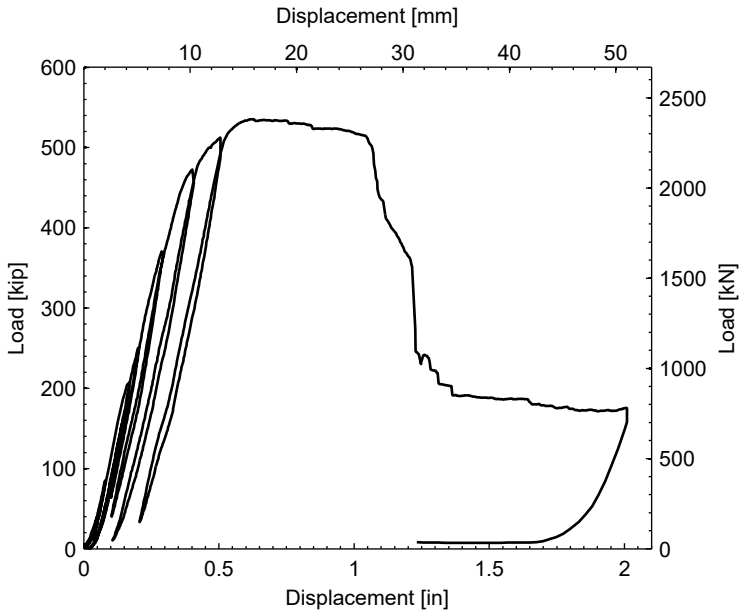

Fig. 6.11 Load-displacement of specimen S3.

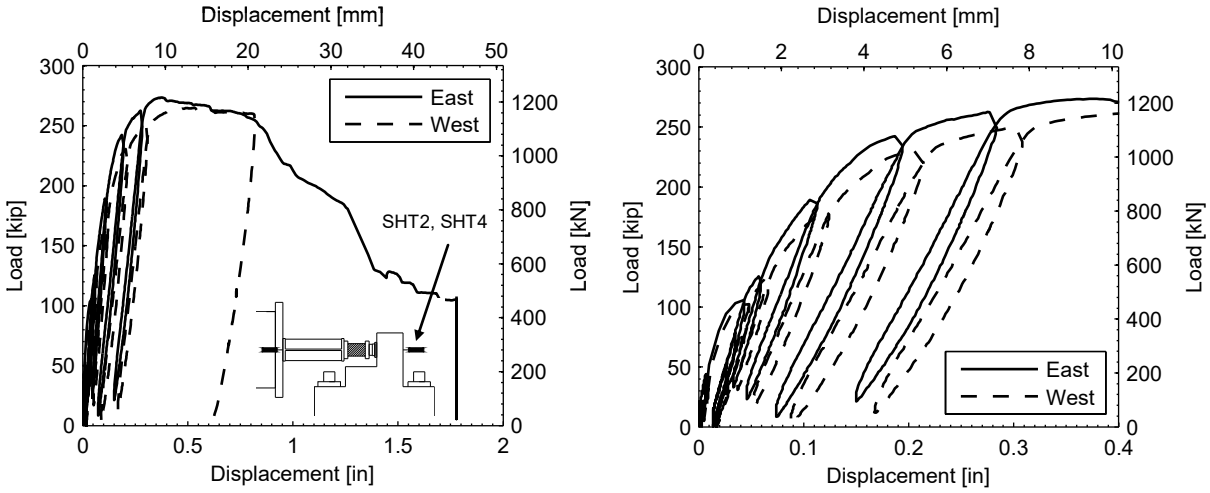

(a) Concrete displacement (b) Zoom of concrete displacement

Fig. 6.12 Load-displacement at bearings of specimen S3.

The maximum strengths of the east and west bearings were 273 kip (1214 kN) and 265 kip (1179 kN), respectively. The corresponding displacements at the peak load were 0.39" (9.9 mm) and 0.42" (10.7 mm) for the east and west bearings, respectively. These displacements were 29% larger than the displacements observed in specimen S2. The increase in the displacement corresponding to the peak load is due to the more ductile failure mode associated with the use of larger bearing plates. The initial stiffnesses considering the concrete seat displacement were

2005 kip/in. (351 kN/mm) and 1668 kip/in. (292 kN/mm) for the east and west bearings, respectively. These values correspond to secant stiffness computed using a 50 kip (22 kN) load.

6.6.3 Seat Deformation Profiles

The seat deformation profile along the in-span hinge length (horizontal deformation of the seat in the test orientation) is shown in Figure 6.13a. The figure shows the displacement at 50%, 75%, and 100% of the maximum specimen load. The displacement profile was measured with 5 instruments, where the instruments SHT2 and SHT4 corresponded to the cross sections of the east and west bearings, respectively. The figure shows that the displacements at the two bearing cross sections were equivalent for 50% and 75% of the maximum load. For 75% of the maximum load, the displacements measured with the instruments at the edges and at the middle represented 72% and 87% of the displacement measured at the two bearings. This deformation profile suggested that the load was resisted more uniformly, compared to specimen S2, throughout the seat length due to the larger bearing plates. At 100% of the maximum load, the displacements of both bearings increased considerably, which agreed with the load-displacement relationship of Figure 6.12, where both sides reached the maximum strength during the test.

The displacement profile along the specimen height at the two bearing cross sections is shown in Figure 6.13b, analogous to specimens S1 and S2. The figure shows the displacement at 50%, 75%, and 100% of the maximum specimen load. This horizontal displacement (in the test orientation) was measured with top (T), middle (M) and bottom (B) displacement transducers. The exact location of these instruments is described in Chapter 3. Figure 6.13b shows a linear displacement variation along the height, which implies a shear deformation profile of the specimen. In contrast, a bending deformation profile is characterized by a cubic displacement variation along the height.

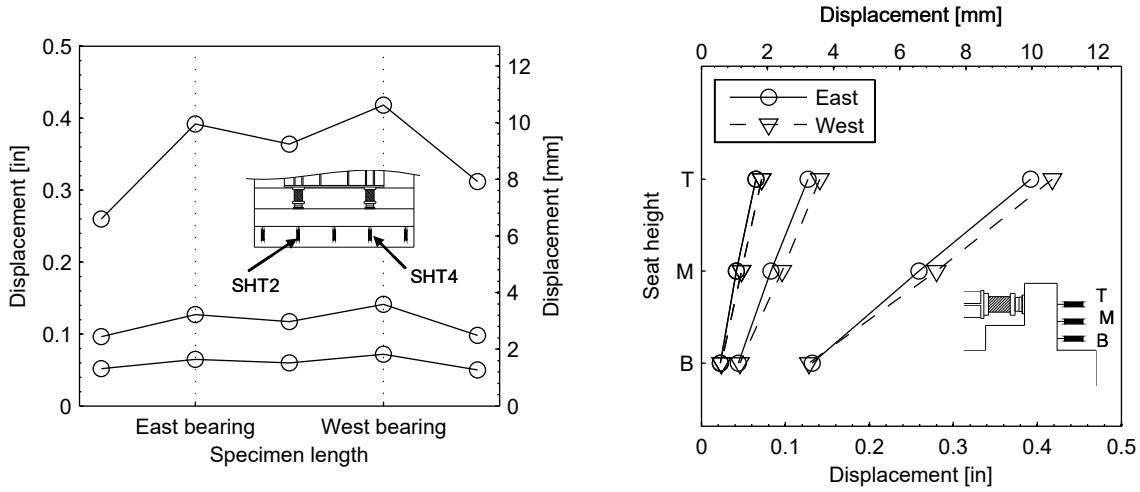

(a) Displacement profile along specimen length

(b) Displacement profile along specimen height, at the bearing cross sections

Fig. 6.13 Seat deformation profiles at 50%, 75%, and 100% of peak load of specimen S3.

6.6.4 Reinforcing Steel Behavior

The strains on the reinforcing steel bars of specimen S3 were measured with a total of 60 strain gages. The details of the reinforcement and the location of the most important strain gages are shown in Figure 6.14. From the strain measurements, reinforcing bar stresses were computed using the stress-strain relationships obtained from the reinforcing bar material tests (Fig. 6.6).

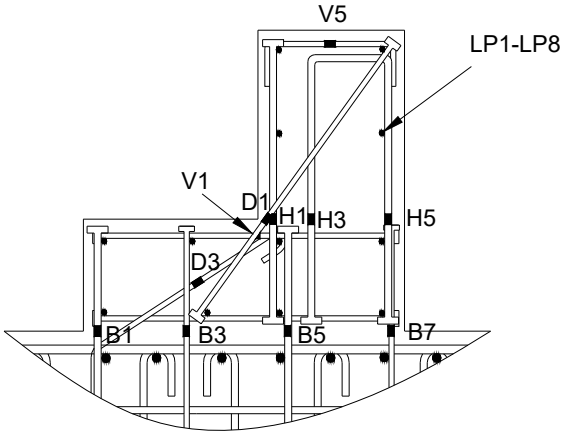

Fig. 6.14 Strain gage locations in specimen S3 (in test orientation).

The relationships of the envelopes of the reinforcement stresses versus the applied load, at both bearing cross sections (east and west), are shown in Figure 6.15. The figure shows that yielding was initiated in diagonal bar D1 (Fig. 6.15a) located at the seat, which yielded at an

applied load of 260 kip (1156 kN). This initial yielding was consistent with the crack initiation near the seat corner with the diaphragm.

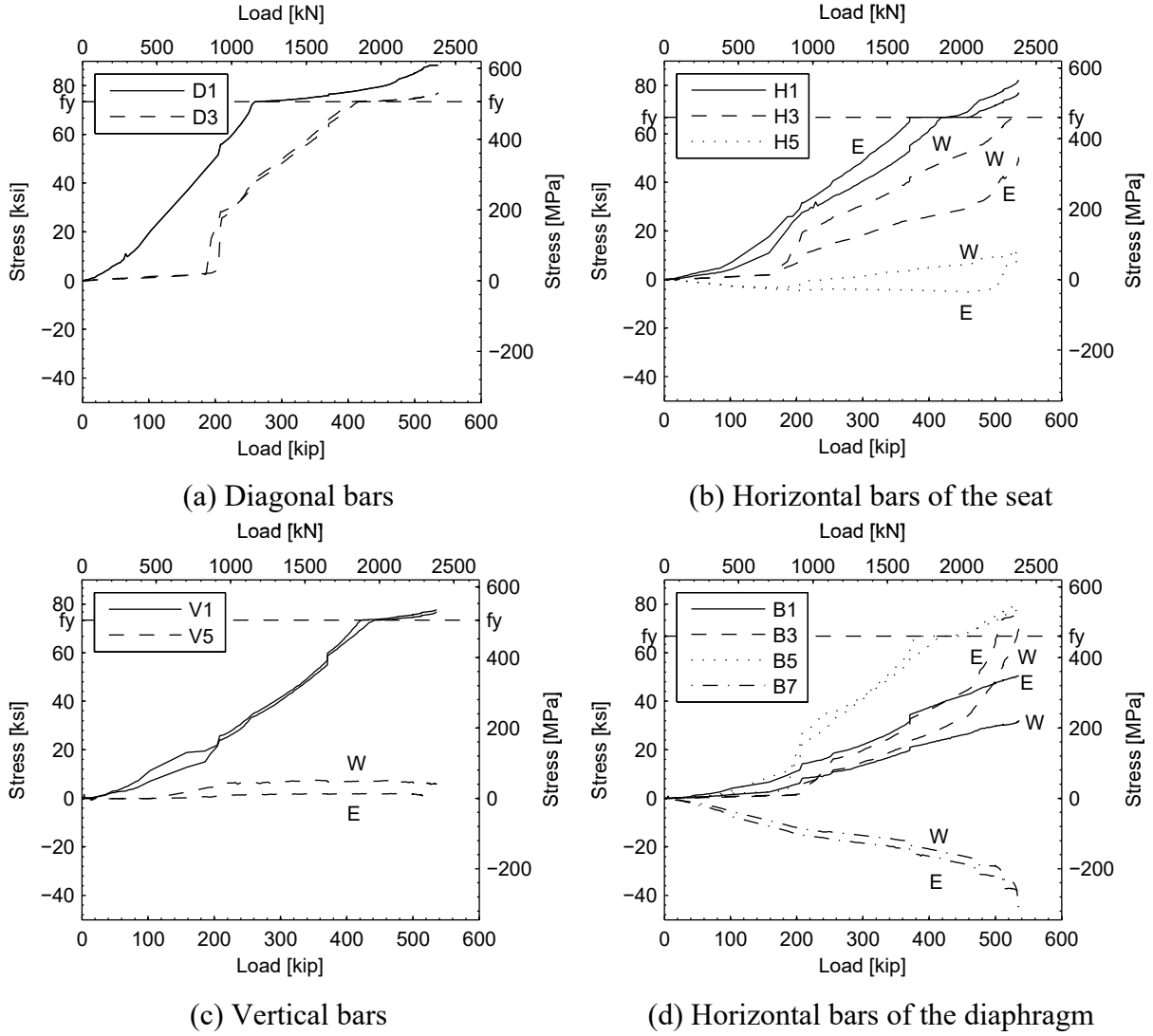

(a) Diagonal bars

(b) Horizontal bars of the seat

(c) Vertical bars

(d) Horizontal bars of the diaphragm

Fig. 6.15 Stresses in reinforcement at bearing cross sections versus applied load of specimen S3.

Figure 6.15b shows that the second bar that reached yielding after diagonal bar D1 was the horizontal (vertical in the test orientation) bar at H1, which yielded at an applied load of 371 kip (1650 kN). The unequal stresses at these horizontal bars (vertical in the test orientation), namely H1, H3, and H5 in Figure 6.14, confirm that the sliding shear mechanism in the seat did not develop during the test. Moreover, major horizontal cracks at the seat-diaphragm sliding surface were not observed during the test.

The stresses of the vertical (horizontal in the test orientation) bars are shown in Figure 6.15c. The figure shows that the vertical bars at the locations V1 reached yielding stress at an applied load of 421 kip (1873 kN). The strain gage V5 on the vertical bar (horizontal in the test orientation) was installed to investigate the punching shear behavior. Figure 6.15c shows negligible stresses in bars V5 because it was found that the bars at the bearing cross sections were not located in the punching shear failure plane.

The stresses in the horizontal (vertical in the test orientation) bars of the diaphragm are shown in Figure 6.15d. The figure shows that yielding occurred only in the bar with the strain gage labeled B5 (and to a lesser extent the bar with the strain gage labeled B3). Again, the unequal stresses of the base bars, namely B1, B3, B5, and B7, suggest that the sliding shear mechanism in the diaphragm did not develop during the test, and major horizontal cracks at the diaphragm-base sliding surface were not observed during the test.

The strain distribution at the seat and at the diaphragm in the bearing cross sections are shown in Figure 6.16. These distributions are shown for 25%, 50%, 75%, and 100% of the maximum applied load at the east and west bearing cross sections. The strain distribution along the seat width (Fig. 6.16a) shows that it is not linear, especially when the maximum strength was achieved. Therefore, Bernoulli's hypothesis of plane sections remaining plane after bending becomes doubtful. At the peak load, the maximum strain observed at H1 was 24300 $\mu\varepsilon$ (2.4%), this strain is about 4 times larger than that measured in specimen S2. The increase in the strains at H1 agrees with the major horizontal crack observed at the seat corner of the west bearing in Figure 6.10h. From the strain distribution along the diaphragm shown in Figure 6.16b, it is concluded that Bernoulli's hypothesis of plane section remaining plane after bending is not applicable at this cross section either. The highest strain was measured at the bar B5, rather than at the extreme bar B1. For both the seat and the diaphragm cross sections, the high bending capacity provided at these sections and the observed strain distributions confirm that this failure mode was unlikely to occur.

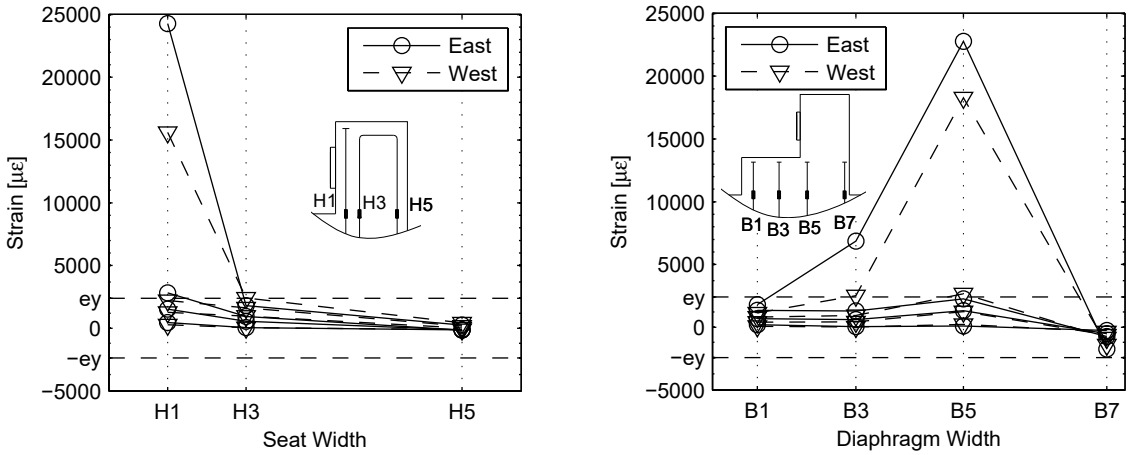

(a) Seat (b) Diaphragm

Fig. 6.16 Horizontal (vertical in test orientation) strain distribution along seat and diaphragm width at 25%, 50%, 75%, and 100% of peak load of specimen S3.

The stress of the longitudinal bar located at the bottom part of the seat (in the prototype orientation) was measured with 8 strain gages (LP1-LP8) located in the vicinity of the bearings, as for specimens S1 and S2. The stress distribution in this bar is shown in Figure 6.17 for 25%, 50%, 75%, and 100% of the maximum applied load. The stress distribution shows the bending action of the seat about the direction perpendicular to the diaphragm. This bending behavior agrees with the observed seat deformation profile and with the vertical (in the test orientation) bending cracks shown in Figure 6.10b. Nevertheless, this bending action was smaller, and without any bar yielding, than that observed in specimen S2 because of the presence of the larger bearing plates.

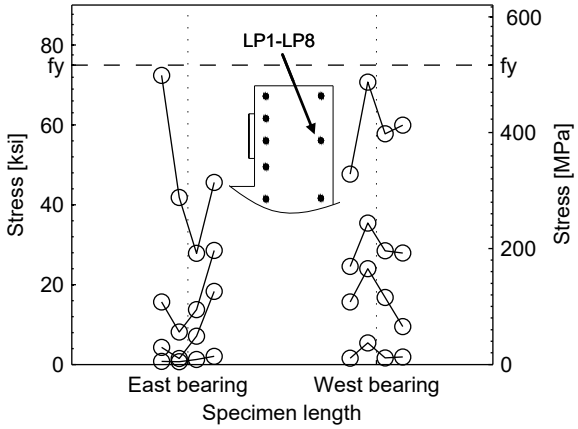

Fig. 6.17 Stress distribution of longitudinal bar at 25%, 50%, 75%, and 100% of peak load of specimen S3.

The strain and stress distributions on the reinforcing bars throughout the specimen length are shown in Figures 6.18–6.20 for 25%, 50%, 75%, and 100% of the maximum applied load. The locations of the bars with their strain gages are shown in Figure 6.14. From the test results, the larger strains were observed in diagonal bars D1 of the seat. The strain and stress distributions of this bar are shown in Figures 6.18a and b, respectively. It can be observed that a peak strain of 29400 $\mu\varepsilon$ (~2.9%) was measured in the vicinity of the west bearing at the maximum applied load. This large strain is about 11 times larger than the yield strain of the reinforcing bar. The stresses of the diagonal bars were distributed uniformly throughout the specimen length, in contrast to specimen S2 where the stresses are concentrated in the vicinity of the bearings for low load levels.

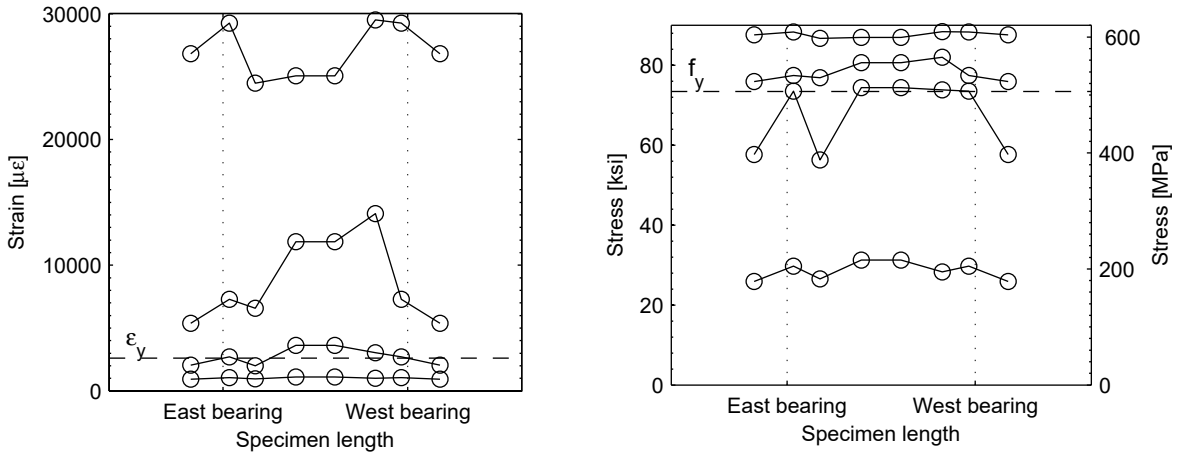

(a) Strains of diagonal bars D1 (b) Stresses of diagonal bars D1

Fig. 6.18 Stresses and strains of diagonal reinforcing bars throughout in-span hinge length at 25%, 50%, 75%, and 100% of peak load of specimen S3.

The strain and stresses of the horizontal (vertical in the test orientation) bars H1 and vertical (horizontal in the test orientation) bars V1 are shown in Figure 6.19a–d. The stresses of these horizontal and vertical bars were lower than those of the diagonal bars and they were also distributed uniformly throughout the specimen length. At the maximum strength of the seat, the yielding of both bars, H1 and V1, was also observed throughout the whole length of the diaphragm, analogous to diagonal bar D1 in Figure 6.18b. The strain and stresses of the vertical (horizontal in the test orientation) bars V5 of the seat is shown in Figure 6.19e and f, respectively. The low level of stresses of these bars (there were no yielding) indicate the absence of the punching shear mechanism in the seat, especially at the free edge of the seat where V5 was

located. Finally, the distributions of strain and stresses of the horizontal (vertical in the test orientation) bars B5 of the diaphragm are shown in Figures 6.20a and b, respectively. These almost uniform distributions suggest that the whole diaphragm length was resisting the applied load.

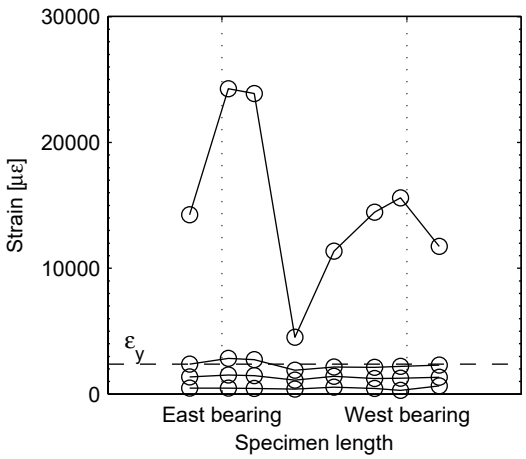

(a) Strains of horizontal bars H1

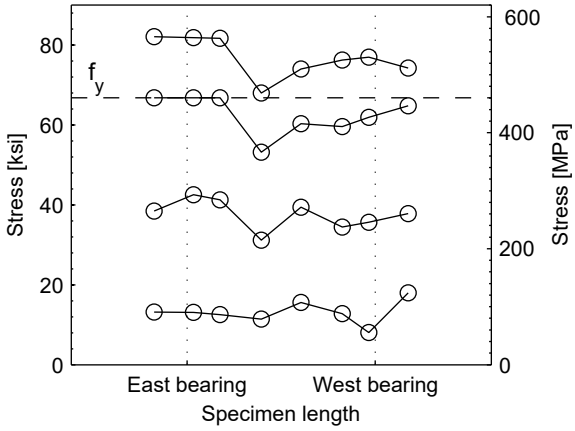

(b) Stresses of horizontal bars H1

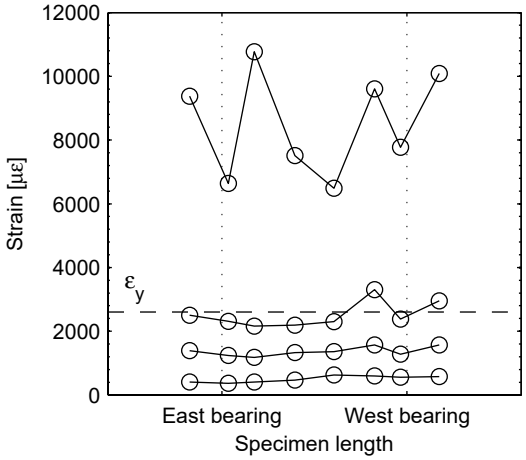

(c) Strains of vertical bars V1

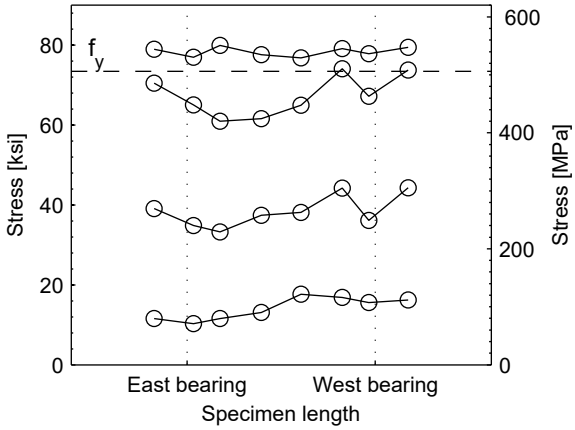

(d) Stresses of vertical bars V1

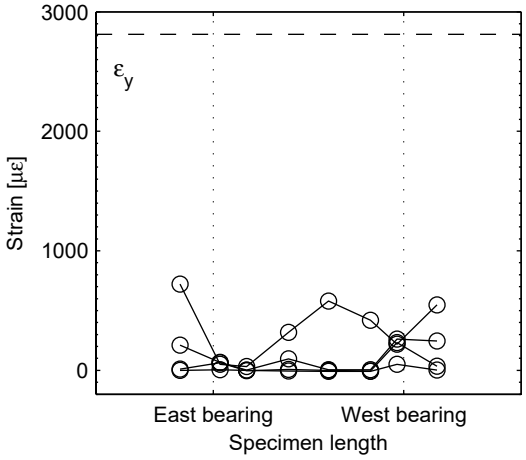

(e) Strains of vertical bars V5

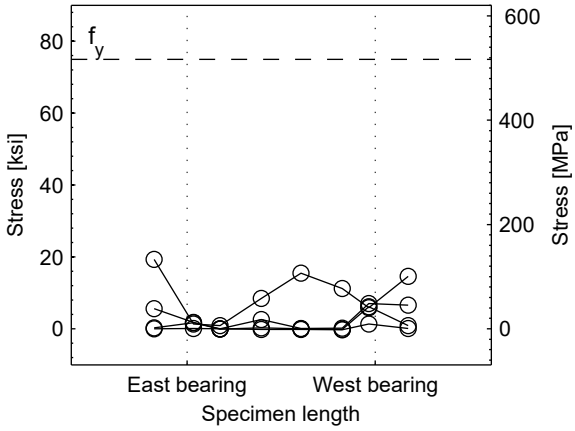

(f) Stresses of vertical bars V5

Fig. 6.19 Stresses and strains of vertical and horizontal reinforcing bars throughout in-span hinge length at 25%, 50%, 75%, and 100% of peak load of specimen S3.

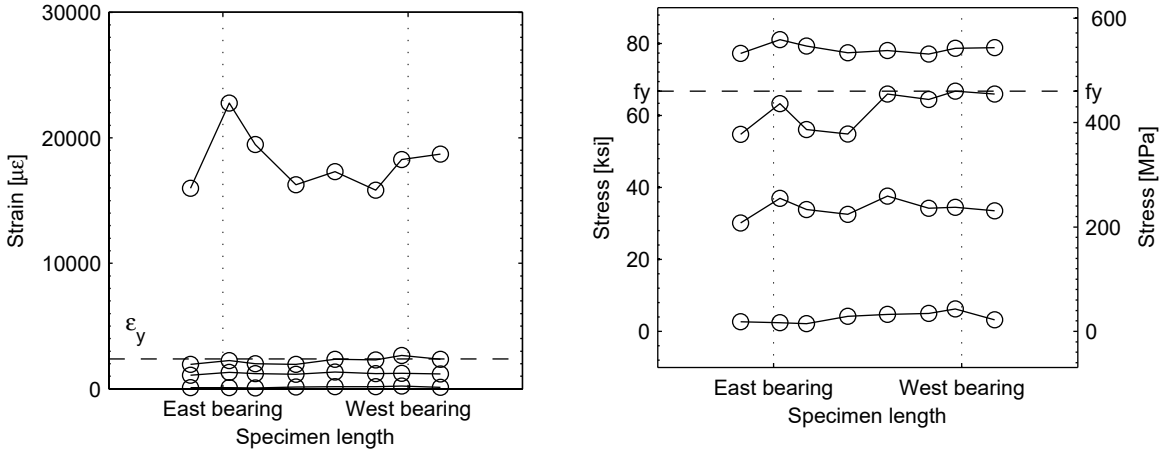

(a) Strains of horizontal bar B5 (b) Stresses of horizontal bar B5

Fig. 6.20 Stresses and strains of diaphragm reinforcing bars throughout in-span hinge length at 25%, 50%, 75%, and 100% of peak load of specimen S3.

6.7 SPECIMEN S4 TEST RESULTS

The experimental results of specimen S4 are presented in this section. Specimen S4 was a new design that considered low reinforcement ratios to improve the constructability and the structural performance, providing uniform strengths for the different failure modes. The geometry of specimen S4 was identical to specimen S1 as they did not have any utility openings. It is to be noted that results shown as envelopes of the cyclic loading are consistent with the envelope of the global force-displacement relationship.

6.7.1 General Observations

Equivalent to the first three specimens, the initial crack appeared near the seat corner with the diaphragm at 0.08" (2.0 mm) peak displacement cycle, as indicated by the arrow in Figure 6.21a. At this displacement, the specimen load was 107 kip (476 kN). At 0.11" (2.8 mm) peak displacement cycle, vertical (in the test orientation) bending cracks appeared behind the bearing plates, as shown in Figure 6.21b. At this displacement, the specimen load was 147 kip (654 kN). The first diagonal crack appeared at the 0.2" (5.1 mm) peak displacement in the seat behind the bearing plates, as shown in Figure 6.21c. The angle of inclination of this crack was 45° as was also observed in specimens S1 and S2. Additionally, a horizontal (in the test orientation) bending

crack appeared at the seat in the bearing side as shown in Figure 6.21d. This horizontal crack was different from the crack pattern observed in specimen S1, which was characterized by diagonal cracks. The damage propagation for the 0.4" peak displacement cycle is shown in Figures 6.21e and f.

When reaching the maximum strength of the specimen, the deformation and damage concentrated at the west side of the specimen. On this side, the width of the vertical (in the test orientation) cracks increased considerably, measuring up to 0.08" (2.0 mm). Subsequently, a horizontal (in the test orientation) crack appeared at the top of the seat between the two bearing plates and finally a vertical (in the test orientation) punching shear crack appeared in the middle of the specimen, as shown in Figure 6.21g. At this load level, increase of the width of the vertical (in the test orientation) crack in the seat located behind the bearing plate occurred because of the lower longitudinal reinforcing steel provided at the seat.

Finally, a combined mode of failure of 1D shear and punching shear was observed in the west bearing. Figure 6.21h shows a top view of the west bearing region with punching shear cracks oriented toward only the middle of the specimen. Additionally, the figure shows anchorage failure of the vertical (horizontal in the test orientation) bars at the end of the seat that were used to resist the punching shear.

The test of specimen S4 was terminated at about 2" (50.8 mm) displacement. At this displacement level, fracture of bars in tension was observed in some diagonal bars of the west side. At this displacement, the total force was reduced to about 16% of the maximum strength. Additionally, rotation of the loading beam was observed toward the west side due to the differential displacements of the two bearings caused by the concentration of damage in the vicinity of the west bearing.

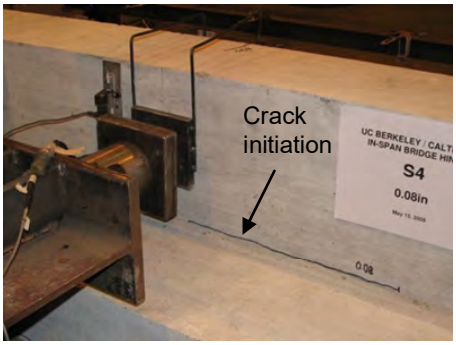

(a) Crack initiation at 0.08" (2.0 mm), east side

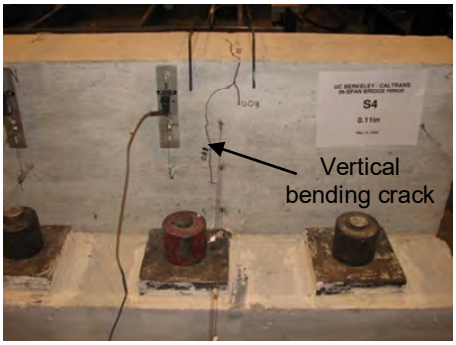

(b) Bending crack at 0.11" (2.8 mm), west side

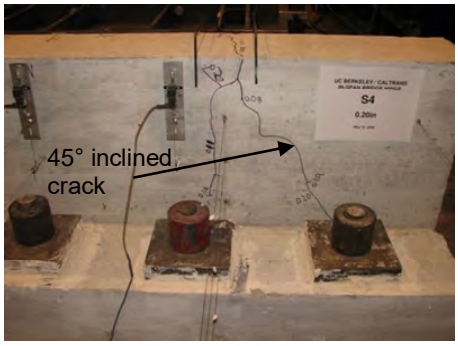

(c) 0.2" (5.1 mm) displacement, west side

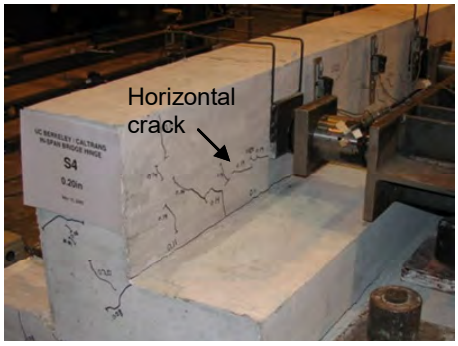

(d) 0.2" (5.1 mm) displacement, west side

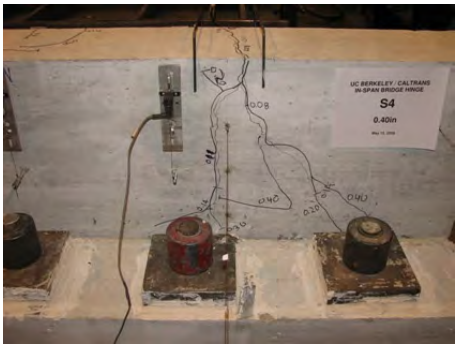

(e) 0.4" (10.2 mm) displacement, west side

(f) 0.4" (10.2 mm) displacement, west side

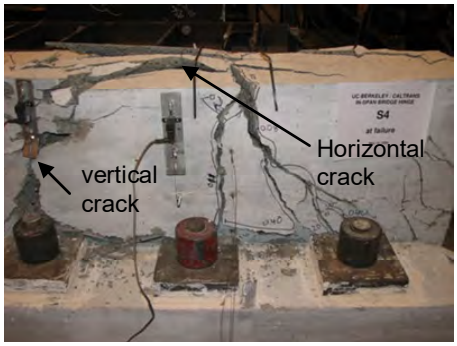

(g) At failure, west side

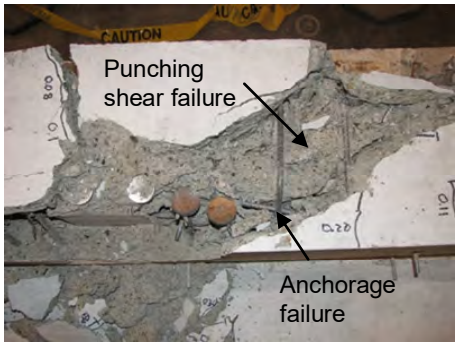

(h) At failure, top view of west bearing region

Fig. 6.21 Damage propagation during test of specimen S4.

6.7.2 Load-Displacement Relationships

The applied load-displacement relationship of specimen S4 is shown in Figure 6.22. The displacement was measured with the built in actuator transducer, and the load corresponded to the sum of the two load cells attached to the loading beam. The peak total load of 380 kip (1690 kN) was achieved at 0.36" (9.1 mm) displacement. This strength was 19% smaller than that of specimen S1, where both specimens did not contain utility openings. This reduction in strength was caused by the lower reinforcement ratio of specimen S4 compared to S1. After the peak load was achieved, the relationship shows a rapid decrease in the capacity and the strength was provided mainly by the tensile force of the diagonal bars, the friction of the shear mechanism and the dowel action of the horizontal bars (vertical in the test orientation).

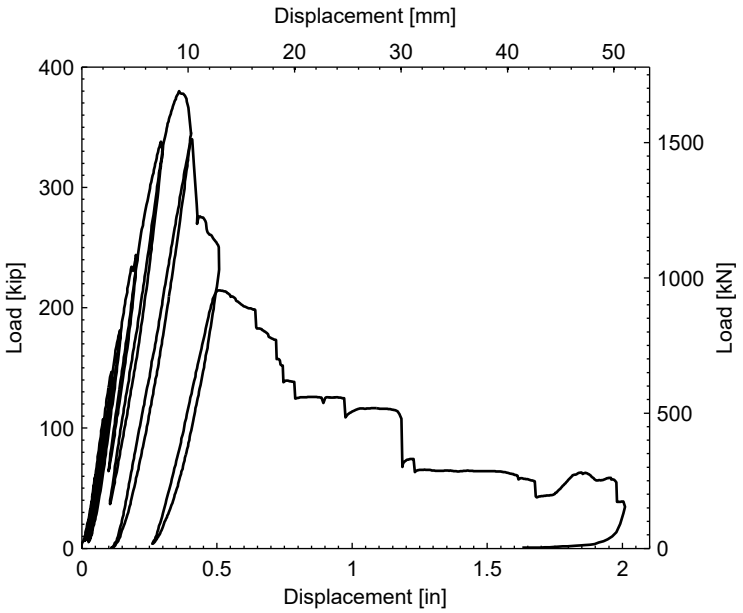

Fig. 6.22 Load-displacement of specimen S4.

The load-displacement relationships at both bearings are shown in Figure 6.23. The figure shows the responses using the displacement of the concrete seat, measured with the instruments SHT2 and SHT4 (Fig. 3.11) for the east and west sides, respectively. The relationships show that the east bearing did not fail during the test, since the east deformation decreased when the west bearing started to fail. The decrease of the east deformation was due to the lower load that was applied by the system caused by the failure observed on the west side.

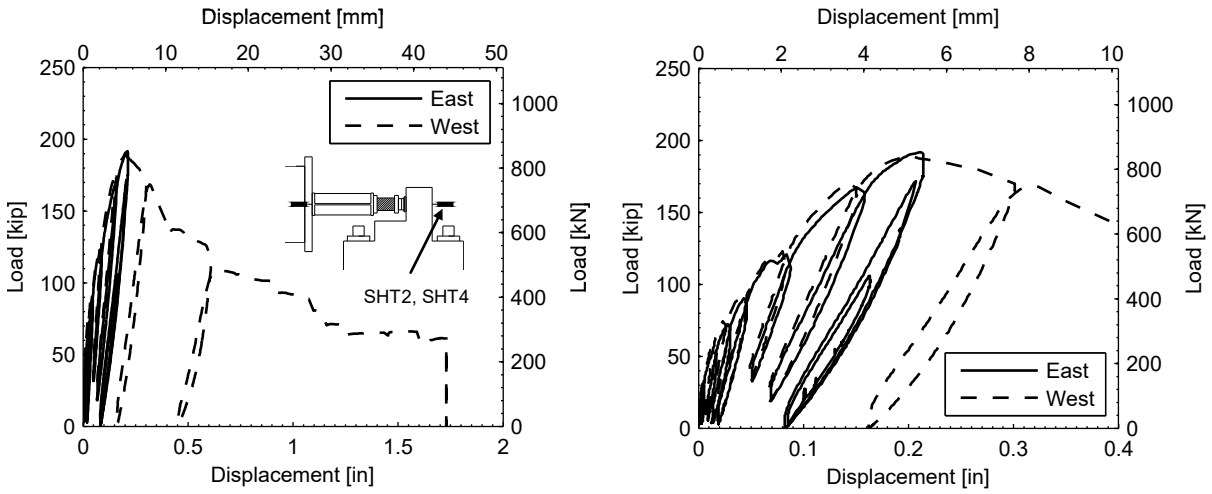

(a) Concrete displacement (b) Zoom of concrete displacement

Fig. 6.23 Load-displacement at bearings of specimen S4.

The maximum strengths of the east and west bearings were 192 kip (854 kN) and 190 kip (845 kN), respectively. The corresponding displacements at the peak loads were 0.20" (5.1 mm) for both bearings. This displacement was 43% smaller than that observed in specimen S1. The initial stiffnesses considering the concrete seat displacement were 4124 kip/in. (722 kN/mm) and 4943 kip/in. (866 kN/mm) for the east and west bearings, respectively. These values correspond to secant stiffness computed using a 50 kip (22 kN) load.

6.7.3 Seat Deformation Profiles

The seat deformation profile along the in-span hinge length (horizontal deformation of the seat in the test position) is shown in Figure 6.24a. The figure shows the displacement at 50%, 75%, and 100% of the maximum specimen load. The displacement profile was measured with five instruments, where the instruments SHT2 and SHT4 corresponded to the cross sections of the east and west bearings, respectively. The figure shows that the displacements at the two bearing cross sections were almost identical for the three load levels. For 75% of the maximum load, the displacements measured with the instruments at the edges and at the middle represented 42% and 64% of the displacement measured at the two bearings. This deformation profile suggested that the load was resisted mainly by the regions of the seat located in the vicinity of the bearings.

The displacement profile along the specimen height at the two bearing cross sections is shown in Figure 6.24b. The figure shows the displacement at 50%, 75%, and 100% of the

maximum specimen load. This horizontal displacement (in the test orientation) was measured with top (T), middle (M), and bottom (B) displacement transducers. The exact location of these instruments is shown in Chapter 3. Figure 6.24b shows a linear displacement variation along the height, which implies a shear deformation profile of the specimen. In contrast, a bending deformation profile is characterized by a cubic displacement variation along the height. This is analogous to specimens S1 and S2.

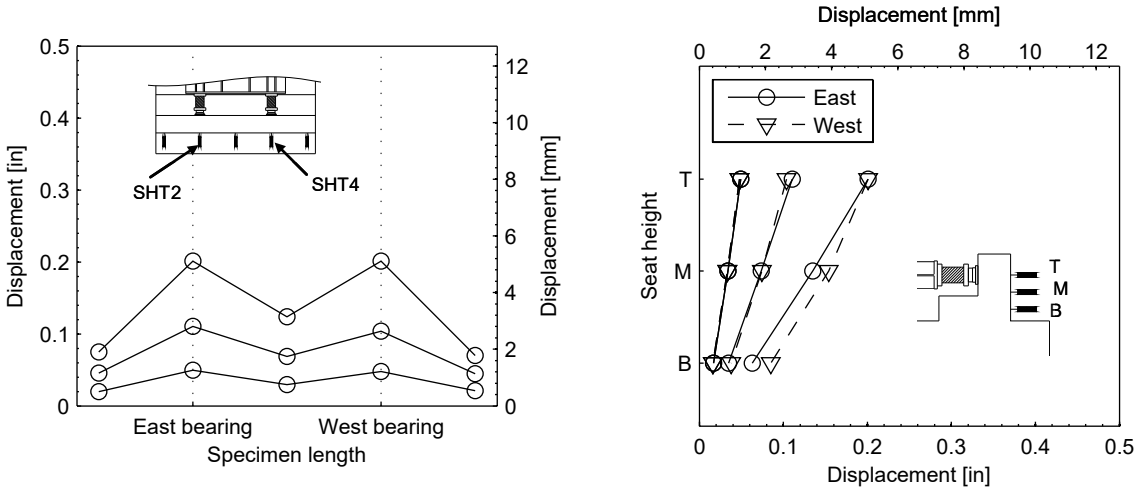

(a) Displacement profile along specimen length

(b) Displacement profile along specimen height, at the bearing cross sections

Fig. 6.24 Seat deformation profiles at 50%, 75%, and 100% of peak load of specimen S4.

6.7.4 Reinforcing Steel Behavior

The strains on the reinforcing steel bars of specimen S4 were measured with a total of 50 strain gages. The details of the reinforcement and the location of the most important strain gages are shown in Figure 6.25. From the strain measurements, reinforcing bar stresses were computed using the stress-strain relationships obtained from the reinforcing bar material tests (Fig. 6.6).

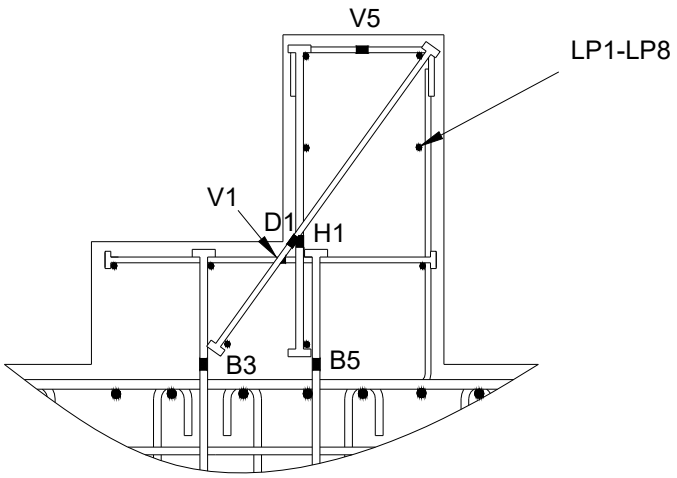

Fig. 6.25 Strain gage locations in specimens S4 and S5 (in test orientation).

The relationships of the envelopes of the reinforcement stresses versus the applied load, at both bearing cross sections (east and west), are shown in Figure 6.26. The figure shows that yielding initiated in diagonal bar D1 (Fig. 6.26a) located at the seat, which yielded at an applied load of 242 kip (1076 kN). This initial yielding was consistent with crack initiation near the seat corner with the diaphragm.

Figure 6.26b shows that the second bar that reached yielding after diagonal bar D1 was the horizontal (vertical in the test orientation) bar at H1, which yielded at an applied load of 286 kip (1272 kN). Unlike specimen S1, this bar yielded before the vertical (horizontal in the test orientation) bar V1 because of the lower bending capacity of the seat in specimen S4 compared to specimen S1.

The stresses of the vertical bars (horizontal in the test orientation) are shown in Figure 6.26c. The figure shows that the vertical bars at the locations V1 reached yielding stress at an applied load of 355 kip (1579 kN). At this larger load, the diagonal and vertical bars were yielding, which corresponded to the development of the SAT mechanism. The strain gage V5 at the vertical bar (horizontal in the test orientation) was installed to determine punching shear behavior. Figure 6.26c shows negligible stresses in these vertical bars, V5, because it was found that these bars at the bearing cross sections were not located in the punching shear failure surface.

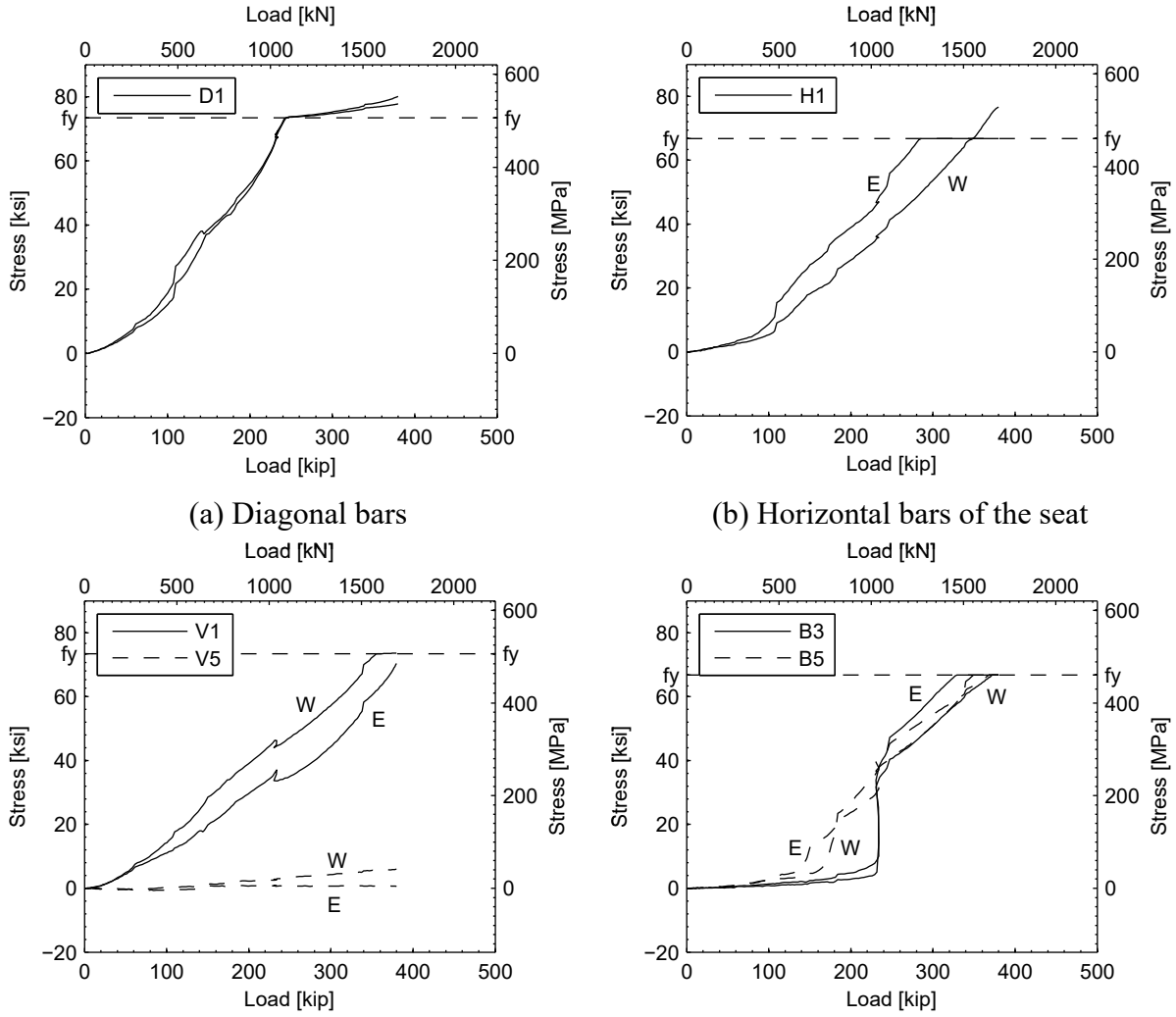

(a) Diagonal bars

(b) Horizontal bars of the seat

(c) Vertical bars

(d) Horizontal bars of the diaphragm

Fig. 6.26 Stresses in reinforcement at bearing cross sections versus applied load of specimen S4.

The stresses in the horizontal bars (vertical in the test orientation) of the diaphragm are shown in Figure 6.26d. The figure shows that yielding occurred in both horizontal bars, B3 and B5, contrary to observations of specimen S1, where only the B5 bar yielded due to the excess of reinforcement in the diaphragm of specimen S1 compared to specimen S4.

The stress of the longitudinal bar located at the bottom part of the seat (in the prototype orientation) was measured with eight strain gages (LP1-LP8) located in the vicinity of the bearings. The stress distribution in this bar is shown in Figure 6.27 for 25%, 50%, 75%, and 100% of the maximum applied load. The stress distribution shows bending action of the seat about the direction perpendicular to the diaphragm. This bending behavior agrees with the

observed seat deformation profile and with the vertical (in the test orientation) bending cracks shown in Figure 6.21b.

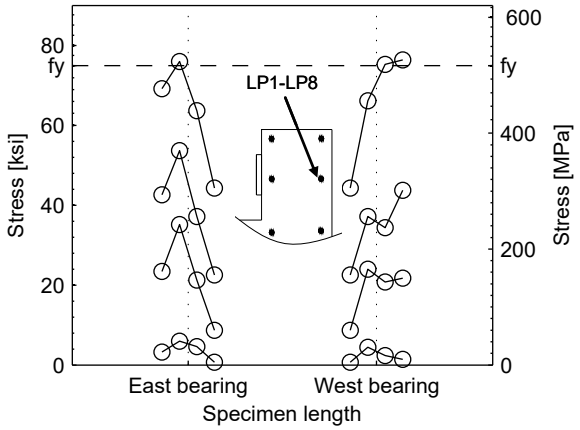

Fig. 6.27 Stress distribution of longitudinal bar at 25%, 50%, 75%, and 100% of peak load of specimen S4.

The distribution of strains and stresses in the reinforcing bars throughout the specimen length are shown in Figures 6.28–6.30 for 25%, 50%, 75%, and 100% of the maximum applied load. The locations of the bars with their strain gages are shown in Figure 6.25. From the test results, the larger strains were observed in diagonal bars D1 of the seat. The strains and stresses distribution of this bar are shown in Figures 6.28a and b, respectively. It can be observed that a peak strain of 11000 $\mu\varepsilon$ (1.1%) was measured in the vicinity of the west bearing at the maximum applied load. This strain corresponded to 38% of the maximum strain measured in specimen S1. The stress distribution shows that the stresses of these diagonal bars were concentrated in the vicinity of the bearings for 25% and 50% of the maximum load. At these low load levels, an effective seat length parallel to the diaphragm axis can be considered to resist the applied load, whereas when the maximum strength of the in-span hinge was achieved, yielding was spread throughout the whole seat length and an effective seat length was not observed.

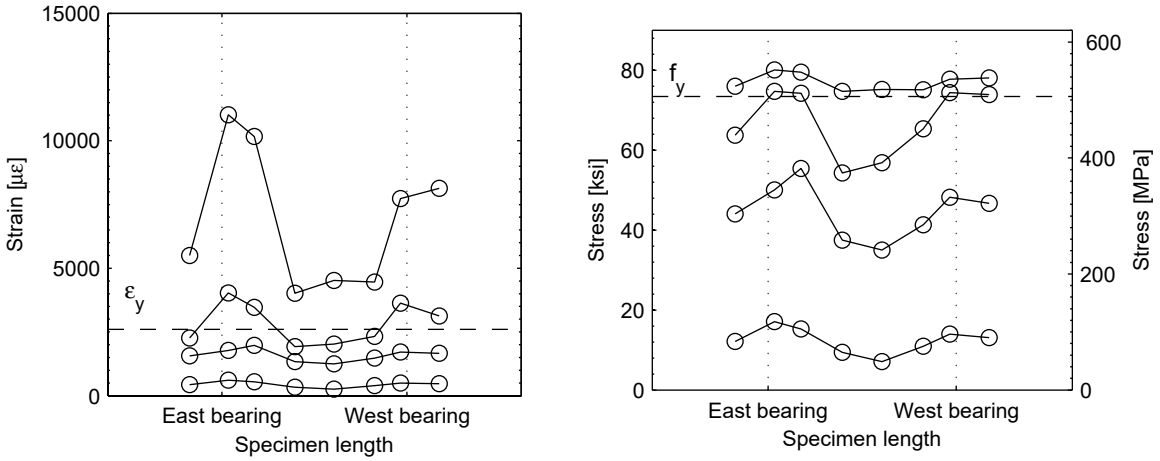

(a) Strains of diagonal bars at D1 (b) Stresses of diagonal bars D1

Fig. 6.28 Stresses and strains of diagonal reinforcing bars throughout in-span hinge length at 25%, 50%, 75%, and 100% of peak load of specimen S4.

The strains and stresses of the horizontal (vertical in the test orientation) bars H1 and vertical (horizontal in the test orientation) bars V1 are shown in Figures 6.29a–d. The stresses of these horizontal and vertical bars were concentrated in the vicinity of the bearings. In contrast to specimen S1, the horizontal (vertical in the test orientation) bars H1 showed more stresses than the vertical (in the test orientation) bars V1 because of the lower bending capacity provided to specimen S4. The strain stresses of the vertical (horizontal in the test orientation) bars V5 of the seat are shown in Figures 6.29e–f. The peak stress of 50 ksi (345 MPa) of these bars agreed with the punching shear crack observed at the west bearing. This bar did not yield due to the anchorage premature failure shown in Figure 6.21h. Finally, the distributions of strains and stresses of the horizontal bars (vertical in the test orientation) of the diaphragm are shown in Figures 6.30a and b, respectively. These distributions suggest that the load was mainly resisted by the regions located in the vicinity of the bearings.

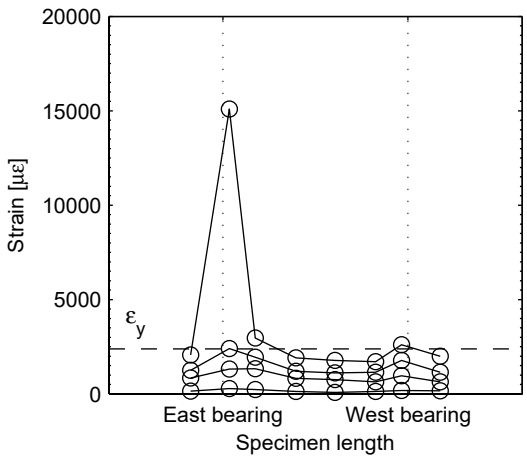

(a) Strains of horizontal bars H1

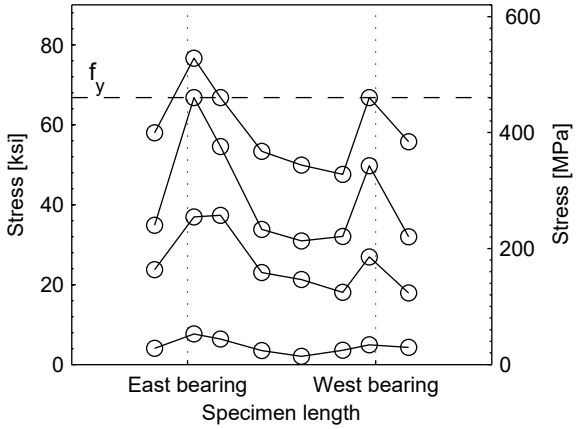

(b) Stresses of horizontal bars H1

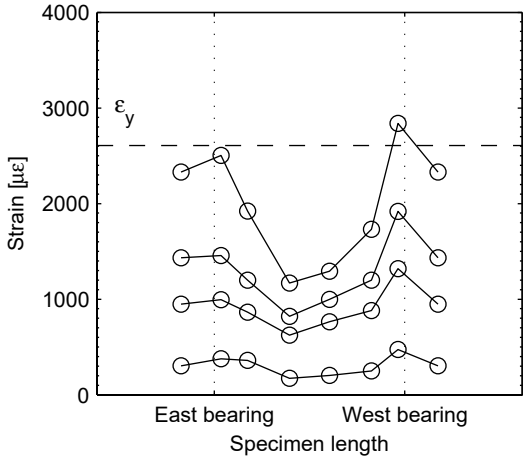

(c) Strains of vertical bars V1

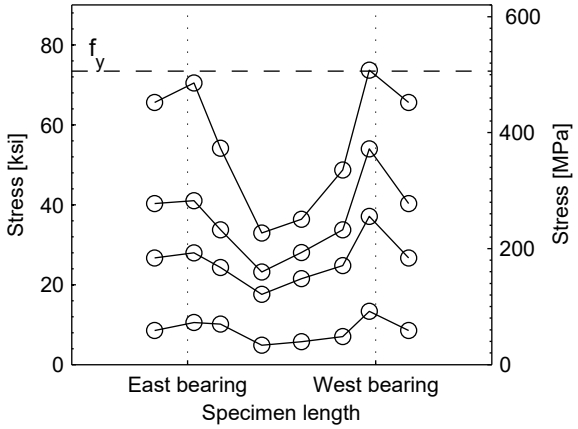

(d) Stresses of vertical bars V1

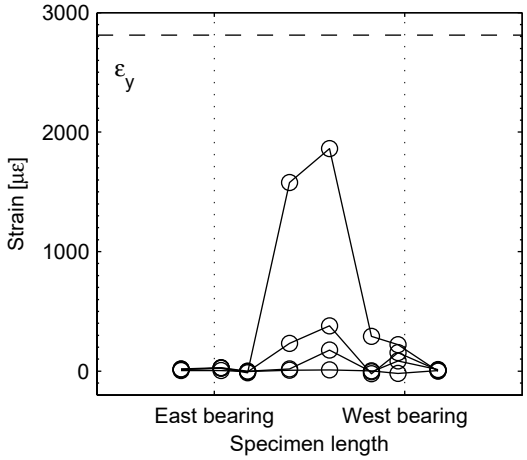

(e) Strains of vertical bars V5

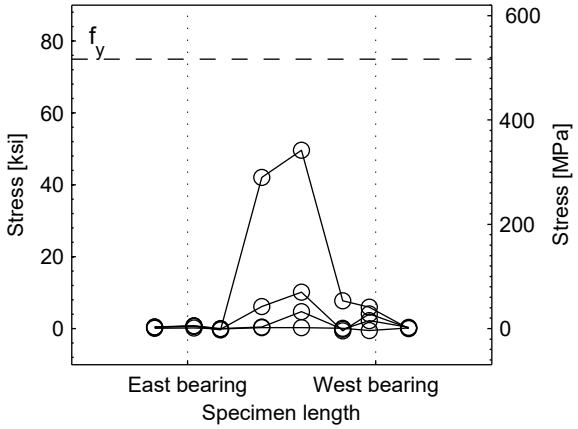

(f) Stresses of vertical bars V5

Fig. 6.29 Stresses and strains of vertical and horizontal reinforcing bars throughout in-span hinge length at 25%, 50%, 75%, and 100% of peak load of specimen S4.

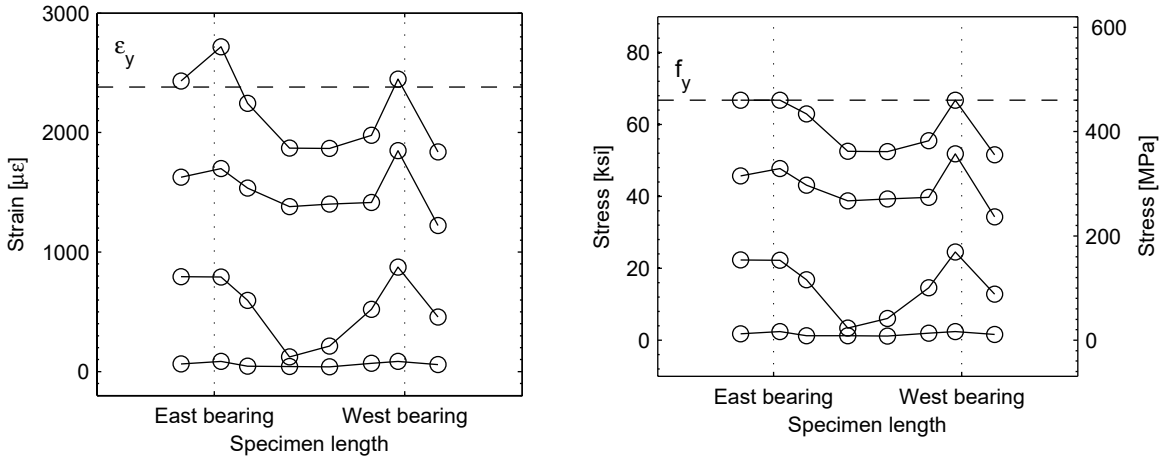

(a) Strains of horizontal bar B5 (b) Stresses of horizontal bar B5

Fig. 6.30 Stresses and strains of diaphragm reinforcing bars throughout the in-span hinge length at 25%, 50%, 75%, and 100% of peak load of specimen S4.

6.8 SPECIMEN S5 TEST RESULTS

The experimental results of specimen S5 are presented in this section. Specimen S5 was identical to specimen S4 but included utility openings, similar to specimens S2 of phase I. It is to be noted that the results shown as envelopes of the cyclic loading are consistent with the envelope of the global force-displacement relationship.

6.8.1 General Observations

Equivalent to the first four specimens, the initial crack appeared near the seat corner with the diaphragm at 0.08" (2.0 mm) peak displacement cycle, as indicated by the arrow in Figure 6.31a. At this displacement, the specimen load was 63 kip (280 kN). At 0.11" (2.8 mm) peak displacement cycle, vertical (in the test orientation) bending cracks appeared behind the bearing plates as shown in Figures 6.31b–c. At this displacement, the specimen load was 111 kip (494 kN). At the 0.2" (5.1 mm) peak displacement cycle and similar to specimen S4, a horizontal crack (in the test orientation) appeared near the seat at the bearing side as shown in Figure 6.31d. This horizontal crack (similar to specimen S2) was different from the crack pattern observed in specimen S1 which was characterized by diagonal cracks. The damage propagation for the 0.4" peak displacement cycle is shown in Figure 6.31e.

When reaching the maximum strength of the specimen, the deformation and damage concentrated at the west side of the specimen. On this side, the width of the vertical (in the test orientation) cracks increased considerably measuring up to 0.07" (1.8 mm). Subsequently, a combined 1D shear and punching shear failure mode was observed in the west bearing. For this specimen, the 1D shear crack of the seat was extended to the free end of the specimen as shown in Figure 6.31f. This shear failure plane is also shown in Figure 6.31g. The punching shear failure occurred in the west bearing toward the middle of the specimen, as shown in Figure 6.31h. Additionally, anchorage failure was observed for the vertical (horizontal in the test orientation) bars at the end of the seat that were used to resist the punching shear.

The test was terminated at about 2" (50.8 mm) displacement. At this displacement level, fracture of bars in tension was observed in some diagonal bars at the west side, and the total force was reduced to about 20% of the maximum strength. Additionally, rotation of the loading beam was observed toward the west side due to the differential displacements of the two bearings caused by the concentration of damage in the vicinity of the west bearing.

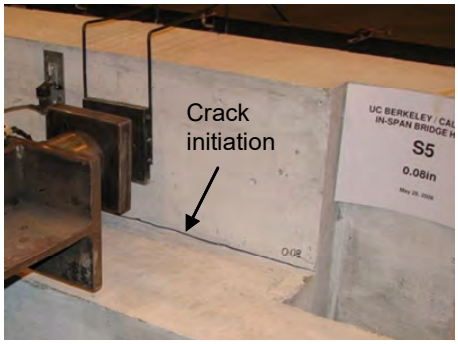

(a) Crack initiation at 0.08" (2.0 mm), east side

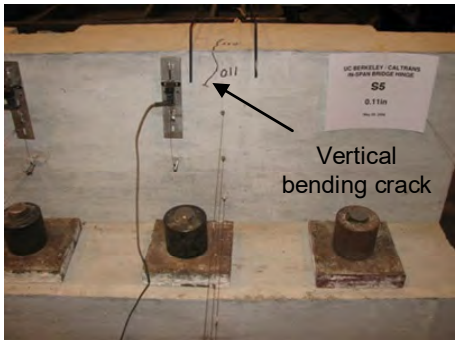

(b) Bending crack at 0.11" (2.8 mm), west side

(c) 0.2" (5.1 mm) displacement, west side

(d) 0.2" (5.1 mm) displacement, west side

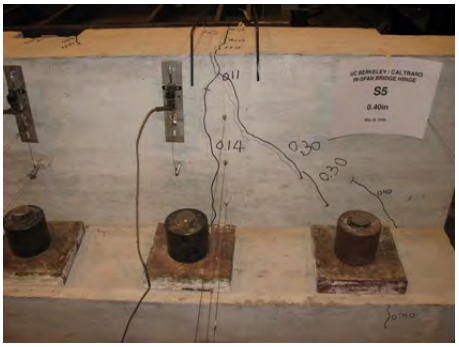

(e) 0.4" (10.2 mm) displacement, west side

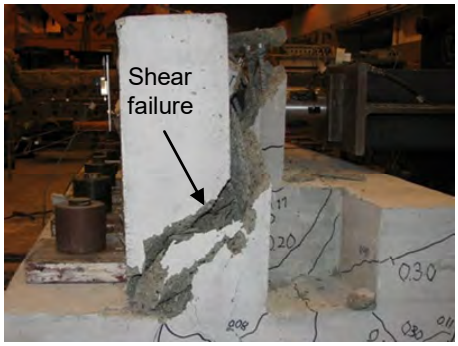

(f) At failure, west side

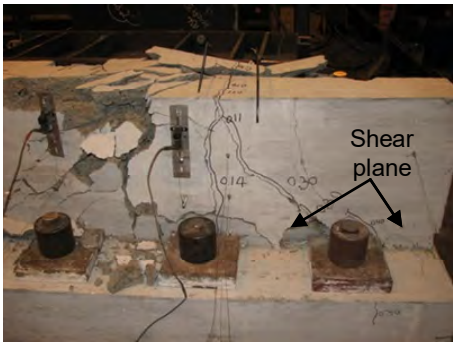

(g) At failure, west side

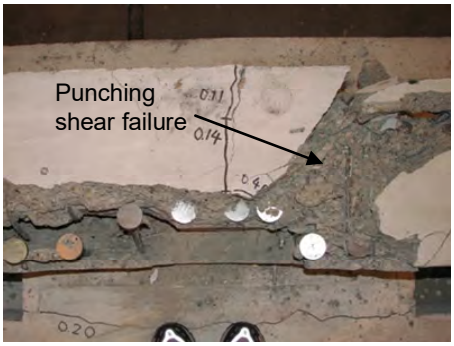

(h) At failure, top view of west bearing region

Fig. 6.31 Damage propagation during test of specimen S5.

6.8.2 Load-Displacement Relationships

The applied load-displacement relationship of specimen S5 is shown in Figure 6.32. The displacement was measured with the built in actuator transducer, and the load corresponded to the sum of the two load cells attached to the loading beam. The peak total load of 384 kip (1708 kN) was achieved at 0.42" (10.7 mm) displacement. This strength was comparable to that of specimen S4 in spite of the presence of utility openings in specimen S5. After the peak load was achieved, the relationship shows a rapid decrease in the capacity and that the strength was provided mainly by the tensile force of the diagonal bars, the friction in the shear mechanism, and the dowel action of the horizontal (vertical in the test orientation) bars.

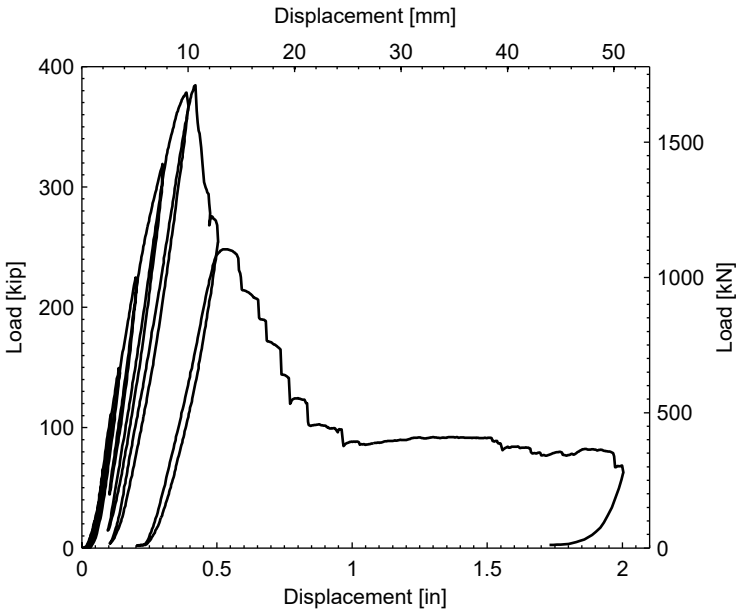

Fig. 6.32 Load-displacement of specimen S5.

The load-displacement relationships at both bearings are shown in Figure 6.33. The figure shows the responses using the displacement of the concrete seat, measured with the instruments SHT2 and SHT4 (Fig. 3.11) for the east and west sides, respectively. The relationships show that the east bearing did not fail during the test, since the east deformation decreased when the west bearing started to fail. The decrease of the east deformation was due to the lower load that was applied by the system caused by the punching shear failure observed on the west side.

The maximum strengths of the east and west bearings were 196 kip (872 kN) and 189 kip (841 kN), respectively. The corresponding displacements at the peak loads were 0.24" (6.1 mm) for both bearings. This displacement was 23% smaller than that observed in specimen S2. The initial stiffnesses considering the concrete seat displacement were 6250 kip/in. (1095 kN/mm) and 4576 kip/in. (801 kN/mm) for the east and west bearings, respectively. These values correspond to secant stiffness computed using a 50 kip (22 kN) load.

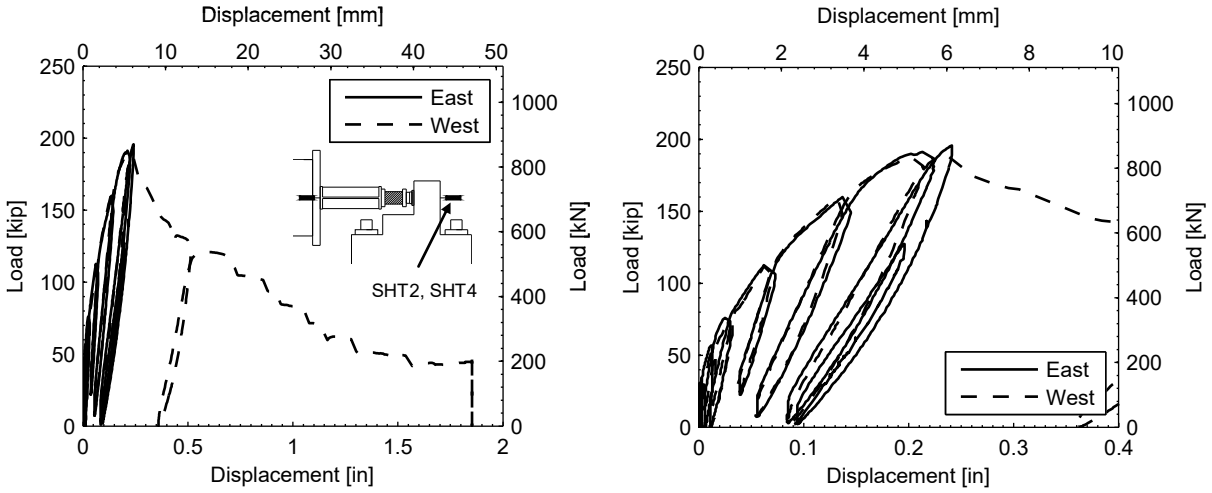

(a) Concrete displacement (b) Zoom of concrete displacement

Fig. 6.33 Load-displacement at bearings of specimen S5.

6.8.3 Seat Deformation Profiles

The seat deformation profile along the in-span hinge length (horizontal deformation of the seat in the test position) is shown in Figure 6.34a. The figure shows the displacement at 50%, 75%, and 100% of the maximum specimen load. The displacement profile was measured with five instruments, where the instruments SHT2 and SHT4 corresponded to the cross sections of the east and west bearings, respectively. The figure shows that the displacements at the two bearing cross sections were almost identical for the three load levels. For 75% of the maximum load, the displacements measured with the instruments at the edges and at the middle represented 56% and 72% of the displacement measured at the two bearings. This deformation profile suggested that the load was resisted mainly by the regions of the seat located in the vicinity of the bearings.

The displacement profile along the specimen height at the two bearing cross sections is shown in Figure 6.34b. The figure shows the displacement at 50%, 75%, and 100% of the

maximum specimen load. This horizontal displacement (in the test orientation) was measured with top (T), middle (M), and bottom (B) displacement transducers. The exact location of these instruments is described in Chapter 3. Figure 6.34b shows a linear displacement variation along the height, which implies a shear deformation profile of the specimen. In contrast, a bending deformation profile is characterized by a cubic displacement variation along the height. This result was also obtained in the first four specimens.

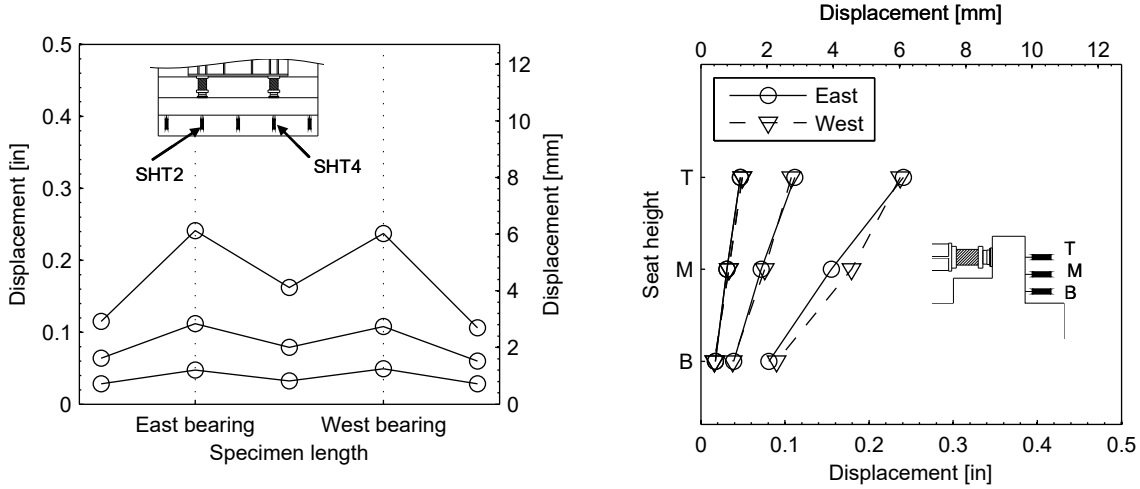

(a) Displacement profile along specimen length

(b) Displacement profile along specimen height, at the bearing cross sections

Fig. 6.34 Seat deformation profiles at 50%, 75%, and 100% of peak load of specimen S5.

6.8.4 Reinforcing Steel Behavior

The strains on the reinforcing steel bars of specimen S5 were measured with a total of 50 strain gages. The details of the reinforcement and the location of the most important strain gages are shown in Figure 6.25. From the strain measurements, reinforcing bar stresses were computed using the stress-strain relationships obtained from the reinforcing bar material tests (Fig. 6.6).

The relationships of the envelopes of the reinforcement stresses versus the applied load, at both bearing cross sections (east and west), are shown in Figure 6.35. The figure shows that yielding was initiated in diagonal bar D1 (Fig. 6.35a) located at the seat, which yielded at an applied load of 248 kip (1103 kN). This initial yielding was consistent with the crack initiation near the seat corner with the diaphragm.

Figure 6.35b shows that the second bar that reached yielding after diagonal bar D1 was the horizontal (vertical in the test orientation) bar at H1, which yielded at an applied load of 328

kip (1459 kN). As in specimen S4 but unlike specimens S1 and S2, this bar yielded before the vertical (horizontal in the test orientation) bar V1 because of the lower bending capacity of the seat in specimens S4 and S5 compared to specimens S1 and S2.

The stresses of the vertical (horizontal in the test orientation) bars are shown in Figure 6.35c. The figure shows that the vertical bars at the locations V1 reached yielding stress at an applied load of 346 kip (1539 kN). At this larger load, the diagonal and vertical bars were yielding, which corresponded to the development of the SAT mechanism. The strain gage V5 at the vertical (horizontal in the test orientation) bar was installed to determine punching shear behavior. Figure 6.35c shows negligible stresses in these vertical bars, V5, because it was found that these bars at the bearing cross sections were not located in the punching shear failure surface.

The stresses in the horizontal (vertical in the test orientation) bars of the diaphragm are shown in Figure 6.35d. The figure shows that yielding occurred in both horizontal bars, B3 and B5, contrary to observations of specimen S2, where only the B5 bar yielded due to the excess of reinforcement in the diaphragm of specimen S2 compared to specimen S5.

The stress of the longitudinal bar located at the bottom part of the seat (in the prototype orientation) was measured with 8 strain gages (LP1-LP8) located in the vicinity of the bearings. The stress distribution in this bar is shown in Figure 6.36 for 25%, 50%, 75%, and 100% of the maximum applied load. The stress distribution shows bending action of the seat about the direction perpendicular to the diaphragm. This bending behavior agrees with the observed seat deformation profile and with the vertical (in the test orientation) bending cracks shown in Figures 6.31b–c.

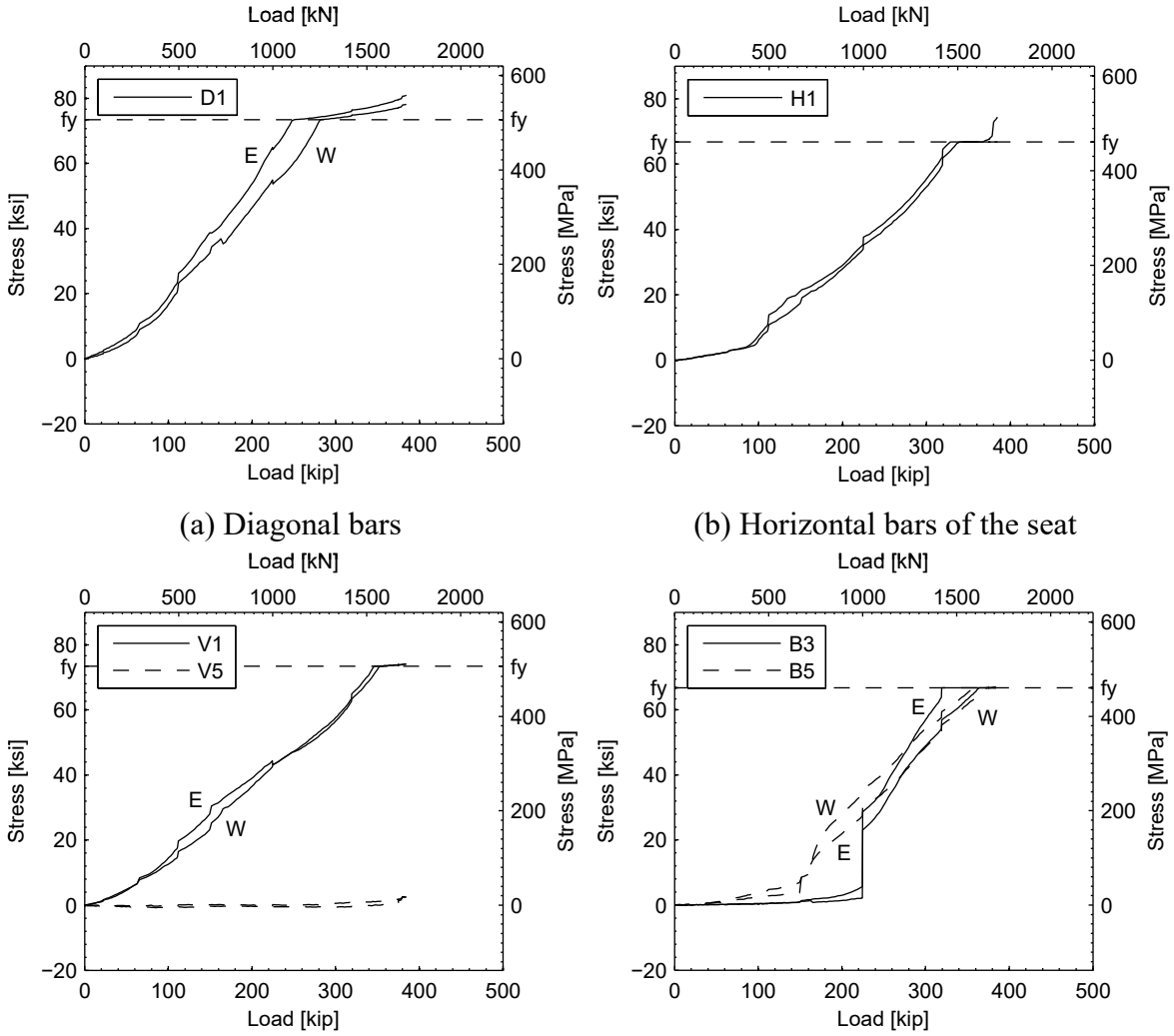

(a) Diagonal bars

(b) Horizontal bars of the seat

(c) Vertical bars

(d) Horizontal bars of the diaphragm

Fig. 6.35 Stresses in reinforcement at bearing cross sections versus applied load of specimen S5.

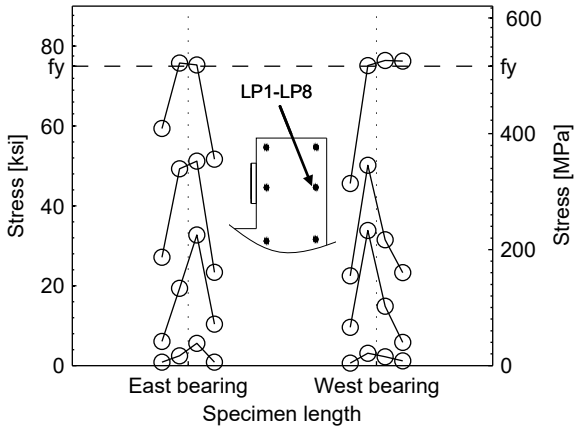

Fig. 6.36 Stress distribution of longitudinal bar at 25%, 50%, 75%, and 100% of peak load of specimen S5.

The distribution of strain and stresses in the reinforcing bars throughout the specimen length are shown in Figures 6.37–6.39 for 25%, 50%, 75%, and 100% of the maximum applied load. The locations of the bars with their strain gages are shown in Figure 6.25. From the test results, the larger strains were observed in diagonal bars D1 of the seat. The strain and stress distribution of this bar is shown in Figures 6.37a and b, respectively. It can be observed that a peak strain of 12400 $\mu\varepsilon$ (~1.2%) was measured in the vicinity of the west bearing at the maximum applied load. This strain corresponded to 45% of the maximum strain measured in specimen S2. The stress distribution shows that the stresses of these diagonal bars were concentrated in the vicinity of the bearings for 25% and 50% of the maximum load. At these low load levels, an effective seat length parallel to the diaphragm axis can be considered to resist the applied load, whereas when the maximum strength of the in-span hinge was achieved, yielding was spread throughout the whole seat length, and an effective seat length was not observed.

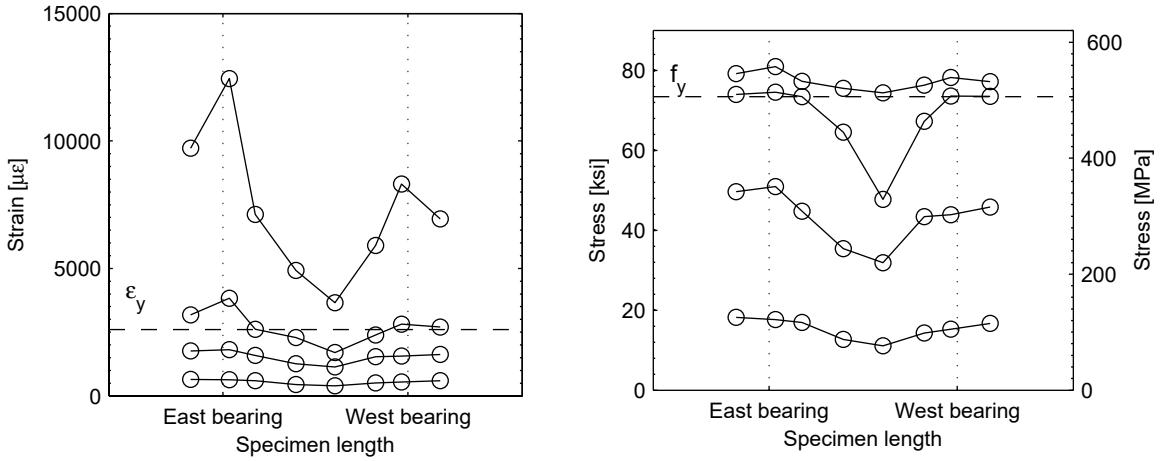

(a) Strains of diagonal bars D1 (b) Stresses of diagonal bars D1

Fig. 6.37 Stresses and strains of diagonal reinforcing bars throughout in-span hinge length at 25%, 50%, 75%, and 100% of peak load of specimen S5.

The strain and stresses of the horizontal (vertical in the test orientation) bars H1 and vertical (horizontal in the test orientation) bars V1 are shown in Figures 6.38a–d. The stresses of these horizontal and vertical bars are concentrated in the vicinity of the bearings. Contrary to specimen S2 and similar to specimen S4, the horizontal (vertical in the test orientation) bars H1 showed more stresses than the vertical (in the test orientation) bars V1 because of the lower bending capacity provided to specimen S5. The strain and stresses of the vertical (horizontal in the test orientation) bars V5 of the seat are shown in Figures 6.38e and f, respectively. The low peak stresses of about 20 ksi (138 MPa) of these bars disagreed with the punching shear failure mechanism observed in the west bearing because anchorage failure was detected for these bars, as shown in Figure 6.31h. Finally, the distributions of strain and stresses of the horizontal (vertical in the test orientation) bars of the diaphragm are shown in Figures 6.39a and b, respectively. These distributions suggest that the load was resisted throughout the whole seat length.

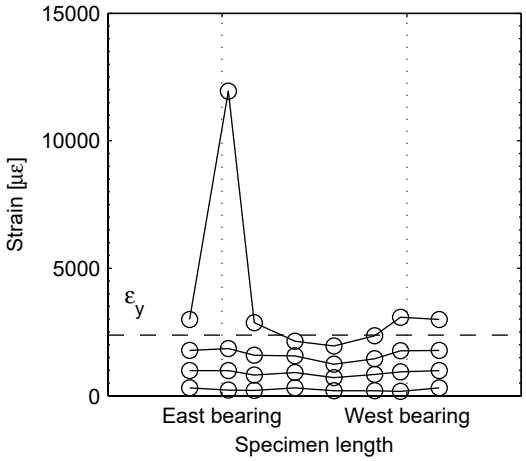

(a) Strains of horizontal bars H1

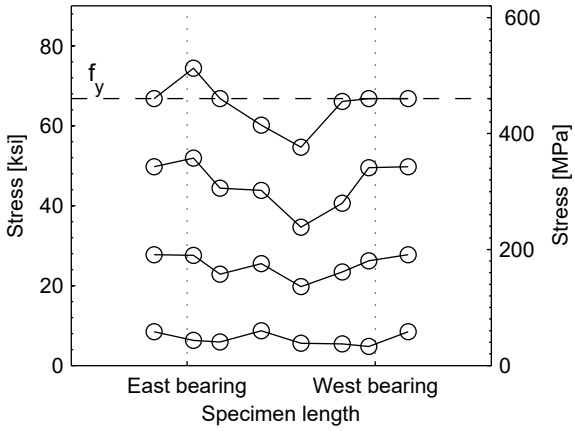

(b) Stresses of horizontal bars H1

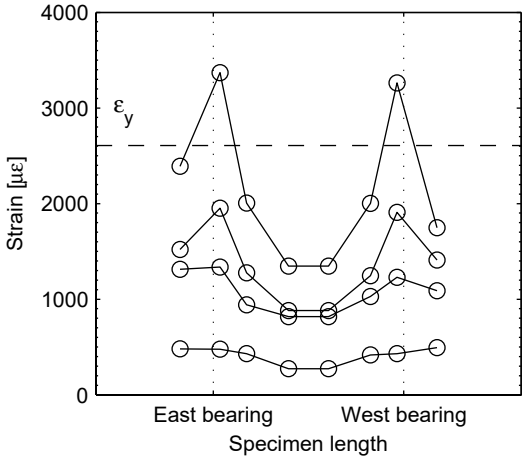

(c) Strains of vertical bars V1

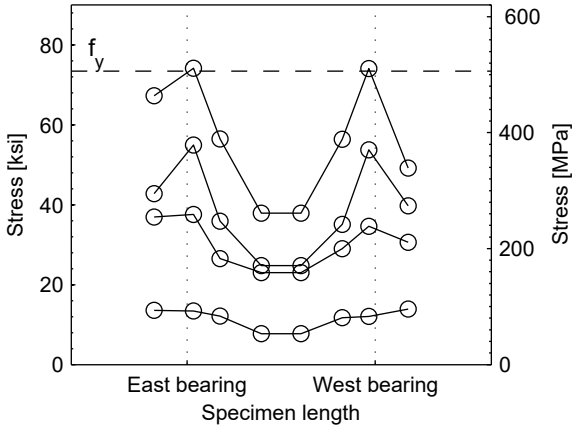

(d) Stresses of vertical bars V1

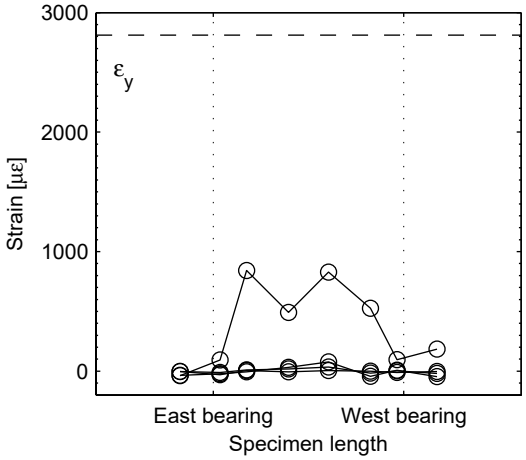

(e) Strains of vertical bars V5

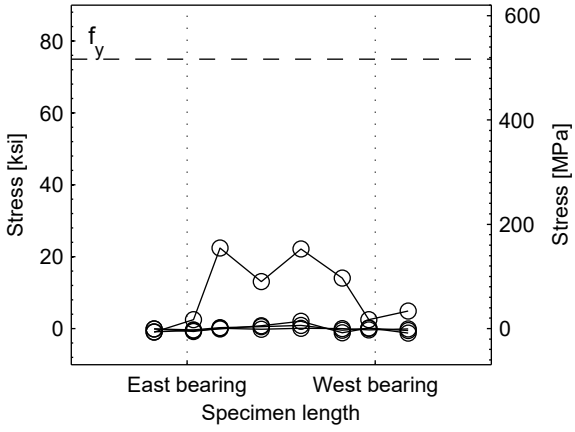

(f) Stresses of vertical bars V5

Fig. 6.38 Stresses and strains of vertical and horizontal reinforcing bars throughout in-span hinge length at 25%, 50%, 75%, and 100% of peak load of specimen S5.

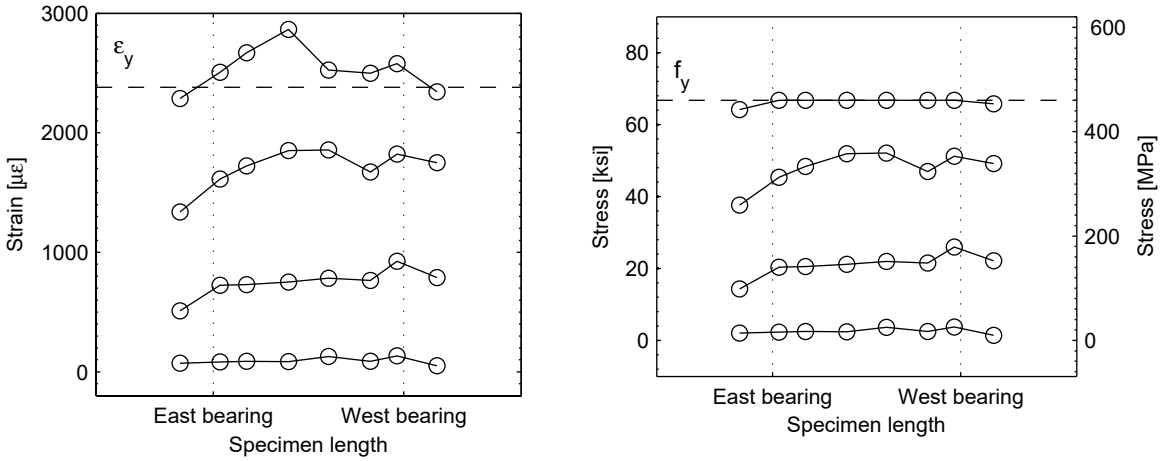

(a) Strains of horizontal bar B5 (b) Stresses of horizontal bar B5

Fig. 6.39 Stresses and strains of diaphragm reinforcing bars throughout in-span hinge length at 25%, 50%, 75%, and 100% of peak load of specimen S5.

6.9 CONCLUDING REMARKS ON NEW DESIGNS

The test results of specimens S3, S4, and S5 of phase II are summarized and compared with the results of phase I in Table 6.5. The comparison between the load-displacement relationships at the bearings for all the specimens is shown in Figure 6.40. The specimens of phase I corresponded to the as-built in-span hinges and the specimens of phase II corresponded to new designs.

From the test results of specimens S1 and S2, it can be concluded that the presence of utility openings of the as-built in-span hinges reduced the strength by 9% but did not affect the displacement at the maximum load, whereas from the test results of specimens S4 and S5, it can be concluded that the presence of utility openings did not affect the strength, but the displacement at the maximum load was increased by 20% for the case with utility openings. Therefore, the strength of the new designs of the in-span hinges is less sensitive to the presence of utility openings than that of the as-built in-span hinges. Additionally, Figure 6.40 shows that the effects of the utility openings on the shape of the load-displacement relationship and on the initial stiffness were negligible. This fact can be observed when comparing specimens S1 and S2, and specimens S4 and S5.

The design of specimen S3 was equivalent to specimen S2 but it was designed with larger bearing plates. This new design was aimed to increase the punching shear strength and also to produce a global 2D mode of failure that involved the whole in-span hinge. From Table 6.5, it

can be concluded that the larger bearing plates reduced the 3D effect of the discrete bearings, increasing the strength of the in-span hinge by 25.6%. Additionally, Figure 6.40 shows that the larger bearing plates of specimen S3 increased the ductility, by improving the strength degradation along the descending branch of the load-displacement relationship.

Table 6.5 Comparison of test results of all test specimens.

	Phase I		Phase II		
	S1	S2	S3	S4	S5
Specimen side that failed	west	Both	both	west	west
Specimen strength [kip (kN)]	467 (2077)	425 (1890)	535 (2380)	380 (1690)	384 (1708)
Average strength per bearing [kip (kN)]	233 (1036)	213 (947)	269 (1197)	191 (850)	193 (858)
Average bearing displacement at maximum load [in (mm)]	0.32 (8.1)	0.31 (7.9)	0.41 (10.4)	0.20 (5.1)	0.24 (6.1)
Initiation of yielding [% of maximum load]	48.0	44.2	48.6	63.7	64.6

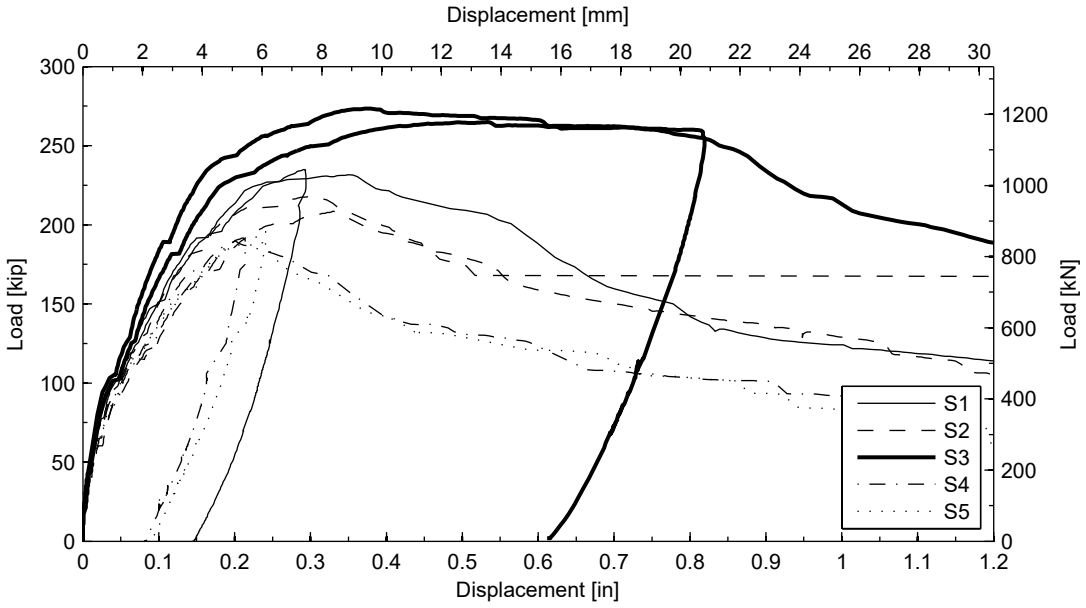

Fig. 6.40 Comparison of load-displacement at bearings of all test specimens.

The design of specimens S4 and S5 was a new design with a low reinforcement ratio aimed to improve the structural performance and constructability of in-span hinges. The new design contained 45% less steel reinforcement than the as-built specimens (specimens S1 and

S2) but the strength was reduced only by 19% and 10% for the cases without (S4 versus S1) and with (S5 versus S2) utility openings, respectively. However, the strength of the new design was about 2.8 times larger than the factored design load suggested by Caltrans. This improvement in the structural performance of the in-span hinge was achieved with an optimized design that eliminated the ineffective bars and considered a uniform and consistent strength of all the possible failure mechanisms. As a result, yielding of the first bar occurred at a larger load, specifically at 63.7% and 64.6% of the maximum load for specimens S4 and S5, respectively. Nevertheless, it is concluded that this new design (specimens S4 and S5) reduced the displacement at the maximum load by 30% when comparing with specimens S1 and S2. Finally, Figure 6.40 shows that the effects of the lower reinforcement ratio of the new design (specimens S4 and S5) on the initial stiffness and on the shape of the descending branch in the load-displacement relationship were negligible

The demand versus capacity (D/C) ratios of all the specimens is shown in Figure 6.41. The demand of the specimens was loosely defined as the maximum strength obtained from each test, and the capacity corresponded to the strength computed using design equations, refer to Chapter 2. From the test results of the five specimens, it can be concluded that the failure mode of in-span hinges was a combination of three modes: 1D shear, SAT, and punching shear. For specimens S1, S2, and S3, Figure 6.41 shows that these three failure modes were the critical ones. On the other hand, for specimens S4 and S5, Figure 6.41 shows that the bending moment at the seat and diaphragm were also critical because these specimens were designed with a uniform strength for all the failure modes. However, a bending failure mode was not fully observed from the tests of specimens S4 and S5.

It is concluded than the 2D SAT model was a lower bound of the capacity because the D/C ratio was larger than 1.0 in Figure 6.41 for all the specimens. The SAT capacity was lower than the demand because it neglected the contribution of the concrete in tension, which is speculated to contribute significantly to the strength of in-span hinges. The proposed SAT mechanisms were observed in all the test specimens because yielding of the bars corresponding to the ties was identified with the use of strain gages.

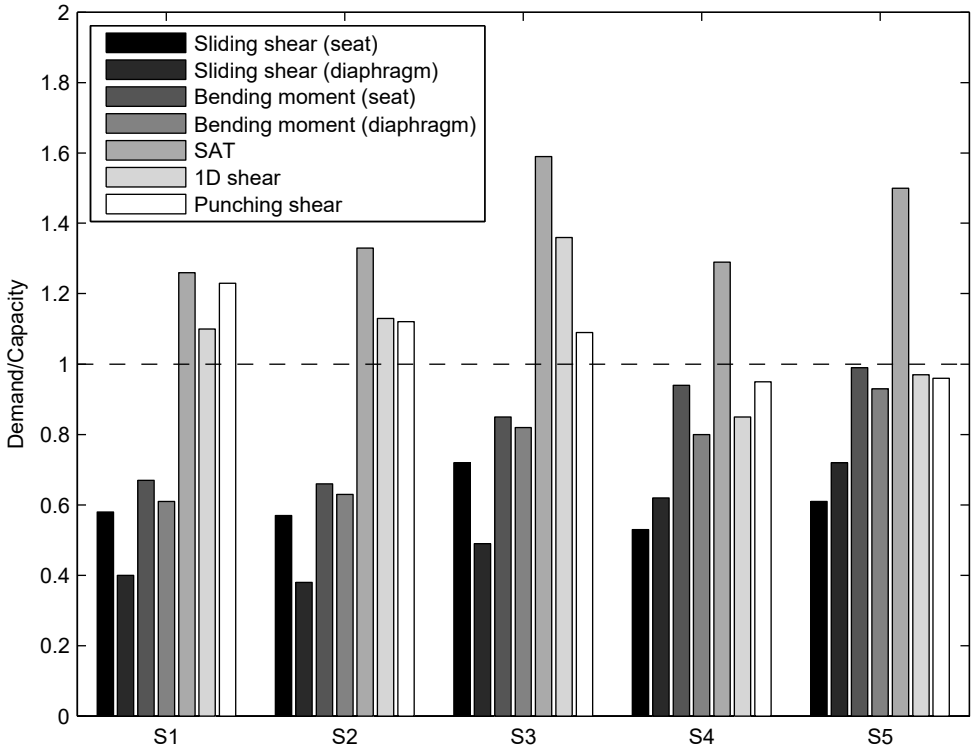

Fig. 6.41 Demand versus capacity ratio of all test specimens.

It can be concluded that the 1D shear and the punching shear modes were the ones that gave the best strength prediction of the in-span hinges. This fact agrees with the dominance of these modes in the previously mentioned combined mode of failure observed in the tests. For both of these failure modes, the first three specimens had D/C ratio larger than 1.0, and the last two specimens had a D/C ratio lower than 1.0. This difference can be attributed to the higher reinforcement ratio of the first three specimens that provided additional confinement to the concrete. For specimen S3, the D/C ratio of the 1D shear mode was significantly larger than that of the punching shear, which agrees with the global 1D shear failure mode mostly observed and induced by the larger bearing plates. In summary, and very important, is that 1D shear and punching shear failure modes have to be included in the design of new in-span hinges and in the evaluation of existing ones.

Finally, it is concluded that the D/C ratio of the sliding shear failure mode in both the diaphragm and the seat for all the tested specimens is smaller than 0.72. Therefore, this failure mode is unlikely to govern the behavior of existing and newly designed in-span hinges tested in this study.

7 Conclusions and Future Extensions

This report presented the results of an experimental program conducted on in-span hinges of prestressed concrete (PC) box-girder bridges in California. The experimental program consisted of five 1/3-scale specimens constructed and tested in two phases (I and II) at the University of California, Berkeley. The in-span hinges were loaded at the bearing locations to study the behavior and strength of these hinges when subjected to extreme vertical loads.

The representative characteristics of in-span hinges of PC box-girder bridges were determined from a survey of eight projects located in California. The in-span hinges are characterized by having congestion of steel reinforcement, where headed bars are usually specified. The use of headed bars in the in-span hinges is clearly appropriate to reduce reinforcement congestion for improving constructability and to provide adequate reinforcement development in the relatively small in-span hinge region.

7.1 FINITE ELEMENT PRE-TEST ANALYSIS

In-span hinges are subjected to complex three-dimensional (3D) loading conditions due to the discrete bearing locations, small aspect ratio of the seat, and the geometric discontinuities when utility openings exist. Therefore, a 3D nonlinear finite element analysis (FEA) was conducted to the first two specimens comprising phase I. The FEA was developed using trilinear brick elements for the concrete and embedded reinforcement. The nonlinear behavior of the concrete was modeled using the total strain concept with a rotating-crack model and considering linear tension softening. The FEA was intended to provide detailed results of the stress state, damage (cracking and crushing of concrete and yielding of reinforcement) initiation and propagation, and deformations experienced in the in-span hinges. This task was conducted prior to finalizing the test plans to confirm the capacity of the test setup and to properly select the location of instrumentation.

The predicted capacity from the pre-test FEA was about 10% lower than the experimental results, which is attributed to lower material strength properties used in the simulation. These FE models will be improved to match the experimental results of the five specimens in a future phase of this research project for the purpose of further computational parametric studies of the in-span hinge regions.

7.2 AS-BUILT IN-SPAN HINGES

Two specimens were built and tested in phase I of the experimental program. These specimens represented the as-built conditions of typical in-span hinges of California PC box-girder bridges. The difference between these two specimens was the presence of utility openings in specimen S2, while specimen S1 did not have any openings. These utility openings are used in box-girder bridges mainly to inspect the bearings located at the in-span hinges. These openings were introduced in specimen S2 to study their effect on the behavior and strength of in-span hinges.

From the experimental results of the as-built in-span hinges, it was concluded that they fail with a combination of three failure modes: (1) one-dimensional (1D) shear, (2) two-dimensional (2D) strut-and-tie (SAT), and (3) punching shear. Therefore, the design of in-span hinges must consider these failure modes and their combination, in addition to the bending and sliding shear modes typically considered in the design approach of short cantilevers followed in the design of in-span hinges. It was also concluded that the measured capacity of the in-span hinges was more than three times (exactly 3.2 times) larger than the factored design load suggested by Caltrans.

The current design of in-span hinges can be optimized based on the observed failure modes. The sliding shear capacities provided at the seat were 73% and 76% larger than the experimental capacities of specimens S1 and S2, respectively. At the diaphragm, the sliding shear capacities were 151% and 165% larger than the experimental capacities of specimens S1 and S2, respectively. It was concluded that the diaphragm and seat were over-reinforced for preventing sliding shear friction. Additionally, the bending capacities provided at the seat were 49% and 51% larger than the experimental capacities of specimens S1 and S2, respectively. At the diaphragm, the bending capacities were 54% and 68% larger than the experimental capacities of specimens S1 and S2, respectively. Therefore, it was concluded that the seat and diaphragm were over-reinforced for preventing bending failure.

Finally, from the test results of specimens S1 and S2, it can be concluded that the presence of utility openings of the as-built in-span hinges reduced the strength by 9%. However, these openings did not affect the displacement corresponding to the maximum load.

7.3 NEW DESIGN OF IN-SPAN HINGES

Three additional specimens were built and tested in phase II of the experimental program. The design of these specimens was based on the experimental results of the as-built in-span hinges in phase I. Specimen 3 was designed identical to specimen S2 but with larger bearing plates to increase the punching shear capacity. Specimen S4 (without openings analogous to specimen S1) and S5 (with openings analogous to specimen S2) were designed with low reinforcement ratios aiming to improve the performance and the constructability of the in-span hinges. The strength of these new designs was controlled by different combinations of the same three failure modes mentioned above, namely 1D shear, 2D SAT, and punching shear.

Specimen S3 was designed with larger bearing plates (233% wider plates for specimen S3 than specimen S2) to increase the punching shear strength, aiming at producing a global mode of failure that involves the whole in-span hinge. This new design represented the upper bound of an in-span hinge capacity because it reduced the 3D effect of the discrete bearings and produced a more global mode of failure. It was concluded that the larger bearing plates increased the strength by 26% and also increased the ductility by improving the rate of degradation of the strength along the descending branch of the load-displacement relationship.

Specimens S4 and S5 were designed with low reinforcement ratios aiming to improve the performance and constructability of the in-span hinges. The new design contained 45% less reinforcing steel than the as-built design, but the strength was reduced only by 19% and 10% for the cases without (specimen S4 compared to specimen S1) and with (specimen S5 compared to specimen S2) utility openings, respectively. It should be noted that the strength of the new design was almost than 3 times (exactly 2.8 times) larger than the factored design load suggested by Caltrans. This improvement in the performance of the in-span hinge was achieved with an optimized design that eliminated the ineffective reinforcing bars and considered a uniform and consistent strength of all the possible failure mechanisms. In fact, the bending strength, with its more ductile mode of failure than the three modes of failure mentioned above, also became critical.

From the test results of specimens S4 and S5 it can be concluded that the presence of utility openings did not affect the strength. Therefore, the strength of the proposed new design was less sensitive to the presence of utility openings than the as-built design of the in-span hinges.

From the test results of the five specimens, it was concluded that the 2D SAT model was a lower bound of the capacity because the demand to capacity ratio (D/C) was larger than 1.0 for all the test specimens. It is speculated that the SAT capacity was lower than the demand because in the used standard SAT model, the contribution of the concrete in tension (i.e., in the ties) was neglected, which contributed significantly to the strength of the in-span hinges, as evident from the preliminary FEA results.

It was concluded that the 1D shear and the punching shear design equations, based on the ACI318 recommendations, were the ones that gave the best strength prediction for in-span hinges with normal sized bearing plates. This fact agreed with the combined mode of failure observed in the in-span hinge tests of specimens S1, S2, S4, and S5, in contrast to the global 1D shear failure mostly observed and caused by the use of larger bearing plates in specimen S3. This conclusion is very important: 1D shear and punching shear failure modes must be included in the design of new in-span hinges and in the evaluation of existing ones.

Finally, it can be concluded that the D/C ratios of sliding shear failure mode in both the diaphragm and seat for all the test specimens were smaller than 0.72. Therefore, this failure mode is unlikely to occur in the studied in-span hinges.

7.4 FUTURE EXTENSIONS

The pre-test FEA conducted for the two specimens of phase I did not predict the experimental response accurately. Therefore, the first future task of this study is to calibrate the FEA model with the experimental results for the five specimens in phases I and II to improve its predictability. For this calibration, the real material properties will be used and different material constitutive models for reinforcement and concrete will be explored. Additionally, different solution strategies will be incorporated for improved convergence in the nonlinear solution. Special attention will be placed in enhancing the capability of the nonlinear FEA to predict the local punching shear failure mode.

After calibrating the nonlinear finite element model with the experimental results, a parametric study will be conducted using the FEA. This parametric study is aimed to develop new guidelines and specifications for the design of in-span hinges comprising the second future task of this study. The parameters that will be investigated are planned to include but may not be limited to (1) the reinforcement ratio of the diagonal bars of the seat, (2) the reinforcement ratio of the vertical bars of the diaphragm, (3) the reinforcement ratio of the longitudinal bars of the seat, (4) the concentration of reinforcement in the vicinity of the bearings, (5) the size of the bearing plates, and (6) the size of the utility openings.

Finally, new guidelines and design specifications will be proposed for in-span hinges of PC box-girder bridges as the third future task of this study. The design specifications will be based on the experimental results and the computational parametric study. The final specifications will combine the contribution of 1D shear, 2D SAT, and punching shear modes of failure to determine a realistic strength of the in-span hinges. In that regard, improved SAT models taking into account the other two modes of failure and the contribution of concrete in tension among other improvements will be developed.

REFERENCES

AASHTO, 2002. Standard Specifications for Highway Bridges, 17th Edition. American Association of State Highway and Transportation Officials, Washington, DC.

ACI Committee 318, 2008. Building Code Requirements for Structural Concrete and Commentary, ACI 318-08. American Concrete Institute, Farmington Hills, MI.

ASTM, 1997. Standard Specification for Welded Headed Bars for Concrete Reinforcement: Designation A970-97, American Society for Testing Materials, West Conshohocken, Pa.

ASTM, 2004a. Standard Test Method for Splitting Tensile Strength of Cylindrical Concrete Specimens: Designation C496/C496M-04. American Society for Testing Materials, West Conshohocken, Pa.

ASTM, 2004b. Standard Specification for Low-Alloy Steel Deformed and Plain Bars for Concrete Reinforcement: Designation A706-04. American Society for Testing Materials, West Conshohocken, Pa.

ASTM, 2004c. Standard Test Methods for Tension Testing of Metallic Materials: Designation E8-04. American Society of Testing Materials, West Conshohocken, Pa.

ASTM, 2005. Standard Test Method for Compressive Strength of Cylindrical Concrete Specimens: Designation C39/C39M -05. American Society for Testing Materials, West Conshohocken, Pa.

ASTM, 2007. Standard Test Method for Flexural Strength of Concrete (Using Simple Beam with Center-Point Loading: Designation C293-07. American Society for Testing Materials, West Conshohocken, Pa.

Bažant, Z.P., and Planas, J., 1998. Fracture and Size Effect in Concrete and Other Quasibrittle Materials. CRC Press LLC, Boca Raton, FL.

Berner, D.E., Gerwick, B.C., Hoff, G.C., 1991. T-Headed Stirrup Bars, *Concrete International*, Vol. 13, No. 5, pp. 49-53.

Caltrans, 2004. *Bridge Design Specifications*, California Department of Transportation, Sacramento.

Caltrans, 2005. Pre-Qualified Product List. http://www.dot.ca.gov/hq/esc/approved_prod- ucts_list/. California Department of Transportation, Sacramento.

Caltrans, 2006. Seismic Design Criteria, Version 1.4. California Department of Transportation, Sacramento.

Caltrans, 2007. Bridge Standard Detail Sheets (XS Sheets). http://www.dot.ca.gov/hq-/esc/-techpubs/manual/bridgemanuals/bridge-standard-detail-sheets/index.html. California Department of Transportation, Sacramento.

Comité Euro-International du Béton, 1990. *CEB-FIP Model Code.*

DesRoches, R., Fenves, G., 2001. Simplified Restrainer Design Procedure for Multiple-Frame Bridges. *Earthquake Spectra*, Vol. 17, No. 4, pp. 551-567.

DIANA, 2007. Diana Finite Element Analysis User's Manual Release 9.2, TNO DIANA vb, The Netherlands.

Dilger, W., Ghali, A., 1997. Double Head Studs as Ties in Concrete Walls and Columns. *ACI Concrete International*, Vol. 19, No. 6, pp. 59-66.

Dwight, A.E., 2006. Preliminary Stress Analysis using Finite Element Method for In-Span Hinge Diaphragms in Pre-stressed Concrete Box-Girder Bridges. Master of Engineering Report, University of California, Berkeley.

EERI, 2005. Northridge Earthquake Reconnaissance Report, Volume 1, *Earthquake Spectra*, 11: pp. 287-372, supplemental report to Volume 11.

Lehman, D., Gookin S., Nacamuli, A., Moehle, J. 2001. Repair of Earthquake-Damaged Bridge Columns. *ACI Structural Journal*, Vol. 98, No. 2, pp. 233-242.

Haroun, M., Pardoen, G., Bhatia, H., Shahi, S., Zazanjy, R., 2000. Structural Behavior of Repaired Pier Walls. *ACI Structural Journal*, Vol. 97, No. 2, pp. 259-267.

Harris, H., Sabnis, G., 1999. Structural Modeling and Experimental Techniques, Second Edition. CRC Press.

Hughes, T. J. 2000. The Finite Element Method, Linear Static and Dynamic Finite Element Analysis. Dover Publications, Mineola, New York.

Maekawa, K., Pimanmas, A., Okamura, H., 2004. *Nonlinear Mechanics of Reinforced Concrete*. Spon Pres, New York, NY.

MacGregor, J., Wight, J., 2005. *Reinforced Concrete, Mechanics and Design, Fourth Edition*. Pearson Prentice Hall. Upper Saddle River, New Jersey.

McMackin, P.J., Slutter, R.G., Fisher, J.W., 1973. Headed Steel Anchor Under Combined Loading. *AISC Engineering Journal*, Vol. 10, No. 2, pp. 43-52.

Megally, S., Silva, P., Seible, F. 2002. *Seismic Response of Sacrificial Shear Keys in Bridge Abutments.* Final Caltrans Report , Univ. of California, San Diego.

Mosalam, K.M., Mosallam, A., 2001. Nonlinear Transient Analysis of Reinforced Concrete Slabs Subjected to Blast Loading and Retrofitted with CFRP Composites. *Composites Part B: Engineering*, Vol. 32, No. 6, pp. 623-636.

Mosalam, K., Naito, C., and Khaykina, S., 2002, Bidirectional Cyclic Performance of Reinforced Concrete Bridge Column-Superstructure Subassemblies. *Earthquake Spectra*, Vol. 18, No. 4, pp. 663-687.

Naito, C., Moehle, J., Mosalam, K., 2001. Experimental and Computational Evaluation of Reinforced Concrete Bridge Beam-Columns Connections for Seismic Performance. PEER Report 2001/08, University of California, Berkeley.

Ranjbaran, A., 1991. Embedding of Reinforcements in Reinforced Concrete Elements Implemented in DENA, *Computer and Structures*, Vol. 40, No. 4, pp. 925-930.

Rilem TC 50-FMC, 1985. *Determination of the Fracture Energy of Mortar and Concrete by Means of Three-point Bend Tests on Notched Beams*. Committee on the Fracture Mechanics of Concrete, Materials and Structures, Vol. 18, No. 106, pp. 285–290.

Rots, J., Nauta, P., Kusters, G., Blaauwendraad, J., 1985. *Smeared Crack Approach and Fracture Localization in Concrete*. *Heron*, Vol. 30, No. 1.

Rots, J., 1991. Smeared and Discrete Representations of Localized Fracture. *International Journal of Fracture*, Vol. 51, No. 1, pp. 45-59.

Schlaich, J., Schäfer, K., Jennewein, M. 1987. Towards a Consistent Design of Structural Concrete. *Journal of the Prestressed Concrete Institute.* Vol. 32, No. 3, pp. 74-150.

Selby, R.G. and Vecchio, F.J., 1993. Three Dimensional Constitutive Relations for Reinforced Concrete. Tech. Report 93-02, Department of Civil Engineering, Univ. of Toronto, Canada.

Stoker, J.R., Boulware, R.L., Crozier, W.F., Swirsky, R.A., 1974. Anchorage Devices for Large Diameter Reinforcing Bars. Caltrans Report CA-DOT-TL-6626-1-73-30, California Department of Transportation, Sacramento.

Thompson, M., Jirsa, J., Breen, J., Klinger, R., 2002. Anchorage Behavior of Headed Reinforcement: Literature Review. Research Report 1855-1, Center for Transportation Research, The University of Texas, Austin.

Thompson, M., Ziehl, M., Jirsa, J., Breen, J. 2005. CCT Nodes Anchored by Headed Bars—Part 1: Behavior of Nodes. *ACI Structural Journal*, Vol. 102, No. 6, pp. 808-815.

Thompson, M., Jirsa J. and Breen J. 2006a. CCT Nodes Anchored by Headed Bars—Part 2: Capacity of Nodes. *ACI Structural Journal*, Vol. 103, No. 1, pp. 65-73.

Thompson, M., Jirsa, J., Breen J., 2006b. Behavior and Capacity of Headed Reinforcement. *ACI Structural Journal*, Vol. 101, No. 4, pp. 522-530.

Tjhin, T.N., Kuchma, D.A., 2002. Computer-Based Tools for Design by Strut-and-Tie Method: Advances and Challenges. *ACI Structural Journal*, Vol. 99, No. 5, pp. 586-594.

Tjhin, T.N., 2004. Analysis and Design Tools for Structural Concrete Using Strut-and-Tie Models. Ph.D. Thesis, University of Illinois at Urbana-Champaign.

Vecchio, F.J., Collins, M.P., 1986. The Modified Compression-Field Theory for Reinforced Concrete Elements Subjected to Shear, *ACI Structural Journal*, Vol. 83 No. 22, pp. 219-231.

Vlassis, A.G., Maragakis, E., Mehdi, S., 2004. Experimental Evaluation of Longitudinal Seismic Performance of Bridge Restrainers at In-Span Hinges. *Journal of Testing and Evaluation*, Vol. 32, No. 2, pp. 96-105.

Voce, E., 1948. The relationship Between Stress and Strain for Homogenous Deformation. *Journal of the Institute of Metals*, Vol. 74, No. 11, pp. 537-562.

Zienkiewicz, O.C., Taylor, R.L. 2005. The Finite Element Method, Sixth Edition. Elsevier Butterworth-Heinemann, Burlington, MA.

Appendix A: Specimen Structural Drawings

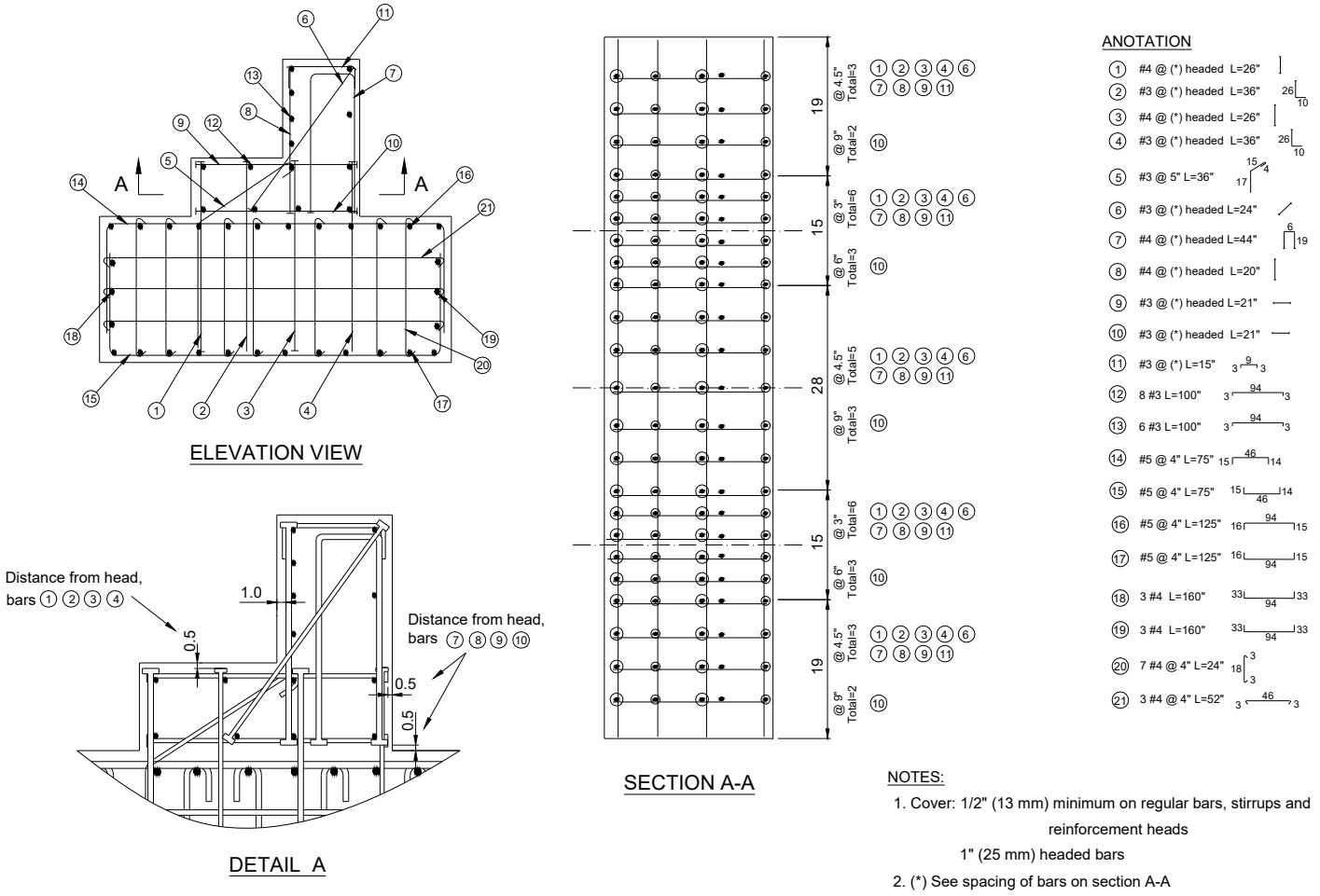

Fig. A.1 Reinforcement details of specimen S1 (Dimensions [in.]: 1"=25.4 mm).

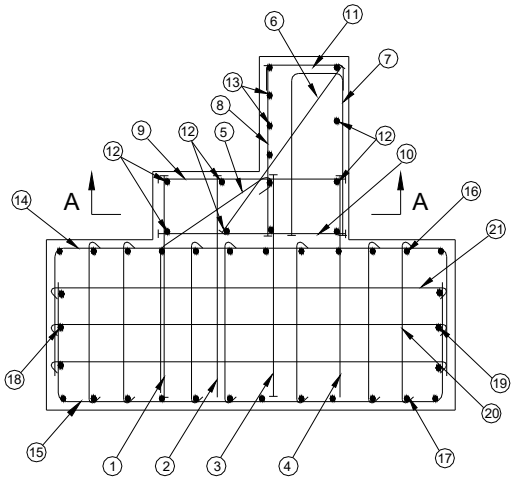

SECTION B-B

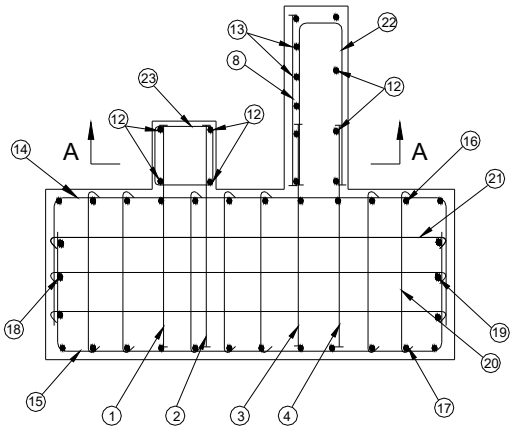

SECTION C-C

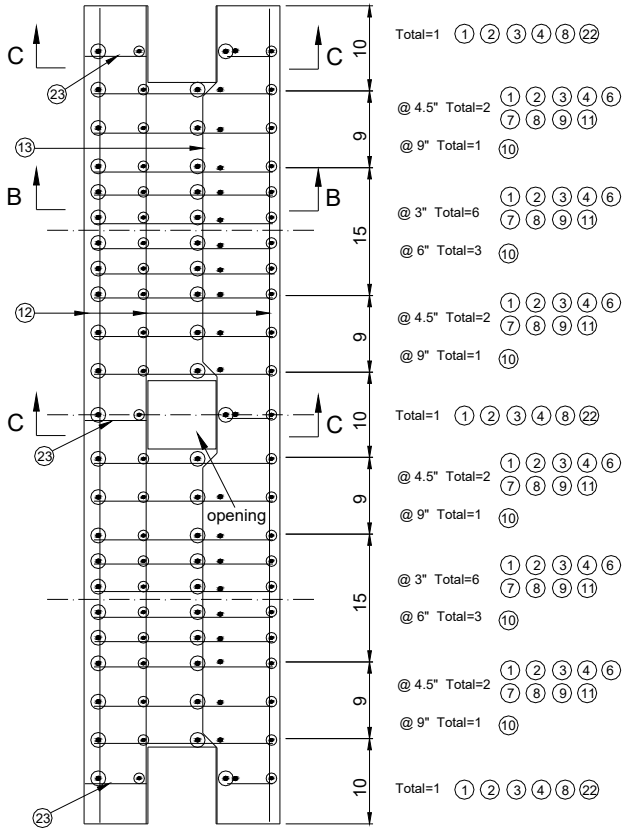

SECTION A-A

Total=1 ① ② ③ ④ ⑧ ㉒

@ 4.5" Total=2 ① ② ③ ④ ⑥ ⑦ ⑧ ⑨ ⑪

@ 9" Total=1 ⑩

@ 3" Total=6 ① ② ③ ④ ⑥ ⑦ ⑧ ⑨ ⑪

@ 6" Total=3 ⑩

@ 4.5" Total=2 ① ② ③ ④ ⑥ ⑦ ⑧ ⑨ ⑪

@ 9" Total=1 ⑩

Total=1 ① ② ③ ④ ⑧ ㉒

@ 4.5" Total=2 ① ② ③ ④ ⑥ ⑦ ⑧ ⑨ ⑪

@ 9" Total=1 ⑩

@ 3" Total=6 ① ② ③ ④ ⑥ ⑦ ⑧ ⑨ ⑪

@ 6" Total=3 ⑩

@ 4.5" Total=2 ① ② ③ ④ ⑥ ⑦ ⑧ ⑨ ⑪

@ 9" Total=1 ⑩

Total=1 ① ② ③ ④ ⑧ ㉒

ANOTATION

① #4 @ (*) headed L=26"

② #3 @ (*) headed L=36" 26, 10

③ #4 @ (*) headed L=26"

④ #3 @ (*) headed L=36" 26, 10

⑤ #3 @ 5" L=36" 15, 4, 17

⑥ #3 @ (*) headed L=24"

⑦ #4 @ (*) headed L=44" 6, 19

⑧ #4 @ (*) headed L=20"

⑨ #3 @ (*) headed L=21"

⑩ #3 @ (*) headed L=21"

⑪ #3 @ (*) L=15" 3, 9, 3

⑫ 8 #3 L=100" 3, 94, 3

⑬ 6 #3 L=98" 8, 31, 9, 31, 8, 12

⑭ #5 @ 4" L=75" 15, 46, 14

⑮ #5 @ 4" L=75" 15, 14, 46

⑯ #5 @ 4" L=125" 16, 94, 15

⑰ #5 @ 4" L=125" 16, 15, 94

⑱ 3 #4 L=160" 33, 33, 94

⑲ 3 #4 L=160" 33, 33, 94

⑳ 7 #4 @ 4" L=24" 18, 3, 3

㉑ 3 #4 @ 4" L=52" 3, 46, 3

㉒ #4 @ (*) L=43" headed 5, 19

㉓ 1+1+1 #3 L=34" 7, 7

NOTES:

1. Cover: 1/2" (13 mm) minimum on regular bars, stirrups and reinforcement heads
   1" (24 mm) headed bars
2. (*) See spacing of bars on section A-A
3. See location of headed bars in detail A of specimen 1

Fig. A.2 Reinforcement details of specimen S2 (Dimensions [in.]: 1"=25.4 mm).

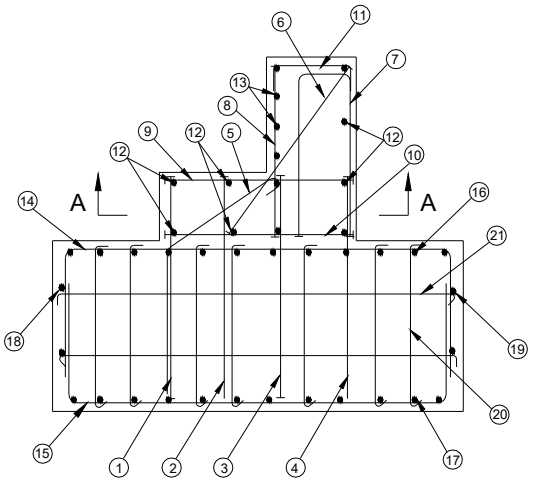

SECTION B-B

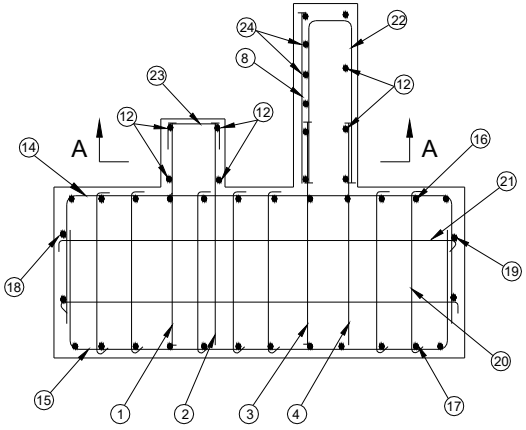

SECTION C-C

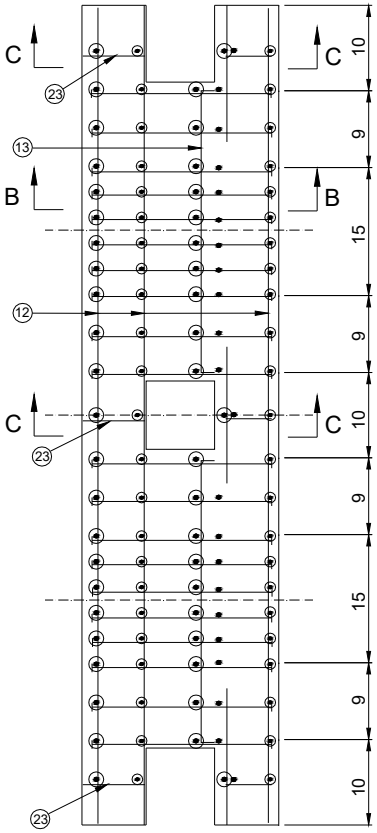

SECTION A-A

Total=1 ① ② ③ ④ ⑧ ㉒

@ 4.5" Total=2 ① ② ③ ④ ⑥ ⑦ ⑧ ⑨ ⑪

@ 9" Total=1 ⑩

@ 3" Total=6 ① ② ③ ④ ⑥ ⑦ ⑧ ⑨ ⑪

@ 6" Total=3 ⑩

@ 4.5" Total=2 ① ② ③ ④ ⑥ ⑦ ⑧ ⑨ ⑪

@ 9" Total=1 ⑩

Total=1 ① ② ③ ④ ⑧ ㉒

@ 4.5" Total=2 ① ② ③ ④ ⑥ ⑦ ⑧ ⑨ ⑪

@ 9" Total=1 ⑩

@ 3" Total=6 ① ② ③ ④ ⑥ ⑦ ⑧ ⑨ ⑪

@ 6" Total=3 ⑩

@ 4.5" Total=2 ① ② ③ ④ ⑥ ⑦ ⑧ ⑨ ⑪

@ 9" Total=1 ⑩

Total=1 ① ② ③ ④ ⑧ ㉒

ANOTATION

① #4 @ (*) headed L=26"
② #3 @ (*) headed L=35" 26, 10
③ #4 @ (*) headed L=26"
④ #3 @ (*) headed L=35" 26, 10
⑤ #3 @ 5" L=36" 15, 4, 17
⑥ #3 @ (*) headed L=24"
⑦ #4 @ (*) headed L=42" 6, 19
⑧ #4 @ (*) headed L=20"
⑨ #3 @ (*) headed L=21"
⑩ #3 @ (*) headed L=21"
⑪ #3 @ (*) L=15" 4, 9, 4
⑫ 8 #3 L=100" 4, 94, 4
⑬ 6+6+6 #3 L=40" 4, 34, 4
⑭ #5 @ 4" L=70" 14, 45, 14
⑮ #5 @ 4" L=70" 14, 45, 14
⑯ #5 @ 4" L=118" 14, 93, 14
⑰ #5 @ 4" L=118" 14, 93, 14
⑱ 2 #4 L=158" 33, 94, 33
⑲ 2 #4 L=158" 33, 94, 33
⑳ 7 #4 @ 4" L=26" 18
㉑ 2 #4 @ 4" L=54" 46
㉒ 1+1+1 #4 L=41" headed 5, 19
㉓ 1+1+1 #3 L=12" 4, 6, 4
㉔ 6+6+6 #3 L=16" 16

NOTES:

1. Cover: 1/2" (13 mm) minimum on regular bars and stirrups
2. (*) See spacing of bars on section A-A
3. See location of headed bars in detail A of specimen 4

Fig. A.3 Reinforcement details of specimen S3 (Dimensions [in.]: 1"=25.4 mm).

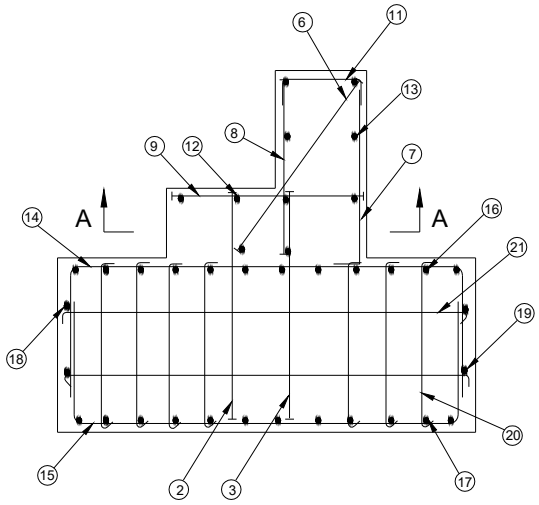

ELEVATION VIEW

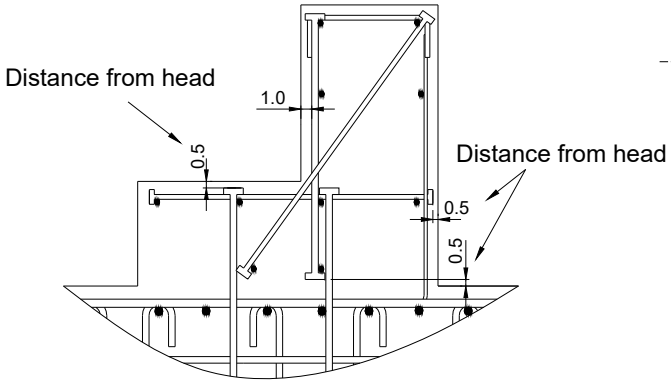

DETAIL A

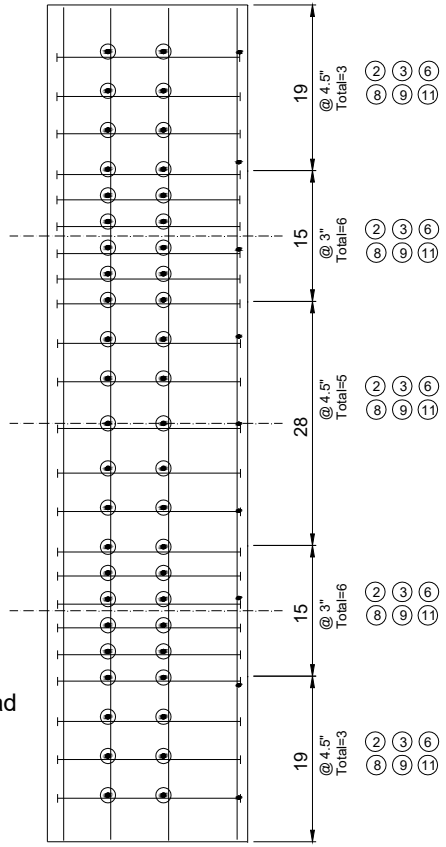

SECTION A-A

ANOTATION

② #4 @ (*) headed L=26"
③ #4 @ (*) headed L=26"
⑥ #3 @ (*) headed L=24"
⑦ #3 @ 10" L=23"
⑧ #4 @ (*) headed L=20"
⑨ #3 @ (*) headed L=21"
⑪ #3 @ (*) L=15"
⑫ 6 #3 L=100"
⑬ 4 #3 L=100"
⑭ #5 @ 4" L=70"
⑮ #5 @ 4" L=70"
⑯ #5 @ 4" L=118"
⑰ #5 @ 4" L=118"
⑱ 2 #4 L=158"
⑲ 2 #4 L=158"
⑳ 7 #4 @ 4" L=26"
㉑ 2 #4 @ 4" L=54"

NOTES:

1. Cover: 1/2" (13 mm) minimum on regular bars and stirrups
2. (*) See spacing of bars on section A-A
3. See location of headed bars in detail A of specimen 4

Fig. A.4 Reinforcement details of specimen S4 (Dimensions [in.]: 1"=25.4 mm).

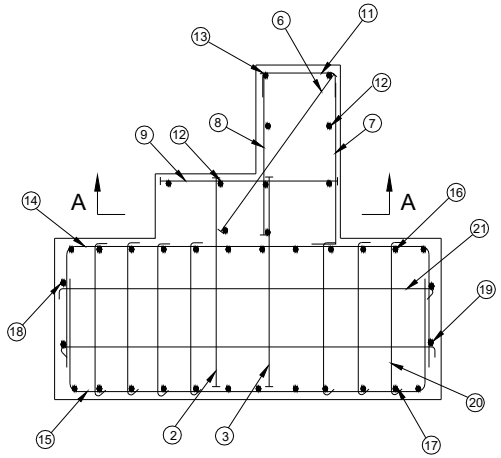

SECTION B-B

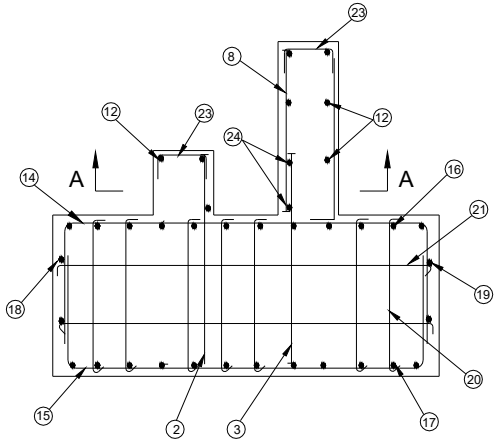

SECTION C-C

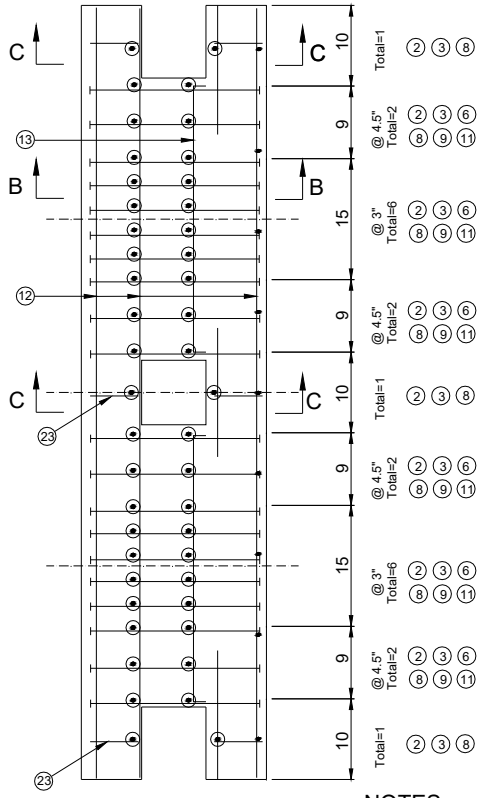

SECTION A-A

ANOTATION

② #4 @ (*) headed L=26"
③ #4 @ (*) headed L=26"
⑥ #3 @ (*) headed L=24"
⑦ #3 @ 10" L=23"
⑧ #4 @ (*) headed L=20"
⑨ #3 @ (*) headed L=21"
⑪ #3 @ (*) L=15"
⑫ 6 #3 L=100"
⑬ 4+4+4 #3 L=40"
⑭ #5 @ 4" L=70"
⑮ #5 @ 4" L=70"
⑯ #5 @ 4" L=118"
⑰ #5 @ 4" L=118"
⑱ 2 #4 L=158"
⑲ 2 #4 L=158"
⑳ 7 #4 @ 4" L=26"
㉑ 2 #4 @ 4" L=54"
㉓ 2+2+2 #3 L=14"
㉔ 4+4+4 #3 L=16"

NOTES:

1. Cover: 1/2" (13 mm) minimum on regular bars and stirrups
2. (*) See spacing of bars on section A-A
3. See location of headed bars in detail A of specimen 4

Fig. A.5 Reinforcement details of specimen S5 (Dimensions [in.]: 1"=25.4 mm).

Appendix B: Material Testing

Extensive material testing was conducted for concrete and reinforcing steel as part of the research program. The details of the material testing are described in this appendix.

B.1 CONCRETE

Normal-weight concrete was used with a characteristic strength of 5 ksi (34.5 MPa) and 3/8" (10 mm) maximum aggregate size. The water/cement ratio of the mix was 0.45 and the detailed mix design is shown in Table B.1.

Table B.1 Concrete mix design.

Material	Saturated surface dry weight [lbf (kgf)]	Volume [ft^3 (L)]
Cement ASTM C-150, Type II/V	564 (338)	2.87 (106)
Fly ash ASTM C-618, Class F	141 (84)	0.98 (36)
Sand ASTM C-33	1681 (1007)	10.22 (379)
Aggregate ASTM C33 3/8" #8	1245 (745)	7.44 (276)
Water ASTM C1602-04, C1603-04	317 (190)	5.08 (188)
Air 1.5%	-	0.41 (15)
Water reducing admixture ASTM C-494 type A&F	-	7 fl. oz (0.021)
Retarder admixture ASTM C-494 Type A.	-	3 fl.oz (0.089)
Total	3948 (2346)	27.0 (1000)

Concrete used in the in-span hinge specimens was subjected to six different tests, three related to compressive behavior and three related to tensile behavior. For determining the compressive characteristics, concrete was tested using compressive strength, compressive stress-strain using load control, and compressive stress-strain using displacement control. For

determining the tensile characteristics, concrete was tested using splitting tensile strength, modulus of rupture, and fracture energy.

B.1.1 Compressive Tests

The compressive strength test was conducted to monitor the strength gain of concrete with time. For this test, standard 6"×12" (152 mm×305 mm) cylinders were used. The cylinders were cured next to the in-span hinge specimens and were stripped at the same age as the in-span hinge specimens. The cylinders were capped with a sulfur compound and were tested in a Universal Testing Machine at a rate of 35 psi/min (0.241 MPa/min) in accordance with ASTM C39-05 (ASTM 2005). The test setup and a tested cylinder are shown in Figure B.1. The test results for the concrete of the two experimental phases are shown in Table B.2. The strength gain of the concrete versus time is shown in Figure B.2.

(a) Test setup (b) Tested concrete cylinder

Fig. B.1 Compressive strength test.

Table B.2 Compressive strength test results.

Phase I: Specimens S1 and S2		
Days	Compressive strength f_c' [ksi (MPa)]	Standard deviation [ksi (MPa)]
7	5.00 (34.5)	0.04 (0.24)
14	5.68 (39.1)	0.17 (1.17)
28	6.10 (42.1)	0.07 (0.45)
78	6.44 (44.4)	0.06 (0.40)
110	6.15 (42.4)	0.05 (0.34)

Phase II: Specimens S3, S4 and S5		
Days	Compressive strength f_c' [ksi (MPa)]	Standard deviation [ksi (MPa)]
7	4.76 (32.8)	0.02 (0.16)
14	6.36 (43.8)	0.06 (0.40)
28	6.76 (46.6)	0.07 (0.50)
29	6.89 (47.5)	0.11 (0.77)
37	6.82 (47.0)	0.14 (0.99)
50	6.91 (47.6)	0.15 (1.04)

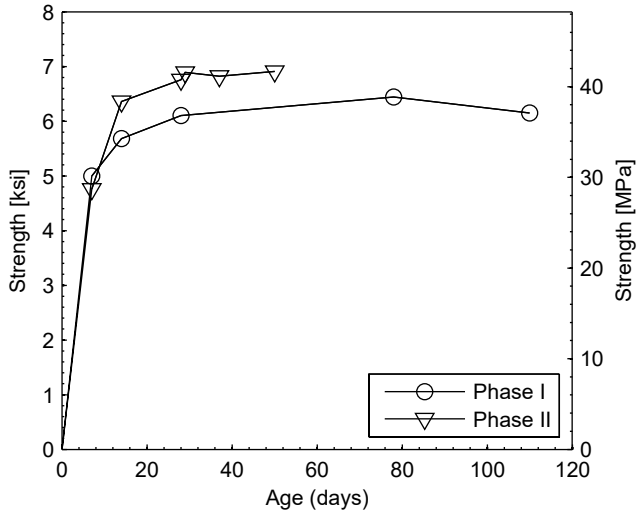

Fig. B.2 Compressive strength versus age for in-span hinge specimens.

A compressive stress-strain test using force control was performed to determine the constitutive behavior of concrete in the compression hardening zone, before the peak load. The test was conducted using standard 6"×12" (152 mm×305 mm) cylinders with a Universal Testing Machine. The test setup is shown in Figure B.3. A total of four cylinders were tested for each in-span hinge specimen at the same age of the in-span hinge test. The load was applied at a constant rate of 35 psi/min (0.241MPa/min), and the deformation was measured using two displacement transducers (LVDT) connected on the opposite sides of the cylinder as shown in Figure B.3. The summary of the test results are shown in Table B.3. From the stress-strain test, the modulus of elasticity E_c of concrete was computed using the secant stiffness at $0.4f_c'$. An example of the

compressive stress-strain test results using force control is shown in Figure B.4. The example corresponds to the four cylinders tested for specimen S1.

(a) Test setup

(b) Instrumentation detail

Fig. B.3 Compressive stress-strain test using force control.

Table B.3 Stress-strain compressive test results using force control.

In-span hinge Specimen	Age [days]	Compressive strength f_c' [ksi (MPa)]		Strain at peak stress ε_o		Modulus of elasticity E_c [ksi (GPa)]	
		Mean	St. dev.	Mean	St. dev.	Mean	St. dev.
S1	78	6.44 (44.4)	0.06 (0.40)	0.0029	0.00007	3240 (22.4)	26.9 (0.19)
S2	110	6.15 (42.4)	0.05 (0.32)	0.0029	0.00005	3100 (21.4)	26.3 (0.18)
S3	29	6.89 (47.5)	0.11 (0.77)	0.0035	0.00008	2940 (20.3)	43.3 (0.30)
S4	37	6.82 (47.0)	0.14 (0.99)	0.0037	0.00012	2860 (19.7)	11.0 (0.08)
S5	50	6.91 (47.6)	0.15 (1.04)	0.0034	0.00016	2940 (20.3)	28.8 (0.20)

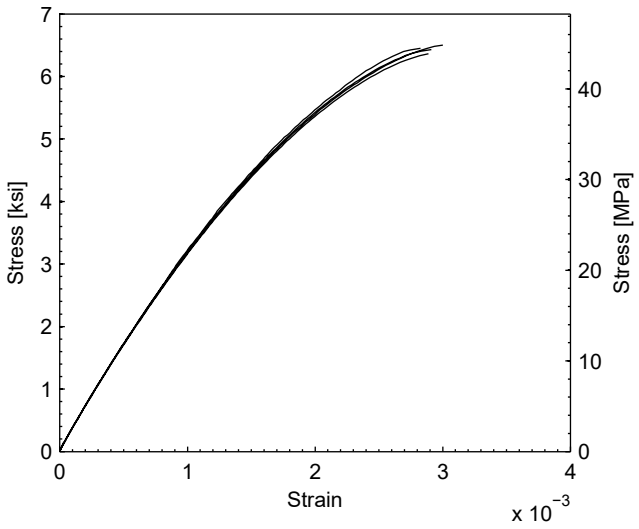

Fig. B.4 Stress-strain test using force control for cylinders of in-span hinge specimen S1.

A compressive stress-strain test using displacement control was conducted to determine the constitutive behavior of concrete after the peak load. The test was performed using standard 6"×12" (152 mm×305 mm) cylinders with an MTS testing machine as shown in Figure B.5a. The deformation of the concrete was measured with two LVDTs as shown in Figure B.5b. The test was conducted using an average velocity of 0.002 in/min (0.051 mm/min) measured at the LVDTs. A total of four cylinders were tested for the concrete of the in-span hinge specimens of phase I at an age of 111 days. The summary of the test results are shown in Table B.4. The compressive fracture energy G_{fc} is obtained using the area under the stress-strain relationship and the gage length of the test. The normalized stress-strain relationships obtained are shown in Figure B.6. These relationships are normalized using the peak strength and the corresponding strain for each test.

(a) Test setup (b) Instrumentation detail

Fig. B.5 Compressive stress-strain test under displacement control.

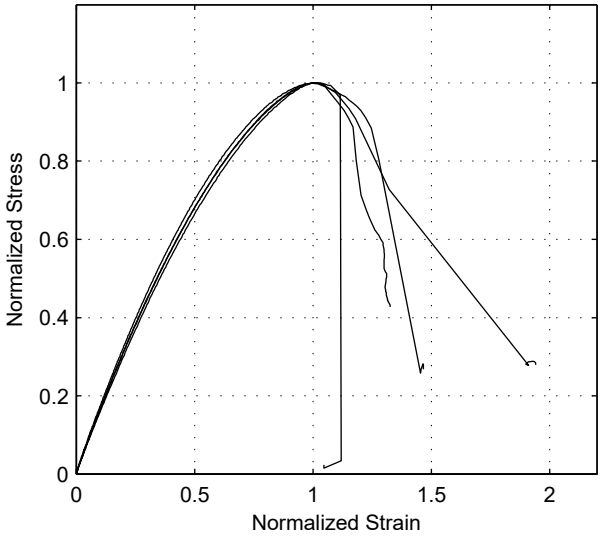

Fig. B.6 Normalized relationships for stress-strain tests using displacement control for cylinders of in-span hinge specimen S1.

Table B.4 Stress-strain compressive test results using displacement control for cylinders of in-span hinge specimen S1.

	Mean	St. dev.
Compressive strength [ksi (MPa)]	5.86 (40.4)	0.07 (0.49)
Strain at peak stress ε_o	0.0029	0.00013
Modulus of elasticity E_c [ksi (GPa)]	3030 (20.9)	34.0 (0.23)
Compression fracture energy G_{fc} [lbf/in. (N/mm)]	131 (22.8)	31.9 (5.6)

B.1.2 Tensile Tests

The splitting tensile strength represents a lower bound of the tensile strength of concrete. The test was conducted using standard 6"×12" (152 mm×305 mm) concrete cylinders according to ASTM C496-04 (ASTM 2004a). A total of four cylinders were tested for each in-span hinge specimen at the same age of the in-span hinge test. To execute the test, the concrete cylinder was placed on its side and loaded in compression as shown in Figure B.7a. The load was applied at a rate of 150 psi/min (1.03 MPa/min) and the maximum load P was recorded. The splitting tensile strength f_{ct} is computed from,

$$f_{ct} = \frac{2P}{\pi l d} \tag{B.1}$$

where l and d are the length and diameter of the standard cylinder, respectively. The test results are summarized in Table B.5.

(a) Splitting strength test setup

(b) Modulus of rupture test setup

Fig. B.7 Determining concrete tensile strength.

The modulus of the rupture test, or flexural test, gives a higher estimate of the tensile capacity than the splitting strength test. The test was performed using 3"×3"×12" (76.2 mm×76.2 mm×305 mm) concrete beams according to ASTM C293-07 (ASTM 2007). A total of 3 beams were tested for each in-span hinge specimen at the same age of the in-span hinge test. The test was conducted with a simply supported beam with span=L=9" (228.6 mm) and four-point bending, as shown in Figure B.7b. The load was applied using a loading rate of 300 psi/min (2.07 MPa/min). From the test, the maximum load P was recorded and the modulus of rupture f_r is computed from,

$$f_r = \frac{PL}{bh^2} \tag{B.2}$$

where b and h are the width and height of the beam cross section, respectively. The test results are summarized in Table B.5.

Table B.5 Splitting and modulus of rupture test results.

In-span hinge specimen	Age [days]	Splitting tensile f_{ct} [ksi (MPa)]		Modulus of rupture f_r [ksi (MPa)]	
		Mean	St. dev.	Mean	St. dev.
S1	78	0.52 (3.59)	0.014 (0.10)	0.89 (6.14)	0.025 (0.17)
S2	110	0.48 (3.31)	0.031 (0.21)	0.86 (5.93)	0.015 (0.10)
S3	29	0.62 (4.27)	0.037 (0.26)	1.00 (6.90)	0.060 (0.42)
S4	37	0.54 (3.72)	0.029 (0.20)	-	-
S5	50	0.56 (3.86)	0.035 (0.24)	0.86 (5.93)	0.054(0.37)

The fracture energy tests were conducted to evaluate the amount of energy released during tensile cracking of concrete. The fracture energy is defined as the amount of energy necessary to create one unit area of crack, and has units of energy per unit area. This energy is to be used in the post-test finite element analysis (FEA) to simulate the post-cracking behavior of concrete. The test was conducted according to the European recommendation (Rilem 1985). For the test, 4"×4"×36" (102 mm×102 mm×914 mm) concrete beams were cast containing a middle notch. The notch was introduced in the beam using a wood insert, such that the area of ligament above the notch A_{lig} was half of the total cross-section height. The beams were simply supported at a span of 32" (813 mm) and were loaded at the mid-point with a rate of 0.003 in/min (0.076 mm/min), as shown in Figure B.8a. The deformation of the beam was measured at the mid-point with a displacement transducer, as shown in Figure B.8b. The load-deformation information was recorded until failure. The fracture energy is computed using,

$$G_f = \frac{W_o + (m_1 + 2m_2)g\delta_0}{A_{lig}} \tag{B.3}$$

where W_o is the area under the load-deformation relationship, m_1 is the mass of the beam between the supports, m_2 is the mass of the loading support not attached to the machine, g is the acceleration of gravity, and δ_0 is the deformation at failure. For the in-span hinge specimens S1 and S2, a total of four beams were tested at a concrete age of 83 days, which is in between the age of the test of the first two in-span hinges. The test results are summarized in Table B.6 and the load-deformation relationships are shown in Figure B.9. The results show a large scatter, which is highly dependent on the crack initiation at the notch.

(a) Test setup

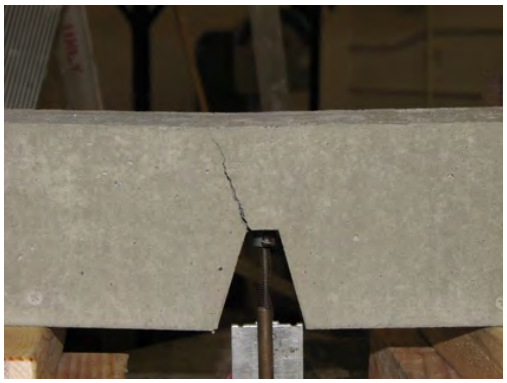

(b) Detail of failed specimen

Fig. B.8 Fracture energy test.

Table B.6 Fracture energy test results.

	Mean	St. dev.
Peak force [lbf (N)]	92.6 (412)	58.2 (259)
Deformation at failure δ_o [in (mm)]	0.053 (1.35)	0.009 (0.24)
Fracture energy G_f [lbf/in. (N/m)]	0.60 (105)	0.23 (40)

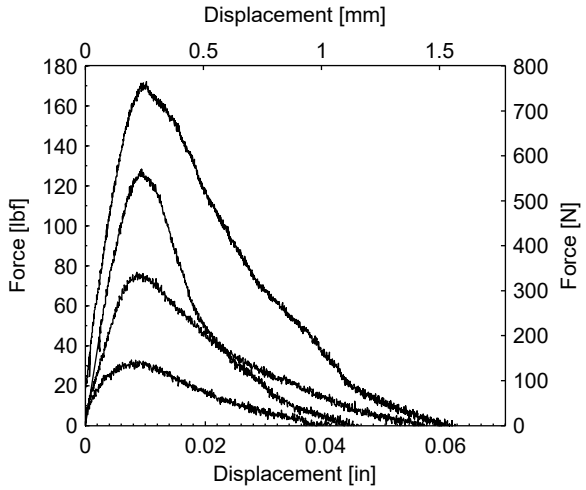

Fig. B.9 Load-deformation relationship obtained in fracture energy tests.

B.2 REINFORCING STEEL

The reinforcing steel used in the experimental program was Grade 60, meeting the requirements of ASTM A706-04 (ASTM 2004b). The in-span hinge specimens consider headed and non-headed reinforcing steel which were provided at each phase from two different sources. The headed bars were fabricated at HRC (Headed Reinforcement Company) and the non-headed bars were provided by a local steel distributor. The reinforcing steel used in the two phases of the in-span hinge specimens was tested in tension to obtain the stress-strain relationship to be used in the post-test FEA.

The in-span hinge specimens considered three different types of reinforcing steel in the in-span hinge region: #3 non-headed bars, #3 headed bars and #4 headed bars. For each type of steel, three coupons were tested using a Universal Testing Machine, as shown in Figure B.10a. The steel coupons were 24" (610 mm) long. To measure deformation, two displacement transducers were attached as shown in Figure B.10b. This deformation was measured between two points separated at 2" (50.8 mm). The bars were loaded according to ASTM E8-04 (ASTM 2004c) with an initial rate of 2000 lbf/min (8.9 kN/min). The test was stopped when a decrease in the strength was observed to prevent damage in the instruments. From the tests, the stress and strain were calculated by dividing the total force by the nominal cross-sectional area of the reinforcing bar and the deformation by the gage length, i.e., 2" (50.8 mm), respectively. The test results of the reinforcing steel of phase I and phase II are summarized in Tables B.7 and B.8, respectively. Test results of reinforcing steel used in phase II, respectively. The stress-strain relationships obtained from all the reinforcing bar tests are shown Figure B.11.

(a) Test setup

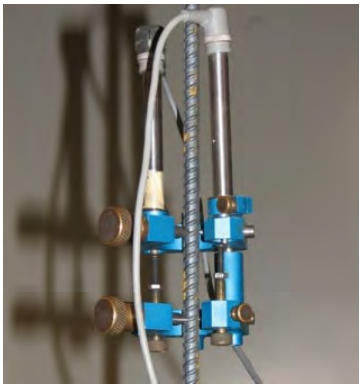

(b) Instrumentation detail

Fig. B.10 Reinforcing steel tensile test.

Table B.7 Test results of reinforcing steel used in phase I.

	#3 Non-headed		#3 Headed		#4 Headed	
	Mean	St. dev.	Mean	St. dev.	Mean	St. dev.
Yield stress f_y [ksi (MPa)]	69.9 (482)	0.46 (3.2)	69.5 (479)	1.3 (8.6)	68.7 (474)	0.21 (1.15)
Ultimate stress f_u [ksi (MPa)]	103.0 (710)	0.61 (4.2)	93.7 (646)	1.01 (7.0)	97.8 (674)	1.81 (12.5)
Modulus of elasticity E_s [ksi (GPa)]	28020 (193)	1300 (9.0)	29170 (201)	977 (6.7)	28390 (196)	142 (1.0)
Yield strain ε_y	0.0025	0.0001	0.0024	0.0001	0.0024	0.0000
Ultimate strain ε_u	0.137	0.020	0.114	0.007	0.123	0.003

Table B.8 Test results of reinforcing steel used in phase II.

	#3 Non-headed		#3 Headed		#4 Headed	
	Mean	St. dev.	Mean	St. dev.	Mean	St. dev.
Yield stress f_y [ksi (MPa)]	74.9 (516)	2.10 (14.5)	73.4 (506)	3.77 (26.0)	66.8 (460)	2.06 (14.2)
Ultimate stress f_u [ksi (MPa)]	102.7 (708)	0.94 (6.5)	95.1 (656)	1.27 (8.8)	94.7 (653)	0.36 (2.5)
Modulus of elasticity E_s [ksi (GPa)]	26640 (184)	741 (5.1)	28140 (194)	1110 (7.7)	28070 (194)	5170 (36)
Yield strain ε_y	0.0028	0.0001	0.0026	0.0001	0.0023	0.0004
Ultimate strain ε_u	0.109	0.007	0.081	0.010	0.121	0.010

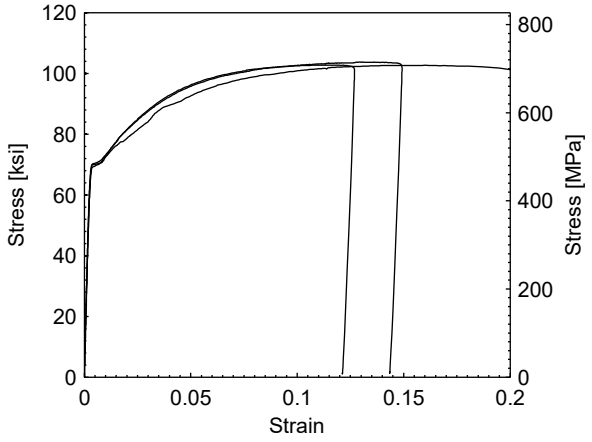

(a) Phase I, #3 non-headed

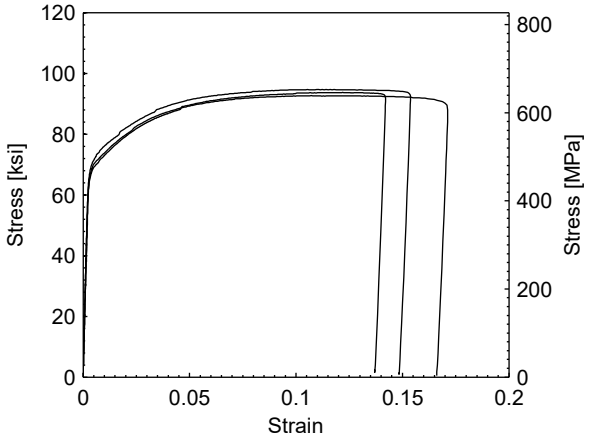

(b) Phase I, #3 headed

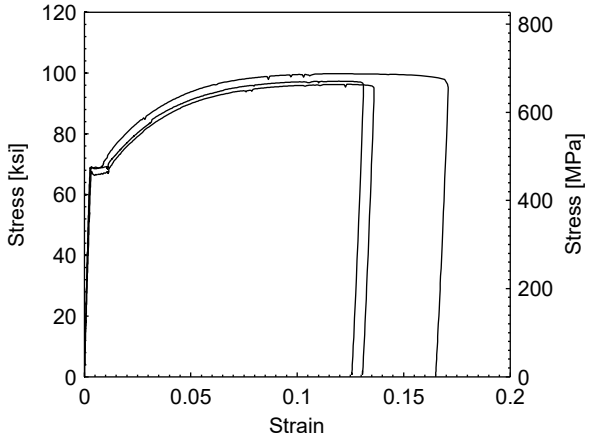

(c) Phase I, #4 headed

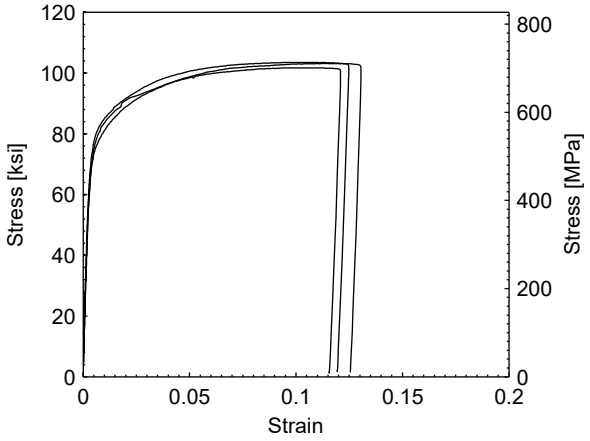

(d) Phase II, #3 non-headed

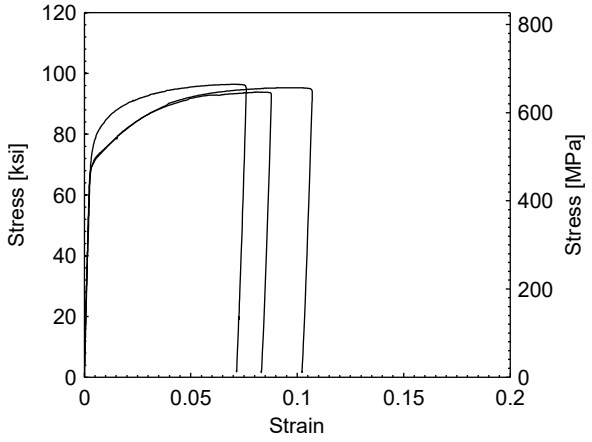

(e) Phase II, #3 headed

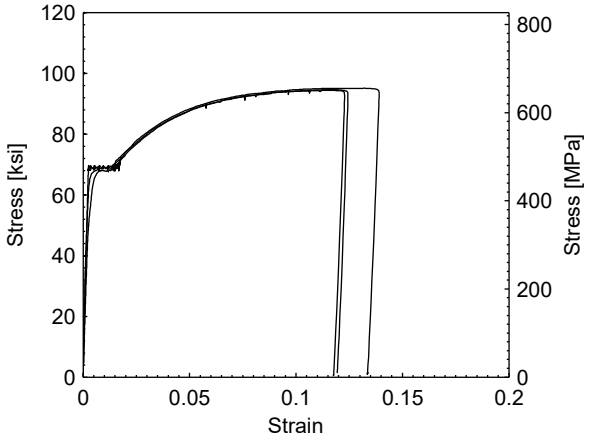

(f) Phase II, #4 headed

Fig. B.11 Stress-strain test results of reinforcing steel.

Appendix C: Load Cell Fabrication and Calibration

This appendix describes the characteristics of the two load cells fabricated specifically for this project. These load cells were fabricated with a target capacity of 300 kip (1334 kN) each and were made of AISI 4140 steel. Each load cell is 7 in. (178 mm) long and has external and internal diameters of 4¾ in (121 mm) and 3¼ in (83 mm), respectively.

C.1 LOAD CELLS INSTRUMENTATION

To measure the strains on the load cells, four tee rosettes were attached at the quadrants of the external surface. Each tee rosette had 120 Ω resistance and a gage length of 0.062 in. (1.58 mm). The rosettes were glued to the cylinder and were treated with three protective coating layers. The eight strain gages of each load cell were connected using a full bridge circuit as shown in Figure C.1.

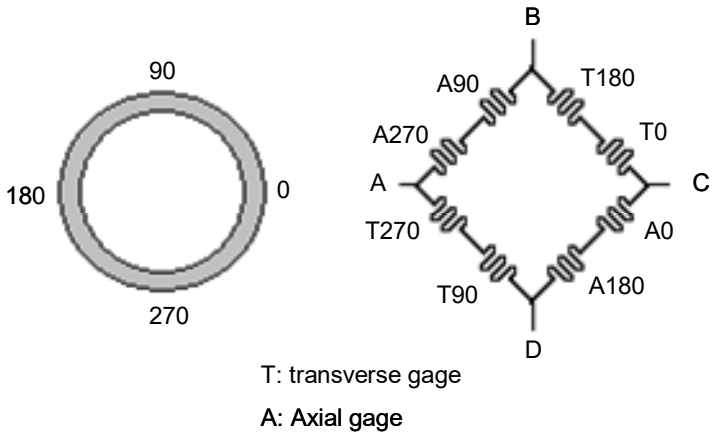

Fig. C.1 Strain gage connection diagram of load cells.

The input voltage of the load cell was applied at the terminals B and D of the Wheatstone bridge of Figure C.1. On the other hand, the output voltage was measured at the terminals A and

C of Figure C.1 and is given by Eq. C.1 (Harris and Sabnis 1999).

$$V_{AC} = \frac{FE}{4}\left(-2\varepsilon_l - 2\nu\varepsilon_l\right) \tag{C.1}$$

where ε_l is the longitudinal strain, E is the input voltage, F is the gage factor, and ν is the steel Poisson's ratio. Therefore, the output of the Wheatstone bridge was amplified by a factor of $2(1+\nu)$. The load cells with the glued rosettes are shown in Figure C.2.

Fig. C.2 Load cells with 300 kip (1335kN) capacity each.

C.2 LOAD CELLS CALIBRATION

The load cells were calibrated using a Universal Testing Machine with a capacity of 400 kip (1779 kN), as shown in Figure C.3. Before the calibration, the load cells were exercised by loading them three times up to 350 kip (1557 kN). The calibration of each load cell was performed using load increments of 30 kip (133.4 kN) and by recording the corresponding micro-strain measurements at the loading and unloading stages. The calibration results of the two load cells are shown in Figure C.4. The calibration revealed excellent linearity of these load cells.

Fig. C.3 Load cell calibration setup.

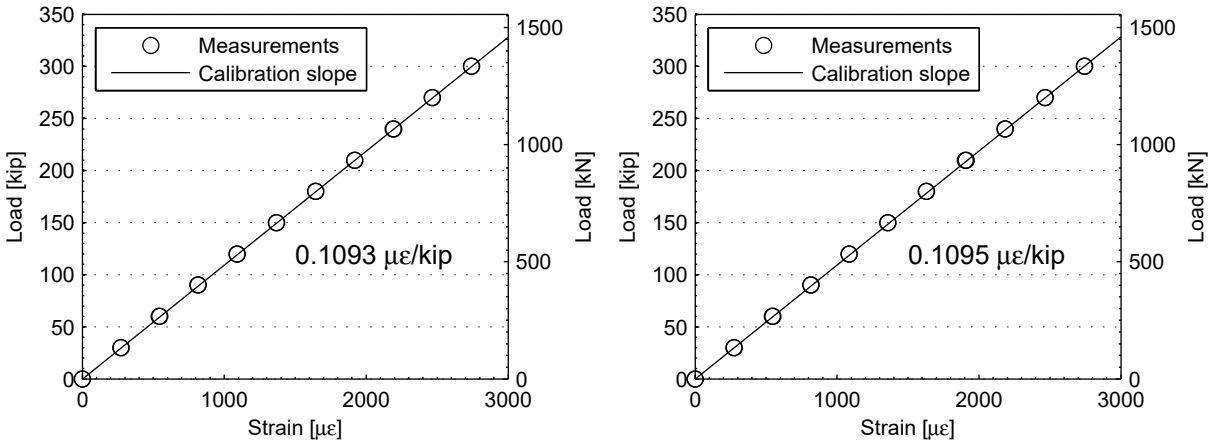

(a) Load cell 1 (b) Load cell 2

Fig. C.4 Load cells calibration results.